Superconductivity in strongly spin-orbit coupled systems

A thesis
submitted in partial fulfilment
of the requirements for the degree of
Doctor of Philosophy in Physics

by

Henri Menke

UNIVERSITY
of
OTAGO

SAPERE AUDE

Te Whare Wānanga o Otāgo

NEW ZEALAND

University of Otago
2020

Abstract

Superconductivity is a low-temperature quantum state of matter, marked by the vanishing of electrical resistance and the expulsion of magnetic flux fields. A thorough microscopic understand of superconductivity was gained through the seminal theory by Bardeen, Cooper, and Schrieffer (BCS theory), in which electrons are bound into so-called Cooper pairs by an attractive interaction in the material. In this theory the origin of the attractive interaction is the coupling of electrons to lattice vibrations which makes electrons pair together in a relative orbital s-wave state.

In the last decades, superconductors with properties that cannot be explained by the predictions of BCS theory have been discovered. The pairing mechanism in these *unconventional superconductors* remains incompletely understood, however, a symmetry-based phenomenological approach has proved to be very useful in determining the stable superconducting states and gap structures even if the pairing mechanism is unknown. More recently, materials with strong spin-orbit coupling have moved into the focus of attention due to their possible unconventional superconductivity. The mixing of orbital and spin degrees of freedom imposes strong constraints on the permissible Cooper pair structures but can be favourable for interesting exotic phenomena.

In this thesis we will theoretically study the physics of superconductors with strong spin-orbit coupling. Using field theory techniques and group theory arguments we investigate the properties of orbitally nontrivial pairing states. The presence of multiple bands qualitatively changes the nodal structure of an inversion-symmetric time-reversal symmetry-breaking superconductor. Instead of point or line nodes, the gap exhibits extended nodal pockets, called Bogoliubov Fermi surfaces.

These surfaces originate from the "inflation" of point and line nodes in the absence of time-reversal symmetry. We present a comprehensive theory for Bogoliubov Fermi surfaces and investigate their thermodynamic stability in a paradigmatic model. We find that a pairing state with Bogoliubov Fermi surfaces can be stabilized at moderate spin-orbit coupling strengths. Our results show that Bogoliubov Fermi surfaces of experimentally relevant size can be thermodynamically stable.

Strontium ruthenate (Sr_2RuO_4) has long been thought to be the textbook example of an odd-parity spin-triplet chiral p-wave superconducting state. However, recent spin-susceptibility measurements have observed a singlet-like response and cast serious doubts on this prediction. We propose an alternative even-parity pairing state, which is consistent with the new experimental observations. This state can be energetically stable once a realistic three-dimensional model of Sr_2RuO_4 is considered. This state naturally gives rise to Bogoliubov Fermi surfaces.

Publications

The following publications accompany this thesis:

[133] P. M. R. Brydon, D. F. Agterberg, **H. Menke**, and C. Timm, "Bogoliubov Fermi surfaces: General theory, magnetic order, and topology", Phys. Rev. B **98**, 224509 (2018).

[140] **H. Menke**, C. Timm, and P. M. R. Brydon, "Bogoliubov Fermi surfaces stabilized by spin-orbit coupling", Phys. Rev. B **100**, 224505 (2019).

[234] H. G. Suh, **H. Menke**, P. M. R. Brydon, C. Timm, A. Ramires, and D. F. Agterberg, "Stabilizing even-parity chiral superconductivity in Sr_2RuO_4", Phys. Rev. Research **2**, 032023 (2020).

The following works were also published during the course of this Phd but are not covered:

▶ **H. Menke** and M. M. Hirschmann, "Topological quantum wires with balanced gain and loss", Phys. Rev. B **95**, 174506 (2017).

▶ F. Weik, R. Weeber, K. Szuttor, K. Breitsprecher, J. de Graaf, M. Kuron, J. Landsgesell, **H. Menke**, D. Sean, and C. Holm, "ESPResSo 4.0 – An Extensible Software Package for Simulating Soft Matter Systems", Eur. Phys. J. Spec. Top. **227**, 1789 (2019).

# Contents

Chapter 1

Introduction

Superconductivity was discovered in 1911 by Kamerlingh Onnes [1] during experiments with liquid helium where it was noticed that the electrical resistance of mercury vanished below a temperature of 4.2 K with a sharp drop. During experiments on the magnetic field distribution outside superconducting samples Meissner and Ochsenfeld [2] discovered that the sample expelled the field. The phenomena of vanishing electrical resistance and expulsion of magnetic flux fields are the defining characteristics of superconductivity. The origin of superconductivity posed a big mystery to the physics community for a long time. After many failed attempts [3] to describe this low-temperature state of quantum matter and the purely phenomenological theories by Pippard [4], London and London [5], and Ginzburg and Landau [6, 7], the seminal proposal by Cooper [8], that electrons bind together in pairs, led to the development of a comprehensive microscopic theory of superconductivity, today known as BCS theory after its creators Bardeen, Cooper, and Schrieffer [9, 10]. During early experiments with elemental superconductors, such as Hg [11, 12], it was discovered that the critical temperature at which superconductivity sets in is related to the ionic mass of the atoms in the crystal [13, 14]. This phenomenon is known as *isotope effect* and indicates that superconductivity depends on the electron lattice interaction. This led to the identification that the attractive force that binds the electrons in pairs finds its origin in the electron-phonon interaction [15].

The starting point of BCS theory is that the normal state of the superconductor can be accurately described by a Fermi sea of non-interacting electrons, i.e. the normal state is a metal. The existence of a Fermi surface simplifies the problem tremendously, because it reduces the scattering problem in the three-dimensional Fermi sea to a two-dimensional one on the Fermi surface. This also results in the fact that superconductivity can arise from an *infinitesimal* attractive interaction, whereas usually a finite attractive interaction is required to form a bound state in three dimensions [15].

The origin of the attractive interaction is rooted in the electron-phonon coupling. This is generally assumed to be local and momentum-independent, due to the weakness of the electron-phonon coupling and the vastly different time-scales of electronic and lattice vibrations [15]. Because of the local pairing in combination with Pauli's exclusion principle, in BCS theory electrons form Cooper pairs in a spin-singlet state with a total angular momentum of zero, i.e. a relative s-wave orbital state. However, this implies that these Cooper pairs are very sensitive to Coulomb repulsion.

1.1 Unconventional Superconductors

The validity of BCS theory has been challenged with the discovery of unconventional superconductors, where the experimental phenomena differ substantially from the predictions of BCS theory. Deviations were first discovered in the heavy fermion compounds [16, 17] where the localized magnetic moments were expected to strongly disfavor superconductivity, such as $CeCu_2Si_2$ [18], UBe_{13} [19], and UPt_3 [20]. The most astonishing de-
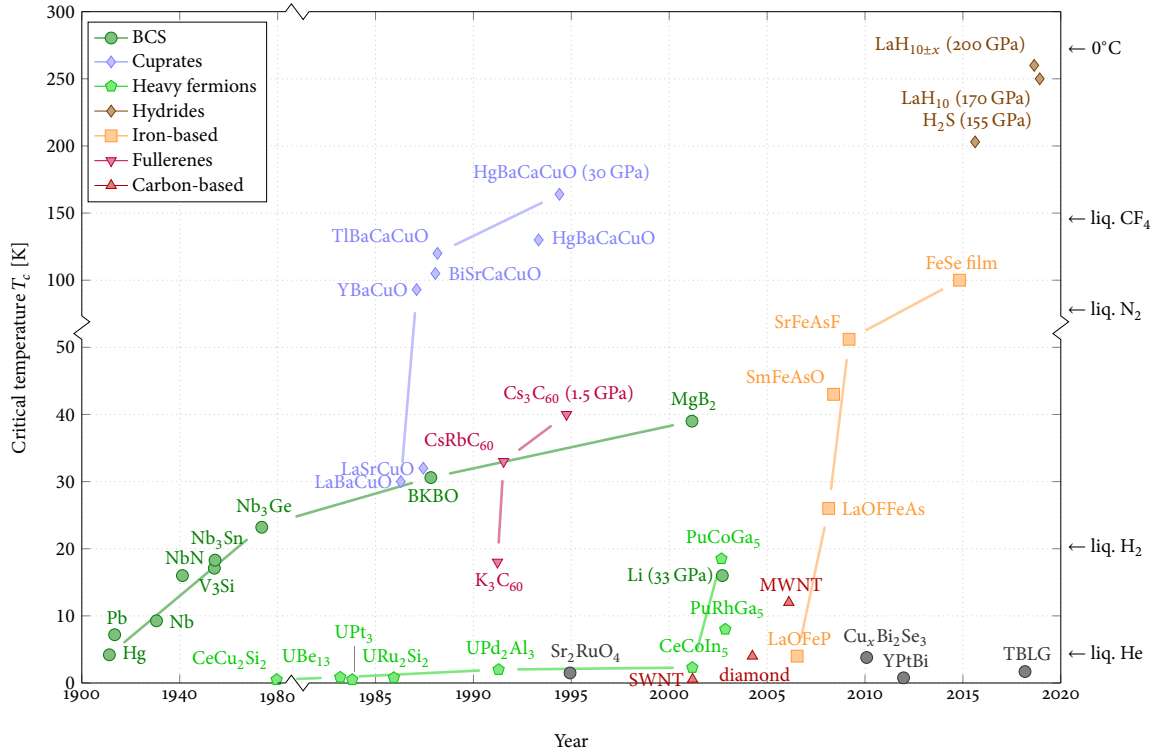
■ *Figure 1.1.* Timeline of transition temperatures in conventional and unconventional superconductors. Not all known superconductors are listed here and the selection is opinionated. Many compounds can be grouped into families which is indicated by colors and plotmarks. For a long time the cuprates were the only high-T_c family until the discovery of the iron-based superconductors. Recently the family of the hydrides has attracted some attention, because their superconductivity is BCS-like with a very high transition temperature.

velopment in this direction came with the discovery of "high T_c" superconductivity in $La_{5-x}Ba_xCu_5O_{5(3-y)}$ [21] with a critical temperature far beyond what was believed to be possible. This discovery led to an extensive survey of related compounds sharing the copper-oxide structure. The most well-known member of the family of these so-called *cuprates* are $YBa_2Cu_3O_{7-\delta}$ [22] ($T_c = 93\,K$) and $Bi_2Sr_2CaCu_2O_{8+x}$ [23] ($T_c = 105\,K$) whose critical temperature exceeds the melting point of liquid nitrogen which opened up the route for all kinds of technical applications [24]. In Fig. 1.1 we show a timeline of transition temperatures in high-temperature superconductors.

One key difference to conventional superconductors is that the cuprates, being ceramics, are insulating and show only ambiguous signs of an isotope effect. Superconductivity develops upon doping these compounds with holes away from the insulating state at zero doping which exhibits antiferromagnetic order. This indicates that the mechanism behind the pairing is no longer driven by the electron-phonon interaction but by magnetic fluctuations of the electrons themselves. However, without a strong electron-phonon interaction, the local Coulomb repulsion cannot be overcome such that the electrons can no longer form Cooper pairs in an orbital *s*-wave state, because the Coulomb repulsion will drive them apart.

For more than two decades, the cuprates stood alone as the only family of high-temperature superconductors until superconductivity was discovered in the iron pnictides [25, 26]. Similar to the cuprates, superconductivity in the iron pnictides also arises upon doping a parent antiferromagnetic state, however, the correlations are

believed to be weaker than in the cuprates [27, 28].

The Fermi surface of the hole-doped cuprates is relatively simple and can be described using only a single band. The situation is vastly different for the iron-based superconductors that were discovered during the last decade [29–34]. In these compounds the electrons have an additional orbital degree of freedom. This results in multiple band crossing the Fermi energy. Hence the formation of Cooper pairs within a single band may pair electrons from different orbitals and it is also possible to pair electrons from different bands. This gives rise to a whole new zoo of possible pairing states with exotic properties.

Recently, materials with strong spin-orbit coupling have moved into the focus of attention, due to their unconventional superconductivity, such as the inversion symmetry-breaking compound $CePt_3Si$ [35–37], locally non-centrosymmetric $Cu_xBi_2Se_3$ [38, 39], or the topological half-Heusler semimetal YPtBi [40]. The strong coupling of spin and orbital degrees of freedom places constraints on the ways the electrons form Cooper pairs. This can nevertheless give rise to or even be beneficial for exotic phenomena such as topological superconductivity.

The class of unconventional superconductors to which the heavy-fermion systems, the cuprates, and the iron pnictides belong remains incompletely understood until today. Whereas in the case of a conventional superconductor, the local electron-phonon interaction always favors a spin-singlet in an orbtial s-wave state, the existence of strong correlations in unconventional superconductors is usually detrimental to such a local pairing state. Instead, to avoid the on-site Coulomb repulsion, electrons form pairs with higher orbital angular momentum to reduce their probability density at the origin. This however also implies that the gap will have nodes in momentum space. When these nodes intersect the Fermi surface the excitation spectrum is no longer fully gapped. A superconductor gains energy over the normal state by opening a gap, however, nodal regions do not contribute to this. Therefore, there is a delicate balance between energy loss through Coulomb repulsion and energy gain through opening a gap.

1.2 Symmetries

Symmetry considerations are a major part of solid state physics. The structure of crystalline solids is invariant under the operations of the space group, which combines the crystallographic point group of the unit cell with the translations of the underlying Bravais lattice. The symmetry operations of the point group consist of reflections, rotations, and improper rotations in symmorphic systems. Non-symmorphic systems may have addtional screw axis and glide plane symmetries. The quantum states can then be classified according to these symmetries within the formalism of group theory [41]. This provides us with a framework to classify unconventional superconductors.

Since we are interested in the formation of superconductivity from fermions in a crystal, the fermions have to be described by a normal-state Hamiltonian that is invariant under the symmetries of the lattice. The pairing potential is also subject to these symmetries, which puts constraints on which pairing states are allowed and enables us to classify the pairing potential according to the irreducible representations of the point group [42]. It turns out that for the cuprates the most likely pairing state is one with $d_{x^2-y^2}$-wave symmetry on the square lattice, resulting in nodes along the Brillouin zone diagonals.

The crystallographic symmetries are not the only ones important for superconductivity. A Cooper pair is a bound state of two fermions and therefore it has to obey the Fermi statistics and therefore change its sign under the exchange of particles. This requirement has been named fermionic antisymmetry. Another important property is time-reversal symmetry, which in fermionic systems is related to Kramers' theorem which implies a double degeneracy of states with half-integer spin in the presence of time-reversal symmetry. However, a

Cooper pair has integer spin and can therefore spontaneously break time-reversal symmetry.

Some point groups have degenerate representations, i.e. there will be multiple allowed pairing states with the same symmetry. Since the superconductor only has a single pairing potential, it may be a linear combination of all the states with the same symmetry. Take as an example the p_x- and p_y-wave on the square lattice where they occupy the E_u representation. These two states transform into one another under the symmetries of the lattice and can therefore be combined together into a $(p_x + ip_y)$-wave state. This is referred to as a *multi-component order parameter* [42, 43].

The pairing potential as a whole has a gauge freedom with respect to global phases. However, the relative phase difference between the individual components is still important, because it might transform non-trivially under the time-reversal operation. Generally speaking when the pairing potential has multiple components and their relative phase differences are not real numbers, then the result will break time-reversal symmetry.

Evidence for a multi-component order parameter has been detected in a variety of compounds from different classes, such as superfluid ^{3}He[44], heavy-fermion superconductors, like the Uranium-based compounds UPt$_3$ [45, 46], UBe$_{13}$ [47], and URu$_2$Si$_2$ [48] or PrOs$_4$Sb$_{12}$ [49, 50], the layered-perovskite Sr$_2$RuO$_4$ [51, 52], the non-centrosymmetric superconductor SrPtAs [53], and epitaxial Bi/Ni bilayers [54]. The multi-component nature of the order parameter manifests itself in broken time-reversal symmetry in most of these compounds, but there are also superconductors where a nematic state is more favourable by the underlying microscopics, e.g. Cu$_x$Bi$_2$Se$_3$ [38].

The electronic structure of the cuprates is well-described by only a single band, however, in many materials the fermions have additional degrees of freedom, such as orbital, valley, or sublattice. For simplicity we will refer to all of these as orbital degrees of freedom. The inclusion of an orbital degree of freedom extends the symmetry classification and pairing states are no longer restricted to spin-singlet and -triplet. Hence an s-wave orbital-antisymmetric spin-triplet pairing state can be in the same symmetry class as the earlier mentioned $d_{x^2-y^2}$-wave spin-singlet state. Because the orbitally non-trivial pairing state has the same symmetry it will also give rise to nodes and appear as a $d_{x^2-y^2}$-wave form factor at the Fermi surface. Although the lack of momentum-dependence of the pairing potential itself implies an s-wave pairing state, because it has nodes we refer to this as an *anomalous s-wave state*. Orbitally non-trivial superconductivity has gained considerable attention over the last decade and has been proposed and studied in a large number of disparate system [55–81].

1.3   Outline

This thesis is organized as follows. Chapter 2 provides an introduction to the field of unconventional superconductivity. After a brief review of the conventional BCS theory we will move on to a generalized formulation of BCS theory and finally discuss superconductivity in multi-band systems. Using group theory arguments we show how to classify the superconducting states according to the symmetries of the lattice. For orbitally non-trivial pairing states in multi-band systems, this gives rise to the anomalous s-wave states.

In Chapter 3 we will combine the concepts introduced in Chapter 2 and construct multi-component order parameters that break time-reversal symmetry from anomalous s-wave states. This can lead to interesting new physics because broken time-reversal symmetry gives rise to a magnetic ordering that lifts the spin degeneracy and inflates the nodes in momentum space into so-called Bogoliubov Fermi surfaces. These Fermi surfaces are topologically protected by a $\mathbb{Z}_2$ invariant. The appearance of the Bogoliubov Fermi surfaces can be understood in terms of a low-energy effective model. We then demonstrate some of the phenomena in a paradigmatic model of $j = 3/2$ fermions in the cubic crystal system and discuss the possible pairing states in a phenomenological

weak-coupling theory.

The topological protection renders the Bogoliubov Fermi surfaces robust against symmetry-preserving perturbations. However, their existence depends on the relative thermodynamic stability of a time-reversal symmetry-breaking pairing state in contrast to one that preserves time-reversal symmetry. To this end, in Chapter 4 we construct the mean-field phase diagram for the paradigmatic model introduced in Chapter 3 as a function of spin-orbit coupling and temperature. We find a rich phase diagram which supports thermodynamically stable Bogoliubov Fermi surface and discuss some experimental signatures.

Recently the unconventional superconductor Sr_2RuO_4 [82] has attracted a lot of attention. After its discovery in 1994 the pairing symmetry of this compound was proposed to be an odd-parity chiral p-wave state [83], however a recent revisiting of nuclear magnetic resonance experiments has cast serious doubts on these initial proposals [84, 85]. In Chapter 5 we propose an alternative pairing state that is consistent with the experimental situation which is an anomalous s-wave pairing state with Bogoliubov Fermi surfaces.

We conclude in Chapter 6 and provide an outlook into future research motivated by the findings in this thesis.

Chapter 2

Introduction to unconventional superconductivity

In this chapter we will briefly review the formulation of conventional BCS theory and then generalise it to non-spin-singlet pairing. Finally we will discuss some phenomena that emerge when considering superconductivity in a system with multiple bands. These discussions lay the mathematical foundation for the subsequent chapters and aim to provide a glimpse into the field.

2.1 BCS theory

Before we begin to generalise the BCS theory, we briefly review what is commonly known as "conventional" BCS theory. For this we start from the pairing Hamiltonian

$$H = \sum_{\boldsymbol{k},\sigma} \xi_{\boldsymbol{k}} c^\dagger_{\boldsymbol{k},\sigma} c_{\boldsymbol{k},\sigma} + \frac{1}{N} \sum_{\boldsymbol{k},\boldsymbol{k}'} g c^\dagger_{\boldsymbol{k},\uparrow} c^\dagger_{-\boldsymbol{k},\downarrow} c_{-\boldsymbol{k}',\downarrow} c_{\boldsymbol{k}',\uparrow}, \tag{2.1}$$

where the operator $c_{\boldsymbol{k},\sigma}$ annihilates an electron with momentum $\boldsymbol{k}$ and spin σ. The first sum describes the normal state of the electrons, where $\xi_{\boldsymbol{k}} = \epsilon_{\boldsymbol{k}} - \mu$ comprises the dispersion $\epsilon_{\boldsymbol{k}}$ and the chemical potential μ. The second term describes the pairing interaction between electrons with an effective attractive interaction potential g. In the original proposal of BCS theory, the origin of this attractive interaction is the electron-phonon interaction [9, 10, 15].

In the next step we perform a mean-field decoupling of (2.1), i.e. we decompose a product of operators A and B by writing it as a sum of the expectation value and the fluctuations around it. That is to say

$$AB = (\langle A \rangle + \tilde{A})(\langle B \rangle + \tilde{B}), \tag{2.2}$$

where $\langle \cdot \rangle$ denotes the expectation value and tilde denotes fluctuations around the expectation value. It follows

$$AB = \langle A \rangle B + A \langle B \rangle - \langle A \rangle \langle B \rangle + \tilde{A}\tilde{B}. \tag{2.3}$$

The mean-field approximation is now that the fluctuations around the expectation value are small and hence the product of fluctuations will be negligible. With that we arrive at

$$AB \approx \langle A \rangle B + A \langle B \rangle - \langle A \rangle \langle B \rangle. \tag{2.4}$$

In the pairing Hamiltonian we identify the annihilation operator $A \equiv c^\dagger_{\boldsymbol{k},\uparrow} c^\dagger_{-\boldsymbol{k},\downarrow}$ and the creation operator $B = c_{-\boldsymbol{k}',\downarrow} c_{\boldsymbol{k}',\uparrow}$ of a Cooper pair. Then we have

$$H_{\mathrm{MF}} = \sum_{\boldsymbol{k},\sigma} \xi_{\boldsymbol{k}} c^\dagger_{\boldsymbol{k},\sigma} c_{\boldsymbol{k},\sigma} + \frac{1}{N} \sum_{\boldsymbol{k},\boldsymbol{k}'} g \Big(\langle c^\dagger_{\boldsymbol{k},\uparrow} c^\dagger_{-\boldsymbol{k},\downarrow} \rangle c_{-\boldsymbol{k}',\downarrow} c_{\boldsymbol{k}',\uparrow} + c^\dagger_{\boldsymbol{k},\uparrow} c^\dagger_{-\boldsymbol{k},\downarrow} \langle c_{-\boldsymbol{k}',\downarrow} c_{\boldsymbol{k}',\uparrow} \rangle - \langle c^\dagger_{\boldsymbol{k},\uparrow} c^\dagger_{-\boldsymbol{k},\downarrow} \rangle \langle c_{-\boldsymbol{k}',\downarrow} c_{\boldsymbol{k}',\uparrow} \rangle \Big). \tag{2.5}$$

Here we introduce the superconducting order parameter which is essentially the expectation value of a Cooper pair creation operator

$$\Delta \equiv \frac{1}{N} \sum_{\boldsymbol{k}} g \langle c_{-\boldsymbol{k},\downarrow} c_{\boldsymbol{k},\uparrow} \rangle. \tag{2.6}$$

This quantity is also referred to as the pairing potential. Here the pairing takes place between quasiparticles with opposite momentum and opposite spin. Plugging in the order parameter, the Hamiltonian reads

$$H_{\mathrm{MF}} = \sum_{\boldsymbol{k},\sigma} \xi_{\boldsymbol{k}} c_{\boldsymbol{k},\sigma}^{\dagger} c_{\boldsymbol{k},\sigma} + \sum_{\boldsymbol{k}} \left(\Delta^{*} c_{-\boldsymbol{k},\downarrow} c_{\boldsymbol{k},\uparrow} + \Delta c_{\boldsymbol{k},\uparrow}^{\dagger} c_{-\boldsymbol{k},\downarrow}^{\dagger} \right) - \frac{N|\Delta|^2}{g}. \tag{2.7}$$

It is often convenient to write the resulting equation in matrix form

$$H_{\mathrm{MF}} = \sum_{\boldsymbol{k}} \begin{pmatrix} c_{\boldsymbol{k},\uparrow}^{\dagger} & c_{-\boldsymbol{k},\downarrow} \end{pmatrix} \begin{pmatrix} \xi_{\boldsymbol{k}} & \Delta \\ \Delta^{*} & -\xi_{-\boldsymbol{k}} \end{pmatrix} \begin{pmatrix} c_{\boldsymbol{k},\uparrow} \\ c_{-\boldsymbol{k},\downarrow}^{\dagger} \end{pmatrix} - \frac{N|\Delta|^2}{g} + \sum_{\boldsymbol{k}} \xi_{\boldsymbol{k}}. \tag{2.8}$$

The Hamiltonian can be diagonalised using the Bogoliubov transformation with the assumption that $\xi_{\boldsymbol{k}}$ is even, i.e. $\xi_{\boldsymbol{k}} = \xi_{-\boldsymbol{k}}$. We introduce new fermionic operators $\gamma_{\boldsymbol{k},\sigma}$,

$$c_{\boldsymbol{k},\uparrow} = u_{\boldsymbol{k}} \gamma_{\boldsymbol{k},\uparrow} + v_{\boldsymbol{k}} \gamma_{-\boldsymbol{k},\downarrow}^{\dagger}, \quad c_{-\boldsymbol{k},\downarrow}^{\dagger} = v_{\boldsymbol{k}}^{*} \gamma_{\boldsymbol{k},\uparrow} + u_{\boldsymbol{k}}^{*} \gamma_{-\boldsymbol{k},\downarrow}^{\dagger}. \tag{2.9}$$

The coefficients $u_{\boldsymbol{k}}$ and $v_{\boldsymbol{k}}$ are complex numbers. Their magnitude is given by

$$|u_{\boldsymbol{k}}|^2 = \frac{1}{2} \left(1 + \frac{\xi_{\boldsymbol{k}}}{\sqrt{\xi_{\boldsymbol{k}}^2 + |\Delta|^2}} \right), \tag{2.10}$$

$$|u_{\boldsymbol{k}}|^2 = \frac{1}{2} \left(1 - \frac{\xi_{\boldsymbol{k}}}{\sqrt{\xi_{\boldsymbol{k}}^2 + |\Delta|^2}} \right), \tag{2.11}$$

and they follow the constraint $|u_{\boldsymbol{k}}|^2 + |v_{\boldsymbol{k}}|^2 = 1$. The transformation is unitary and therefore retains the anticommutation relations of the fermionic operators. This transformation diagonalises the matrix Hamiltonian

$$H_{\mathrm{MF}} = \sum_{\boldsymbol{k}} \begin{pmatrix} \gamma_{\boldsymbol{k},\uparrow}^{\dagger} & \gamma_{-\boldsymbol{k},\downarrow} \end{pmatrix} \begin{pmatrix} E_{\boldsymbol{k}} & 0 \\ 0 & -E_{\boldsymbol{k}} \end{pmatrix} \begin{pmatrix} \gamma_{\boldsymbol{k},\uparrow} \\ \gamma_{-\boldsymbol{k},\downarrow}^{\dagger} \end{pmatrix} - \frac{N}{g} |\Delta|^2 + \sum_{\boldsymbol{k}} \xi_{\boldsymbol{k}}. \tag{2.12}$$

The additional last term $\sum_{\boldsymbol{k}} \xi_{\boldsymbol{k}}$ stems from the anti-commutation relations of the fermionic operators. However, it only contributes an overall constant energy offset, so it is usually neglected. The energy eigenvalues $E_{\boldsymbol{k}}$ determine the excitation spectrum in the superconductor,

$$E_{\boldsymbol{k}} = \sqrt{\xi_{\boldsymbol{k}}^2 + |\Delta|^2}. \tag{2.13}$$

The quasiparticles are gapped out by $2|\Delta|$ at the Fermi surface. In Fig. 2.1 we show a quadratic dispersion of free fermions which is gapped out by superconductivity. More details on the theory of conventional superconductivity can be found in [86].

2.2 Generalised BCS theory

However, this conventional theory of superconductivity has shortcomings. The phonon-mediated pairing it is built upon cannot explain the unusually high critical temperatures in the cuprates and the pnictide superconductors. Superconductivity in these materials usually arises by doping away from a magnetically ordered state. As
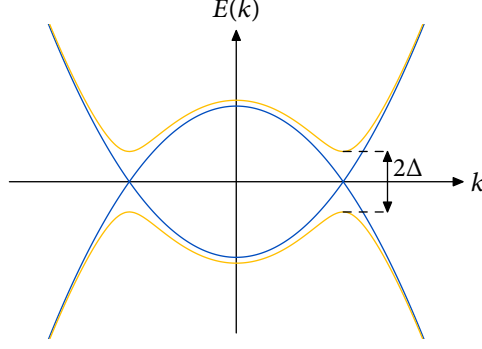
■ *Figure 2.1.* The normal state dispersion is shown in blue, which is Nambu doubled. The excitation spectrum of a conventional BCS superconductor is shown in orange. A full isotropic gap opens at the Fermi surface.

the magnetic order is suppressed superconductivity may emerge as a result of strong spin fluctuations [87]. For the theory of superconductivity that means that we can no longer safely assume that g is independent of spin and momentum. We have to move on to a generalised BCS theory. Let us write again the pairing Hamiltonian

$$H = \sum_{\boldsymbol{k},\sigma} \xi_{\boldsymbol{k}} c^\dagger_{\boldsymbol{k},\sigma} c_{\boldsymbol{k},\sigma} + \frac{1}{N} \sum_{\substack{\boldsymbol{k},\boldsymbol{k}' \\ \sigma_1 \sigma_2 \sigma_3 \sigma_4}} V_{\boldsymbol{k},\boldsymbol{k}';\sigma_1 \sigma_2 \sigma_3 \sigma_4} c^\dagger_{\boldsymbol{k},\sigma_1} c^\dagger_{-\boldsymbol{k},\sigma_2} c_{-\boldsymbol{k}',\sigma_3} c_{\boldsymbol{k}',\sigma_4}. \tag{2.14}$$

The pairing interaction is now a complicated function of both spin and momentum. We can immediately infer the following constraints from the anti-commutation relations of the fermionic operators in (2.14)

$$V_{\boldsymbol{k},\boldsymbol{k}';\sigma_1 \sigma_2 \sigma_3 \sigma_4} = -V_{-\boldsymbol{k},\boldsymbol{k}';\sigma_2 \sigma_1 \sigma_3 \sigma_4} = -V_{\boldsymbol{k},-\boldsymbol{k}';\sigma_1 \sigma_2 \sigma_4 \sigma_3} = V_{-\boldsymbol{k},-\boldsymbol{k}';\sigma_2 \sigma_1 \sigma_4 \sigma_3}. \tag{2.15}$$

Performing a mean-field decomposition analogous to the conventional case before, we identify the generalised pairing potential as

$$\Delta_{\boldsymbol{k};\sigma_1 \sigma_2} = \sum_{\boldsymbol{k}',\sigma_3 \sigma_4} V_{\boldsymbol{k},\boldsymbol{k}';\sigma_1 \sigma_2 \sigma_3 \sigma_4} \langle c_{-\boldsymbol{k}',\sigma_3} c_{\boldsymbol{k}',\sigma_4} \rangle. \tag{2.16}$$

This expectation value contains two fermionic annihilation operators, i.e. it annihilates a two-fermion state. As such, this two-fermion state has to obey the proper statistics, which requires that the state is overall antisymmetric under particle exchange

$$\Delta_{-\boldsymbol{k};\sigma_2,\sigma_1} = -\Delta_{\boldsymbol{k};\sigma_1,\sigma_2}. \tag{2.17}$$

We will henceforth refer to this requirement as *fermionic antisymmetry.*

Analogous to the conventional theory we may write Hamiltonian in Bogoliubov-de-Gennes (BdG) form:

$$H_{\mathrm{MF}} = \frac{1}{2} \sum_{\boldsymbol{k}} \Psi^\dagger_{\boldsymbol{k}} \begin{pmatrix} \xi_{\boldsymbol{k}} \sigma_0 & \Delta(\boldsymbol{k}) \\ \Delta^\dagger(\boldsymbol{k}) & -\xi_{-\boldsymbol{k}} \sigma_0 \end{pmatrix} \Psi_{\boldsymbol{k}} + K, \tag{2.18}$$

with the Nambu spinor $\Psi_{\boldsymbol{k}} = (c_{\boldsymbol{k},\uparrow}, c_{\boldsymbol{k},\downarrow}, c^\dagger_{-\boldsymbol{k},\uparrow}, c^\dagger_{-\boldsymbol{k},\downarrow})^T$ and the C-number contribution

$$K = \sum_{\boldsymbol{k}} \xi_{\boldsymbol{k}} - \frac{1}{2} \sum_{\boldsymbol{k},\boldsymbol{k}'} \sum_{\sigma_1,\sigma_2,\sigma_3,\sigma_4} V_{\boldsymbol{k},\boldsymbol{k}';\sigma_1,\sigma_2,\sigma_3,\sigma_4} \langle c^\dagger_{\boldsymbol{k},\sigma_1} c^\dagger_{-\boldsymbol{k},\sigma_2} \rangle \langle c_{-\boldsymbol{k}',\sigma_3} c_{\boldsymbol{k}',\sigma_4} \rangle. \tag{2.19}$$

The prefactor of $1/2$ in front of (2.18) is due to the fact that in the Nambu spinor there are now creation and annihilation operators for both spin up and spin down, i.e. the number of fermions has been doubled. To reverse

the double counting, we divide by two or alternatively the momentum space summation could be limited to only half the Brillouin zone.

The additional spin degree of freedom in the Nambu spinor implies that the pairing potential $\Delta(\mathbf{k})$ is a 2×2 matrix. Because the three Pauli matrices and the unit matrix form a basis for all 2×2 matrices, we may write the matrix pairing potential as a linear combination.

$$\Delta(\mathbf{k}) = \begin{pmatrix} \Delta_{\uparrow\uparrow} & \Delta_{\uparrow\downarrow} \\ \Delta_{\downarrow\uparrow} & \Delta_{\downarrow\downarrow} \end{pmatrix} = \psi_{\mathbf{k}} i\sigma_2 + \mathbf{d}_{\mathbf{k}} \cdot \boldsymbol{\sigma} i\sigma_2 \tag{2.20}$$

where $\boldsymbol{\sigma} = (\sigma_1, \sigma_2, \sigma_3)^T$ is the vector of Pauli matrices. Now fermionic antisymmetry implies

$$\Delta(\mathbf{k}) = -\Delta^T(-\mathbf{k}). \tag{2.21}$$

This is one of the most important principles when determining the pairing states. This means also that in the decomposition (2.20)

$$\psi_{\mathbf{k}} = \psi_{-\mathbf{k}}, \quad \mathbf{d}_{\mathbf{k}} = -\mathbf{d}_{\mathbf{k}}, \tag{2.22}$$

i.e. the pairing function of the singlet is always even, whereas the pairing vector of the triplet is always odd in momentum. The matrix pairing potential is called *unitary* if the product $\Delta\Delta^\dagger$ is proportional to the unit matrix, otherwise it is called *non-unitary*.

To determine the electronic structure of the superconductor we introduce a generalised Bogoliubov transformation, which now also takes into account the spin degree of freedom,

$$\Psi_{\mathbf{k}} = \begin{pmatrix} u_{\mathbf{k}} & v_{\mathbf{k}} \\ v_{-\mathbf{k}}^* & u_{-\mathbf{k}}^* \end{pmatrix} \Gamma_{\mathbf{k}}, \qquad \Gamma_{\mathbf{k}} = (\gamma_{\mathbf{k},+}, \gamma_{\mathbf{k},-}, \gamma_{-\mathbf{k},+}^\dagger, \gamma_{-\mathbf{k},-}^\dagger)^T, \tag{2.23}$$

where $u_{\mathbf{k}}$ and $v_{\mathbf{k}}$ are now 2×2 matrices. This diagonalises the mean-field Hamiltonian and we find

$$H_{\mathrm{MF}} = \frac{1}{2} \sum_{\mathbf{k}} \Gamma_{\mathbf{k}}^\dagger \begin{pmatrix} E_{\mathbf{k},+} & 0 & 0 & 0 \\ 0 & E_{\mathbf{k},-} & 0 & 0 \\ 0 & 0 & -E_{-\mathbf{k},+} & 0 \\ 0 & 0 & 0 & -E_{-\mathbf{k},-} \end{pmatrix} \Gamma_{\mathbf{k}} + K, \tag{2.24}$$

where the electronic dispersions can take on the two forms

$$\begin{aligned} \text{singlet:} \quad & E_{\mathbf{k}} = E_{\mathbf{k},\pm} = \sqrt{\xi_{\mathbf{k}}^2 + |\psi_{\mathbf{k}}|^2}, \\ \text{triplet:} \quad & E_{\mathbf{k},\pm} = \sqrt{\xi_{\mathbf{k}}^2 + |\mathbf{d}_{\mathbf{k}}|^2 \pm |\mathbf{d}_{\mathbf{k}} \times \mathbf{d}_{\mathbf{k}}^*|}. \end{aligned} \tag{2.25}$$

Here we have assumed that the pairing function has a definite parity, i.e. it is either even or odd in momentum. This is possible if the underlying crystal has a centre of inversion and therefore the electronic states possess inversion symmetry. We also find that the degeneracy of the excitation spectrum is lifted in the case of triplet pairing when $|\mathbf{d}_{\mathbf{k}} \times \mathbf{d}_{\mathbf{k}}^*|$ is non-zero.

On a side note, inversion symmetry is not a requirement and there exist materials without a centre of inversion, such as MnSi and CePt$_3$Si [35]. In this case singlet and triplet pairing can coexist which gives rise to many interesting phenomena in these *non-centrosymmetric superconductors* [88, 89].

The energy eigenvalues in (2.25) will only vanish when $\xi_{\mathbf{k}} = 0$ and $|\psi_{\mathbf{k}}| = 0$ in the singlet case or $|\mathbf{d}_{\mathbf{k}}|^2 \pm |\mathbf{d}_{\mathbf{k}} \times \mathbf{d}_{\mathbf{k}}^*| = 0$ in the triplet case at the same time. The conditions that the superconducting term is vanishing

full gap   line nodes   point nodes
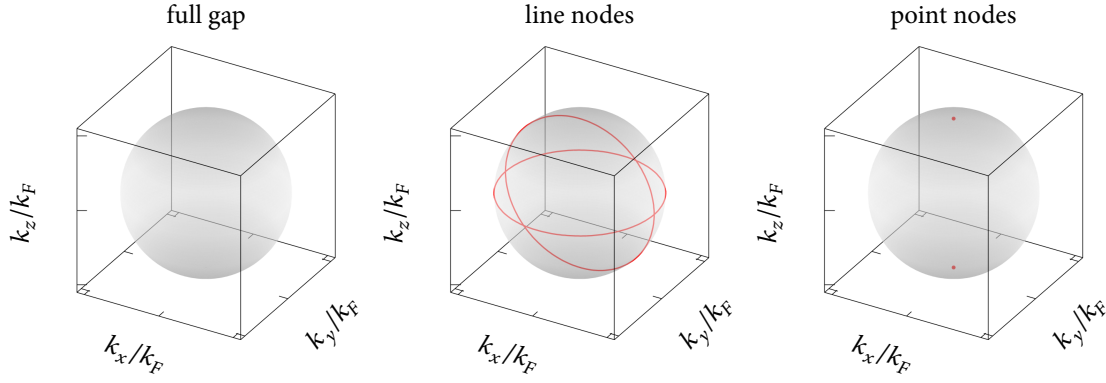
■ *Figure 2.2.* The three different types of nodal gap structures. In transparent grey we show the normal-state Fermi sphere, overlaid with the nodal lines and points in red. In the conventional BCS theory there is always a full gap, however, if we take the spin degree of freedom into account, the gap can vanish on the normal-state Fermi surface at points or along lines. The location of the point and line nodes in this picture is enforced by symmetry.

is only satisfied on lines or planes in momentum space, resulting in only point or line nodes on the Fermi surface, respectively. In Fig. 2.2 we show different configurations of symmetry-enforced nodes for a quadratic normal-state dispersion, i.e. the Fermi surface is a sphere. Generally the shape and position of these nodes is dictated by symmetry, as we will see in the next section, but accidental nodes are possible.

2.2.1 Symmetries of the normal state

Symmetries are important for the selection of the pairing wave function, so we will study this on the example of an electronic system with a single band in two dimensions on the square lattice, which is often used as a toy model for the cuprates. Since we are describing electrons in a crystal system, the Hamiltonian in (2.14) must be invariant under transformations representing the elements of the appropriate point group. The crystal structure of the cuprates forms a tetragonal crystal system, whose associated point group is D_{4h}, which we also use for our single band system. The elements of this group are

$$D_{4h} = \{E, 2C_4, C_2, 2C_2', 2C_2'', I, 2S_4, \sigma_h, 2\sigma_v, 2\sigma_d\}, \tag{2.26}$$

where E is the identity, $2C_4$ are clockwise and counterclockwise four-fold rotations around the z axis (principal axis), C_2 is a two-fold rotations around are the z axis, $2C_2'$ are two-fold rotations around the x and y axis, $2C_2''$ are two-fold rotations around the axes $x = y$ and $x = -y$, I is inversion, $2S_4$ are rotoinversions which are combinations of $2C_4$ and I, σ_h is reflection at the $z = 0$ plane, $2\sigma_v$ are reflections at the $x = 0$ and $y = 0$ planes, and $2\sigma_d$ are reflections at the $(x - y) = 0$ and $(x + y) = 0$ planes.

In the present case there is only a single band, so we don't have to worry about orbital degrees of freedom. Hence we only have to look at the transformation of the spin under the crystal symmetries. A general spin rotation by angle ϕ around the axis parallel to the vector $\boldsymbol{n}$ is given by

$$C_{\boldsymbol{n}}(\phi) = \exp\left(-i\frac{\phi}{\hbar}\boldsymbol{n} \cdot \boldsymbol{S}\right) \quad \text{with} \quad \boldsymbol{S} = \frac{\hbar}{2}\boldsymbol{\sigma}. \tag{2.27}$$

The reflection of a spin at plane with normal vector $\boldsymbol{n}$ is equivalent to a rotation by π around the axis parallel to $\boldsymbol{n}$, as illustrated in Fig. 2.3. This behaviour stems from the fact that a spin carries a magnetic dipole moment
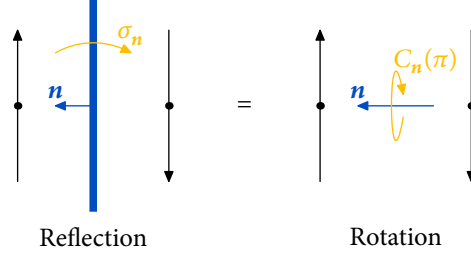
Figure 2.3. For a spin the symmetry operation of reflection at a plane with normal vector $\boldsymbol{n}$ is equivalent to a rotation by π around the axis parallel to $\boldsymbol{n}$.

and therefore inherits the same pseudovector structure under improper rotations such as reflection. Hence the reflection operation for spins takes the simple form

$$\sigma_{\boldsymbol{n}} = i\boldsymbol{n} \cdot \boldsymbol{\sigma}. \tag{2.28}$$

With these generic properties we can easily derive the matrix form of the symmetry operations in D_{4h} in the basis of the Pauli matrices

$$C_4 = \exp\left(-i\frac{\pi}{4}\sigma_3\right), \qquad C_2'(x) = \exp\left(-i\frac{\pi}{2}\sigma_1\right), \qquad C_2''(x=y) = \exp\left(-i\frac{\pi}{2}\frac{\sigma_1 + \sigma_2}{\sqrt{2}}\right),$$

$$\sigma_h = i\sigma_3, \qquad \sigma_v(x) = i\sigma_2, \qquad \sigma_d(x=y) = i\frac{\sigma_1 - \sigma_2}{\sqrt{2}}.$$

We assume the presence of an inversion centre and no non-trivial sublattice structure, such that the inversion operator acts trivially on spin. Inversion symmetry I is implemented by the unitary operator U_P

$$I: \quad U_P H(-\boldsymbol{k})U_P^\dagger = H(\boldsymbol{k}), \quad U_P = \sigma_0. \tag{2.29}$$

Now we can determine the character of the Pauli matrices with respect to these operations. The behaviour of the i-th Pauli matrix σ_i under the operation represented by the matrix Λ is determined by $\Lambda^\dagger \sigma_i \Lambda$. If this evaluates to $\pm\sigma_i$ we denote this by ± 1, otherwise we give the resulting matrix. These are listed in the following table, where we have omitted the identity and inversion because they are trivial and the rotoinversion because it corresponds to C_4 in the case that inversion is trivial

$$
\begin{array}{c|cccccc}
 & C_4 & C_2' & C_2'' & \sigma_h & \sigma_v & \sigma_d \\
\hline
\sigma_0 & +1 & +1 & +1 & +1 & +1 & +1 \\
\sigma_1 & \sigma_2 & +1 & \sigma_2 & -1 & -1 & -\sigma_2 \\
\sigma_2 & -\sigma_1 & -1 & \sigma_1 & -1 & +1 & -\sigma_1 \\
\sigma_3 & +1 & -1 & -1 & +1 & -1 & -1
\end{array}
\tag{2.30}
$$

As we can see, the matrices σ_0 and σ_3 are closed under the set of operations, i.e. we can assign them uniquely to an irreducible representation. The matrices σ_1 and σ_2 transform into one another under the operations, which means that they belong to a two-dimensional irreducible representation. Comparing the character of the Pauli matrices that we just determined with the character table of D_{4h} in Tab. A.1 in the Appendix, we find

$$\sigma_0 \in A_{1g}, \quad \{\sigma_1, \sigma_2\} \in E_g, \quad \sigma_3 \in A_{2g}. \tag{2.31}$$

Having determined the transformation properties of the basis matrices we can now proceed to construct the normal-state Hamiltonian. Since the normal-state Hamiltonian describes the motion of free electrons in the D_{4h} crystal system, it has to be invariant under the operations of the point group and therefore transform like A_{1g}. The Hamiltonian is given by

$$\mathcal{H} = \sum_{\boldsymbol{k}} \Phi_{\boldsymbol{k}}^{\dagger} H(\boldsymbol{k}) \Phi_{\boldsymbol{k}} \tag{2.32}$$

with the Nambu spinor $\Phi_{\boldsymbol{k}} = (c_{\boldsymbol{k},\uparrow}, c_{\boldsymbol{k},\downarrow})$ and the BdG-Hamiltonian $H(\boldsymbol{k})$, which can be expanded in terms of the basis matrices with scalar coefficients $h_i(\boldsymbol{k})$

$$H(\boldsymbol{k}) = \sum_{i=0}^{4} h_i(\boldsymbol{k}) \sigma_i = \xi_{\boldsymbol{k}} \sigma_0 + \boldsymbol{l}(\boldsymbol{k}) \cdot \boldsymbol{\sigma}. \tag{2.33}$$

This is usually expressed in the "pretty" form on the right hand side, where we have separated the spin-independent term proportional to σ_0 from the spin-dependent term proportional to the Pauli vector. This form of spin-dependent hopping is identified with spin-orbit coupling, which commonly breaks inversion symmetry.

For the Hamiltonian to transform like A_{1g}, each term has to transform like A_{1g}, which implies that the coefficient $h_i(\boldsymbol{k})$ has the same symmetry as the corresponding matrix σ_i. For example, σ_3 transforms like A_{2g}, therefore $h_3(\boldsymbol{k})$ has to transform like A_{2g}. Usually the corresponding polynomials of a few low orders are given alongside the character table in many textbooks. Table A.2 in the Appendix lists the rotations and Cartesian products for the D_{4h} point group up to fifth order (g-wave).

Further we assume that the normal-state Hamiltonian preserves time-reversal symmetry. The effect of time reversal can be summarised by

$$\mathcal{T}: \boldsymbol{k} \rightarrow -\boldsymbol{k}, \quad |\uparrow\rangle \rightarrow |\downarrow\rangle, \quad |\downarrow\rangle \rightarrow -|\uparrow\rangle, \quad i \rightarrow -i. \tag{2.34}$$

This can be cast into the form of an anti-unitary operator $\mathcal{T} = U_T \mathcal{K}$, which can be written as the combination of a unitary operator U_T and the anti-unitary complex conjugation $\mathcal{K}$. Applied to the BdG-Hamiltonian this implies

$$\mathcal{T}: \quad U_T H^*(-\boldsymbol{k}) U_T^{\dagger} = H(\boldsymbol{k}), \quad U_T = i\sigma_2. \tag{2.35}$$

The form of the unitary part is specific to the present model with a single band.

The terms proportional to the Pauli vector must break either time-reversal or inversion symmetry, but the D_{4h} point group requires inversion symmetry and we will further assume that time-reversal symmetry is preserved. From Tab. A.2 in the Appendix we extract the two lowest orders for A_{1g} and truncate the resulting expression at nearest neighbour hopping to construct the spin-independent dispersion

$$\xi_{\boldsymbol{k}} = -2t(\cos(k_x a) + \cos(k_y a)) - 4t' \cos(k_x a)\cos(k_y a) - \mu, \tag{2.36}$$

with the nearest neighbour hopping t, next-nearest neighbour hopping t', chemical potential μ, and lattice constant a.

2.2.2 Symmetries of the pairing potential

Since the Hamiltonian (2.14) has the symmetry group of the lattice, so does the pairing potential. Similar to the normal-state Hamiltonian, we can expand the pairing potential in the basis of the Pauli matrices with symmetry-related coefficients.
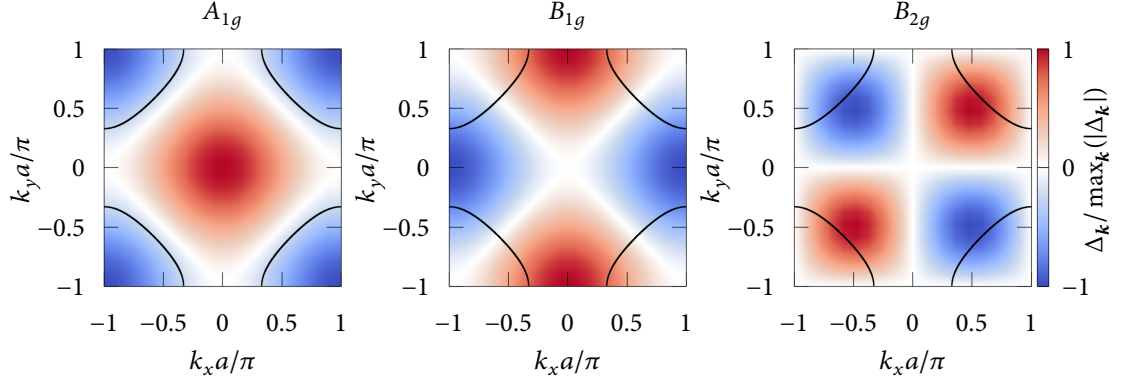
Figure 2.4. Types of nodal gap structures for the three momentum-dependent even-parity gap functions in (2.37). The colour represents the sign and the magnitude of the gap normalised to the maximum in momentum space. Black solid lines denote the normal state Fermi surface.

▶ Even-parity spin singlet

We can easily construct the singlet pairing states because they are scalar, so we simply have to choose form factors of the appropriate symmetry from Tab. A.2 in the Appendix. For spin-singlet pairing up to next-nearest-neighbour the possible gap functions are

irrep	$\psi_{\boldsymbol{k}}$	name	pairing
A_{1g}	Δ_0	s-wave	on-site
	$\Delta_0(\cos(k_x a) + \cos(k_y a))$	extended s-wave	nearest neighbour
B_{1g}	$\Delta_0(\cos(k_x a) - \cos(k_y a))$	$d_{x^2-y^2}$-wave	nearest neighbour
B_{2g}	$2\Delta_0 \sin(k_x a) \sin(k_y a)$	d_{xy}-wave	next-nearest neighbour
E_g	$\Delta_0 \sin(k_z a)\{\sin(k_x a), \sin(k_y a)\}$	d_{xz}/d_{yz}-wave	next-nearest neighbour

$$(2.37)$$

Here we have left out the A_{2g} irrep because the lowest order is g-wave, which corresponds to a next-next-next-nearest neighbour hopping which is longer in range than the normal-state hoppings. The E_g irrep can also be discarded because we are only considering a two-dimensional system and the corresponding $\psi_{\boldsymbol{k}}$ contains an out-of-plane pairing term. The momentum-dependent pairing potentials in (2.37) all vanish along lines in momentum space. If they happen to intersect the Fermi surface, the excitation spectrum will exhibit a node as well, as already discussed in the context of (2.25). In Fig. 2.4 we show the magnitude of the momentum-dependent pairing potentials in the first Brillouin zone, overlaid with the normal-state Fermi surface. The extended s-wave (A_{1g}) pairing may or may not have nodes, depending on the band parameters of the normal-state. Because these nodes may appear by chance, they are referred to as *accidental nodes*. The $d_{x^2-y^2}$-wave (B_{1g}) and the d_{xy}-wave (B_{2g}) pairings on the other hand will always have gap nodes. These are enforced by those symmetries that have a character of -1 in the character table Tab. A.1. Therefore, the pairing potential in these two irreps will exhibit nodes in the corresponding mirror planes.

▶ Odd-parity spin triplet

To construct the odd-parity pairing states we have to construct a $\boldsymbol{d}$-vector. The three components of the $\boldsymbol{d}$-vector are generated from rotations in Tab. A.2 in the Appendix. These rotations, however, correspond to irreps with even parity, i.e. they are to be combined with form factors of odd parity to fulfil the requirement of fermionic antisymmetry for the overall pairing wavefunction. To this end we have to form the products between the

irreps with odd and even parity. When we truncate the range again at nearest-neighbour pairing, like for the spin-singlet, we find according to Tab. A.3 in the Appendix the possible products

irrep	form factor	name
A_{2u}	$\sin(k_z a)$	p_z-wave
E_u	$\{\sin(k_x a), \sin(k_y a)\}$	$\{p_x, p_y\}$-wave

$\otimes$

irrep rotation	
A_{2g}	σ_z
E_g	$\{\sigma_1, \sigma_2\}$

$=$

irrep	d_k
A_{1u}	$\sin(k_z a)\hat{z}, \sin(k_x a)\hat{x} + \sin(k_y a)\hat{y}$
A_{2u}	$\sin(k_y a)\hat{x} - \sin(k_x a)\hat{y}$
B_{1u}	$\sin(k_x a)\hat{x} - \sin(k_y a)\hat{y}$
B_{2u}	$\sin(k_y a)\hat{x} + \sin(k_x a)\hat{y}$
E_u	$\{\sin(k_x a), \sin(k_y a)\}\hat{z}, \sin(k_z a)\{\hat{x}, \hat{y}\}$

Since we are only interested in pairing in the plane, we can discard the A_{1u} and the E_u pairings that have an out-of-plane component. All the other pairing states have only in-plane components. Note also that the remaining pairings have their d-vector in the plane, with the exception of the E_u pairing state that has its d-vector along $\hat{z}$. Another interesting property of the odd-parity states is that their nodes are located at the time-reversal invariant momenta $k_{x,y,z} a = -\pi, 0, \pi$ of the Brillouin zone, i.e. only at the centre and at the boundaries of the Brillouin zone. Therefore these nodes will never appear on the normal-state Fermi surface and the excitation spectrum will remain fully gapped in the absence of fine tuning. This is illustrated in Fig. 2.5 where we show the magnitude of the gap and the orientation of the d-vector in the first Brillouin zone for the pairing states with the d-vector in the plane.

▶ Chiral p-wave superconductivity

The E_u representation is special because it has two components $\{\sin(k_x a), \sin(k_y a)\}\hat{z}$ which are degenerate. However, there is only a single pairing potential, which means that these two components may appear together at the same time in a linear combination

$$d_k = \Delta_0(\alpha \sin(k_x a) + \beta \sin(k_y a))\hat{z}, \quad \alpha, \beta \in \mathbb{C}, \tag{2.38}$$

with normalisation constraint $|\alpha|^2 + |\beta|^2 = 1$. To maximise the condensation energy it is favourable to enhance the gap magnitude over the Fermi surface so we can assume that α and β are chosen such that $|d_k|$ is maximal [42, 90]. One such possibility is $\alpha = 1/\sqrt{2}$ and $\beta = \pm i/\sqrt{2}$ which gives rise to the so-called *chiral p-wave superconductivity*. This pairing state is degenerate with its complex conjugate. Moving around the Γ point the phase of the pairing potential does not return to its original value. Two cycles are necessary to restore the initial phase. This is called phase winding and the choice of the relative sign between α and β defines the direction of the phase winding which is referred to as *chirality*. In Fig. 2.6 we show the magnitude and the phase of the chiral p-wave state in the first Brillouin zone.

The degeneracy of the two chiralities has another interesting consequence. The pairing potential is said to preserve time-reversal symmetry if it satisfies

$$\mathcal{T} : \tilde{\Delta}(k) = U_T \tilde{\Delta}^*(-k) U_T^\dagger \tag{2.39}$$

with $\Delta(k) = \tilde{\Delta}(k) U_T$.

In (2.25) we had found that the excitation spectrum of a triplet superconductor is given by

$$E_{k,\pm} = \sqrt{\xi_k^2 + |d_k|^2 \pm |d_k \times d_k^*|} \tag{2.40}$$

where the term $|d_k \times d_k^*|$ lifts the degeneracy if it is non-zero. This is obviously the case if $d_k \neq d_k^*$ which implies that d_k is not invariant under time-reversal symmetry. The lifting of the excitation spectrum degeneracy can be attributed to the lowering of global symmetry due to breaking of time-reversal symmetry [42].
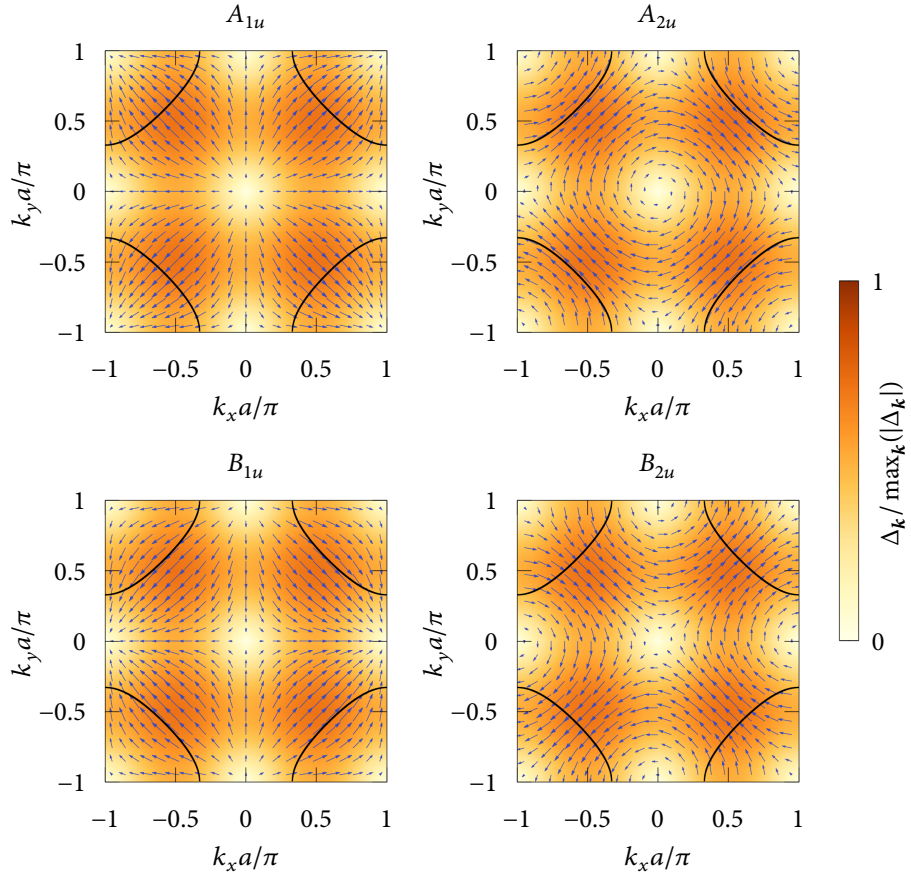
■ *Figure 2.5.* The pairing states of odd parity. The colour scale indicates the gap magnitude, the arrows point in the direction of the d vector. All pairing states have the same momentum dependence of the magnitude but the orientation of the d vector differs.
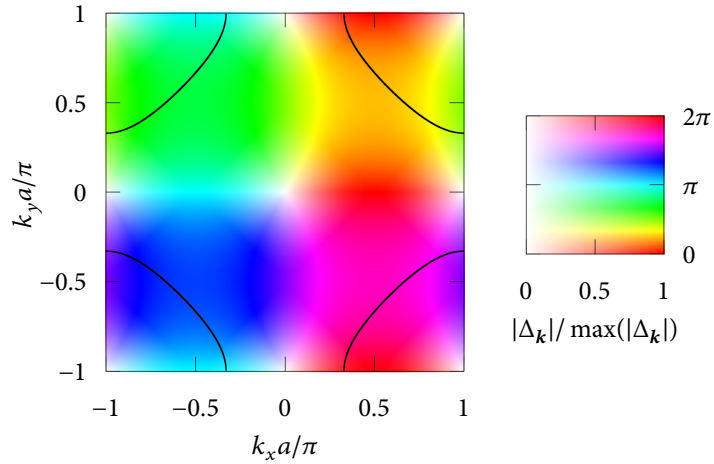
■ *Figure 2.6.* The chiral p-wave state only has point nodes at the time-reversal invariant momenta in the Brillouin zone and is therefore always fully gapped on the whole Fermi surface. The intensity (hue) of the colour scale denotes the magnitude (phase) of the gap. The phase of the gap winds around the Brillouin zone centre by 2π for one revolution.

In this context we will also further explore the concept of non-unitary pairing. Consider a pairing potential with both, singlet and triplet components

$$\Delta_{\boldsymbol{k}} = (\psi_{\boldsymbol{k}} + \boldsymbol{d}_{\boldsymbol{k}} \cdot \boldsymbol{\sigma})U_T. \tag{2.41}$$

With this we define the *gap product*

$$\Delta_{\boldsymbol{k}}\Delta_{\boldsymbol{k}}^\dagger = (|\psi_{\boldsymbol{k}}|^2 + |\boldsymbol{d}_{\boldsymbol{k}}|^2)\sigma_0 + 2\operatorname{Re}[\psi_{\boldsymbol{k}}^*\boldsymbol{d}_{\boldsymbol{k}}] \cdot \boldsymbol{\sigma} + i(\boldsymbol{d}_{\boldsymbol{k}} \times \boldsymbol{d}_{\boldsymbol{k}}^*) \cdot \boldsymbol{\sigma}. \tag{2.42}$$

The terms proportional to the unit matrix σ_0 are called the unitary part, the terms proportional to $\boldsymbol{\sigma}$ the non-unitary part. Evidently in this case only triplet pairing states can give rise to a non-unitary gap product.

Applying the time-reversal operation to the gap product yields its time-reversed counterpart

$$U_T\Delta_{-\boldsymbol{k}}^*(\Delta_{-\boldsymbol{k}}^\dagger)^*U_T^\dagger = (|\psi_{\boldsymbol{k}}|^2 + |\boldsymbol{d}_{\boldsymbol{k}}|^2)\sigma_0 + 2\operatorname{Re}[\psi_{\boldsymbol{k}}^*\boldsymbol{d}_{\boldsymbol{k}}] \cdot \boldsymbol{\sigma} - i(\boldsymbol{d}_{\boldsymbol{k}} \times \boldsymbol{d}_{\boldsymbol{k}}^*) \cdot \boldsymbol{\sigma}. \tag{2.43}$$

Here we have used the fact that irregardless of the form of U_T, since $\boldsymbol{\sigma}$ is a spin it has to be odd under time-reversal, i.e. $U_T\boldsymbol{\sigma}^*U_T^\dagger = -\boldsymbol{\sigma}$. By subtracting the time-reversed gap product from the gap product itself we can isolate only the part that is odd under time reversal

$$\Delta_{\boldsymbol{k}}\Delta_{\boldsymbol{k}}^\dagger - U_T\Delta_{-\boldsymbol{k}}^*(\Delta_{-\boldsymbol{k}}^\dagger)^*U_T^\dagger = 2i(\boldsymbol{d}_{\boldsymbol{k}} \times \boldsymbol{d}_{\boldsymbol{k}}^*) \cdot \boldsymbol{\sigma}. \tag{2.44}$$

Because this expression is quadratic in the pairing potential, we refer to is as the *time-reversal odd bilinear* (TROB).

To gain further insight into the consequences of a non-unitary pairing state and its relation to broken time-reversal symmetry, we consider the spin polarisation $\operatorname{Tr}[\Delta_{\boldsymbol{k}}^\dagger\boldsymbol{\sigma}\Delta_{\boldsymbol{k}}]$ of the pairing state at $\boldsymbol{k}$. Because the Pauli matrices are traceless, this will only be non-vanishing if the pairing state is non-unitary. Those states that give rise to a finite spin-polarisation are also referred to as *ferromagnetic* [42]. The onset of the spin polarisation coincides with the onset of superconductivity and its magnitude scales with the pairing potential squared.

▶ Thermodynamic response

The superconducting states that we have discussed here survey a range of different nodal structures that serves as a good basis to discuss low-temperature properties of unconventional superconductors. In an isotropic *s*-wave superconductor with a full gap there are no low-lying collective excitations because the spectrum is completely gapped out. This naturally leads to exponential dependence of physical observables, such as the specific heat or the relaxation time of nuclear magnetic resonance. In unconventional superconductors the excitations across point or line nodes close the gap in the excitation spectrum momentarily and modify the response functions.

The density of states is generically defined as

$$\rho(\omega) = \sum_{\boldsymbol{k}} \delta(\omega - E_{\boldsymbol{k}}) \tag{2.45}$$

where $E_{\boldsymbol{k}}$ are the energy eigenvalues of the Hamiltonian. First, for a conventional *s*-wave superconductor with a full isotropic gap across the Fermi surface the density of states is zero inside the gap

$$\rho(\omega) = 0 \quad (\omega < \Delta). \tag{2.46}$$

To discuss the effect of point nodes we move to a rotationally symmetric system in three dimensions which is given by the Anderson-Brinkham-Morel state (*A*-phase) of superfluid ^{3}He [91]. This state is analogous to the

chiral p-wave pairing state discussed earlier, but the Fermi surface is a sphere and therefore has point nodes at the poles. In this case the density of states scales as ω^2 at low energies

$$\rho(\omega) = \omega^2 \quad (\omega \ll \Delta). \tag{2.47}$$

Finally for a state with line nodes the density of states scales like

$$\rho(\omega) = \omega \quad (\omega \ll \Delta), \tag{2.48}$$

at low energies. The scaling behaviour of the density of states at low energies in the cases discussed here only depends on the topology of the gap, i.e. is independent of the location of the nodes.

The density of states is closely related to other physical observables such as the specific heat C, the magnetic penetration depth λ, and the relaxation time of nuclear magnetic resonance T_1 [42, 92, 93]. Nodes in the excitation spectrum give rise to characteristic power-law behaviour at low temperatures in these thermodynamic quantities, which we briefly summarise in the following table

gap	$\rho(\omega)$	$C(T)$	$\lambda(T)$	$1/T_1$
gapless	const	T		T
full gap	0	$T^{-2}e^{-\Delta/k_B T}$	no generic form	$T^{-1/2}e^{-\Delta/k_B T}$
line nodes	ω	T^2	T	T^3
point nodes	ω^2	T^3	T^2	T^5

$$\tag{2.49}$$

## 2.3 Superconductivity in multiband systems

In many materials the electronic structure is more complicated and involves electrons with more than one degree of freedom. These additional degrees of freedom can be of different kinds such as multiple orbitals in many transition metal compounds, like the iron pnictide superconductors [25], different "valleys" in hexagonal systems [94], or non-equivalent sublattices, e.g. in $Cu_x Bi_2 Se_3$ [38]. These additional degrees of freedom are generally non-degenerate and give rise to multiple bands [95]. When multiple bands cross the Fermi surface we have to reformulate and generalise our mean-field theory to take this into account

$$H_{\mathrm{MF}} = \sum_{\boldsymbol{k},\sigma} \sum_{n \in \mathrm{bands}} \xi_{\boldsymbol{k},n} c^\dagger_{\boldsymbol{k},n,\sigma} c_{\boldsymbol{k},n,\sigma} + \sum_{\boldsymbol{k},\sigma,\sigma'} \sum_{n,n' \in \mathrm{bands}} (\Delta_{n,\sigma;n',\sigma'}(\boldsymbol{k}) c^\dagger_{\boldsymbol{k},n,\sigma} c^\dagger_{-\boldsymbol{k},n',\sigma'} + \mathrm{h.c.}), \tag{2.50}$$

where the index n enumerates the bands and $\xi_{\boldsymbol{k},n}$ is the free dispersion of band n. We note that the pairing potential $\Delta_{n,\sigma;n',\sigma'}(\boldsymbol{k})$ has acquired two new band indices and an additional distinction in the classification of the superconducting gap is possible. The fermionic antisymmetry of the Cooper pair can also be encoded in the band index. If both band indices are the same, i.e. $n = n'$, electrons from the same band form a Cooper pair which is referred to as *intraband pairing*. On the other hand, if the band indices are not equal, i.e. $n \neq n'$, electrons from different bands form Cooper pairs which is referred to as *interband pairing*. This is illustrated with two bands in Fig. 2.7. Generally, at the Fermi surface the bands are well separated, so we would expect interband pairing to be weak. Nevertheless, it leads to interesting physics because it has profound impacts on the symmetry classification.
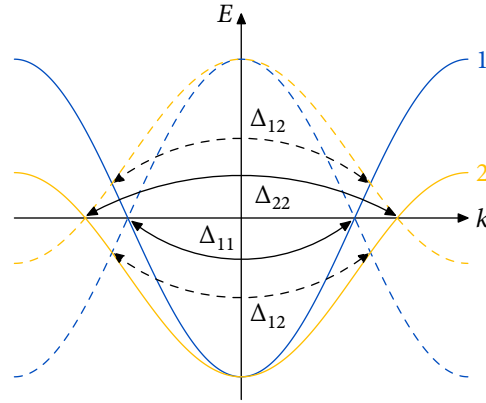
■ *Figure 2.7.* Illustration of the difference between intra- and interband pairing in a model with two bands (solid lines) coloured in blue and orange, each displayed with its particle-hole-reversed counterpart (dashed lines) due to fermion doubling. Superconductivity pairs electrons on opposite sides of the spectrum, which is indicated by arrows. While intraband pairing (Δ_{11} and Δ_{22}) opens a gap at the Fermi level, interband pairing opens a gap away from the Fermi surface (Δ_{12}).

2.3.1 Raghu's model

Since the detection of superconductivity with high transition temperature in the family of the iron pnictides a lot of effort has been invested into understanding the pairing mechanism in these compounds [30–32, 96, 97]. The superconductivity in the iron pnictides is most likely unconventional as evidenced by the resonance peak observed in neutron-scattering experiments which implies that the gap has different sign on different sheets of the Fermi surface [98]. Furthermore, signatures of magnetic excitations in the superconducting state in inelastic neutron scattering experiments suggest a direct coupling between the superconductivity and magnetism, akin to the heavy-fermion superconductors, such as UPt_3 [99, 100]. Thermodynamic probes, such as the discontinuity of the specific heat, scale differently in the iron pnictides than in conventional superconductors ($\Delta C \propto T_c^3$ vs. T_c^2 in conventional superconductors) [25, 101–104]. Electronic correlations in these materials are thought to be weak [27, 105, 106].

To describe the superconductivity in these compounds theoretically, several models were proposed starting from all five $3d$ orbitals of the Fe atoms [107, 108]. Others showed that it is possible to capture the basic physics with fewer orbitals [109–111]. The full five-orbital models are generally considered necessary for detailed quantitative calculations. However, these are very unwieldy, and so simpler models capturing the essence of the physics are useful. The most popular of these reduced models is the one proposed by Raghu *et al.* [111] who developed a minimal two-band model for the superconducting Fe-pnictides. The states at the Fermi surface are derived from the $3d$ orbitals of the Fe atoms which disperse only weakly in the z direction. It was shown by Raghu *et al.* [111] and Mazin *et al.* [112] that the plethora of bands can be reduced, approximating the band structure by two effective orbitals of d_{xz} and d_{yz} character which are degenerate at each site of a square lattice in two dimensions. The point group of the iron pnictides is D_{4h}, so we can extend the discussion from the previous section.

The basis of the Nambu spinors has increased due to the additional orbital degree of freedom. Orbital and spin degrees of freedom are independent and therefore the classification of the basis matrices in spin space from the previous section still applies. Because the orbital degree of freedom also has two components, it can be expressed in Pauli matrices that form a basis of all 2×2 matrices. The effect of the point group

symmetry operations on the orbitals can be derived by considering the transformation properties of the angular momentum, which is shown in Appendix B.1. Here we summarise the matrix form of these operations

$$C_4 : \begin{pmatrix} d_{yz} \to -d_{xz} \\ d_{xz} \to d_{yz} \end{pmatrix} \equiv \begin{pmatrix} 0 & 1 \\ -1 & 0 \end{pmatrix},$$
(2.51)

$$C_2(x) : \begin{pmatrix} d_{yz} \to d_{yz} \\ d_{xz} \to -d_{xz} \end{pmatrix} \equiv \begin{pmatrix} 1 & 0 \\ 0 & -1 \end{pmatrix},$$
(2.52)

$$C_2(x = y) : \begin{pmatrix} d_{yz} \to -d_{xz} \\ d_{xz} \to -d_{yz} \end{pmatrix} \equiv \begin{pmatrix} 0 & -1 \\ -1 & 0 \end{pmatrix},$$
(2.53)

$$\sigma_h : \begin{pmatrix} d_{yz} \to -d_{yz} \\ d_{xz} \to -d_{xz} \end{pmatrix} \equiv \begin{pmatrix} -1 & 0 \\ 0 & -1 \end{pmatrix},$$
(2.54)

$$\sigma_v(x) : \begin{pmatrix} d_{yz} \to -d_{yz} \\ d_{xz} \to d_{xz} \end{pmatrix} \equiv \begin{pmatrix} -1 & 0 \\ 0 & 1 \end{pmatrix},$$
(2.55)

$$\sigma_d(x = y) : \begin{pmatrix} d_{yz} \to d_{xz} \\ d_{xz} \to d_{yz} \end{pmatrix} \equiv \begin{pmatrix} 0 & 1 \\ 1 & 0 \end{pmatrix},$$
(2.56)

$$I : \begin{pmatrix} d_{yz} \to d_{yz} \\ d_{xz} \to d_{xz} \end{pmatrix} \equiv \begin{pmatrix} 1 & 0 \\ 0 & 1 \end{pmatrix}.$$
(2.57)

To avoid confusion we denote the Pauli matrices in orbital space by η. The character of these matrices under the symmetry operations of the D_{4h} point group is summarised in the following table

	C_4	C_2'	C_2''	σ_h	σ_v	σ_d
η_0	+1	+1	+1	+1	+1	+1
η_1	−1	−1	+1	+1	−1	+1
η_2	+1	−1	−1	+1	−1	−1
η_3	−1	+1	−1	+1	+1	−1

(2.58)

Comparing this with the character table for D_{4h} in Tab. A.1 in the Appendix we infer that the matrices can be assigned irreducible representations as such

$$\eta_0 \in A_{1g}, \quad \eta_1 \in B_{2g}, \quad \eta_2 \in A_{2g}, \quad \eta_3 \in B_{1g}.$$
(2.59)

To construct the normal-state Hamiltonian we limit ourselves to terms that are even under time-reversal symmetry. To verify this we evaluate the condition (2.39) for the direct product of orbital and spin matrices. For the spin degree of freedom the unitary part of the time-reversal operator is represented by $i\sigma_2$. We further assume that time-reversal acts trivially on the orbitals, i.e. is represented by η_0. This leads to $U_T = i\eta_0\sigma_2$. With this we evaluate

$$U_T(\eta_\nu \sigma_\mu)^* U_T^\dagger = \pm \eta_\nu \sigma_\mu$$
(2.60)

where the sign determines whether it is odd or even under time-reversal. In the present case where U_T is antisymmetric, i.e. $U_T^T = -U_T$, this leads to another property. We also use the fact that the Pauli matrices are Hermitian, i.e. $\sigma_i = \sigma_i^\dagger$ and therefore $\sigma^* = \sigma^T$. Using these properties we can perform some straight-forward

matrix manipulation on (2.60)

$$
U_T(\eta_\nu \sigma_\mu)^* U_T^\dagger = \pm \eta_\nu \sigma_\mu
$$
$$
-(\eta_\nu \sigma_\mu U_T)^T U_T^\dagger = \pm \eta_\nu \sigma_\mu \qquad | \cdot U_T
$$
$$
-(\eta_\nu \sigma_\mu U_T)^T = \pm \eta_\nu \sigma_\mu U_T. \tag{2.61}
$$

This relation crossed us earlier in (2.21) under the name fermionic antisymmetry and is the necessary requirement for the existence of an even-parity pairing state. Therefore we can conclude that any matrix that is even under time-reversal symmetry, also gives a valid even-parity pairing state. We can therefore summarise time-reversal symmetry and fermionic antisymmetry in a single table, where $+1$ (-1) indicates that the corresponding direct product is (is not) symmetric under both operations

	σ_0	σ_1	σ_2	σ_3
η_0	$+1$	-1	-1	-1
η_1	$+1$	-1	-1	-1
η_2	-1	$+1$	$+1$	$+1$
η_3	$+1$	-1	-1	-1

$$(2.62)$$

We have determined the irreps that the spin and orbital Pauli matrices belong to in (2.31) and (2.59), respectively. The irreps of the resulting direct products can be determined from the product table of D_{4h} in Tab. A.3 in the Appendix. In the following table we show the irreps for all possible direct products, the ones allowed by time-reversal symmetry and fermionic antisymmetry are enclosed in brackets

	σ_0	σ_1	σ_2	σ_3
η_0	$[A_{1g}]$	E_g	E_g	A_{2g}
η_1	$[B_{2g}]$	E_g	E_g	B_{1g}
η_2	A_{2g}	$[E_g]$	$[E_g]$	$[A_{1g}]$
η_3	$[B_{1g}]$	E_g	E_g	B_{2g}

$$(2.63)$$

The non-bracketed terms are not antisymmetric with respect to exchange of spin and orbital degrees of freedom. This implies that pairing states involving these must be odd in momentum to maintain overall fermionic antisymmetry. Taking into account orbital degrees of freedom, the pairing wavefunction can also contain same spins if it is antisymmetric in the orbital degree of freedom.

The introduction of the additional orbital degree of freedom gives rise to a rich structure. We summarise the result of the classification again in the following table

(a,b)	C_4	C_2'	C_2''	σ_h	σ_v	σ_d	irrep	spin	orbital
$(0,0)$	$+1$	$+1$	$+1$	$+1$	$+1$	$+1$	A_{1g}	singlet	even
$(2,3)$	$+1$	$+1$	$+1$	$+1$	$+1$	$+1$	A_{1g}	triplet	odd
$(3,0)$	-1	$+1$	-1	$+1$	$+1$	-1	B_{1g}	singlet	even
$(1,0)$	-1	-1	$+1$	$+1$	-1	$+1$	B_{2g}	singlet	even
$(2,1)$	$+(2,2)$	-1	$-(2,2)$	-1	$+1$	$+(2,2)$	E_g	triplet	odd
$(2,2)$	$-(2,1)$	$+1$	$-(2,1)$	-1	-1	$+(2,1)$	E_g	triplet	odd

$$(2.64)$$

We proceed to construct the normal-state Hamiltonian similar to (2.33). If we take all of the allowed terms from (2.64) into account and truncate the hoppings at next-nearest neighbours we arrive at

$$H = \sum_{a,b} h_{ab}\eta_a\sigma_b = \epsilon_0(\boldsymbol{k})\eta_0\sigma_0 + \epsilon_{x^2-y^2}(\boldsymbol{k})\eta_3\sigma_0 + \epsilon_{xy}(\boldsymbol{k})\eta_1\sigma_0 + \lambda\eta_2\sigma_3 + \lambda_{xz}(\boldsymbol{k})\eta_2\sigma_1 + \lambda_{yz}(\boldsymbol{k})\eta_2\sigma_2. \qquad (2.65)$$

The first term is already familiar, it describes the spin-independent hopping and is the same as for the single-band model. The second term is also spin-independent but has opposite signs on each orbital which is why it is referred to as orbital-anisotropic hopping. The third term is also spin-independent but exchanges the two orbitals which is why it is referred to as inter-orbital hopping. The remaining terms are anisotropic in both orbital and spin, so it comes as no surprise that they are referred to as spin-orbit coupling terms. The last two terms have form factors from the E_g irreducible representation. However, as already noted in the single-band model, these do not have any in-plane components, so we will neglect them from now on.

It is generally possible in the presence of time-reversal and inversion symmetry to block diagonalise the Hamiltonian. Neglecting the $\boldsymbol{k}$-dependent spin-orbit coupling terms has the advantage that it brings the Hamiltonian in block diagonal form with one block for each spin sector

$$H = \begin{pmatrix} H_{s=+1} & 0 \\ 0 & H_{s=-1} \end{pmatrix}, \qquad (2.66)$$

where each block can be parameterised with the spin quantum number s as

$$H_s = \epsilon_0(\boldsymbol{k})\eta_0 + \epsilon_{x^2-y^2}(\boldsymbol{k})\eta_3 + \epsilon_{xy}(\boldsymbol{k})\eta_1 + s\lambda\eta_2 = \begin{pmatrix} \epsilon_0(\boldsymbol{k}) + \epsilon_{x^2-y^2}(\boldsymbol{k}) & \epsilon_{xy}(\boldsymbol{k}) - si\lambda \\ \epsilon_{xy}(\boldsymbol{k}) + si\lambda & \epsilon_0(\boldsymbol{k}) + \epsilon_{x^2-y^2}(\boldsymbol{k}) \end{pmatrix}. \qquad (2.67)$$

Diagonalising each block yields eigenvalues

$$E_\pm = \epsilon_0 \pm \sqrt{\epsilon_{x^2-y^2}^2 + \epsilon_{xy}^2 + \lambda^2}. \qquad (2.68)$$

In Fig. 2.8 we show the resulting band structure along a high-symmetry path in the Brillouin zone and the Fermi surface using the band parameters from [111] with a small spin-orbit coupling. The inclusion of spin-orbit coupling lifts the band degeneracy at the Γ and M points in the Brillouin zone. Without this additional spin-orbit term, there would be an artificial four-fold degeneracy at the these points. Note that the Fermi surface shows strong orbital polarisation.

2.3.2 Pseudospin basis

The fact that the Hamiltonian is even under inversion and time-reversal symmetry leads to a double degeneracy of the states. This makes it possible to find a unitary transform which allows these states to transform under inversion and time-reversal like a spin. This can be summarised as

$$\begin{aligned} \mathcal{I}\psi_{\pm,\Uparrow}(\boldsymbol{k}) &= \psi_{\pm,\Uparrow}(-\boldsymbol{k}), \quad \mathcal{I}\psi_{\pm,\Downarrow}(\boldsymbol{k}) = \psi_{\pm,\Downarrow}(-\boldsymbol{k}) \\ \mathcal{T}\psi_{\pm,\Uparrow}(\boldsymbol{k}) &= \psi_{\pm,\Downarrow}(-\boldsymbol{k}), \quad \mathcal{T}\psi_{\pm,\Downarrow}(\boldsymbol{k}) = -\psi_{\pm,\Uparrow}(-\boldsymbol{k}), \end{aligned} \qquad (2.69)$$

where ⇑ and ⇓ label the pseudospin up and down states and ± is the band index. Additionally the pseudospin basis can be chosen such that the states also transform like a spin under the symmetries of the lattice.

The simplicity of Raghu's model and the fact that it can be diagonalised analytically makes it a nice candidate to discuss the pseudospin basis. Generally, the pseudospin is not equivalent to the electronic spin. To diagonalise
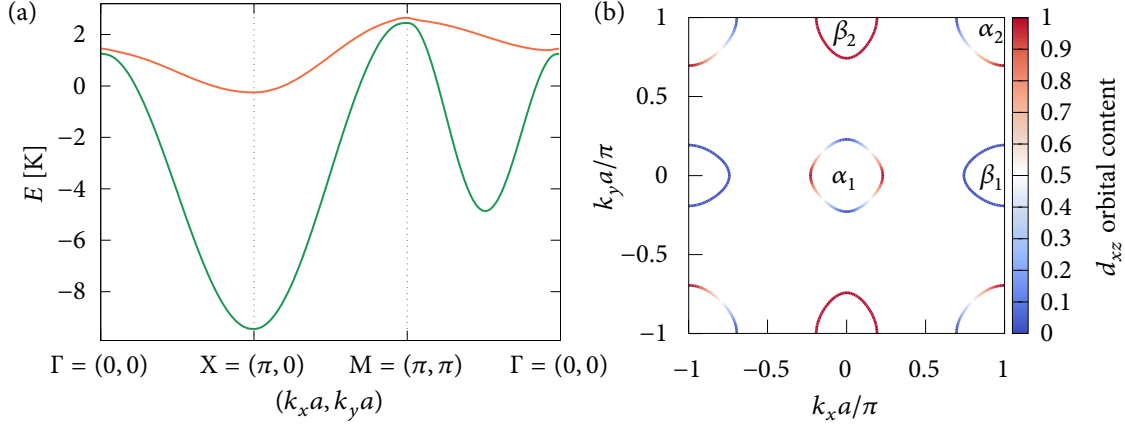
■ *Figure 2.8.* Electronic structure of Raghu's model in the presence of weak spin-orbit coupling. (a) Band structure along high symmetry lines in the first Brillouin zone. The band splitting at the Γ and M point is equal to the spin-orbit coupling strength. Without the inclusion of spin-orbit coupling there would be an artificial four-fold degeneracy at these points. (b) Fermi surface with hole pockets $\alpha_{1,2}$ and electron pockets $\beta_{1,2}$. The colour scale indicates the d_{xz} orbital content on each sheet.

Raghu's model, we exploit the fact that every 2×2 matrix can be written as a linear combination of Pauli matrices. In particular it can be written in terms of the Pauli vector

$$H = d_0 \eta_0 + \boldsymbol{d_k} \cdot \boldsymbol{\eta}, \quad \boldsymbol{d_k} = |\boldsymbol{d}| \begin{pmatrix} \sin\theta_{\boldsymbol{k}} \cos\phi_{\boldsymbol{k}} \\ \sin\theta_{\boldsymbol{k}} \sin\phi_{\boldsymbol{k}} \\ \cos\theta_{\boldsymbol{k}} \end{pmatrix} \tag{2.70}$$

where we parameterise the orientation of the coefficient vector $\boldsymbol{d}$ in spherical coordinates. For Raghu's model the parameters are given by

$$d_0 = \epsilon_0, \tag{2.71}$$

$$|\boldsymbol{d}| = \sqrt{\epsilon_{x^2-y^2}^2 + \epsilon_{xy}^2 + \lambda^2}, \tag{2.72}$$

$$\theta_{\boldsymbol{k}} = \arccos\left(\frac{\epsilon_{x^2-y^2}}{\sqrt{\epsilon_{x^2-y^2}^2 + \epsilon_{xy}^2 + \lambda^2}}\right), \tag{2.73}$$

$$\phi_{\boldsymbol{k}} = \arctan\left(\frac{\lambda}{\epsilon_{xy}}\right). \tag{2.74}$$

The eigenvalues are given by

$$E_{\boldsymbol{k},\pm} = d_0 \pm |\boldsymbol{d}| = \epsilon_0 \pm \sqrt{\epsilon_{x^2-y^2}^2 + \epsilon_{xy}^2 + \lambda^2}, \tag{2.75}$$

and the eigenvectors can be expressed in terms of the angular parameters

$$\psi_{\boldsymbol{k},s,+} = \begin{pmatrix} \cos(\theta_{\boldsymbol{k}}/2)e^{-is\phi_{\boldsymbol{k}}} \\ \sin(\theta_{\boldsymbol{k}}/2) \end{pmatrix}, \quad \psi_{\boldsymbol{k},s,-} = \begin{pmatrix} \sin(\theta_{\boldsymbol{k}}/2)e^{-is\phi_{\boldsymbol{k}}} \\ -\cos(\theta_{\boldsymbol{k}}/2) \end{pmatrix}. \tag{2.76}$$

Lining these up in the basis of (2.65), we find the following form of the pseudospin basis

$$\psi_{\boldsymbol{k},+,\Uparrow} = \begin{pmatrix} e^{-i\phi}\cos(\theta/2) \\ 0 \\ \sin(\theta/2) \\ 0 \end{pmatrix}, \quad \psi_{\boldsymbol{k},-,\Uparrow} = \begin{pmatrix} e^{-i\phi}\sin(\theta/2) \\ 0 \\ -\cos(\theta/2) \\ 0 \end{pmatrix}, \tag{2.77}$$

$$\psi_{\boldsymbol{k},+,\Downarrow} = \begin{pmatrix} 0 \\ -e^{i\phi}\cos(\theta/2) \\ 0 \\ -\sin(\theta/2) \end{pmatrix}, \quad \psi_{\boldsymbol{k},-,\Downarrow} = \begin{pmatrix} 0 \\ -e^{i\phi}\sin(\theta/2) \\ 0 \\ \cos(\theta/2) \end{pmatrix}. \tag{2.78}$$

These obey the transformation properties in (2.69) and therefore, albeit unsurprisingly, we have found a good pseudospin basis.

We now arrange the eigenvectors $\psi_{\boldsymbol{k},s,\pm}$ as columns of a unitary matrix U, which serves as our pseudospin transformation. Obviously this pseudospin transformation diagonalises the normal-state Hamiltonian

$$\tilde{H} = U^\dagger H U = \begin{pmatrix} E_{\boldsymbol{k},+} & 0 \\ 0 & E_{\boldsymbol{k},-} \end{pmatrix}. \tag{2.79}$$

Writing the full BdG-Hamiltonian in this band basis reveals an interesting structure

$$\tilde{H}_{\mathrm{BdG}} = \begin{pmatrix} \tilde{H}(\boldsymbol{k}) & \tilde{\Delta} \\ \tilde{\Delta}^\dagger & -\tilde{H}^T(-\boldsymbol{k}) \end{pmatrix} = \begin{pmatrix} U^\dagger H(\boldsymbol{k})U & U^\dagger \Delta U^* \\ U^T \Delta^\dagger U & -U^T \tilde{H}^T(-\boldsymbol{k})U^* \end{pmatrix} \tag{2.80}$$

The blocks on the diagonal are now diagonal themselves which means that we have changed from the original orbital and spin basis into a band and pseudospin basis. This also implies that the off-diagonal block can now be separated into intra- and interband contributions. Indeed, we can generically express the pairing potential of an even-parity state in the pseudospin basis as

$$\tilde{\Delta} = U^\dagger \Delta U^* = \begin{pmatrix} \psi_{\boldsymbol{k},+} is_2 & (\psi_{\boldsymbol{k},I} - i\boldsymbol{d}_{\boldsymbol{k}} \cdot \boldsymbol{s})is_2 \\ (\psi_{\boldsymbol{k},I} + i\boldsymbol{d}_{\boldsymbol{k}} \cdot \boldsymbol{s})is_2 & \psi_{\boldsymbol{k},-} is_2 \end{pmatrix}, \tag{2.81}$$

where $\boldsymbol{s} = (s_1, s_2, s_3)^T$ is the Pauli vector of pseudospin operators and with the intraband pairing potentials $\psi_{\boldsymbol{k},\pm}$, the interband singlet pairing potential $\psi_{\boldsymbol{k},I}$, and the interband triplet pairing potential $\boldsymbol{d}_{\boldsymbol{k}}$. The diagonal blocks of this matrix are the intraband pairing contributions, whereas the off-diagonal blocks denote the interband pairing contributions. The intraband pairing has no triplet component because of inversion symmetry. Hence an even-parity pairing state always implies an intraband pseudospin singlet, whereas an odd-parity pairing state implies an intraband pseudospin triplet. The interband components cannot be simplified in such a way and are just generic 2×2 matrices. However, they can still be decomposed into a part that is even and a part that is odd under inversion. Independent of the basis the pairing potential has to obey the requirement of fermionic antisymmetry which relates the two off-diagonal blocks to one another and results in a sign change in the pseudospin-triplet component. The prefactor of i was introduced to ensure that $\boldsymbol{d}_{\boldsymbol{k}}$ is a vector with only real entries in the absence of time-reversal symmetry breaking.

Projecting all the allowed pairing states into the pseudospin basis and isolating only the intraband pairing

potentials $\psi_{k,\pm}$ gives the expressions listed in the following table:

irrep	Δ	$\psi_\pm(\boldsymbol{k})$	interband
A_{1g}	$\eta_0 \otimes \sigma_0$	1	no
A_{1g}	$\eta_2 \otimes \sigma_3$	$\pm\dfrac{\lambda}{\sqrt{\lambda^2 + \epsilon_{x^2-y^2}(k)^2 + \epsilon_{xy}(k)^2}}$	yes
B_{1g}	$\eta_3 \otimes \sigma_0$	$\pm\dfrac{\epsilon_{x^2-y^2}(k)}{\sqrt{\lambda^2 + \epsilon_{x^2-y^2}(k)^2 + \epsilon_{xy}(k)^2}}$	yes
B_{2g}	$\eta_1 \otimes \sigma_0$	$\pm\dfrac{\epsilon_{xy}(k)}{\sqrt{\lambda^2 + \epsilon_{x^2-y^2}(k)^2 + \epsilon_{xy}(k)^2}}$	yes
E_g	$\{\eta_2 \otimes \sigma_1, \eta_2 \otimes \sigma_2\}$	0	yes

$$(2.82)$$

The first column lists the different irreducible representations, the second column gives the matrix pairing potential in the orbital and spin basis, the third columns lists the functional form of the intraband pairing potential, and the last column indicates whether this state has a non-zero interband pairing potential.

The matrix pairing potentials that are listed in the second column are independent of momentum. However, by projecting these *a priori* momentum-independent pairing states into the pseudospin basis, they pick up a momentum dependence, i.e. they interact with the spin-orbital texture of the Fermi surface. This implies that, e.g. the $\eta_3\sigma_0$ pairing state in B_{1g} will give rise to an $d_{x^2-y^2}$-wave state at the Fermi surface, because the same nodal structure is enforced by mirror symmetry. Since the matrix pairing potential is of s-wave type it is the same throughout the whole Brillouin zone, which implies that when the intraband pairing potential is vanishing at a node, the interband pairing potential is maximal.

Generally d-wave pairing is thought to arise from nearest-neighbour interactions. However, in this case the orbitally non-trivial B_{1g} state can arise from local pairings, because it is independent of momentum. It may still give rise to an effective form factor at the Fermi surface that is reminiscent of those states that arise from nearest-neighbour interaction. However, as we find from (2.82), some sort of hopping or spin-orbit coupling has to exist in the out-of-plane direction to stabilise such a pairing state by opening an intraband gap at the Fermi surface. In fact, this concept has been generalised and formulated in a rigorous manner and is now known as the "superconducting fitness" [113, 114].

A related situation arises in quasi-two-dimensional materials, where hopping in the out-of-plane direction exists but is heavily suppressed. This usually leads to the assumption that nearest-neighbour pairings in the out-of-plane direction must also be suppressed and can be neglected. Nevertheless, orbitally non-trivial superconductivity with local pairings can still give rise to a pairing state that resembles one with an out-of-plane component at the Fermi surface.

The pairing state realised in the Fe pnictides is an $s_\pm$-wave pairing state. It has a full gap on all sheets of the Fermi surface but reverses sign between the electron-like and the hole-like pockets. It can be written as an orbitally trivial spin-singlet pairing state with an appropriate form factor

$$\Delta_{\boldsymbol{k}} = \Delta_0 \cos(k_x a) \cos(k_y a)\eta_0\sigma_0(i\sigma_2). \tag{2.83}$$

The magnitude and the sign of the gap in the first Brillouin zone are shown in Fig. 2.9(a).

However, it is hard to reconcile this pairing state with the observation of nodeless superconductivity in $A_x Fe_2 Se_2$ [115] and single-layer FeSe [116], where the hole pockets are absent. Their absence jeopardises the
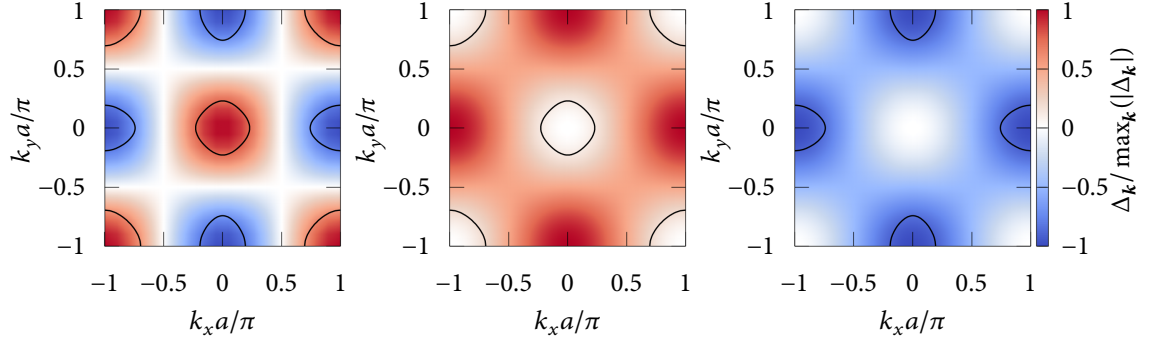
■ *Figure 2.9.* Possible pairing states for $s_{\pm}$ pairing in the Fe pnictides. (a) An orbitally trivial pairing state with a higher harmonic form factor in the A_{1g} irrep will have a full gap on each Fermi surface but reverse sign between the two bands. (b) An orbitally non-trivial pairing state can have the same properties but higher orbital angular momentum to avoid the Coulomb interaction.

phase cancellation between the electron and hole pockets which minimises the on-site Coulomb repulsion. It is also hard to explain how the system could easily transition from a nodeless $s_{\pm}$ state to a nodal state upon doping away the electron pockets in $Ba_{1-x}K_xFe_2As_2$ [117]. To rectify this shortcoming, it was pointed out by Ong *et al.* [58] that there is another possibility for an A_{1g} pairing state that has the same properties. This pairing state is constructed by multiplying a matrix from B_{1g} and B_{2g} with a form factor of the same irrep, respectively. This product will end up in A_{1g} and will have the required structure at the Fermi surface

$$\Delta_{\boldsymbol{k}} = \Delta_0(\alpha[\cos(k_xa) - \cos(k_ya)]\eta_3\sigma_0 + \beta\sin(k_xa)\sin(k_ya)\eta_1\sigma_0)(i\sigma_2), \tag{2.84}$$

where $s_{\pm}$ pairing is realised for the coefficients α and β of the same sign. The gap magnitude in the first Brillouin zone one the two different bands is shown in Fig. 2.9(b).

Orbitally non-trivial superconductivity in the iron pnictides was also discussed by Vafek and Chubukov [118] who proposed a pairing mechanism with only local interactions. In this mechanism orbitally non-trivial pairing states are independent of the intra-orbital Coulomb repulsion. Renormalized interaction parameters give rise to an effective attractive interaction for these anomalous s-wave channels. The resulting pairing state is consistent with the experiments on KFe_2As_2.

Chapter 3

Bogoliubov Fermi surfaces

The material presented in this chapter has been published previously in

[133]   P. M. R. Brydon, D. F. Agterberg, H. Menke, and C. Timm, "Bogoliubov Fermi surfaces: General theory, magnetic order, and topology", Phys. Rev. B **98**, 224509 (2018).

In the previous discussion we have encountered full gaps and gaps with point and line nodes. However, it was recently understood that in inversion-symmetric multiband superconductors that break time-reversal symmetry these nodes may inflate into extended nodal surfaces in the Brillouin zone. These surfaces were named *Bogoliubov Fermi surfaces* and were first reported in [66]. Below we will formulate a comprehensive theory of these Bogoliubov Fermi surfaces, investigating their emergence and phenomena.

3.1   General Theory

As already mentioned, Bogoliubov Fermi surfaces only emerge in centrosymmetric multiband superconductors. Therefore we will start from the most general two-band Hamiltonian with time-reversal and inversion symmetry, which describes fermions with two internal degrees of freedom apart from spin, be it orbital, sublattice, or valley. To simplify the discussion we will just always refer to this internal degree of freedom as orbital. As we saw previously in Section 2.3.1 a two-band Hamiltonian contains one orbitally trivial term and several orbitally non-trivial terms, cf. (2.65). Any such Hamiltonian can be written as

$$H_0 = (\epsilon_{\boldsymbol{k},0} - \mu)\mathbb{1} + \vec{\epsilon}_{\boldsymbol{k}} \cdot \vec{\gamma}, \tag{3.1}$$

where $\vec{\epsilon}_{\boldsymbol{k}} = (\epsilon_{\boldsymbol{k},1}, \ldots, \epsilon_{\boldsymbol{k},5})$ and $\vec{\gamma} = (\gamma_1, \ldots, \gamma_5)$ with five anti-commuting Dirac matrices γ_i ($i = 1, \ldots, 5$) satisfying the Clifford algebra $\{\gamma_a, \gamma_b\} = 2\delta_{ab}$, real coefficients $\epsilon_{\boldsymbol{k},i}$, and the chemical potential μ. Assuming that the inversion operator is trivial, inversion symmetry dictates that the real coefficients $\epsilon_{\boldsymbol{k},i}$ are even functions of $\boldsymbol{k}$, i.e. $\epsilon_{\boldsymbol{k},i} = \epsilon_{-\boldsymbol{k},i}$. The Dirac matrices γ_i may be chosen such that $\gamma_{1,2,3}$ are real and $\gamma_{4,5}$ are complex. Then the time-reversal operator is given as $\mathcal{T} = \gamma_4\gamma_5\mathcal{K} = U_T\mathcal{K}$ where $\mathcal{K}$ denotes complex conjugation.

In the absence of symmetry breaking and interactions the eigenvalues of H_0 are two-fold degenerate for each spin direction. We distinguish these two bands by the $\pm$ index. The eigenvalues are given by $E_{\boldsymbol{k},\pm} - \mu$ where

$$E_{\boldsymbol{k},\pm} = \epsilon_{\boldsymbol{k},0} \pm |\vec{\epsilon}_{\boldsymbol{k}}|. \tag{3.2}$$

Adding in superconductivity, an even-parity pairing potential likewise has to be even under inversion symmetry and therefore only pairing matrices that are even under inversion may appear. The most general matrix pairing potential consistent with this is

$$\Delta_{\boldsymbol{k}} = \eta_{\boldsymbol{k},0}U_T + \vec{\eta}_{\boldsymbol{k}} \cdot \vec{\gamma}\,U_T \tag{3.3}$$

with complex pairing amplitudes $\eta_{\boldsymbol{k},i}$ that are even in momentum and the unitary part of the time-reversal operator U_T. The first term which is proportional to the unit matrix describes pairing between time-reversed partners from the same orbital. This has previously been named "internally isotropic". The the second term describes the pairing between states which are not time-reversed partners. These states are referred to as "internally anisotropic".

The presence of inversion and time-reversal symmetry guarantees that we can label our states with a pseudospin index s. States labelled by the pseudospin shall transform according to (2.69). Transforming the pairing into the pseudospin basis it assumes the general form given by (2.81). The intraband part of the pairing is always independent of the choice of the pseudospin basis and can be expressed as

$$\psi_{\boldsymbol{k},\pm} = \eta_{\boldsymbol{k},0} \pm \frac{\vec{\epsilon}_{\boldsymbol{k}} \cdot \vec{\eta}_{\boldsymbol{k}}}{|\vec{\epsilon}_{\boldsymbol{k}}|} \tag{3.4}$$

On the other hand, the form of the interband pairing depends on the choice of the pseudospin basis but it must satisfy the generic relation

$$|\psi_{\boldsymbol{k},I}|^2 + |\boldsymbol{d}_{\boldsymbol{k}}|^2 = |\vec{\eta}_{\boldsymbol{k}}|^2 - \frac{|\vec{\epsilon}_{\boldsymbol{k}} \cdot \vec{\eta}_{\boldsymbol{k}}|^2}{|\vec{\epsilon}_{\boldsymbol{k}}|^2}. \tag{3.5}$$

We note at this point that the above expression for the interband pairing potential only involves internally anisotropic pairings, whereas the internally isotropic channel only appears in the expression for the intraband part.

3.1.1 Non-unitary pairing

We have already seen previously in (2.42) that the presence of internally anisotropic channels implies that pairing is non-unitary, i.e. the product of the gap with its Hermitian conjugate is not proportional to the unit matrix. In the orbital basis this reads

$$\Delta(\boldsymbol{k})\Delta^\dagger(\boldsymbol{k}) = (|\eta_{\boldsymbol{k},0}|^2 + |\vec{\eta}_{\boldsymbol{k}}|^2)\mathbb{1}_4 + 2\operatorname{Re}(\eta_{\boldsymbol{k},0}^*\vec{\eta}_{\boldsymbol{k}}) \cdot \vec{\gamma} + \sum_{n>m>0} 2i\operatorname{Im}(\eta_{\boldsymbol{k},n}\eta_{\boldsymbol{k},m}^*)\gamma^n\gamma^m. \tag{3.6}$$

The first term is the unitary part, proportional to the unit matrix and is the only one that includes the internally isotropic channel. The two other terms that can only be non-vanishing in the presence of orbitally non-trivial pairing channels. More precisely, these terms are only non-zero if there are multiple components in the internally anisotropic channel. Additionally for the last term to be non-zero there has to be a non-trivial phase difference between the components.

The gap product may also be expressed in the pseudospin basis where it leads to the rather large expression

$$\tilde{\Delta}(\boldsymbol{k})\tilde{\Delta}^\dagger(\boldsymbol{k}) = \left[\frac{1}{2}(|\psi_{\boldsymbol{k},+}|^2 + |\psi_{\boldsymbol{k},-}|^2) + |\psi_{\boldsymbol{k},I}|^2 + |\boldsymbol{d}_{\boldsymbol{k}}|^2\right]\mathbb{1}$$

$$+ \begin{pmatrix} \frac{1}{2}(|\psi_{\boldsymbol{k},+}|^2 - |\psi_{\boldsymbol{k},-}|^2)s_0 + (i\boldsymbol{d}_{\boldsymbol{k}}\times\boldsymbol{d}_{\boldsymbol{k}}^* + 2\operatorname{Im}(\psi_{\boldsymbol{k},I}\boldsymbol{d}_{\boldsymbol{k}}^*))\cdot\boldsymbol{s} & (\psi_{\boldsymbol{k},+}\psi_{\boldsymbol{k},I}^* + \psi_{\boldsymbol{k},-}^*\psi_{\boldsymbol{k},I})s_0 + i(\psi_{\boldsymbol{k},+}\boldsymbol{d}_{\boldsymbol{k}}^* + \psi_{\boldsymbol{k},-}^*\boldsymbol{d}_{\boldsymbol{k}})\cdot\boldsymbol{s} \\ (\psi_{\boldsymbol{k},-}\psi_{\boldsymbol{k},I}^* + \psi_{\boldsymbol{k},+}^*\psi_{\boldsymbol{k},I})s_0 - i(\psi_{\boldsymbol{k},+}^*\boldsymbol{d}_{\boldsymbol{k}} + \psi_{\boldsymbol{k},-}\boldsymbol{d}_{\boldsymbol{k}}^*)\cdot\boldsymbol{s} & \frac{1}{2}(|\psi_{\boldsymbol{k},-}|^2 - |\psi_{\boldsymbol{k},+}|^2)s_0 + (i\boldsymbol{d}_{\boldsymbol{k}}\times\boldsymbol{d}_{\boldsymbol{k}}^* - 2\operatorname{Im}(\psi_{\boldsymbol{k},I}\boldsymbol{d}_{\boldsymbol{k}}^*))\cdot\boldsymbol{s} \end{pmatrix}. \tag{3.7}$$

The diagonal entries of the non-unitary part are going to be important later. In particular the terms proportional to the Pauli vector of pseudospin matrices, because these give rise to an effective pseudospin polarisation $\operatorname{Tr}[\Delta^\dagger(\boldsymbol{k})\mathcal{P}_{\boldsymbol{k},\pm}\check{s}\mathcal{P}_{\boldsymbol{k},\pm}\Delta(\boldsymbol{k})]$ with projection operators $\mathcal{P}_{\boldsymbol{k},\pm}$ onto the normal-state Hilbert space and

$$\check{s} \equiv \begin{pmatrix} \boldsymbol{s} & 0 \\ 0 & \boldsymbol{s} \end{pmatrix}. \tag{3.8}$$

As mentioned before, these contributions arise from the fact that time-reversal symmetry is broken and we indicated that these stem entirely from the presence of internally anisotropic pairing channels. To gain some more insight we therefore examine only the part of the gap product that is odd under time-reversal. That is to say we form the gap product and subtract its time-reversed form.

$$\Delta_{\boldsymbol{k}}\Delta_{\boldsymbol{k}}^{\dagger} - U_T \Delta_{-\boldsymbol{k}}^{*}\Delta_{-\boldsymbol{k}}^{T}U_T^{\dagger} = (\vec{\eta}_{\boldsymbol{k}} \cdot \vec{\gamma})(\vec{\eta}_{\boldsymbol{k}}^{*} \cdot \vec{\gamma}) - (\vec{\eta}_{\boldsymbol{k}}^{*} \cdot \vec{\gamma})(\vec{\eta}_{\boldsymbol{k}} \cdot \vec{\gamma}) \tag{3.9}$$

$$= \sum_{i,j}(\eta_i \eta_j^{*} - \eta_i^{*}\eta_j)\gamma_i\gamma_j \tag{3.10}$$

There is no physical observable related to this operator which is quadratic in the gap amplitude and it is generally referred to as *time-reversal odd bilinear* (TROB) [119].

3.1.2 Topological protection

In addition to inversion symmetry (or parity symmetry) $\mathcal{P}$ that we required earlier, the BdG Hamiltonian of superconductivity has an additional particle-hole symmetry. Particle-hole symmetry (or charge-conjugation symmetry) $\mathcal{C}$ is anti-unitary. It is less of a symmetry in the classic sense, because that means that it could be spontaneously broken. Instead, from a mathematical perspective particle-hole symmetry is a consequence of the Nambu doubling and is therefore an intrinsic property of any single-particle BdG-Hamiltonian without interactions. In a superconductor particle-hole symmetry is dictated by the fermionic antisymmetry of the pairing wave function which means that any superconducting Hamiltonian can be written in the BdG-form. Its functional form $\mathcal{C} = U_C\mathcal{K}$ can be detailed as follows

$$\mathcal{C}: \quad U_C H^{*}(-\boldsymbol{k})U_C^{\dagger} = -H(\boldsymbol{k}), \quad U_C = \tau_x \otimes \mathbb{1}. \tag{3.11}$$

The combination of both these symmetries is denoted as $\mathcal{CP}$ and acts on the Hamiltonian like

$$\mathcal{CP}: \quad U_{CP} H^{*}(\boldsymbol{k})U_{CP}^{\dagger} = -H(\boldsymbol{k}), \quad U_{CP} = U_C U_P^{*} = \tau_x \otimes \mathbb{1}. \tag{3.12}$$

This leads to the property $(\mathcal{CP})^2 = +1$ which guarantees the existence of a Pfaffian [66, 120–122]. This implies that the Bogoliubov Fermi surfaces are topologically protected against $\mathcal{CP}$-preserving perturbations. The Hamiltonian can be unitarily transformed into skew-symmetric form

$$\tilde{H}_{\boldsymbol{k}} = \Omega H_{\boldsymbol{k}}\Omega^{\dagger}, \tag{3.13}$$

with the Majorana transformation

$$\Omega = \frac{1}{\sqrt{2}}\begin{pmatrix} 1 & 1 \\ i & -i \end{pmatrix} \otimes \mathbb{1}. \tag{3.14}$$

For a skew-symmetric matrix, the determinant can be written as the square of a polynomial, which is called the Pfaffian and is defined for a $2N \times 2N$ skew-symmetric matrix A as

$$\mathrm{Pf}(A) = \frac{1}{2^N N!}\sum_{\sigma \in S_{2N}} \mathrm{sgn}(\sigma)A_{\sigma(1),\sigma(2)} \cdots A_{\sigma(2N-1),\sigma(2N)}, \tag{3.15}$$

where S_{2N} is the set of $2N$ permutations and $\mathrm{sgn}(\sigma)$ is the parity of the permutation σ. By definition it holds that $\mathrm{Pf}(A)^2 = \det(A)$. For $\tilde{H}_{\boldsymbol{k}}$ the Pfaffian takes the form

$$P(\boldsymbol{k}) = \mathrm{Pf}\,\tilde{H}_{\boldsymbol{k}} = \left(\langle \underline{\epsilon}_{\boldsymbol{k}}, \underline{\epsilon}_{\boldsymbol{k}}\rangle\rangle - \langle \underline{\eta}_{\boldsymbol{k}}, \underline{\eta}_{\boldsymbol{k}}^{*}\rangle\right)^2 + 4|\langle \underline{\epsilon}_{\boldsymbol{k}}, \underline{\eta}_{\boldsymbol{k}}\rangle|^2 + \langle \underline{\eta}_{\boldsymbol{k}}, \underline{\eta}_{\boldsymbol{k}}\rangle\langle \underline{\eta}_{\boldsymbol{k}}^{*}, \underline{\eta}_{\boldsymbol{k}}^{*}\rangle - \langle \underline{\eta}_{\boldsymbol{k}}, \underline{\eta}_{\boldsymbol{k}}^{*}\rangle^2, \tag{3.16}$$

with the six-vectors

$$\underline{\epsilon}_{\boldsymbol{k}} = (\epsilon_{\boldsymbol{k},0} - \mu, \vec{\epsilon}_{\boldsymbol{k}}), \quad \underline{\eta}_{\boldsymbol{k}} = (\eta_{\boldsymbol{k},0}, \vec{\eta}_{\boldsymbol{k}}), \tag{3.17}$$

and the covariant product

$$\langle \underline{a}, \underline{b} \rangle = a_0 b_0 - \vec{a} \cdot \vec{b}. \tag{3.18}$$

The corresponding topological invariant is defined as [66]

$$(-1)^l = \mathrm{sgn}[P(\boldsymbol{k}_-)P(\boldsymbol{k}_+)], \tag{3.19}$$

where $\boldsymbol{k}_{\pm}$ are momenta inside and outside the Bogoliubov Fermi surface, respectively. At the Bogoliubov Fermi surface itself the Pfaffian vanishes.

Evidently, the first two terms in the expression for the Pfaffian $P(\boldsymbol{k})$ are strictly positive, due to the square, whereas the contribution of the two latter terms may change the overall sign of $P(\boldsymbol{k})$. This can be made more explicit by writing the pairing potential as an amplitude and a phase, i.e. $\eta_{\boldsymbol{k},n} = |\eta_{\boldsymbol{k},n}|e^{i\phi_{\boldsymbol{k},n}}$. Then the last two terms read

$$\langle \underline{\eta}_{\boldsymbol{k}}, \underline{\eta}_{\boldsymbol{k}} \rangle \langle \underline{\eta}_{\boldsymbol{k}}^*, \underline{\eta}_{\boldsymbol{k}}^* \rangle - \langle \underline{\eta}_{\boldsymbol{k}}, \underline{\eta}_{\boldsymbol{k}}^* \rangle^2 = 4 \sum_{n>0} |\eta_{\boldsymbol{k},0}|^2 |\eta_{\boldsymbol{k},n}|^2 \sin^2(\phi_{\boldsymbol{k},0} - \phi_{\boldsymbol{k},n}) - 4 \sum_{n>m>0} |\eta_{\boldsymbol{k},n}|^2 |\eta_{\boldsymbol{k},m}|^2 \sin^2(\phi_{\boldsymbol{k},n} - \phi_{\boldsymbol{k},m}) \tag{3.20}$$

The first term shows that coexistence of internally isotropic and anisotropic channels does not constitute a sign change of the Pfaffian. Only the coexistence of multiple components of the internally anisotropic channels may lead to a negative contribution, but only if their relative phases are non-trivial, i.e. if the overall superconducting state breaks time-reversal symmetry. The negative contribution is maximal if time-reversal symmetry is broken maximally, i.e. the relative phase between components is $\pi/2$. Interestingly the presence of this term is also equivalent to the existence of the time-reversal odd bilinear and therefore the non-unitary part of the gap product that leads to a non-zero pseudospin polarisation.

3.2 Effective low-energy model

To gain further understanding about the origin of the Bogoliubov Fermi surfaces and make a more direct connection with the non-unitary pairing we will now study how the pseudomagnetic field influences the states at the Fermi surface. To this end we project the Hamiltonian into a pseudospin basis

$$\tilde{H}_{\boldsymbol{k}} = \begin{pmatrix} H_{\boldsymbol{k},+} & H_{\boldsymbol{k},I} \\ H_{\boldsymbol{k},I}^{\dagger} & H_{\boldsymbol{k},-} \end{pmatrix} \tag{3.21}$$

where the intra- and interband blocks are given by

$$H_{\boldsymbol{k},\pm} = \begin{pmatrix} E_{\boldsymbol{k},\pm} s_0 & \psi_{\boldsymbol{k},\pm}(is_2) \\ -\psi_{\boldsymbol{k},\pm}^* is_2 & -E_{\boldsymbol{k},\pm} s_0 \end{pmatrix}, \quad H_{\boldsymbol{k},I} = \begin{pmatrix} 0 & (\psi_{\boldsymbol{k},I} - i\boldsymbol{d}_{\boldsymbol{k}} \cdot \boldsymbol{s})is_2 \\ -(\psi_{\boldsymbol{k},I}^* + i\boldsymbol{d}_{\boldsymbol{k}}^* \cdot \boldsymbol{s})is_2 & 0 \end{pmatrix}. \tag{3.22}$$

If the bands are split far apart, then interband pairing $H_{\boldsymbol{k},I}$ can be assumed to be weak and we can treat it as a perturbation to the intraband Hamiltonian $H_{\boldsymbol{k},\pm}$. To this end we extract the Green's function of the above Hamiltonian

$$(i\omega_n - \tilde{H}_{\boldsymbol{k}})G(\boldsymbol{k}, i\omega_n) = \begin{pmatrix} i\omega_n - H_{\boldsymbol{k},+} & H_{\boldsymbol{k},I} \\ H_{\boldsymbol{k},I}^{\dagger} & i\omega_n - H_{\boldsymbol{k},-} \end{pmatrix} \begin{pmatrix} G_+(\boldsymbol{k}, i\omega_n) & G_I(\boldsymbol{k}, i\omega_n) \\ G_I^{\dagger}(\boldsymbol{k}, i\omega_n) & G_-(\boldsymbol{k}, i\omega_n) \end{pmatrix} = \mathbb{1} \tag{3.23}$$

We are interested in the Green's functions of both bands, so we solve the resulting Gor'kov equations for them and find

$$G_+^{-1}(\boldsymbol{k}, i\omega_n) = i\omega_n - H_{\boldsymbol{k},+} - H_{\boldsymbol{k},I}(i\omega_n - H_{\boldsymbol{k},-})^{-1}H_{\boldsymbol{k},I}^\dagger \equiv i\omega_n - H_{\boldsymbol{k},+}^{\text{eff}}, \tag{3.24}$$

$$G_-^{-1}(\boldsymbol{k}, i\omega_n) = i\omega_n - H_{\boldsymbol{k},-} - H_{\boldsymbol{k},I}^\dagger(i\omega_n - H_{\boldsymbol{k},+})^{-1}H_{\boldsymbol{k},I} \equiv i\omega_n - H_{\boldsymbol{k},-}^{\text{eff}}, \tag{3.25}$$

where we have defined the effective Hamiltonian $H_{\boldsymbol{k},\pm}^{\text{eff}}$ for each band. At this point we have not applied any approximation and the effective Hamiltonian still contains the full dynamics of the interband pairing. The most naïve approximation is to completely neglect the interband pairing which is equivalent to dropping the off-diagonal block in (3.21). This means for the effective Hamiltonian that

$$H_{\boldsymbol{k},+}^{\text{eff}} \approx H_{\boldsymbol{k},\pm}. \tag{3.26}$$

Essentially we have completely decoupled the two bands from each other and are now left with two independent "copies" of a single-band superconductor. However, we already know the physics of single-band superconductors and we know well that the only nodal structure that can arise in this situation are point and/or line nodes. This implies that only internally anisotropic terms give rise to Bogoliubov Fermi surfaces and therefore interband pairing is expected to be important which is not present in $H_{\boldsymbol{k},\pm}$, as only the intraband part $\psi_{\boldsymbol{k},\pm}(is_2)$ appears.

Hence we have to take into account the second term in the effective Hamiltonian. Treating this term in full is not tractable and since we are only interested in its influence on the states right at the Fermi surface we can apply the static limit $\omega_n = 0$ because only energies close to zero are relevant [70]. Below we apply this approximation to the Green's function for the + band, but the steps for the − band are analogous. The correction to the Hamiltonian for the + is given by

$$\delta H_{\boldsymbol{k},+} = H_{\boldsymbol{k},I}(i\omega_n - H_{\boldsymbol{k},-})^{-1}H_{\boldsymbol{k},I}^\dagger \approx -H_{\boldsymbol{k},I}H_{\boldsymbol{k},-}^{-1}H_{\boldsymbol{k},I}^\dagger \tag{3.27}$$

We have assumed that the bands are split far apart, so we may further assume that the gap on the opposite band is vanishing $\psi_{\boldsymbol{k},\pm} = 0$ and therefore the Hamiltonian of the opposite band simplifies to $H_{\boldsymbol{k},\pm} \approx (E_{\boldsymbol{k},\pm} - \mu)s_0\tau_3$. This Hamiltonian is diagonal, so its inverse is trivial to compute

$$\delta H_{\boldsymbol{k},+} \approx -(E_{\boldsymbol{k},-} - \mu)^{-1}H_{\boldsymbol{k},I}s_0\tau_3 H_{\boldsymbol{k},I}^\dagger. \tag{3.28}$$

Furthermore we may assume that the same band is approximately constant and equal to the chemical potential $\mu \approx E_{\boldsymbol{k},\mp}$ at the Fermi surface, so the effective Hamiltonian is inversely proportional to the band splitting

$$\delta H_{\boldsymbol{k},+} \approx -(E_{\boldsymbol{k},-} - E_{\boldsymbol{k},+})^{-1}H_{\boldsymbol{k},I}s_0\tau_3 H_{\boldsymbol{k},I}^\dagger \tag{3.29}$$

$$= -\frac{1}{2|\vec{\epsilon}_{\boldsymbol{k}}|}H_{\boldsymbol{k},I}s_0\tau_3 H_{\boldsymbol{k},I}^\dagger. \tag{3.30}$$

These steps may be performed analogously for the other band and results in the expression

$$\delta H_{\boldsymbol{k},-} \equiv H_{\boldsymbol{k},I}^\dagger(i\omega_n - H_{\boldsymbol{k},+})^{-1}H_{\boldsymbol{k},I} \approx -\frac{1}{2|\vec{\epsilon}_{\boldsymbol{k}}|}H_{\boldsymbol{k},I}^\dagger s_0\tau_3 H_{\boldsymbol{k},I}. \tag{3.31}$$

We know that $H_{\boldsymbol{k},I}$ has only off-diagonal elements, which means that the product with $s_0\tau_3$ will turn $\delta H_{\boldsymbol{k},\pm}$ into a block diagonal matrix, where we can further write the blocks as a decomposition of pseudospin Pauli matrices

$$\delta H_{\boldsymbol{k},\pm} = \begin{pmatrix} \delta\epsilon_{\boldsymbol{k},\pm}s_0 + \delta\boldsymbol{h}_{\boldsymbol{k},\pm} \cdot \boldsymbol{s} & 0 \\ 0 & -\delta\epsilon_{\boldsymbol{k},\pm}s_0 - \delta\boldsymbol{h}_{\boldsymbol{k},\pm} \cdot \boldsymbol{s}^T \end{pmatrix}, \tag{3.32}$$

Plugging in the form of $H_{k,I}$ we find

$$\delta\epsilon_{k,\pm} = \pm\frac{|\psi_{k,I}|^2 + |d_k|^2}{2|\vec{\epsilon}_k|}, \tag{3.33}$$

$$\delta h_{k,\pm} = \pm\frac{id_k \times d_k^* - 2\operatorname{Im}[\psi_{k,I}d_k^*]}{2|\vec{\epsilon}_k|} = -\frac{\operatorname{Tr}[\mathcal{P}_{k,\pm}\Delta_k\Delta_k^\dagger\mathcal{P}_{k,\pm}\check{s}]}{2|\vec{\epsilon}_k|}, \tag{3.34}$$

where the term $\delta\epsilon_{k,\pm}$ describes a shift of the chemical potential and $\delta h_{k,\pm}$ acts like a magnetic field on the pseudospin, hence the name pseudomagnetic field. First of all we note that $\delta\epsilon_{k,\pm}$ is generally non-zero in the presence of internally anisotropic pairing channels and does not require broken time-reversal symmetry. Its effect is to shift the nodes of the superconducting gap away from the original Fermi surface. This phenomenon has been noted before in models for orbitally non-trivial superconductivity in the iron based superconductors [59, 60]. The pseudomagnetic field $\delta h_{k,\pm}$ on the other hand only emerges if the superconductivity breaks time-reversal symmetry. Its effect on the low energy states is analogous to a real magnetic field as it lifts the pseudospin degeneracy and shifts the nodes to finite energies, forming pockets that have been named Bogoliubov Fermi surfaces. Another interesting observation about the pseudomagnetic field is that its functional form is directly related to the gap product projected into the pseudospin sector. Hence, the existence of Bogoliubov Fermi surfaces is deeply linked to the non-unitarity of the gap.

The eigenvalues of the low-energy effective Hamiltonian can easily be computed and are given by

$$E_{k,\pm}^{\text{eff}} = \alpha|\delta h_{k,\pm}| + \beta\sqrt{(E_{k,\pm} + \delta\epsilon_{k,\pm} - \mu)^2 + |\psi_{k,\pm}|^2} \tag{3.35}$$

with the two signs $\alpha, \beta = \pm 1$ which may be chosen independently.

3.3 Paradigmatic model

As a paradigmatic model Hamiltonian for Bogoliubov Fermi surfaces is the Luttinger-Kohn Hamiltonian for $j = 3/2$ fermions of the cubic point group O_h [123, 124] has been established, because its functional form is relatively simple with only four band parameters. Two of the band parameters control spin-orbit coupling, which can be tuned such that the Hamiltonian preserves full rotational SO(3) symmetry, rather than "just" O_h. Coupling of an $l = 1$ orbital angular momentum with $s = 1/2$ spins gives rise to states with total angular momentum $j = 3/2$ and $j = 1/2$, see Appendix B.2 for a derivation. Assuming that the $j = 3/2$ and $j = 1/2$ states are well-separated in energy and only the $j = 3/2$ bands are close to the Fermi energy, it is possible to neglect the $j = 1/2$ states and arrive at a model of purely $j = 3/2$ fermions. It is also the model in which Bogoliubov Fermi surfaces were first numerically detected by Carsten Timm [66].

The Luttinger-Kohn Hamiltonian was originally devised to describe the low-energy electronic structure of zinc-blende semiconductors [125]. It generically features a quadratic band touching point and has since been applied to describe pyrochlore iridates [126–129] and half-Heusler compounds [64, 130–132]. In the context of superconductivity and Bogoliubov Fermi surfaces the Luttinger-Kohn Hamiltonian was originally used to discuss the pairing states in the half-Heusler compound YtPtBi [64] where it describes a $k \cdot p$ theory for the $j = 3/2$ fermions of the Γ_8 band that arise from the strong atomic spin-orbit coupling of $s = 1/2$ spins with $l = 1$ orbital angular momentum. The Hamiltonian is given by

$$H_0 = \sum_k \Phi_k^\dagger H_k \Phi_k \tag{3.36}$$

with $\Phi_{\boldsymbol{k}} = (c_{\boldsymbol{k},3/2}, c_{\boldsymbol{k},1/2}, c_{\boldsymbol{k},-1/2}, c_{\boldsymbol{k},-3/2})^T$ where $c_{\boldsymbol{k},\sigma}$ is the annihilation operation of a fermion with momentum $\boldsymbol{k}$ and spin σ and the BdG-Hamiltonian

$$H_{\boldsymbol{k}} = (\alpha|\boldsymbol{k}|^2 - \mu) + \beta \sum_i k_i^2 J_i^2 + \gamma \sum_{i \neq j} k_i k_j J_i J_y, \tag{3.37}$$

where $i = x, y, z$ and $i + 1 = y$ if $i = x$, etc., and J_i are the 4×4 matrix representations of the angular momentum operators $j = 3/2$ which are given by

$$J_x = \frac{1}{2}\begin{pmatrix} 0 & \sqrt{3} & 0 & 0 \\ \sqrt{3} & 0 & 2 & 0 \\ 0 & 2 & 0 & \sqrt{3} \\ 0 & 0 & \sqrt{3} & 0 \end{pmatrix}, \quad J_y = \frac{i}{2}\begin{pmatrix} 0 & -\sqrt{3} & 0 & 0 \\ \sqrt{3} & 0 & -2 & 0 \\ 0 & 2 & 0 & -\sqrt{3} \\ 0 & 0 & \sqrt{3} & 0 \end{pmatrix}, \quad J_z = \frac{1}{2}\begin{pmatrix} 3 & 0 & 0 & 0 \\ 0 & 1 & 0 & 0 \\ 0 & 0 & -1 & 0 \\ 0 & 0 & 0 & -3 \end{pmatrix}. \tag{3.38}$$

The band parameters comprise a spin-independent dispersion coefficient α, the chemical potential μ, and the symmetry-allowed spin-orbit coupling terms proportional to β and γ. The Hamiltonian has doubly degenerate eigenvalues given by $(E_{\boldsymbol{k},\pm} - \mu)$ with

$$E_{\boldsymbol{k},\pm} = \left(\alpha + \frac{5}{4}\beta\right)|\boldsymbol{k}|^2 \pm \beta\sqrt{\sum_i \left[k_i^4 + \left(\frac{3\gamma^2}{\beta^2} - 1\right)k_i^2 k_{i+1}^2\right]}. \tag{3.39}$$

The band structure has a four-fold degenerate quadratic band touching point at Γ. Away from Γ spin-orbit coupling $\beta, \gamma \neq 0$ lifts the four-fold degeneracy, yet the bands remain doubly degenerate. This allows for the states to be labelled by a pseudospin-1/2 index [133]. If the band splitting controlled by β and γ is small, both bands curve the same way and there are two Fermi surfaces. For large band splitting one of the bands can curve in opposite directions and there is only a single Fermi surface. This latter situation is referred to as inverted band structure.

We can bring this Hamiltonian into the form of (3.1) using the parameterization

$$\epsilon_{\boldsymbol{k},0} = (\alpha + 5\beta/4)k^2 - \mu, \tag{3.40}$$

$$\epsilon_{\boldsymbol{k},1} = \frac{1}{2}\beta\left(k_z^2 - \frac{1}{2}(k_x^2 + k_y^2)\right) \quad \gamma_1 = \frac{1}{3}(2J_z^2 - J_x^2 - J_y^2), \tag{3.41}$$

$$\epsilon_{\boldsymbol{k},2} = \frac{\sqrt{3}}{2}\beta(k_x^2 - k_y^2) \quad \gamma_2 = \frac{1}{\sqrt{3}}(J_x^2 - J_y^2), \tag{3.42}$$

$$\epsilon_{\boldsymbol{k},3} = \sqrt{3}\gamma k_y k_z \quad \gamma_3 = \frac{1}{\sqrt{3}}(J_y J_z + J_z J_y), \tag{3.43}$$

$$\epsilon_{\boldsymbol{k},4} = \sqrt{3}\gamma k_x k_z \quad \gamma_4 = \frac{1}{\sqrt{3}}(J_x J_z + J_z J_x), \tag{3.44}$$

$$\epsilon_{\boldsymbol{k},5} = \sqrt{3}\gamma k_x k_y \quad \gamma_5 = \frac{1}{\sqrt{3}}(J_x J_y + J_y J_x). \tag{3.45}$$

In this choice $\gamma_{1,2,4}$ are real and $\gamma_{3,5}$ are complex. Hence the time-reversal operator is given by

$$U_T = \gamma_5 \gamma_3 = \begin{pmatrix} 0 & 0 & 0 & 1 \\ 0 & 0 & -1 & 0 \\ 0 & 1 & 0 & 0 \\ -1 & 0 & 0 & 0 \end{pmatrix} \tag{3.46}$$

At this point it is important to note that the parameterization that we have chosen here is not unique and was selected merely for convenience of notation. We will use this parameterization of the Luttinger-Kohn Hamiltonian to highlight generic features of Bogoliubov Fermi surfaces.

Adding in superconductivity the most general even-parity pairing potential is given by [64–67, 71, 72, 75–77, 79, 134–136]

$$\Delta_{\boldsymbol{k}} = \sum_l \eta_{\boldsymbol{k},l}\Gamma_l \tag{3.47}$$

where the $\eta_{\boldsymbol{k},l}$ are complex pairing amplitudes and Γ_l are pairing matrices which can be classified according to the irreducible representations of the point group

$$A_{1g}: \qquad \Gamma_s = U_T, \tag{3.48}$$

$$E_g: \quad \Gamma_{3z^2-r^2} = \gamma_1 U_T = \frac{1}{3}(2J_z^2 - J_x^2 - J_y^2)U_T, \tag{3.49}$$

$$\Gamma_{x^2-y^2} = \gamma_2 U_T = \frac{1}{\sqrt{3}}(J_x^2 - J_y^2)U_T, \tag{3.50}$$

$$T_{2g}: \qquad \Gamma_{yz} = \gamma_3 U_T = \frac{1}{\sqrt{3}}(J_y J_z + J_z J_y)U_T, \tag{3.51}$$

$$\Gamma_{xz} = \gamma_4 U_T = \frac{1}{\sqrt{3}}(J_x J_z + J_z J_x)U_T, \tag{3.52}$$

$$\Gamma_{xy} = \gamma_5 U_T = \frac{1}{\sqrt{3}}(J_x J_y + J_y J_x)U_T. \tag{3.53}$$

The single internally isotropic singlet-channel occupies the A_{1g} representation. The internally anisotropic channels, which represent Cooper pairs with total angular momentum $J = 2$, i.e. quintet states, split into the two-component E_g and three-component T_{2g} representations. As mentioned in the previous chapter, since the time-reversal operator is antisymmetric, fermionic antisymmetry is equivalent to time-reversal symmetry and therefore all the single-matrix pairing potentials above are even under and therefore preserve time-reversal symmetry. Assuming only local pairings, the interaction Hamiltonian can be written in the general form

$$H_{\text{pair}} = \sum_j \sum_l \sum_{l_i \in l} V_l b_{l_i,j}^\dagger b_{l_i,j}, \tag{3.54}$$

where the fermion bilinear $b_{l_i,j}^\dagger$ is the annihilation operator of a Cooper pair at site j in channel l_i belonging to the irrep l and V_l is the interaction potential in that irrep [64].

3.3.1 Weak-coupling pairing states from symmetry

In weak-coupling theory the pairing state that is realised below the critical temperature T_c is the one that minimises the mean-field free energy. We will pursue this approach later, but first we will take a look at the Landau expansion of the free energy. This purely phenomenological theory is based on the concept of symmetry-breaking, where the macroscopic order parameter has a lower symmetry in the low-temperature ordered phase than in the high-temperature unordered phase. The macroscopic order parameter vanishes above the critical temperature but attains a finite value below.

In the Landau expansion of the free energy the order parameter is related to gap amplitudes which transform under symmetry operations of the point group in the same way. Since the free energy is derived from the Hamiltonian, it shall transform equivalently under symmetry operations. To obtain all the allowed terms in the expansion, product groups of appropriate order have to be formed and only the terms that transform trivially are kept. This is laborious and has been done previously for several different point groups in [42].

For the point group O_h the Landau expansion up to fourth order in the E_g representation reads

$$
\begin{aligned}
F_{E_g} &= \alpha(|h_{3z^2-r^2}|^2 + |h_{x^2-y^2}|^2) + \beta_1(|h_{3z^2-r^2}|^2 + |h_{x^2-y^2}|^2)^2 + \beta_2(h^*_{3z^2-r^2}h_{x^2-y^2} - h_{3z^2-r^2}h^*_{x^2-y^2})^2 \\
&= \alpha|\boldsymbol{h}|^2 + \beta_1|\boldsymbol{h}|^4 + \beta_2|\boldsymbol{h} \times \boldsymbol{h}^*|^2
\end{aligned}
\tag{3.55}
$$

where we have introduced $\boldsymbol{h} = (h_{3z^2-r^2}, h_{x^2-y^2})^T$ as a vector notation of the order parameter. For the three-component T_{2g} representation the expansion reads

$$
\begin{aligned}
F_{T_{2g}} &= \alpha(|l_{yz}|^2 + |l_{xz}|^2) + \beta_1(|l_{yz}|^2 + |l_{xz}|^2 + |l_{xy}|^2)^2 + \beta_2|l_{yz}^2 + l_{xz}^2 + l_{xy}^2|^2 \\
&\qquad\qquad + \beta_3(|l_{yz}|^2|l_{xz}|^2 + |l_{xz}|^2|l_{xy}|^2 + |l_{xy}|^2|l_{yz}|^2) \\
&= \alpha|\boldsymbol{l}|^2 + \beta_1|\boldsymbol{l}|^4 + \beta_2|\boldsymbol{l}\cdot\boldsymbol{l}|^2 + \beta_3\sum_{n>m}|l_n|^2|l_m|^2
\end{aligned}
\tag{3.56}
$$

with the ordering vector $\boldsymbol{l} = (l_{yz}, l_{xz}, l_{xy})^T$.

Below the critical temperature the coefficient α of the second-order term assumes a negative value whereas the fourth-order term is always positive definite. This implies that the fourth-order term selects the minimum of the free energy, which puts some constraints on the values of β. From tables like [42] we find

$$
\tag{3.57}
$$

	Pairing	Constraint	TRS
E_g:	$\boldsymbol{h} = (1,0)$	$\beta_2 < 0$	unbroken
E_g:	$\boldsymbol{h} = (1,i)$	$\beta_2 > 0$	broken
T_{2g}:	$\boldsymbol{l} = (1,0,0)$	$4\beta_2 < \beta_3, \beta_3 > 0$	unbroken
T_{2g}:	$\boldsymbol{l} = (1,1,1)$	$\beta_2, \beta_3 < 0$	unbroken
T_{2g}:	$\boldsymbol{l} = (1,i,0)$	$0 < \beta_3 < 4\beta_2$	broken
T_{2g}:	$\boldsymbol{l} = (1,\omega,\omega^2)$	$\beta_3 < 0 < \beta_2$	broken

and any symmetry-related vectors with $\omega = e^{i\pi/3}$. By construction, this expansion only holds true right below the critical temperature. As we will see later, at lower temperatures, intermediate states between the time-reversal symmetric and the maximally time-reversal symmetry breaking states will emerge.

3.3.2 Validity of the low-energy theory and pseudomagnetic field

Thanks to the double degeneracy of the bands (3.39), the states can be labelled by a pseudospin index s which transforms like a spin-1/2 under inversion and time-reversal symmetry. For the Hamiltonian (3.37) such a pseudospin basis can be found [133] with the basis states

$$
\psi_{\boldsymbol{k},+,\uparrow} = \frac{1}{\sqrt{2}}\begin{pmatrix} -ie^{-i\phi}\sin\theta\cos\frac{\zeta-\xi}{2} \\ -i\cos\frac{\zeta+\xi}{2} + \cos\theta\sin\frac{\zeta-\xi}{2} \\ -ie^{-i\phi}\sin\theta\sin\frac{\zeta-\xi}{2} \\ -i\sin\frac{\zeta+\xi}{2} + \cos\theta\cos\frac{\zeta-\xi}{2} \end{pmatrix}, \qquad
\psi_{\boldsymbol{k},+,\downarrow} = \frac{1}{\sqrt{2}}\begin{pmatrix} i\sin\frac{\zeta+\xi}{2} + \cos\theta\cos\frac{\zeta-\xi}{2} \\ -ie^{i\phi}\sin\theta\sin\frac{\zeta-\xi}{2} \\ i\cos\frac{\zeta+\xi}{2} + \cos\theta\sin\frac{\zeta-\xi}{2} \\ -ie^{i\phi}\sin\theta\cos\frac{\zeta-\xi}{2} \end{pmatrix},
\tag{3.58a}
$$

$$
\psi_{\boldsymbol{k},-,\uparrow} = \frac{1}{\sqrt{2}}\begin{pmatrix} -ie^{-i\phi}\sin\theta\cos\frac{\zeta+\xi}{2} \\ i\cos\frac{\zeta-\xi}{2} - \cos\theta\sin\frac{\zeta+\xi}{2} \\ ie^{-i\phi}\sin\theta\sin\frac{\zeta+\xi}{2} \\ -i\sin\frac{\zeta-\xi}{2} + \cos\theta\cos\frac{\zeta+\xi}{2} \end{pmatrix}, \qquad
\psi_{\boldsymbol{k},-,\downarrow} = \frac{1}{\sqrt{2}}\begin{pmatrix} i\sin\frac{\zeta-\xi}{2} + \cos\theta\cos\frac{\zeta+\xi}{2} \\ ie^{i\phi}\sin\theta\sin\frac{\zeta+\xi}{2} \\ -i\cos\frac{\zeta-\xi}{2} - \cos\theta\sin\frac{\zeta+\xi}{2} \\ -ie^{i\phi}\sin\theta\cos\frac{\zeta+\xi}{2} \end{pmatrix}.
\tag{3.58b}
$$

The angles are defined as

$$\phi = \arctan\left(\frac{\epsilon_{\boldsymbol{k},yz}}{\epsilon_{\boldsymbol{k},xz}}\right), \qquad\qquad \theta = \arctan\left(\frac{\sqrt{\epsilon_{\boldsymbol{k},yz}^2 + \epsilon_{\boldsymbol{k},xz}^2}}{\epsilon_{\boldsymbol{k},xy}}\right), \tag{3.59a}$$

$$\xi = \arctan\left(\frac{\epsilon_{\boldsymbol{k},3z^2-r^2}}{\epsilon_{\boldsymbol{k},x^2-y^2}}\right), \qquad\qquad \zeta = \arctan\left(\frac{\sqrt{\epsilon_{\boldsymbol{k},x^2-y^2}^2 + \epsilon_{\boldsymbol{k},3z^2-r^2}^2}}{\sqrt{\epsilon_{\boldsymbol{k},yz}^2 + \epsilon_{\boldsymbol{k},xz}^2 + \epsilon_{\boldsymbol{k},xy}^2}}\right). \tag{3.59b}$$

It is immediately evident that this basis is not well-defined when the numerator and the denominator of the expressions in the angles vanish simultaneously, which happens along the [100] and [111] lines in the Brillouin zone. This, however, does not pose a problem because the choice of the pseudospin basis is not unique and we can therefore in principle choose a different, well-defined basis along these lines. In practice this is not necessary.

The intraband pairing potential is independent of the choice of the pseudospin basis, but expressed in terms of the pseudospin basis chosen above we find

$$\psi_{\boldsymbol{k},\pm} = \eta_{\boldsymbol{k},0} \pm \vec{\eta}\cdot\hat{\epsilon}_{\boldsymbol{k}} = \eta_0 \pm \left[(\eta_{3z^2-r^2}\sin\xi + \eta_{x^2-y^2}\cos\xi)\sin\zeta + (\eta_{xy}\cos\theta + \eta_{xz}\sin\theta\cos\phi + \eta_{yz}\sin\theta\sin\phi)\cos\zeta\right]. \tag{3.60}$$

The interband pairing potentials on the other hand are always basis-dependent. In the basis we have chosen before, the singlet part takes on a very compact form

$$\psi_{\boldsymbol{k},I} = \eta_{3z^2-r^2}\cos\xi - \eta_{x^2-y^2}\sin\xi = [\vec{\eta}_{\boldsymbol{k},E_g} \times \hat{\epsilon}_{\boldsymbol{k},E_g}]_z, \tag{3.61}$$

whereas the triplet part has the form

$$\boldsymbol{d_k} = \cos\zeta(\eta_{3z^2-r^2}\sin\xi + \eta_{x^2-y^2}\cos\xi)\begin{pmatrix}\sin\theta\sin\phi\\\sin\theta\cos\phi\\\cos\theta\end{pmatrix}$$

$$-\sin\zeta\left[\begin{pmatrix}\eta_{yz}\\\eta_{xz}\\\eta_{xy}\end{pmatrix}\cdot\begin{pmatrix}\sin\theta\sin\phi\\\sin\theta\cos\phi\\\cos\theta\end{pmatrix}\right]\begin{pmatrix}\sin\theta\sin\phi\\\sin\theta\cos\phi\\\cos\theta\end{pmatrix} + \begin{pmatrix}\eta_{yz}\\\eta_{xz}\\\eta_{xy}\end{pmatrix}\times\begin{pmatrix}\sin\theta\sin\phi\\\sin\theta\cos\phi\\\cos\theta\end{pmatrix} \tag{3.62}$$

$$= \frac{|\vec{\epsilon}_{\boldsymbol{k},T_{2g}}|}{|\vec{\epsilon}|}(\vec{\eta}_{\boldsymbol{k},E_g}\cdot\hat{\epsilon}_{\boldsymbol{k},E_g})\hat{\epsilon}_{\boldsymbol{k},T_{2g}} - \frac{|\vec{\epsilon}_{\boldsymbol{k},E_g}|}{|\vec{\epsilon}|}(\vec{\eta}_{\boldsymbol{k},T_{2g}}\cdot\hat{\epsilon}_{\boldsymbol{k},T_{2g}})\hat{\epsilon}_{\boldsymbol{k},T_{2g}} + \vec{\eta}_{\boldsymbol{k},T_{2g}}\times\hat{\epsilon}_{\boldsymbol{k},T_{2g}}, \tag{3.63}$$

where we have used the shorthand notation

$$\vec{v} = (v_{3z^2-r^2}, v_{x^2-y^2}, v_{xy}, v_{xz}, v_{yz})^T, \tag{3.64}$$

$$\vec{v}_{E_g} = (v_{3z^2-r^2}, v_{x^2-y^2})^T, \tag{3.65}$$

$$\vec{v}_{T_{2g}} = (v_{xy}, v_{xz}, v_{yz})^T, \tag{3.66}$$

$$\hat{\boldsymbol{v}} = \boldsymbol{v}/|\vec{v}|, \tag{3.67}$$

with v being either $\epsilon_{\boldsymbol{k}}$ or $\eta_{\boldsymbol{k}}$.

Low-energy structure of the time-reversal symmetry breaking states

In this section we will briefly review the expressions of the low-energy theory for the different time-reversal symmetry-breaking pairing states from (3.57). We will also show plots of the Bogoliubov Fermi surfaces for these

pairing states and the associated pseudomagnetic fields. In general a magnetic field gives rise to a magnetisation, which can also be computed for the pseudomagnetic field [133]

$$m_{\boldsymbol{k},\mu} = -\frac{1}{|\boldsymbol{v}_{\boldsymbol{k},-}|} \delta \boldsymbol{h}_{\boldsymbol{k},-} \cdot \text{Tr}[\mathcal{P}_{\boldsymbol{k},-} \boldsymbol{s} \mathcal{P}_{\boldsymbol{k},-} J_\mu]. \tag{3.68}$$

Figures 3.1, 3.2, and 3.4 below use band parameters for an inverted band structure, i.e. there is only a single Fermi surface. For illustration purposes these figures also use an unphysically large gap amplitude to clearly distinguish the Bogoliubov Fermi surfaces from line and point nodes.

▶ E_g representation: $\boldsymbol{h} = (1, i)$

One possibility to arrange the gap functions of the E_g representation in a time-reversal symmetry-breaking combination is

$$\Delta = \frac{\Delta_0}{2}(\Gamma_{3z^2-r^2} + i\Gamma_{x^2-y^2}). \tag{3.69}$$

Projecting this pairing state onto the + band using the pseudospin transformation (3.58) we find in the different representations

$$\psi_{\boldsymbol{k},+} = \frac{\Delta_0}{2} \sin\zeta(\sin\xi + i\cos\xi) \tag{3.70}$$

$$= \frac{\Delta_0}{\epsilon_{\boldsymbol{k},+} - \epsilon_{\boldsymbol{k},-}}(\epsilon_{\boldsymbol{k},3z^2-r^2} + i\epsilon_{\boldsymbol{k},x^2-y^2}) \tag{3.71}$$

$$= \frac{\beta\Delta_0}{2} \frac{k_z^2 + e^{i2\pi/3}k_x^2 + e^{i4\pi/3}k_y^2}{\sqrt{\beta^2 \sum_i k_i^4 + (3\gamma^2 - \beta^2)\sum_i k_i^2 k_{i+1}^2}}. \tag{3.72}$$

This will have nodes along all the diagonals of the Brillouin zone and will therefore give rise to eight point nodes.

We proceed to evaluate the shift in the chemical potential, that is always introduced by interband pairing, independent of time-reversal symmetry breaking. In terms of the pseudospin basis it is given by (3.33) and in the different representations we find

$$\delta\epsilon_{\boldsymbol{k},+} = \frac{1}{8} \frac{|\Delta_0|^2}{\epsilon_{\boldsymbol{k},+} - \epsilon_{\boldsymbol{k},-}}[3 + 2\cos(2\zeta)] \tag{3.73}$$

$$= \frac{|\Delta_0|^2}{2(\epsilon_{\boldsymbol{k},+} - \epsilon_{\boldsymbol{k},-})^3}[(\epsilon_{\boldsymbol{k},+} - \epsilon_{\boldsymbol{k},-})^2 - 2\epsilon_{\boldsymbol{k},3z^2-r^2}^2 - 2\epsilon_{\boldsymbol{k},x^2-y^2}^2] \tag{3.74}$$

$$= \frac{|\Delta_0|^2}{16} \frac{\beta^2 \sum_i k_i^4 + (6\gamma^2 - \beta^2)\sum_i k_i^2 k_{i+1}^2}{\left(\beta^2 \sum_i k_i^4 + (3\gamma^2 - \beta^2)\sum_i k_i^2 k_{i+1}^2\right)^{3/2}}. \tag{3.75}$$

The direction of the pseudomagnetic field (3.34) is basis-dependent and for convenience we therefore only give its representation in terms of the angles (3.59)

$$\delta h_{x,\boldsymbol{k},+} = \frac{1}{2} \frac{|\Delta_0|^2}{\epsilon_{\boldsymbol{k},+} - \epsilon_{\boldsymbol{k},-}} \cos\zeta \sin\theta \sin\phi \tag{3.76}$$

$$\delta h_{y,\boldsymbol{k},+} = \frac{1}{2} \frac{|\Delta_0|^2}{\epsilon_{\boldsymbol{k},+} - \epsilon_{\boldsymbol{k},-}} \cos\zeta \sin\theta \cos\phi \tag{3.77}$$

$$\delta h_{z,\boldsymbol{k},+} = \frac{1}{2} \frac{|\Delta_0|^2}{\epsilon_{\boldsymbol{k},+} - \epsilon_{\boldsymbol{k},-}} \cos\zeta \cos\theta. \tag{3.78}$$
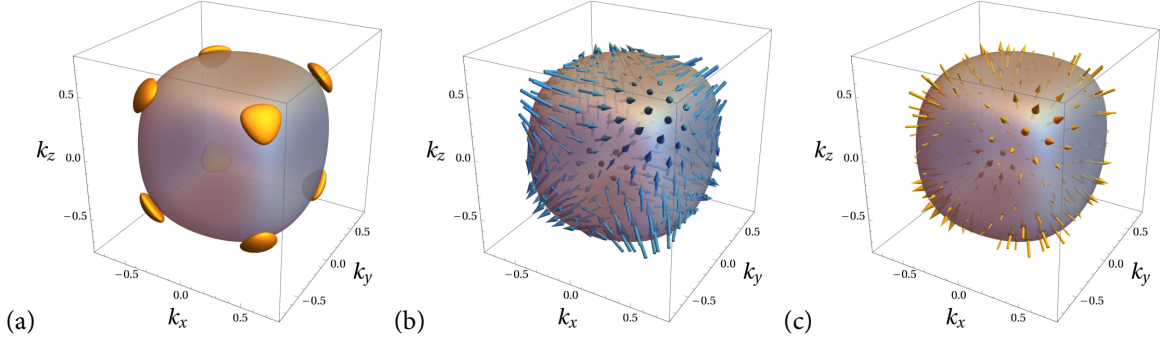
■ *Figure 3.1.* Low-energy structure of the time-reversal symmetry-breaking E_g pairing state. (a) Bogoliubov Fermi surfaces are shown in yellow on top of the normal-state Fermi surface in transparent grey. (b) Pseudomagnetic field in the pseudospin basis (3.58). (c) Physical magnetisation of the states at the Fermi surface due to the pseudomagnetic field. *Reprinted figure with permission from P. M. R. Brydon* et al., *Phys. Rev. B* **98**, 224509 (2018). Copyright © 2018 by the American Physical Society.

Its magnitude on the other hand is basis-independent and ultimately responsible for the formation of the Bogoliubov Fermi surfaces. Therefore we give it again in all three representations

$$|\delta h_{k,+}| = \frac{1}{2} \frac{|\Delta_0|^2}{\epsilon_{k,+} - \epsilon_{k,-}} \cos \zeta \tag{3.79}$$

$$= \frac{|\Delta_0|^2}{(\epsilon_{k,+} - \epsilon_{k,-})^2} \sqrt{\epsilon_{k,yz}^2 + \epsilon_{k,xz}^2 + \epsilon_{k,xy}^2} \tag{3.80}$$

$$= \frac{\sqrt{3}\gamma|\Delta_0|^2}{4} \frac{\sqrt{k_y^2 k_z^2 + k_x^2 k_z^2 + k_x^2 k_y^2}}{\beta^2 \sum_i k_i^4 + (3\gamma^2 - \beta^2) \sum_i k_i^2 k_{i+1}^2}. \tag{3.81}$$

In Fig. 3.1 we show the Bogoliubov Fermi surfaces, the pseudomagnetic field in the basis defined in (3.58), and the associated physical magnetisation. In panel (a) we see that the eight point nodes are inflated into pockets. The pseudomagnetic field in panel (b) exhibits an octupolar structure. The octupolar structure implies that the magnetisation shown in panel (c) vanishes on average.

▶ T_{2g} representation: $\boldsymbol{l} = (1, i, 0)$

The gap functions in the T_{2g} representation can be arranged in two distinct ways to yield a time-reversal symmetry-breaking pairing state. Here we will begin with the chiral state with ordering vector $\boldsymbol{l} = (1, i, 0)$, which will be investigated in more detail later. One possible way to write this is

$$\Delta = \frac{\Delta_0}{2}(\Gamma_{xy} + i\Gamma_{yz}). \tag{3.82}$$

Projected into the + band we find the intraband gap

$$\psi_{k,+} = \frac{\Delta_0}{2} \cos \zeta \sin \theta (\cos \phi + i \sin \phi) \tag{3.83}$$

$$= \Delta_0 \frac{\epsilon_{k,xz} + i\epsilon_{k,yz}}{\epsilon_{k,+} - \epsilon_{k,-}} \tag{3.84}$$

$$= \frac{\sqrt{3}\gamma\Delta_0}{2} \frac{(k_x + ik_y)k_z}{\sqrt{\beta^2 \sum_i k_i^4 + (3\gamma^2 - \beta^2) \sum_i k_i^2 k_{i+1}^2}}, \tag{3.85}$$

which is reminiscent of a chiral d-wave state with an equatorial line node at $k_z = 0$ and point nodes at the poles $k_x = k_y = 0$.

The shift of the chemical potential in all three representations is given by

$$\delta\epsilon_{\boldsymbol{k},+} = -\frac{1}{16}\frac{|\Delta_0|^2}{\epsilon_{\boldsymbol{k},+} - \epsilon_{\boldsymbol{k},-}}[-7 + \cos(2\zeta) - 2\cos^2\zeta\cos(2\theta)] \tag{3.86}$$

$$= \frac{|\Delta_0|^2}{2(\epsilon_{\boldsymbol{k},+} - \epsilon_{\boldsymbol{k},-})^3}[(\epsilon_{\boldsymbol{k},+} - \epsilon_{\boldsymbol{k},-})^2 - 2\epsilon_{\boldsymbol{k},xz}^2 - 2\epsilon_{\boldsymbol{k},yz}^2] \tag{3.87}$$

$$= \frac{|\Delta_0|^2}{16}\frac{2\beta^2\sum_i k_i^4 + (3\gamma^2 - 2\beta^2)\sum_i k_i^2 k_{i+1}^2 + 6\gamma^2 k_x^2 k_y^2}{\left(\beta^2\sum_i k_i^4 + (3\gamma^2 - \beta^2)\sum_i k_i^2 k_{i+1}^2\right)^{3/2}}, \tag{3.88}$$

and the pseudomagnetic field in only the representation of the angles (3.59)

$$\delta h_{x,\boldsymbol{k},+} = -\frac{1}{2}\frac{|\Delta_0|^2}{\epsilon_{\boldsymbol{k},+} - \epsilon_{\boldsymbol{k},-}}\sin\theta(\sin\zeta\cos\phi + \cos\theta\sin\phi) \tag{3.89}$$

$$\delta h_{y,\boldsymbol{k},+} = -\frac{1}{2}\frac{|\Delta_0|^2}{\epsilon_{\boldsymbol{k},+} - \epsilon_{\boldsymbol{k},-}}\sin\theta(\cos\theta\cos\phi - \sin\zeta\sin\phi) \tag{3.90}$$

$$\delta h_{z,\boldsymbol{k},+} = -\frac{1}{2}\frac{|\Delta_0|^2}{\epsilon_{\boldsymbol{k},+} - \epsilon_{\boldsymbol{k},-}}\cos^2\theta. \tag{3.91}$$

The magnitude of the pseudomagnetic field can be expressed in the following way

$$|\delta\boldsymbol{h}_{\boldsymbol{k},+}| = \frac{1}{4}\frac{|\Delta_0|^2}{\epsilon_{\boldsymbol{k},+} - \epsilon_{\boldsymbol{k},-}}\sqrt{3 - 2\cos(2\zeta)\sin^2\theta + \cos(2\theta)} \tag{3.92}$$

$$= \frac{|\Delta_0|^2}{(\epsilon_{\boldsymbol{k},+} - \epsilon_{\boldsymbol{k},-})^2}\sqrt{\epsilon_{\boldsymbol{k},3z^2-r^2}^2 + \epsilon_{\boldsymbol{k},x^2-y^2}^2 + \epsilon_{\boldsymbol{k},xy}^2} \tag{3.93}$$

$$= \frac{\sqrt{3}\gamma|\Delta_0|^2}{4}\frac{\sqrt{\beta^2\sum_i k_i^4 - \beta^2\sum_i k_i^2 k_{i+1}^2 + 3\gamma^2 k_x^2 k_y^2}}{\beta^2\sum_i k_i^4 + (3\gamma^2 - \beta^2)\sum_i k_i^2 k_{i+1}^2}. \tag{3.94}$$

In Fig. 3.2 we show the Bogoliubov Fermi surfaces, the pseudomagnetic field in the basis defined in (3.58), and its associated physical magnetisation. In panel (a) we see that the point nodes at the poles are inflated into pockets, whereas the equatorial line node obtained a ribbon-like shape. This state breaks crystal symmetry. The pseudomagnetic field in panel (b) involves both dipolar and octupolar contribution. The dipolar contribution gives rise to an overall magnetisation in z direction, shown in panel (c). Whether this magnetisation will have a measurable impact on the superconductor will be discussed in further detail in Section 4.6.

Before moving on to the cyclic T_{2g} pairing state, we will take a brief look at the validity of the low-energy theory which we can easily assess now that we have expressions for the chemical potential shift and pseudomagnetic field. In Fig. 3.3 we show the band structure of the BdG-Hamiltonian and the effective low-energy theory for three sets of band parameters in the presence of the chiral T_{2g} pairing state with a small gap amplitude.

In panel (a), where the band splitting is weak and the band structure has two Fermi surfaces, the low-energy theory fails miserably. This is not surprising because the magnitude of the pseudomagnetic field scales inversely with the band splitting squared, i.e. when the band splitting is small, the corrections are no longer small and the assumption of the perturbation theory breaks down. This also gives rise to enormous Bogoliubov Fermi surfaces. For moderate band splitting in panel (b) the perturbation theory is still not applicable over wide ranges of momentum space, but in a narrow window around the Fermi energy the reproduction of the exact
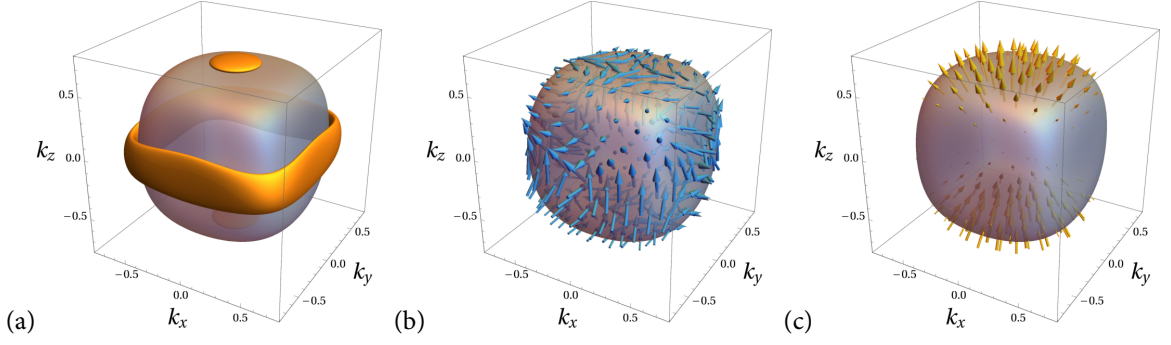
■ *Figure 3.2.* Low-energy structure of the time-reversal symmetry-breaking T_{2g} pairing state with ordering vector $\boldsymbol{l} = (1, i, 0)$. (a) Bogoliubov Fermi surfaces are shown in yellow on top of the normal-state Fermi surface in transparent grey. (b) Pseudomagnetic field in the pseudospin basis (3.58). (c) Physical magnetisation of the states at the Fermi surface due to the pseudomagnetic field. *Reprinted figure with permission from P. M. R. Brydon* et al., *Phys. Rev. B* **98**, *224509 (2018). Copyright © 2018 by the American Physical Society.*

band structure is sufficient to qualitatively reproduce quantities like the density of states (see later in Fig. 4.11). When the band splitting is very large and the band structure is inverted such that there is only a single Fermi surface, the low-energy theory fits the exact band structure over a wide range of momentum space. In this regime Bogoliubov Fermi surfaces are correctly described using the low-energy effective theory.

▶ T_{2g} representation: $\boldsymbol{l} = (1, \omega, \omega^2)$

Finally we consider the cyclic T_{2g} pairing state with ordering vector $\boldsymbol{l} = (1, \omega, \omega^2)$. One possible combination of gap functions to realise this time-reversal symmetry-breaking state is

$$\Delta = \frac{\Delta_0}{2}(\Gamma_{xz} + e^{i2\pi/3}\Gamma_{yz} + e^{i4\pi/3}\Gamma_{xy}). \tag{3.95}$$

Projected into the + band the intraband gap can be represented by

$$\psi_{\boldsymbol{k},+} = \frac{\Delta_0}{2}\cos\zeta\big(\sin\theta\cos\phi + e^{i2\pi/3}\sin\theta\sin\phi + e^{i4\pi/3}\cos\theta\big) \tag{3.96}$$

$$= \frac{\Delta_0}{\epsilon_{\boldsymbol{k},+} - \epsilon_{\boldsymbol{k},-}}\big(\epsilon_{\boldsymbol{k},xz} + e^{i2\pi/3}\epsilon_{\boldsymbol{k},yz} + e^{i4\pi/3}\epsilon_{\boldsymbol{k},xy}\big) \tag{3.97}$$

$$= \frac{\sqrt{3}\gamma\Delta_0}{2}\frac{k_xk_z + e^{i2\pi/3}k_yk_z + e^{i4\pi/3}k_xk_y}{\sqrt{\beta^2\sum_i k_i^4 + (3\gamma^2 - \beta^2)\sum_i k_i^2 k_{i+1}^2}}. \tag{3.98}$$

For this choice of distributing the relative phases the gap has point nodes along the principal axes and along the [111] direction.

The expressions for the chemical potential shift are a lot more complicated than for the other pairing states we discussed. In the three different representations

$$\delta\epsilon_{\boldsymbol{k},+} = \frac{1}{8}\frac{|\Delta_0|^2}{\epsilon_{\boldsymbol{k},+} - \epsilon_{\boldsymbol{k},-}}[5 - \cos(2\zeta) + \cos^2\zeta(\sin^2\theta\sin(2\phi) + \sin(2\theta)(\sin\phi + \cos\phi))] \tag{3.99}$$

$$= \frac{|\Delta_0|^2}{2(\epsilon_{\boldsymbol{k},+} - \epsilon_{\boldsymbol{k},-})^3}[3\epsilon_{\boldsymbol{k},3z^2-r^2}^2 + 3\epsilon_{\boldsymbol{k},x^2-y^2}^2 + 2\epsilon_{\boldsymbol{k},xy}^2 + 2\epsilon_{\boldsymbol{k},xz}^2 + 2\epsilon_{\boldsymbol{k},yz}^2 + \epsilon_{\boldsymbol{k},yz}\epsilon_{\boldsymbol{k},xz} + \epsilon_{\boldsymbol{k},yz}\epsilon_{\boldsymbol{k},xy} + \epsilon_{\boldsymbol{k},xz}\epsilon_{\boldsymbol{k},xy}] \tag{3.100}$$

$$= \frac{|\Delta_0|^2}{16}\frac{3\beta^2\sum_i k_i^4 + (6\gamma^2 - 3\beta^2)\sum_i k_i^2 k_{i+1}^2 + 3\gamma^2(k_x^2 k_y k_z + k_x k_y^2 k_z + k_x k_y k_z^2)}{\left(\beta^2\sum_i k_i^4 + (3\gamma^2 - \beta^2)\sum_i k_i^2 k_{i+1}^2\right)^{3/2}}. \tag{3.101}$$
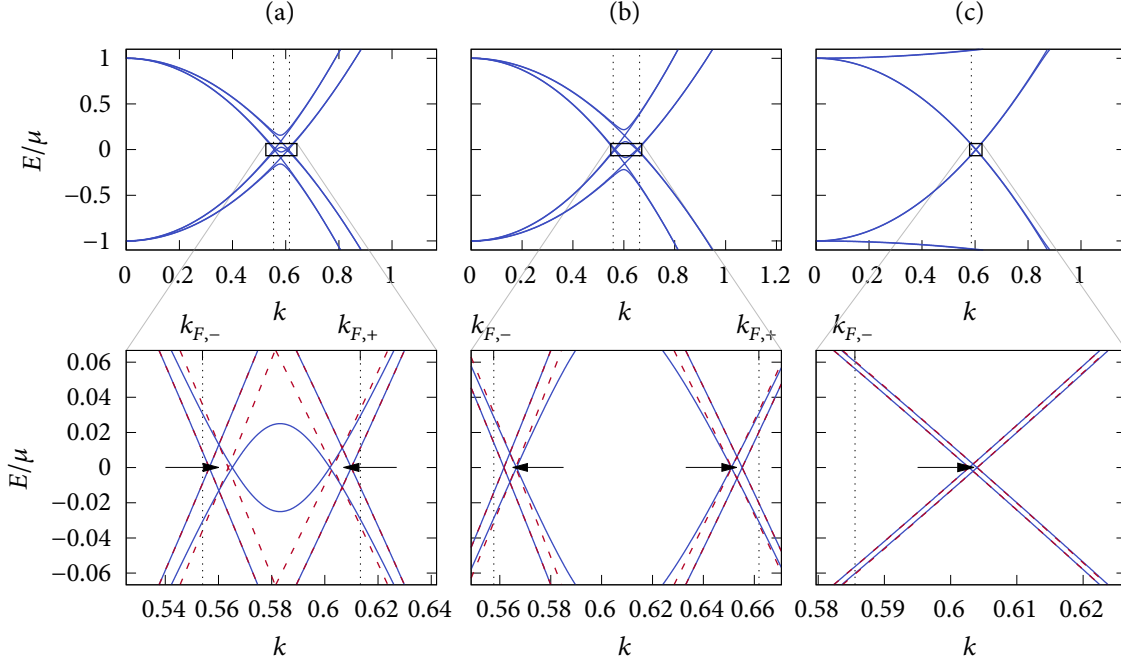
Figure 3.3. Validity of the low-energy theory. All panels show the band structure along the [100] direction where we would expect the equatorial line node. Solid lines denote the exact eigenvalues of the BdG-Hamiltonian, dashed the effective low-energy theory. The gap is small with an amplitude $\Delta_0 = \mu/300$. Vertical dashed lines mark the location of the normal-state Fermi surface. Arrows point to the location of the Bogoliubov Fermi surfaces. The panels in the upper row show the band structure in the radial direction from $k = 0$ to $k \approx 2k_F$. The panels in the lower row are zoomed in on the boxes in the upper row. Column (a) For weak spin-orbit coupling the resemblance is poor. Column (b) For moderate spin-orbit coupling Bogoliubov Fermi surfaces are stable and the effective theory is valid in a narrow window around the Fermi energy. Column (c) For the case of the inverted band structure the perturbative approach works best. The Bogoliubov Fermi surfaces are very small.

Likewise, the expressions for the pseudomagnetic field are also much more complicated. We have in terms of angles (3.59)

$$\delta h_{x,\boldsymbol{k},+} = \frac{\sqrt{3}}{4} \frac{|\Delta_0|^2}{\epsilon_{\boldsymbol{k},+} - \epsilon_{\boldsymbol{k},-}} \left[\cos\theta(\sin\zeta - \sin\theta\sin\phi) - \sin\theta(\cos\phi(\sin\zeta + \sin\theta\sin\phi) + \sin\theta\sin^2\phi) \right] \quad (3.102)$$

$$\delta h_{y,\boldsymbol{k},+} = -\frac{\sqrt{3}}{4} \frac{|\Delta_0|^2}{\epsilon_{\boldsymbol{k},+} - \epsilon_{\boldsymbol{k},-}} \left[\sin\zeta(\cos\theta - \sin\theta\sin\phi) + \sin\theta\cos\phi(\sin\theta(\sin\phi + \cos\phi) + \cos\theta) \right] \quad (3.103)$$

$$\delta h_{z,\boldsymbol{k},+} = -\frac{\sqrt{3}}{8} \frac{|\Delta_0|^2}{\epsilon_{\boldsymbol{k},+} - \epsilon_{\boldsymbol{k},-}} \cos^2\theta [2\sin\zeta\sin\theta(\sin\phi - \cos\phi) + \sin(2\theta)(\sin\phi + \cos\phi) + \cos(2\theta) + 1]. \quad (3.104)$$

The magnitude of the pseudomagnetic field is given by

$$|\delta \boldsymbol{h}_{\boldsymbol{k},+}| = \frac{1}{4} \frac{|\Delta_0|^2}{\epsilon_{\boldsymbol{k},+} - \epsilon_{\boldsymbol{k},-}} \sqrt{6 + 3\cos^2\zeta(\sin^2\theta\sin(2\phi) + \sin(2\theta)(\sin\phi + \cos\phi)) - 3\cos(2\zeta)} \quad (3.105)$$

$$= \frac{|\Delta_0|^2}{(\epsilon_{\boldsymbol{k},+} - \epsilon_{\boldsymbol{k},-})^2} \frac{\sqrt{3}}{2} \sqrt{3\epsilon_{\boldsymbol{k},3z^2-r^2}^2 + 3\epsilon_{\boldsymbol{k},x^2-y^2}^2 + (\epsilon_{\boldsymbol{k},yz} + \epsilon_{\boldsymbol{k},xz} + \epsilon_{\boldsymbol{k},xy})^2} \quad (3.106)$$

$$= \frac{3\gamma|\Delta_0|^2}{4} \frac{\sqrt{\beta^2 \sum_i k_i^4 + (\gamma^2 - \beta^2) \sum_i k_i^2 k_{i+1}^2}}{\beta^2 \sum_i k_i^4 + (3\gamma^2 - \beta^2) \sum_i k_i^2 k_{i+1}^2}. \quad (3.107)$$
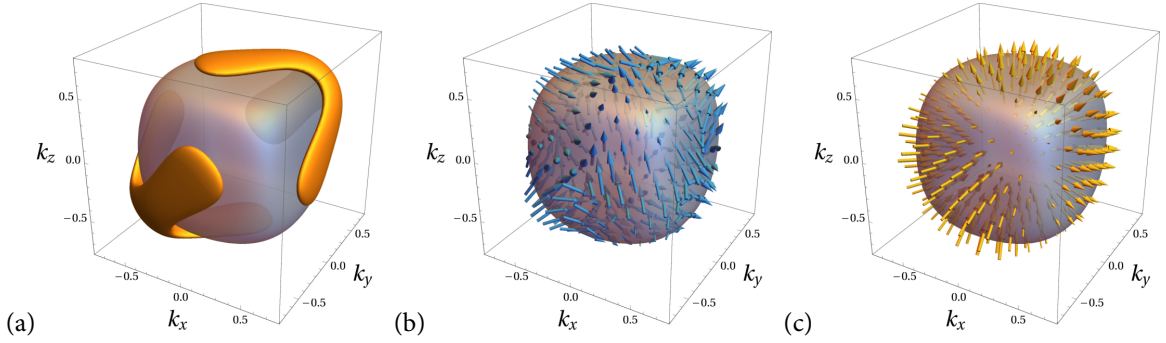
■ *Figure 3.4.* Low-energy structure of the time-reversal symmetry-breaking T_{2g} pairing state with ordering vector $\boldsymbol{l} = (1, \omega, \omega^2)$. (a) Bogoliubov Fermi surfaces are shown in yellow on top of the normal-state Fermi surface in transparent grey. (b) Pseudomagnetic field in the pseudospin basis (3.58). (c) Physical magnetisation of the states at the Fermi surface due to the pseudomagnetic field. *Reprinted figure with permission from P. M. R. Brydon et al., Phys. Rev. B **98**, 224509 (2018). Copyright © 2018 by the American Physical Society.*

The pseudomagnetic field has the largest magnitude of the pairing states considered so far, which has interesting consequences on the formation of the Bogoliubov Fermi surfaces.

In Fig. 3.4 we show the Bogoliubov Fermi surfaces, the pseudomagnetic field in the basis defined in (3.58), and its associated physical magnetisation. We would expect that the eight point nodes of (3.95) inflate into eight distinct pockets like in the case of the E_g pairing state. However, looking at panel (a) this is not the case and instead we have two gigantic Bogoliubov Fermi surfaces which connect four point nodes each. This is an effect of the large pseudomagnetic field mentioned earlier. The euclidean distance between the point nodes in momentum space is shorter than in the E_g case and therefore the gap between them is much shallower. This pairing state breaks crystal symmetry. Like for the chiral state, the pseudomagnetic field in panel (b) encompasses both dipolar and octupolar contributions, however, this time the overall magnetisation in panel (c) points along the three-fold axis.

3.4   Summary

In this chapter we have introduced the concept of Bogoliubov Fermi surfaces. These extended nodal surfaces appear generically in any multiband even-parity superconductor that breaks time-reversal symmetry. We have studied the origin, the stability, and the effects of Bogoliubov Fermi surfaces in a paradigmatic model with two bands. Care has been taken to draw conclusion as general as possible to not depend on this specific model. The generalisation to more than two bands is straight-forward.

The presence of multiple orbitals facilitates the existence of orbitally non-trivial *s*-wave pairing states, which we called anomalous *s*-wave states or *internally anisotropic pairing* states. If these pairing states break time-reversal symmetry it implies that they give rise to a non-unitary gap product. Treating the interband pairing perturbatively we derived an effective low-energy theory which explains the origin of the Bogoliubov Fermi surfaces in terms of a pseudomagnetic field, which inflates point and line nodes into extended surfaces. The time-reversal odd part of the non-unitary gap product is directly related to this pseudomagnetic field. The Bogoliubov Fermi surfaces are topologically protected by a $\mathbb{Z}_2$ Pfaffian invariant.

The general properties of the Bogoliubov Fermi surfaces have been illustrated on the example of the Luttinger-Kohn Hamiltonian of $j = 3/2$ fermions, which has served as a paradigmatic model of Bogoliubov Fermi surfaces in the literature [66, 76, 77, 133, 135, 136].

Chapter 4

Bogoliubov Fermi surfaces stabilised by spin-orbit coupling

The material presented in this chapter has been published previously in

[140] H. Menke, C. Timm, and P. M. R. Brydon, "Bogoliubov Fermi surfaces stabilized by spin-orbit coupling", Phys. Rev. B **100**, 224505 (2019).

In the previous chapter we have introduced the concept of Bogoliubov Fermi surfaces, their general theory and topological protection. In this chapter we are going to investigate the thermodynamic stability of these Bogoliubov Fermi surface on the example of the paradigmatic model introduced in Section 3.3. We numerically extract the mean-field phase diagram as a function of spin-orbit coupling and temperature and compare the results with Ginzburg-Landau theory. We find a stable pairing state with Bogoliubov Fermi surfaces for moderate values of the spin-orbit coupling. Multiband effects and cubic anisotropy give rise to a rich phase diagram. Finally we will discuss some experimental signatures of the state with Bogoliubov Fermi surfaces.

4.1 Known limits

Previous work on two-band superconductors has dealt with the influence of spin-orbit coupling on the selection of the superconducting instability [64, 66, 70, 133, 137]. In the following we will briefly review these results.

Vanishing spin-orbit coupling

Ho and Yip [137] have studied pairing in $j = 3/2$ free fermionic fluids in the context of cold atomic gases. This corresponds to the limit of vanishing spin-orbit coupling in the Luttinger-Kohn model, which implies that the bands are four-fold degenerate [137, 138]. Evaluating the Ginzburg-Landau free energy (D.9) for this system yields the same form as that of a general d-wave singlet superfluid. The possible ground states of this have been determined previously by Mermin [139]. For fermions with spin $j = 3/2$ in the $J = 2$ quintet channel the stable solution is a real state, i.e. any state where the pairing potential is real up to a constant global phase factor. Hence time-reversal symmetry remains unbroken. Due to the four-fold degeneracy of the bands and the absence of band splitting, the normal-state Hamiltonian and the pairing can be simultaneously diagonalised by a momentum-independent spin rotation, which can be determined straight-forwardly by diagonalising the matrix pairing potential, because the normal-state Hamiltonian is already diagonal in the absence of band splitting. Hence the problem essentially separates into two single-band s-wave singlet superconductors with a uniform gap across the whole Fermi surface.

For a time-reversal symmetry-breaking pairing state the situation is different, because two of the four degenerate Fermi surfaces remain ungapped, as can be seen easily from the matrix representation of an exemplary pairing state:

$$
\Gamma_{xz} + i\Gamma_{yz} = \begin{pmatrix} 0 & 0 & \sqrt{2} & 0 \\ 0 & 0 & 0 & 0 \\ -\sqrt{2} & 0 & 0 & 0 \\ 0 & 0 & 0 & 0 \end{pmatrix} \equiv c_{3/2}c_{-1/2} - c_{-1/2}c_{3/2}. \tag{4.1}
$$

In this case only $j = 3/2$ and $j = -1/2$ bands will be gapped. Since a time-reversal symmetric pairing state will always open a gap on all Fermi surfaces it is energetically more favourable. Spin-orbit coupling lifts the four-fold degeneracy and leads to the appearance of nodes on the Fermi surface. However, for sufficiently weak spin-orbit coupling we expect the fully-gapped time-reversal-symmetric state found by Ho and Yip [137] to be realised, because the energy difference between a time-reversal symmetric and a time-reversal symmetry breaking pairing state is generically finite.

Strong spin-orbit coupling

When the spin-orbit coupling becomes much larger than the pairing potential the interband pairing can be treated as a perturbation to the single-band physics, as we have seen before in Section 3.2. In this limit the intraband gap for the Luttinger-Kohn Hamiltonian for a general pairing state in the T_{2g} irrep is given as

$$
\psi_{\boldsymbol{k},\pm} = \pm \frac{\sqrt{3}\gamma}{2} \frac{\Delta_{yz}k_yk_z + \Delta_{xz}k_xk_z + \Delta_{xy}k_xk_y}{\sqrt{\sum_i [\beta^2 k_i^4 + (3\gamma^2 - \beta^2)k_i^2 k_{i+1}^2]}}. \tag{4.2}
$$

The interplay of the normal-state spin-orbital texture at the Fermi surface with the $J = 2$ quintet pairing gives rise to a d-wave-like form factor. In this case it is preferred that time-reversal symmetry is broken maximally because that will remove intersecting line nodes to enhance the overall gap magnitude and lower the free energy [42]. This can be understood within the Landau expansion which gives the difference between normal-state and superconducting state free energy in powers of the pairing potential $F = \alpha|\Delta|^2 + \mathcal{O}(|\Delta|^4)$. Superconductivity is driven by the quadratic term, which is called the condensation energy. The condensation energy depends on the square of the pairing potential averaged over the Fermi surface, so nodes are generally detrimental to superconductivity. It might still be favourable to form nodes in some situations depending on the microscopic pairing mechanism. When two or more equivalent gap functions are degenerate, like here in the T_{2g} manifold of the d-wave functions, they can form a linear combination, such as $d_{xz} \pm id_{yz}$, whose absolute value squared is greater than that of the individual parts. For a spherical Fermi surface this state will replace the vertical line nodes of each individual wave function with only point nodes [90].

4.2 Ginzburg-Landau theory

It is possible to evaluate the Ginzburg-Landau free energy in a very generic fashion up to the point where the integrals over momentum space have to be evaluated. Thanks to inversion and time-reversal symmetry we can conveniently parameterise the Greens function of (3.1) in terms of two poles

$$
G(\boldsymbol{k},\omega) = \frac{1}{2}\left[\frac{1}{i\omega - E_{\boldsymbol{k},+}}\left(\mathbb{1}_4 + \frac{\vec{\epsilon}_{\boldsymbol{k}}\cdot\vec{\gamma}}{|\vec{\epsilon}_{\boldsymbol{k}}|} \right) + \frac{1}{i\omega - E_{\boldsymbol{k},-}}\left(\mathbb{1}_4 - \frac{\vec{\epsilon}_{\boldsymbol{k}}\cdot\vec{\gamma}}{|\vec{\epsilon}_{\boldsymbol{k}}|} \right) \right]. \tag{4.3}
$$

The hole-like Green's function is related to the electron-like one by

$$\tilde{G}(\boldsymbol{k}, \omega) = -G^T(\boldsymbol{k}, -i\omega_n) = \frac{1}{2} \left[\frac{1}{i\omega + E_{\boldsymbol{k},+}} \left(\mathbb{1}_4 + \frac{\vec{\epsilon}_{\boldsymbol{k}} \cdot \vec{\gamma}^T}{|\vec{\epsilon}_{\boldsymbol{k}}|} \right) + \frac{1}{i\omega + E_{\boldsymbol{k},-}} \left(\mathbb{1}_4 - \frac{\vec{\epsilon}_{\boldsymbol{k}} \cdot \vec{\gamma}^T}{|\vec{\epsilon}_{\boldsymbol{k}}|} \right) \right]. \qquad (4.4)$$

Expanding the Ginzburg-Landau free energy up to fourth order for a multi-component order parameter $\vec{\Delta} = (\Delta_1, \dots, \Delta_N)$ we can generically write it as

$$F_{\text{GL}} = \sum_{ij} \Delta_i^* \alpha_{ij} \Delta_j + \sum_{ijkl} \Delta_i^* \Delta_j^* \beta_{ijkl} \Delta_k \Delta_l. \qquad (4.5)$$

The leading instability is determined by the stationary point of F_{GL} to lowest order

$$\frac{\partial F_{\text{GL}}}{\partial \Delta_i^*} = \sum_j \alpha_{ij} \Delta_j + \mathcal{O}(|\vec{\Delta}|^3) = 0. \qquad (4.6)$$

This matrix equation always has the trivial solution $\vec{\Delta} = 0$. For non-trivial solutions to exist, the determinant of the matrix α must vanish. This procedure, however, cannot distinguish between a time-reversal invariant and a time-reversal symmetry-breaking state, so to find the true ground state the fourth-order coefficient has to be taken into account. Group theory dictates that all superconducting states within the same irreducible representation have the same critical temperature [42]. In the following, whenever we are talking about the critical temperature T_c we refer to its definition in terms of the second-order phase transition within the Ginzburg-Landau framework where the second-order coefficient has a stationary point.

Therefore, in the simplest approach to study the time-reversal symmetry-breaking phase transition we evaluate the fourth-order term of the Ginzburg-Landau free energy for both a time-reversal invariant and a time-reversal symmetry-breaking pairing state and determine the crossover point as a function of spin-orbit coupling. We can use the Green's functions defined above which is more convenient for numerical evaluation, or we can project the Hamiltonian into the pseudospin basis where the Green's function is simply diagonal. The details of the explicit expressions and their evaluation are unimportant and are therefore deferred to Appendix D.

The Ginzburg-Landau approach has been used previously to asses the stability of Bogoliubov Fermi surfaces in [66]. However, there the limit of inverted band structure with very strong spin-orbit coupling was assumed where only a single band crosses the Fermi surface. It was found that in this limit a time-reversal symmetry-breaking state with Bogoliubov Fermi surfaces is stable and a lower bound was set on the required strength of the spin-orbit coupling. As we will see in the next section, this estimate is too conservative. Therefore we reevaluate the Ginzburg-Landau treatment without approximating the band structure and compare and contrast with numerical results from direct minimisation of the free energy, to assess the correctness of the Ginzburg-Landau approach.

A Ginzburg-Landau treatment of the paradigmatic Luttinger-Kohn Hamiltonian has been performed in the literature [73, 134]. In this scenario the system has full spherical symmetry and the band structure is inverted with the chemical potential at the band touching point such that the density of states at the Fermi point is zero. In this case a weak-coupling instability is insufficient to give rise to superconductivity. For this "strong coupling" scenario it is found that the leading instability is a uniaxial nematic state.

4.3 Time-reversal symmetry-breaking in the spherical limit

From the previous discussion we expect a time-reversal symmetric state for vanishing spin-orbit coupling and a time-reversal symmetry-breaking state in the limit of very strong spin-orbit coupling where the Bogoliubov

Fermi surfaces will be infinitesimally small and indistinguishable from point and line nodes. It is clear that there will be a time-reversal symmetry-breaking phase transition, however, the question is whether the resulting Bogoliubov Fermi surfaces will be observable or not. If the Bogoliubov Fermi surfaces were too small to distinguish them from point and line nodes, their experimental signatures would also be indistinguishable, rendering their observation very difficult.

In this section we will investigate this time-reversal symmetry-breaking phase transition on the example of the paradigmatic Luttinger-Kohn model. In the limit $\beta = \gamma$ the Hamiltonian (3.37) transforms under SO(3) and can be reduced to

$$h(\boldsymbol{k}) = (\alpha|\boldsymbol{k}|^2 - \mu)\mathbb{1} + \beta(\boldsymbol{k} \cdot \boldsymbol{J})^2 \tag{4.7}$$

with doubly degenerate eigenvalues

$$E_{\boldsymbol{k},\pm} = \left(\alpha + \frac{5\beta}{4} \pm \beta\right)|\boldsymbol{k}|^2 - \mu. \tag{4.8}$$

We are interested in the point of time-reversal symmetry-breaking as a function of the band splitting. In Fig. 4.1 we show representative band structures for the different cases we anticipate at fixed chemical potential μ. In panel (a) in the absence of band splitting ($\beta = 0$) the bands are four-fold degenerate and there is only a single Fermi surface. This is the case that has been discussed by Ho and Yip [137] and therefore we expect a time-reversal symmetric pairing state to be realised. If we choose the sign of β negative, one of the bands starts splitting down. For moderate values of β, as shown in panel (b), there are two Fermi surfaces. The band splitting at the Fermi surface is also moderate, so we cannot expect the effective single-band theory to hold. For large magnitudes of β one of the bands will bend completely downwards and not appear at the Fermi level anymore. In this case the band splitting is very large and if the gap is small compared to the band splitting the effective single-band theory is a good approximation. In fact, this is the case the effective single-band model was originally formulated for [64]. From this we naïvely expect that for the situation in panel (a) time-reversal symmetry is preserved whereas in panel (c) time-reversal symmetry will be broken.

Aside from verifying this hypothesis there are more questions to be answered. What is the minimal band splitting sufficient to realise a time-reversal symmetry-broken state? How will the system evolve from a time-reversal-symmetric into a time-reversal symmetry-breaking state? Does the "+" band in Fig. 4.1 have to curve downwards before Bogoliubov Fermi surfaces can appear? What will the size of the Bogoliubov Fermi surfaces be and will they be clearly distinguishable in size from point and line nodes?

4.3.1 Time-reversal symmetry breaking at the critical temperature

In the following we are going to focus on the T_{2g} manifold of the pairing states. The results do not differ qualitatively for the E_g manifold. As we have discussed earlier in the context of the Landau expansion of the free energy, there are four distinct equilibrium states for the T_{2g} manifold, which are $\boldsymbol{l} = (1, 0, 0), (1, 1, 1), (1, i, 0), (1, \omega, \omega^2)$. The first two are time-reversal symmetric, whereas the latter two break time-reversal symmetry. In the spherical limit the Ginzburg-Landau expansion up to fourth order cannot distinguish the true equilibrium among the time-reversal symmetric $(1, 0, 0)$ and $(1, 1, 1)$ states, as well as the time-reversal symmetry breaking $(1, i, 0)$ and $(1, \omega, \omega^2)$ states, respectively [134]. So at the level of Ginzburg-Landau theory we will consider the time-reversal symmetry-breaking phase transition from $(1, 0, 0)$ to $(1, i, 0)$, but the results readily apply to the $(1, 1, 1)$ to $(1, \omega, \omega^2)$ transition as well.

To check the validity of our Ginzburg-Landau theory, we will compare the fourth-order coefficient to the one that we extract from the full mean-field Helmholtz free energy (C.46). To this end we pick a critical
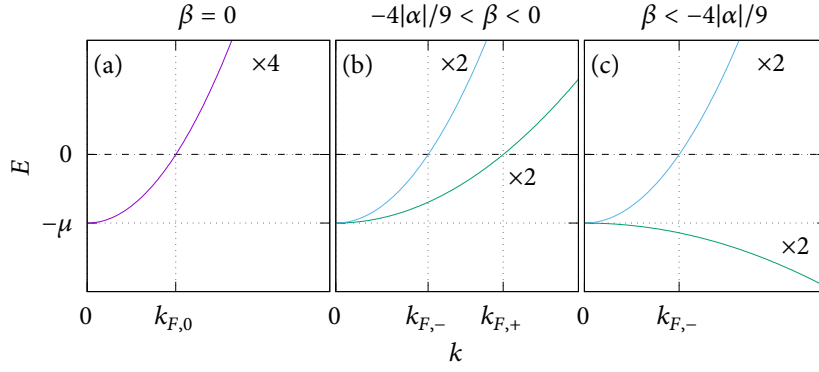
Figure 4.1. Representative spectra along the radial direction for the spherically symmetric model described by Eq. (4.7). (a) In the absence of spin-orbit coupling, the bands are four-fold degenerate. The single Fermi surface has a radius $k_{F,0} = \sqrt{\mu/\alpha}$. We chose $\alpha > 0$ so that the band has positive effective mass. (b) Moderate spin-orbit coupling lifts the four-fold degeneracy, yet both doubly degenerate bands still have positive effective mass. There are now two Fermi surfaces with wave vectors $k_{F,\pm} = \sqrt{\mu/(\alpha + 5\beta/4 \pm \beta)}$. (c) For $\beta < -4\alpha/9$, the effective mass of one of the bands becomes negative, and there is only a single Fermi surface. *Reprinted figure with permission from H. Menke et al., Phys. Rev. B **100**, 224505 (2019). Copyright © 2019 by the American Physical Society.*

temperature T_c and choose the attractive interaction $V_{T_{2g}} = g_0$ in (3.54) such that the second-order coefficient of the Ginzburg-Landau free energy is zero, i.e. at T_c the lowest order non-zero term in the free energy is the fourth-order term. This allows us to fit the Helmholtz free energy with a polynomial of the form $F(\Delta_0) = \delta|\Delta_0|^4$ for small gap amplitudes Δ_0. The coefficient δ is then equivalent to the fourth-order coefficient in the Ginzburg-Landau free energy. The coefficient δ depends on the choice of the pairing state as well as the band parameters, hence a crossing will mark the point of the time-reversal symmetry breaking phase transition. Of course, the Helmholtz free energy also contains terms of order higher than four, so we expect some deviations between the two.

In Fig. 4.2 we plot the fourth-order coefficient of the Helmholtz free energy and the Ginzburg-Landau free energy just below the critical temperature for a time-reversal symmetric $(1, 0, 0)$ or $(1, 1, 1)$ and a time-reversal symmetry-breaking $(1, i, 0)$ or $(1, \omega, \omega^2)$ pairing state. At some point the time-reversal symmetry-breaking state will assume a lower value than the time-reversal symmetric state, which marks the point of the time-reversal symmetry-breaking phase transition. This point differs slightly for the Helmholtz and the Ginzburg-Landau free energy, yet they are in very good agreement.

One peculiarity about the fourth-order coefficient in Fig. 4.2 is that there is a region where it assumes a negative value. In this area the minimum of the free energy is no longer determined by the fourth-order coefficient, but by higher order terms which also implies the presence of a first-order phase transition. We will go into more detail about that later.

4.3.2 A temperature-dependent phase diagram

The Ginzburg-Landau theory can only give us information about what happens just below the critical temperature. For lower temperatures we will have to find the self-consistent gap by direct minimisation of the Helmholtz free energy. For this we will focus on a submanifold of the T_{2g} states spanned by the $(1, 0, 0)$ and
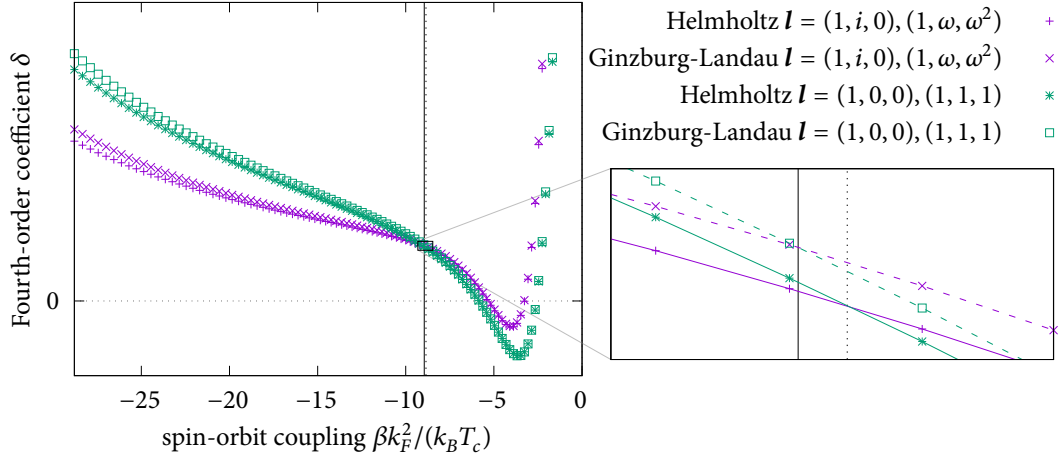
■ *Figure 4.2*. Comparison of the fourth-order coefficient of the free energy as obtained analytically from Ginzburg-Landau theory and numerically from the Helmholtz free energy. The inset is a zoom of the box marked in the full size plot where the points have been connected by lines as a guide to the eye, where solid refers to the Helmholtz free energy and dashed to the Ginzburg-Landau free energy. The solid and dashed vertical line denote the point of time-reversal symmetry breaking as predicted by the Ginzburg-Landau and Helmholtz free energy, respectively.

$(1, i, 0)$. Therefore we choose the mean-field ansatz:

$$\Delta = \Delta_{xz}\Gamma_{xz} + i\Delta_{yz}\Gamma_{yz}, \tag{4.9}$$

with two *real* variational parameters Δ_{xz} and Δ_{xz}. If one of the parameters is zero, the resulting state is equivalent to the $(1, 0, 0)$ state, which preserves time-reversal symmetry. For non-zero Δ_{xz} and Δ_{yz} the state breaks time-reversal symmetry, which is maximally broken for $\Delta_{xz} = \Delta_{yz}$, which in turn corresponds to a $(1, i, 0)$ state. The restriction to the xz and yz pairing states may seem artificial in the cubic system, but these are the only pairing states that are also degenerate in other crystal systems, including hexagonal (E_{1g} in D_{6h}) and tetragonal (E_g in D_{4h}). For example, a chiral d-wave state with the same symmetry is believed to be realised in tetragonal URu$_2$Si$_2$ [141]. In contrast to the E_g representation which also features two degenerate pairings, the $(1, i, 0)$ features an equatorial line node, whereas the other T_{2g} state $(1, \omega, \omega^2)$ and the E_g states only have point nodes. This results in a larger penalty to the free energy, such that in the worst case, we underestimate the stability of the time-reversal symmetry-breaking state with Bogoliubov Fermi surfaces. It is therefore expected that our conclusions qualitatively apply to any superconductor with two degenerate pairing potentials. The pairing state in the spherically symmetric limit has also been considered in Refs. [74, 134, 142].

In Fig. 4.3, we present the phase diagram as a function of temperature and spin-orbit coupling. In Figs. 4.4(a)–4.4(f) we show the band structure for the points labelled in Fig. 4.3 along the [100] direction where we expect nodes from the projected gap. That implies that gaps along this direction are entirely due to interband pairing. To obtain comparable results over a wide range of values for the spin-orbit coupling, we fix the critical temperature T_c by varying the attractive interaction g_0 such that the second-order coefficient of the Ginzburg-Landau free energy vanishes at the chosen critical temperature, here $k_B T_c = \mu/60$. This eliminates effects due to changing density of states at the Fermi energy as we tune through the spin-orbit coupling.

Starting at $\beta = 0$ we find a fully gapped time-reversal symmetric state as was predicted earlier by Ho and Yip [137], which we label "nodeless TRS". As we turn on the spin-orbit coupling ($\beta < 0$), the projection of
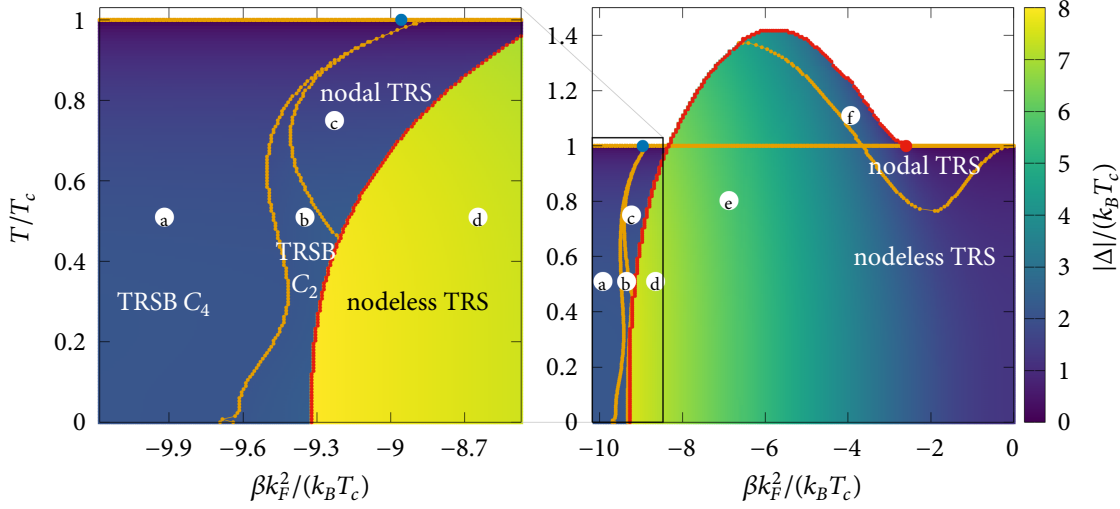
■ *Figure 4.3.* Phase diagram for the T_{2g} pairing states given by Eq. (4.9) as a function of spin-orbit coupling and temperature. The left panel is a zoom of the box in the right panel. The colour code indicates the gap magnitude $\sqrt{\Delta_{xz}^2 + \Delta_{yz}^2}$ where brighter colours mean larger gaps and white means no superconductivity. The horizontal line at $T/T_c = 1$ denotes the critical temperature T_c as defined by Ginzburg-Landau theory which remains fixed. Lines of first-order (second-order) phase transitions are indicated in red (orange). The blue dot in both panels indicates the point of the time-reversal symmetry-breaking phase transition, the red dot in the panel on the right denotes the onset of the first-order phase transition, both estimated by Ginzburg-Landau theory. The label "TRS" ("TRSB") indicates that the ground state is time-reversal symmetry-preserving (-breaking). The labels C_2 and C_4 indicate the rotational symmetry of the corresponding energy spectrum. Spin-orbit coupling β is plotted as an effective spin-orbit energy $\beta k_F^2/(k_B T_c)$ where $k_F^2 = \mu/(\alpha + 5\beta/4)$. *Reprinted figure with permission from H. Menke et al., Phys. Rev. B **100**, 224505 (2019). Copyright © 2019 by the American Physical Society.*
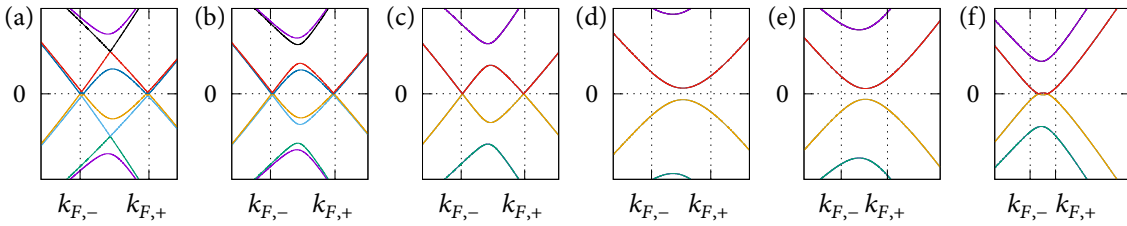
■ *Figure 4.4.* (a)–(f) Band structure in the vicinity of the Fermi energy for parameter sets indicated by the corresponding labels in Fig. 4.3 along the [100] direction where we expect nodes in a nodal state. The Fermi wave vectors are given by $k_{F,\pm} = \sqrt{\mu/(\alpha + 5\beta/4 \pm \beta)}$. *Reprinted figure with permission from H. Menke et al., Phys. Rev. B **100**, 224505 (2019). Copyright © 2019 by the American Physical Society.*
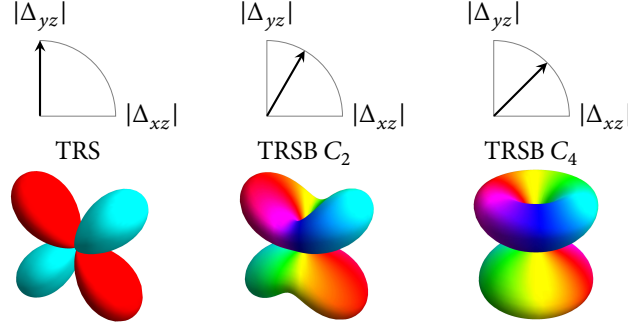
■ *Figure 4.5.* Sketch of the pairing amplitudes $|\Delta_{xz}|$ and $|\Delta_{yz}|$ and of the gap structure in the nodal TRS, TRSB C_2, and TRSB C_4 phases, see Fig. 4.3. The TRSB C_2 state breaks both TRS and C_4 symmetry. *Reprinted figure with permission from H. Menke* et al., *Phys. Rev. B* **100**, *224505 (2019). Copyright © 2019 by the American Physical Society.*

the normal-state spin-orbital texture gives rise to nodes ("nodal TRS"). As the four-fold degeneracy of the bands is lifted, the distinction between intra- and interband pairing becomes possible. For small amplitude of the pairing potential, i.e. close to T_c, interband pairing is not strong enough to gap out the nodes. As the temperature is lowered the interband pairing potential increases, shifting the nodes away from the Fermi surface at $k_{F,\pm} = \sqrt{\mu/(\alpha + 5\beta/4 \pm \beta)}$, which can be seen in the band structure at point (f) in Fig. 4.4. At a critical value of the pairing potential, the nodes meet and annihilate, marking the recovery of the nodeless TRS phase.

Further increasing the spin-orbit coupling we find that the transition into the superconducting state becomes first order. This was already indicated by the sign change of the fourth-order coefficient in Fig. 4.2. From the rightmost zero of the fourth-order coefficient in Fig. 4.2 we can estimate the location of the onset of the first-order phase transition in a tricritical point. We find very good agreement between the numerical calculation and our GL theory, cf. the red dot at $\beta k_F^2 \approx -2.59\,k_B T_c$ in the right panel of Fig. 4.3. In the region where the superconductivity is enhanced beyond the expected critical temperature, the pairing potential also has a much larger magnitude than is expected from BCS theory. The accompanying very large interband pairing potential ensures a full gap across the full Fermi surface as can be seen in points (d) and (e) in Fig. 4.3. This state will be referred to as the "large-gap" phase, in contrast to the other, "small-gap" phases. The origin of the large-gap phase will be discussed later.

Increasing the spin-orbit coupling beyond $\beta k_F^2 \approx -8.4\,k_B T_c$, we observe an abrupt drop in the magnitude of the pairing potential and the large-gap nodeless TRS phase gives way to a small-gap nodal state. Close to T_c, a time-reversal symmetric state is realised ("nodal TRS") whose gap is well approximated by the projected gap in (3.85) and exhibits line nodes. The line nodes appear along the [100] direction and are shown in point (e) in Fig. 4.4. As time-reversal symmetry-breaking takes place, the superconducting state exhibits reentrant behaviour with the time-reversal symmetric state below the critical temperature. In the region of reentrance a time-reversal symmetry-breaking state is realised but time-reversal symmetry is not broken maximally because Δ_{xz} and Δ_{yz} have unequal magnitude. This intermediate state between $(1, 0, 0)$ and $(1, i, 0)$ only appears below T_c and breaks the C_4 rotational symmetry of the spectrum down to C_2, which is why we label it with "TRSB C_2". As the spin-orbit coupling is increased further, the magnitudes of Δ_{xz} and Δ_{yz} converge and the $(1, i, 0)$ state is realised which restores the C_4 symmetry and is therefore labelled with "TRSB C_4". The intermediate TRSB C_2 state can be visualised as a continuous rotation of the vector $\boldsymbol{l}$ from $(1, 0, 0)$ to $(1, i, 0)$, see Fig. 4.5. The boundary of the TRSB C_4 phase shows reentrant behaviour, but it is realised at all temperatures beyond
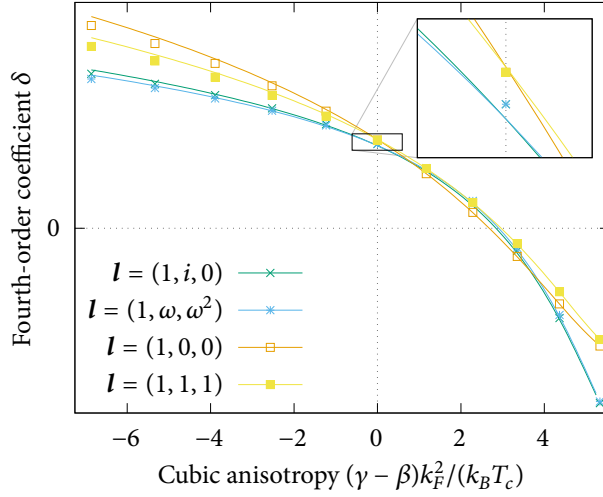
■ *Figure 4.6.* Comparison of the fourth-order coefficient of the free energy as obtained analytically from Ginzburg-Landau theory (points) and numerically from the Helmholtz free energy (lines) in the presence of cubic anisotropy. The value $\beta k_F^2 = -9.92\,k_B T_c$ is fixed. The inset is a zoom of the box marked in the full size plot.

$\beta k_F^2 \approx -9.7\,k_B T_c$. Both the TRSB C_4 and the C_2 phases have extended Bogoliubov Fermi Surfaces.

In the previous section we have estimated the critical value of the spin-orbit coupling where the TRSB C_4 state becomes stable just below T_c from Ginzburg-Landau theory, cf. Fig. 4.2, which is located at $\beta k_F^2 \approx -8.957\,k_B T_c$. We show this estimate as a blue dot in both panels of Fig. 4.3. As already noted earlier, this estimate is in very good agreement with the value that we get from mean-field theory. In a previous analysis in [66] the critical spin-orbit energy was estimated at $\beta k_F^2 \approx -11.572 k_B T_c$ (expressed in our units) and, therefore, overestimated it by about 30%. This disagreement stems from from the approximation adopted in [66] that the bands are split by a constant instead of by the momentum-dependent splitting βk^2. Nevertheless, we confirm that the TRSB C_4 state with Bogoliubov Fermi surfaces is realised at moderate values of spin-orbit coupling.

4.4 Lifting degeneracies with cubic anisotropy

Cubic anisotropy is introduced by $\gamma \neq \beta$ in (3.37). This has the effect that we are no longer able to analytically evaluate the angular integrals. It is still possible to evaluate the integrals numerically, but convergence is slow. Hence we use the approach discussed earlier of evaluating the Helmholtz free energy at T_c as a function of the magnitude of the pairing potential Δ and fitting a fourth-order polynomial to it to extract the fourth-order coefficient of the free energy. The result is shown in Fig. 4.6 where points represent the Ginzburg-Landau expansion and lines the numerically calculated Helmholtz free energy. The agreement is not exact and the deviation increases with increasing cubic anisotropy but the trend is reproduced correctly, which is why we use the fourth-order coefficient extracted from the Helmholtz free energy in the following.

We note that cubic anisotropy splits apart the $(1, 0, 0)$ and $(1, 1, 1)$, as well as the $(1, i, 0)$ and $(1, \omega, \omega^2)$ solutions which we found to be degenerate in the spherical limit earlier. Positive anisotropy ($|\gamma| > |\beta|$) lowers the free energy of the $(1, 0, 0)$ and $(1, i, 0)$ states, whereas negative anisotropy ($|\gamma| < |\beta|$) favours the $(1, 1, 1)$ and $(1, \omega, \omega^2)$ states.

In Fig. 4.7 we show a phase diagram just below the critical temperature as a function of spin-orbit coupling
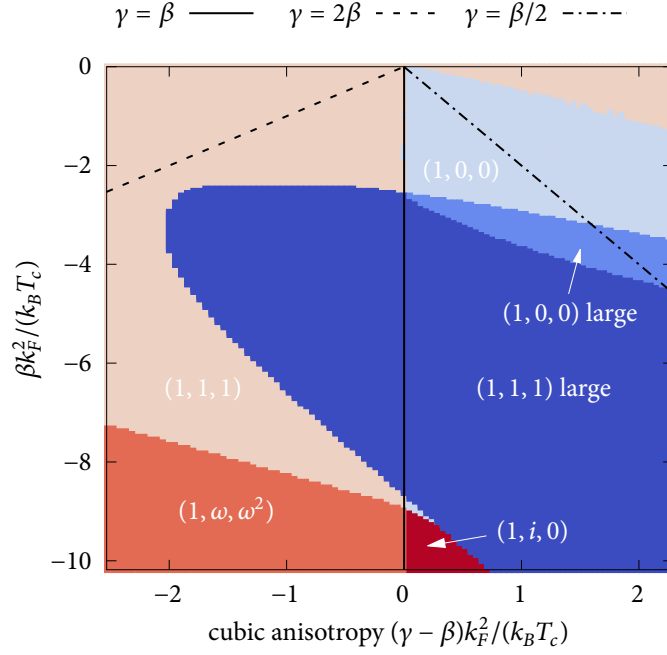
Figure 4.7. Phase diagram just below the critical temperature as a function of spin-orbit coupling and cubic anisotropy obtained numerically from the Helmholtz free energy. The colour code indicates the superconducting state.

and cubic anisotropy. There is a pronounced asymmetry in the phase diagram between $|\gamma| < |\beta|$ and $|\gamma| > |\beta|$. In the region where $|\gamma| > |\beta|$, the $(1, 1, 1)$ and $(1, \omega, \omega^2)$ states are stabilised, whereas for $|\gamma| < |\beta|$ we find the $(1, 0, 0)$ and $(1, i, 0)$ phases to be more stable. We find the regions of first-order transitions by performing a direct minimisation of the free energy at T_c. A minimum away from $\Delta = 0$ indicates a large gap state with a first-order phase transition into the normal state. Whether the phase is "$(1, 0, 0)$ large" or "$(1, 1, 1)$ large" is decided by which free energy is lower. In the region $\gamma < \beta$ the first-order phase transition is suppressed and disappears entirely for sufficiently large γ. At the same time the time-reversal symmetry-breaking phase transition moves to smaller $|\beta|$. These trends are reversed for $\gamma > \beta$.

In Fig. 4.8 we show temperature-dependent phase diagrams along two cuts through Fig. 4.7, viz. $\gamma = 2\beta$ (dashed line) and $\gamma = \beta/2$ (dash-dotted line). As expected no first-order transition is found along the cut $\gamma = 2\beta$. The estimate for the point of the time-reversal symmetry-breaking phase transition that we obtain from Ginzburg-Landau theory agrees with the numerical phase diagram. We still find remnants of the large-gap phase below T_c in the nodeless TRS phase, because the gap magnitude is still enhanced beyond the expectation from BCS theory, however the transition into the nodal TRS phase is steep but not abrupt. The intermediate TRSB C_2 phase is suppressed to very low temperatures and has become very narrow. Along the other cut $\gamma = \beta/2$ we do not recover the small-gap phase within the limits of our phase diagram. The onset of the first-order phase transition in a tricritical point is predicted correctly by Ginzburg-Landau theory. Time-reversal symmetry breaking on the other hand is not observed because it is obstructed by the large-gap phase.
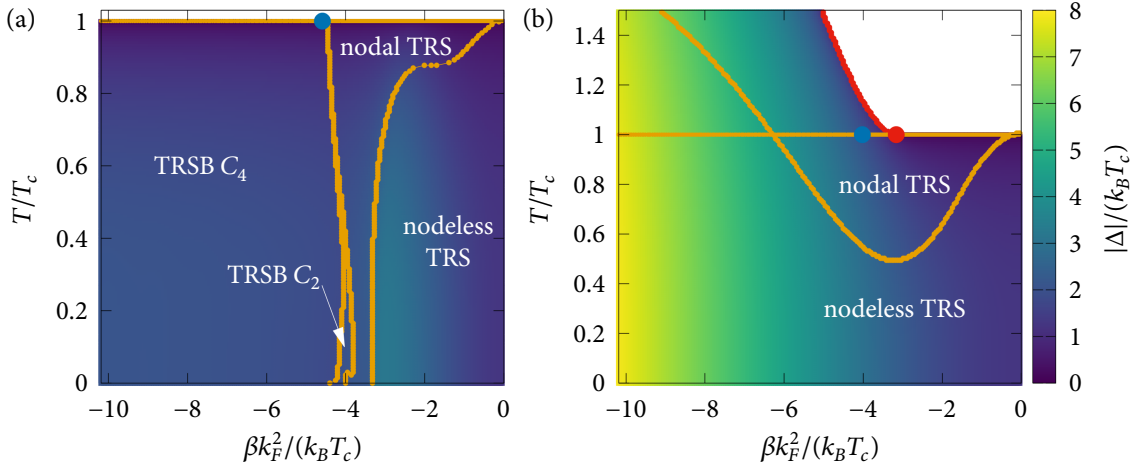
Figure 4.8. Phase diagram as a function of temperature along cuts through Fig. 4.7. The colour code represents the gap magnitude where darker corresponds to smaller, brighter corresponds to larger gap, and white means no gap. (a) Cut along the direction $\gamma = 2\beta$. The first-order phase transition is not present at T_c. Below T_c we find a high-gap phase but the transition is only weakly first-order. (b) Along the $\gamma = \beta/2$ cut the high-gap phase is present, as expected from Fig. 4.7. The critical temperature is strongly enhanced and larger gap sizes are found. In both figures, the blue dot at T_c is the point of time-reversal symmetry breaking and the red dot at T_c is the tri-critical point as predicted by the Ginzburg-Landau free energy. *Reprinted figure with permission from H. Menke* et al., *Phys. Rev. B* **100**, *224505 (2019). Copyright © 2019 by the American Physical Society.*

4.5   Simple model for the first-order phase transition

The first-order phase transition into the large-gap phase, that we observe in Figs. 4.2, 4.3, 4.6, and 4.7 is a remarkable feature of our phase diagram. Including cubic anisotropy, however, suppresses the first-order phase transition as shown in Fig. 4.7. This indicates that its appearance depends on the balance between the two spin-orbit coupling terms. It becomes clear that the transition is controlled by the relative magnitude of the intra- and interband pairing potentials, which are directly related to the spin-orbit coupling terms of the normal-state Hamiltonian.

In the Luttinger-Kohn model the ratio between the intra- and interband components of the pairing is fixed by spin-orbit coupling. In our simple model we will instead introduce an independent parameter r to control the balance. We further remove the spin degree of freedom from the model such that we end up with the following spinless two-band Hamiltonian

$$h(\boldsymbol{k}) = \begin{pmatrix} \xi_{\boldsymbol{k},+} & 0 \\ 0 & \xi_{\boldsymbol{k},-} \end{pmatrix}, \quad \Delta = \eta \begin{pmatrix} r & \sqrt{1-r^2} \\ \sqrt{1-r^2} & -r \end{pmatrix}, \tag{4.10}$$

with the dispersions $\xi_{\boldsymbol{k},\pm} = (1 \pm \delta)\epsilon_{\boldsymbol{k}} - \mu$, where δ parameterises the band splitting and the precise form of $\epsilon_{\boldsymbol{k}}$ is unimportant. The band splitting parameter δ plays a role analogous to the spin-orbit coupling terms in the full model where the band splitting is characterised by differing effective masses of the Luttinger-Kohn bands in the spherical limit as illustrated in Fig. 4.1. The pairing potential is determined by the momentum-independent magnitude η and the parameter r ($0 \leq r \leq 1$) determines the ratio between intra- and interband pairing, where $r = 0$ corresponds to pure interband pairing and $r = 1$ to pure intraband pairing. The intraband pairing has opposite sign on each band, cf. (3.4). In Fig. 4.7 we observe the first-order phase transition only in the
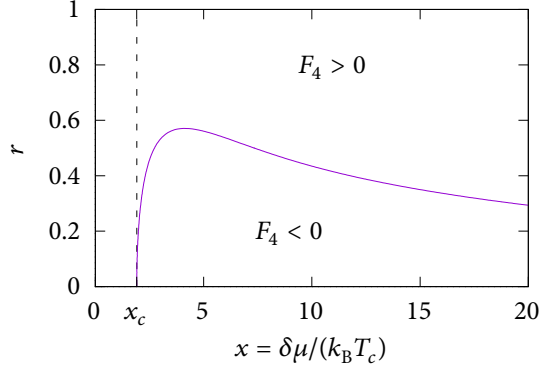
■ *Figure 4.9.* Phase diagram of the simple model as a function of the pairing ratio r and the effective band splitting energy $x = \delta\mu/(k_B T_c)$. A first-order phase transition is only possible for $x > x_c$ because only then there is a region where $F_4 < 0$. *Reprinted figure with permission from H. Menke* et al., *Phys. Rev. B* **100**, *224505 (2019). Copyright © 2019 by the American Physical Society.*

time-reversal symmetric phase and therefore, without loss of generality, we assume η to be real.

In our simple model the magnitude of the pairing potential and the ratio between intra- and interband pairing are both momentum-independent, whereas in the Luttinger-Kohn model these quantities vary across the Fermi surface. It is nevertheless possible to define this ratio for the Luttinger-Kohn model in terms of the Fermi-surface average,

$$r^2 = \frac{1}{\Delta_{xz}^2 + \Delta_{yz}^2} \int \frac{d\Omega}{4\pi} |\psi_{\boldsymbol{k},\pm}|^2. \tag{4.11}$$

To investigate the phase diagram of our simple model, we compute the Ginzburg-Landau free energy up to fourth order

$$F = F_2\eta^2 + F_4\eta^4 + \mathcal{O}(\eta^6), \tag{4.12}$$

and extract the fourth-order coefficient

$$F_4 = k_B T \sum_{\boldsymbol{k},i\omega_n} \left[\frac{(1-r^2)^2}{2} (\tilde{G}_-^2 G_+^2 + \tilde{G}_+^2 G_-^2) - 2r^2(1-r^2)\tilde{G}_+\tilde{G}_- G_+ G_- + \frac{r^4}{2}(\tilde{G}_+^2 G_+^2 + \tilde{G}_-^2 G_-^2) \right.$$
$$\left. + r^2(1-r^2)(\tilde{G}_+ G_+ + \tilde{G}_- G_-)(\tilde{G}_+ G_- + \tilde{G}_- G_+) \right], \tag{4.13}$$

where $G_\pm = (i\omega_n - \xi_{\boldsymbol{k},\pm})^{-1}$ and $\tilde{G}_\pm = (i\omega_n + \xi_{\boldsymbol{k},\pm})^{-1}$. An overall negative sign of the fourth-order coefficient marks the existence of a first-order phase transition. In Fig. 4.9 we show a phase diagram for the sign of the fourth-order coefficient as a function of the ratio r and the band splitting δ. For sufficiently small r, i.e. mostly intraband pairing, we find that F_4 is positive at small band splitting δ, but becomes negative for increasing δ, and finally returns to a positive value. Under the assumption that higher-order terms in the Ginzburg-Landau free energy can be ignored, this indicates that the phase transition becomes discontinuous beyond a critical band splitting, but a continuous transition is recovered as the band splitting is further increased.

This conclusion for the simple model is in qualitative agreement with the phase diagram for the Luttinger-Kohn model in Figs. 4.3 and 4.7. Calculating the Fermi surface average in (4.11) for a time-reversal symmetric Γ_{xz} or Γ_{yz} pairing state in the spherical limit gives $r = 1/\sqrt{5}$. According to the simple model, the phase transition at this value of r becomes discontinuous at $|x| = |\delta\mu/(k_B T_c)| \approx 2.460$, which is in very good agreement with the location of the tricritical point for the full model at $|x| \approx 2.594$ (red dot in Fig. 4.3) for which we related the band

splitting δ of the simple model to the effective band splitting in the Luttinger-Kohn model $\delta = \beta/(\alpha + 5\beta/4)$. Furthermore the simple model can explain the asymmetry of the region of first-order phase transition that we observed in Fig. 4.7. For $|\gamma| > |\beta|$, the intraband pairing potential is enhanced, which, in turn, increases the value of r and, thus, suppresses the first-order transition. Conversely, $|\gamma| < |\beta|$ reduces the intraband pairing potential and, thus, r and favours the first-order transition.

In both the simple model and the Luttinger-Kohn model the first-order phase transition eventually disappears again, recovering a second-order phase transition at sufficiently large values of the band splitting δ. However, the reappearance of the second-order phase transition is not marked by a tricritical point but by a discontinuous jump in the minimum of the free energy and therefore in the gap magnitude. We can observe this in Fig. 4.3 where there is a jump from a large-gap nodeless TRS to a small-gap nodal TRS also below T_c. To properly capture this behaviour an expansion of the Ginzburg-Landau free energy to at least eighth order in η would be required, which is not performed here.

The appearance of the region of first-order phase transition in Fig. 4.7 can therefore be understood within this simplified model which removes any complications like nodal gap structure and time-reversal symmetry breaking. In summary, we have found that the first-order phase transition only depends on the ratio between intra- and interband pairing.

## 4.6   Properties of the time-reversal symmetry breaking state

Returning to superconductivity in the Luttinger-Kohn model in the spherically symmetric limit. In this section we will discuss some of the properties of the time-reversal symmetry breaking state, because it displays Bogoliubov Fermi surfaces and therefore the behaviour is expected to be different from a pairing state with only point and line nodes. In the $(1, i, 0)$ state time-reversal symmetry is broken maximally and therefore we can write the pairing wave function as $\Delta = \Delta_0(\Gamma_{xz} + i\Gamma_{yz})$ where Δ_0 is the gap magnitude and can be chosen to be real. For the further investigation we choose the parameters that are labelled with (a) in Figs. 4.3 and 4.4.

### 4.6.1   Bogoliubov Fermi surfaces

To map out the Bogoliubov Fermi surfaces we search for zeros of the energy eigenvalues. Thanks to the rotational symmetry around the z axis and inversion symmetry, we can restrict ourselves to a slice through the first octant. The resulting nodal surfaces are shown in figure 4.10. The size of the Bogoliubov Fermi surfaces scales with the magnitude of the pseudomagnetic field, which is inversely proportional to the band splitting. Since the band splitting grows as $|\boldsymbol{k}|^2$, we expect the inner Bogoliubov Fermi surface to be larger than the outer one, which is confirmed in Fig. 4.10. The Bogoliubov Fermi surfaces have the largest volume close to the boundary with the TRSB C_2 phase, because there the band splitting is smallest. In this region the Bogoliubov Fermi surfaces are clearly distinguishable from point and line nodes.

4.6.2   Density of states

The Bogoliubov Fermi surfaces will lead to a residual density of states in the superconducting gap because in the nodal regions Cooper pairs are being broken, which is not expected for clean superconductors. To this end we compute the density of states numerically from the mean-field dispersions and analytically from the low-energy single band theory.
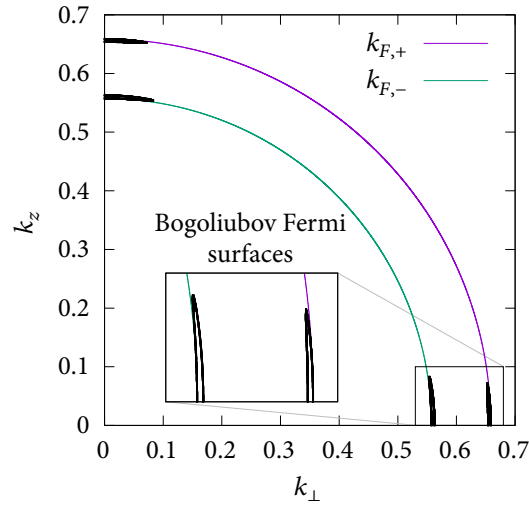
■ *Figure 4.10.* Bogoliubov Fermi surfaces for the parameters labelled with (c) in Fig. 4.3 (thick black lines). The thin coloured solid lines denote the normal state Fermi surfaces of the "+" and the "−" band and $k_\perp$ is the radial component of the momentum in the $k_x k_y$ plane. *Reprinted figure with permission from H. Menke et al., Phys. Rev. B **100**, 224505 (2019). Copyright © 2019 by the American Physical Society.*
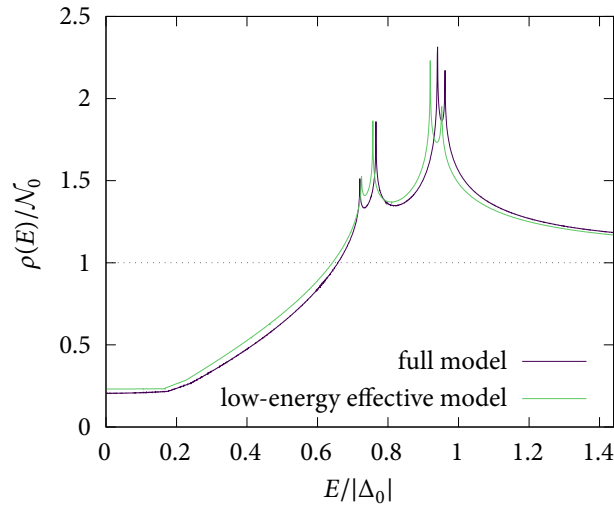
■ *Figure 4.11.* Density of states in the superconducting state for the parameters labelled by (a) in Figs. 4.3 and 4.4, based on a full two-band calculation (purple curve) and on a low-energy single-band approximation (green curve). The results of the two approaches agree very well. The residual density of states at zero energy is as large as 20% of the normal-state at the Fermi energy. *Reprinted figure with permission from H. Menke et al., Phys. Rev. B **100**, 224505 (2019). Copyright © 2019 by the American Physical Society.*

Before we can evaluate the density of states in the low-energy theory we have to apply some approximations. Close to the Fermi surface we can assume that the magnitude of the momentum is constant with $k_{F,\pm} = \sqrt{\mu/(\alpha + 5\beta/4 \pm \beta)}$ and therefore the pseudomagnetic field and the projected gap only depend on the value of the polar angle θ. Then we have for the magnitude of the pseudomagnetic field

$$|\boldsymbol{h}_\pm(\theta)| \approx \frac{|\eta|^2 \sqrt{5 + 3\cos(4\theta)}}{\sqrt{8}|\beta|k_{F,\pm}^2}, \tag{4.14}$$

and for the projected gap

$$|\psi_\pm(\theta)| \approx 3|\eta \cos\theta \sin\theta|^2. \tag{4.15}$$

Then the density of states in the $\pm$ band is then given by

$$\rho_\pm(E) = \mathcal{N}_{0,\pm} \sum_{a,b} \int_0^\pi \frac{b(E - a|\boldsymbol{h}_\pm(\theta)|)\sin\theta\, d\theta}{\sqrt{(E - a|\boldsymbol{h}_\pm(\theta)|)^2 - |\psi_\pm(\theta)|^2}} \tag{4.16}$$

where the normal-state density of states $\mathcal{N}_{0,\pm}$ is given by

$$\mathcal{N}_{0,\pm} = \frac{4\pi\sqrt{\mu}}{(\alpha + 5\beta/4 \pm \beta)^{3/2}}. \tag{4.17}$$

We have assumed the normal-state density of states $\mathcal{N}_{0,\pm}$ to be constant in the range of the superconducting gap by which we have also neglected the shift of the chemical potential $\gamma_{\boldsymbol{k},\pm}$. Evaluating (4.16) numerically, we find excellent agreement with the numerical results, as shown in Fig. 4.11.
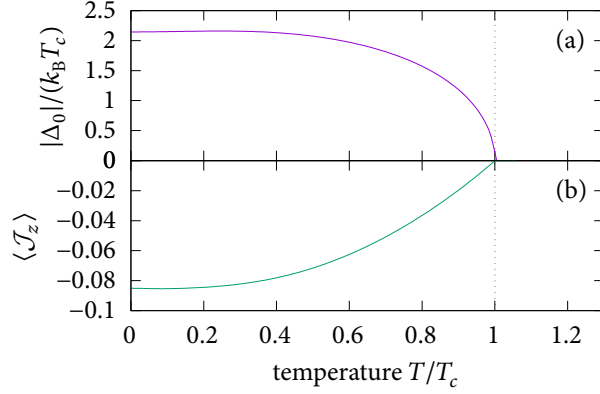
We clearly see the large residual density of states at zero energy in the superconducting gap. This contribution is as large as 20% of the normal-state density of states. The plateau at zero energy results from the lifting of the pseudospin degeneracy by the pseudomagnetic field $\boldsymbol{h}$. The effect is that the nodal contribution of each pseudospin species is shifted in energy leading to the scaling $\rho(E) \propto (|E + |\boldsymbol{h}|| + |E - |\boldsymbol{h}||)/2$ instead of $\rho(E) \propto |E|$. This gives a constant DOS for $-|\boldsymbol{h}| < E < |\boldsymbol{h}|$, as also reported in Ref. [93]. Another effect of the pseudomagnetic field is a splitting of the coherence peaks: In the absence of the pseudomagnetic field, we expect a single coherence peak at $|E| = \Delta_0$. Upon adding the pseudomagnetic field, it is split into four coherence peaks at $\Delta_0 + |\boldsymbol{h}_\pm(\theta = \pi/4)|$ and $\Delta_0 - |\boldsymbol{h}_\pm(\theta = \pi/4)|$, where $\theta = \pi/4$ is the angle of maximum gap. The splitting of the coherence peaks is different on the two Fermi surfaces, which is seen by the smaller splitting of the coherence peaks in Fig. 4.11.

4.6.3 Induced magnetic order parameter

It was pointed out in Ref. [133] that the pseudomagnetic field is related to the manifestation of a subdominant secondary magnetic order parameter, which is induced by the superconductivity. The subdominant order parameter is related to the time-reversal odd bilinear that was introduced in (3.10). Evaluating the time-reversal odd gap product for the $(1, i, 0)$ state yields

$$\Delta\Delta^\dagger - U_T\Delta^*\Delta^T U_T^\dagger = \frac{4}{3}\Delta_0^2(7J_z - 4J_z^3) \equiv 2\Delta_0^2\mathcal{J}_z. \tag{4.18}$$

where we have defined $\mathcal{J}_z$ as the matrix part of the subdominant order parameter. The form of this order parameter also describes the two-in-two-out order on the elementary tetrahedra of the pyrochlore lattice, which is associated with a polarisation along the z-axis, where it leads to interesting spin-ice physics [143, 144]. Because the subdominant magnetic order parameter arises from the time-reversal odd part of the superconducting

order parameter and therefore exist jointly, they are referred to as *intertwined orders* [145, 146]. In a similar spirit it was recently shown that the time-reversal odd part of the superconducting order parameter of the chiral *d*-wave state on the honeycomb lattice gives rise to a loop current order [119].

In Fig. 4.12, we show the expectation value of $\mathcal{J}_z$ together with the superconducting gap as functions of temperature. While both superconductivity and magnetism appear together below the critical temperature, their onset is notably different: The gap magnitude scales with $\Delta_0 \sim |T - T_c|^{1/2}$ whereas the magnetic order parameter scales with $\langle \mathcal{J}_z \rangle \sim |T - T_c|$. The linear temperature dependence underlines the subdominant nature of the order parameter and its relation to the time-reversal odd gap product which suggest that it should go as $\sim |\Delta_0|^2$.

A finite expectation value of $\mathcal{J}_z$ generically gives rise to a finite pseudomagnetic field and therefore also to a momentum-dependent spin polarisation. To understand the interplay between magnetism and superconductivity we include the subdominant magnetic order parameter m_z in the Ginzburg-Landau expansion from Appendix D, such that it couples to the superconductivity. Following [147], we redefine:

$$\Sigma = \begin{pmatrix} \mathcal{M}_z & \Delta \\ \Delta^\dagger & -\mathcal{M}_z^T \end{pmatrix}, \tag{4.19}$$

in Eq. (D.7), where $\mathcal{M}_z = m_z \mathcal{J}_z$. The lowest-order term that involves a coupling between the superconducting and magnetic order parameters occurs at third order and has the form

$$iF_3 m_z (\Delta_{xz} \Delta_{yz}^* - \Delta_{xz}^* \Delta_{yz}), \tag{4.20}$$

which clearly indicates that the TRSB superconducting state induces the magnetism.

Similar to Appendix D the third-order coefficient can be expanded in products of Green's functions $G_\pm$ and $\tilde{G}_\pm$. We exclude the magnitude of the order parameters and denote the rest as F_3 such that

$$k_B T \sum_{\boldsymbol{k}, \omega_n} \frac{1}{3} \mathrm{Tr}[(G\Sigma)^3] = F_3 m_z |\Delta_0|^2. \tag{4.21}$$

There are 12 terms generated but four of them have vanishing coefficients. It remain eight terms in two groups

of four,

$$F_3 = k_B T \sum_{\mathbf{k}, \omega_n} \left[\frac{8(\epsilon_{\mathbf{k},xz}^2 + \epsilon_{\mathbf{k},yz}^2)}{|\vec{\epsilon}_{\mathbf{k}}|^2} (-G_- \tilde{G}_- G_+ - G_- G_+ \tilde{G}_+ + \tilde{G}_- G_+ \tilde{G}_+ + G_- \tilde{G}_- \tilde{G}_+) \right.$$

$$\left. + \frac{8(\epsilon_{\mathbf{k},3z^2-r^2}^2 + \epsilon_{\mathbf{k},x^2-y^2}^2 + \epsilon_{\mathbf{k},xy}^2)}{|\vec{\epsilon}_{\mathbf{k}}|^2} (-\tilde{G}_- G_+ G_+ + G_- \tilde{G}_+ \tilde{G}_+ + \tilde{G}_- \tilde{G}_- G_+ - G_- G_- \tilde{G}_+) \right] \quad (4.22)$$

All products of Green's functions involve Green's functions with different band index. This shows that the coupling to the magnetic order parameter requires interband pairing. The combination of Green's functions appearing in the first line couples the interband component of the magnetic order parameter to one interband and one intraband component of the superconducting pairing potential. On the other hand, the combination of Green's functions in the second line couples the intraband component of the magnetic order parameter to two interband components of the superconducting order. The latter terms correspond to the coupling of the magnetic order parameter with the pseudomagnetic field in the low-energy effective model.

In the spherical limit, the coefficients do not depend on the radial component of the momentum whereas the Green's functions do not depend on the angular component. Therefore the evaluation of the coefficients and the Green's functions can be separated. Writing the coefficients in terms of spherical coordinates yields

$$\frac{8(\epsilon_{\mathbf{k},xz}^2 + \epsilon_{\mathbf{k},yz}^2)}{|\vec{\epsilon}_{\mathbf{k}}|^2} = \frac{8(\epsilon_{\mathbf{k},xz}^2 + \epsilon_{\mathbf{k},yz}^2)}{\epsilon_{\mathbf{k},3z^2-r^2}^2 + \epsilon_{\mathbf{k},x^2-y^2}^2 + \epsilon_{\mathbf{k},xy}^2 + \epsilon_{\mathbf{k},xz}^2 + \epsilon_{\mathbf{k},yz}^2} = 6\sin^2(2\theta), \quad (4.23)$$

$$\frac{8(\epsilon_{\mathbf{k},3z^2-r^2}^2 + \epsilon_{\mathbf{k},x^2-y^2}^2 + \epsilon_{\mathbf{k},xy}^2)}{|\vec{\epsilon}_{\mathbf{k}}|^2} = \frac{8(\epsilon_{\mathbf{k},3z^2-r^2}^2 + \epsilon_{\mathbf{k},x^2-y^2}^2 + \epsilon_{\mathbf{k},xy}^2)}{\epsilon_{\mathbf{k},3z^2-r^2}^2 + \epsilon_{\mathbf{k},x^2-y^2}^2 + \epsilon_{\mathbf{k},xy}^2 + \epsilon_{\mathbf{k},xz}^2 + \epsilon_{\mathbf{k},yz}^2} = 5 + 3\cos(4\theta). \quad (4.24)$$

The angular integrals are easily evaluated

$$\int_0^{2\pi} d\phi \int_0^{\pi} d\theta \, [6\sin^2(2\theta)] \sin\theta = \frac{64\pi}{5}, \quad (4.25)$$

$$\int_0^{2\pi} d\phi \int_0^{\pi} d\theta \, [5 + 3\cos(4\theta)] \sin\theta = \frac{96\pi}{5}. \quad (4.26)$$

Now it comes to integrating the energy and frequency dependence of each term. Before we evaluate the integration we simplify the terms in each group, because we will see that there are only even terms in ω_n which allows us to treat ω_n as positive, making the Matsubara sum a lot easier (it also gives an additional factor of 2).

$$-G_- \tilde{G}_- G_+ - G_- G_+ \tilde{G}_+ + \tilde{G}_- G_+ \tilde{G}_+ + G_- \tilde{G}_- \tilde{G}_+ = -\frac{2(\epsilon_- + \epsilon_+)}{(\omega_n^2 + \epsilon_-^2)(\omega_n^2 + \epsilon_+^2)}. \quad (4.27)$$

A similar transformation is available for the second term, although it is not so simple

$$-\tilde{G}_- G_+ G_+ + G_- \tilde{G}_+ \tilde{G}_+ + \tilde{G}_- \tilde{G}_- G_+ - G_- G_- \tilde{G}_+$$

$$= -\frac{4\epsilon_-^2}{(\omega_n^2 + \epsilon_-^2)^2(\epsilon_- + \epsilon_+)} - \frac{2(\epsilon_- - \epsilon_+)}{(\omega_n^2 + \epsilon_-^2)(\epsilon_- + \epsilon_+)^2} + \frac{2(\epsilon_- - \epsilon_+)}{(\epsilon_- + \epsilon_+)^2(\omega_n^2 + \epsilon_+^2)} - \frac{4\epsilon_+^2}{(\epsilon_- + \epsilon_+)(\omega_n^2 + \epsilon_+^2)^2}. \quad (4.28)$$

For the first group we find the extremely simple result

$$2 \sum_{\omega_n=0}^{\infty} \int_{-\infty}^{\infty} d\epsilon_0 \, (\text{first group}) = 0. \quad (4.29)$$

$$2 \sum_{\omega_n=0}^{\infty} \int_{-\infty}^{\infty} d\epsilon_0 \, (\text{second group}) = -\frac{1}{\pi k_B T_c} \tilde{\beta} \, \text{Im}\left[\psi^{(1)}\left(\frac{1}{2} + \frac{i\tilde{\beta}\mu}{2k_B T_c \pi}\right) \right], \quad (4.30)$$

where $\psi^{(n)}(z)$ is the Polygamma function of n-th order. As noted earlier, the second group corresponds to the coupling of the magnetic order parameter with the pseudomagnetic field, so it is not surprising that this gives a non-vanishing contribution. Putting everything together we find

$$
\begin{aligned}
F_3 &= -\mathcal{N}_0 \frac{24}{\pi k_B T_c} g_M |\Delta_0|^2 \tilde{\beta} \operatorname{Im}\left[\psi^{(1)}\left(\frac{1}{2} + \frac{i\tilde{\beta}\mu}{2\pi k_B T_c} \right) \right] \\
&\approx \frac{\mathcal{N}_0}{\mu} \frac{48}{5} g_M |\Delta_0|^2,
\end{aligned}
\tag{4.31}
$$

where the last approximation is valid when the band splitting $\tilde{\beta}\mu$ is much larger than $k_B T_c$.

Here we have assumed that the density of states is constant at the Fermi surface. However, F_3 scales like $\mathcal{N}_0/\mu \approx \mathcal{N}_0'$, the derivative of the density of states at the Fermi surface. Therefore we should include particle-hole asymmetric terms of the normal-state density of states into the calculation. To this end we expand the density of states $\mathcal{N}(\epsilon_0) = \mathcal{N}_0[1 + \epsilon_0/(2\mu)]$ and consider the same frequency integrals as before, but with this additional energy dependence included. For the second group of terms it becomes a lot more difficult because the Matsubara sum doesn't converge anymore. Therefore we have to introduce a cutoff frequency Λ of the attractive pairing interaction

$$
\sum_{\omega_n=0}^{\infty} \to \sum_{\omega_n=0}^{\Lambda} \quad \text{or in terms of } n \quad \sum_{n=0}^{-\frac{1}{2}+\frac{\Lambda}{2\pi k_B T}}
\tag{4.32}
$$

This gives us for the first group

$$
2 \sum_{\omega_n=0}^{\Lambda} \int_{-\infty}^{\infty} d\epsilon_0 \frac{\epsilon_0}{2\mu} (\text{first group}) = -\frac{H_{\frac{\Lambda}{2k_B T \pi}} + \ln 4}{\mu(1-\hat{\beta}^2)}
\tag{4.33}
$$

where H_n is the analytic continuation of the n-th harmonic number. For the second group we find

$$
2 \sum_{\omega_n=0}^{\Lambda} \int_{-\infty}^{\infty} d\epsilon_0 \frac{\epsilon_0}{2\mu} (\text{second group}) = \frac{1}{2\mu}\left(2\operatorname{Re}\left[H_{-\frac{1}{2}+\frac{i\tilde{\beta}\mu}{2k_B T \pi}} \right] - 2\operatorname{Re}\left[H_{\frac{i\tilde{\beta}\mu+\Lambda}{2k_B T \pi}} \right] \right).
\tag{4.34}
$$

Combining these results with the contribution of the term for constant density of states, we obtain

$$
\begin{aligned}
F_3 &= \mathcal{N}_0 g_M |\Delta_0|^2 \frac{24}{5\pi}\left\{ -\frac{\tilde{\beta}}{k_B T_c} \operatorname{Im}\left[\psi^{(1)}\left(\frac{1}{2} + \frac{i\tilde{\beta}\mu}{2\pi k_B T_c} \right) \right] - \frac{2\pi}{3} \frac{H_{\frac{\Lambda}{2k_B T_c \pi}} + \ln 4}{\mu(1-\tilde{\beta}^2)} + \frac{\pi}{\mu} \operatorname{Re}\left[H_{-\frac{1}{2}+\frac{i\tilde{\beta}\mu}{2k_B T_c \pi}} - H_{\frac{i\tilde{\beta}\mu+\Lambda}{2k_B T_c \pi}} \right] \right\} \\
&\approx g_M \frac{\mathcal{N}_0}{\mu} \frac{48}{5}\left[1 - \frac{\ln\frac{2\Lambda e^{\gamma}}{\pi k_B T_c}}{3(1-\tilde{\beta}^2)} - \frac{1}{4}\ln\left(1 + \frac{\Lambda^2}{\tilde{\beta}^2\mu^2} \right) \right],
\end{aligned}
\tag{4.35}
$$

where the second line is valid in the limit $\Lambda, \tilde{\beta}\mu \gg k_B T_c$ and γ is the Euler-Mascheroni constant.

To gain further insight, we note that the matrix part of the magnetic order parameter $\mathcal{J}_z$ is not diagonal in the band basis, but contributes both interband and intraband components. Its intraband component couples directly to the pseudomagnetic field generated by the interband pairing potential. This produces the cutoff-independent contribution to F_3. The interband components of the magnetic order parameter, on the other hand, couple to both the intra- and interband pairing potentials which results in a cutoff-dependent contribution to F_3. The two contributions have opposite signs and the contribution from the interband component is likely dominant when $\Lambda \gg k_B T_c$. This is surprising, since the intraband component of the pseudomagnetic field is most obvious at the Fermi surface.

It is instructive to compare our results to the textbook case of the coupling between ferromagnetic and superconducting order parameters in a single-band time-reversal symmetry-breaking superconductor [148]. Similar to our case it was found that the third-order coefficient is proportional to $\mathcal{N}_0/\mu$, which implies that the magnetisation in the superconducting state is on the order of Δ_0^2/μ^2 and is, hence, expected to be weak. This has been discussed previously in the context of time-reversal symmetry-breaking superconductors [149, 150]. In the present case it can be understood in terms of the $j = 1/2$ and $= -3/2$ quasiparticles that do not participate in the pairing, cf. (4.1). The spin of these unpaired quasiparticles then compensates the polarisation of the Cooper pairs as is the case for a non-unitary spin-1/2 superconductor where only the up spin electrons are paired and the unpaired down spin electrons compensate the polarisation [148]. The presence of a Bogoliubov Fermi surface, therefore, does not imply a strong magnetisation of the superconductor. A weak magnetisation will be screened out by Meissner currents at the surface of the superconductor, but we do not consider this Meissner screening here.

4.7   Summary

In this chapter we have investigated the thermodynamic stability and some experimental signatures of a pairing state with Bogoliubov Fermi surfaces in the paradigmatic Luttinger-Kohn model. While the topological protection of the Bogoliubov Fermi surfaces guarantees their stability with respect to symmetry-preserving perturbations, to exist at all they have to be thermodynamically more stable than a pairing state without them. It is known that when the bands are four-fold degenerate, the ground state will preserve time-reversal symmetry and therefore Bogoliubov Fermi surfaces cannot exist in this limit [137]. When the band splitting is very large compared to the gap, on the other hand, the Bogoliubov Fermi surfaces are small as predicted by the low-energy effective theory and are therefore hard to distinguish from point or line nodes. In this case it is argued that a time-reversal symmetry-breaking state is always preferred because it reduces the nodal region [42]. From this discussion we expect a time-reversal symmetry-breaking phase transition to occur as a function of band splitting. In the context of the Luttinger-Kohn model, band splitting is controlled by spin-orbit coupling.

To this end, we study the evolution from a time-reversal-symmetric to a time-reversal symmetry-breaking quintet state as a function of spin-orbit coupling and temperature using mean-field theory. Just below the critical temperature the phase diagram is well-described by the phenomenological Ginzburg-Landau theory. We find a rich phase diagram that confirms the predictions in the previous paragraph. For weak spin-orbit coupling a time-reversal-symmetric pairing state is realised. Upon increasing the spin-orbit coupling strength, the transition from the normal state into the superconducting state becomes first order. The existence of the first-order phase transition can be understood in terms of the competition between intra- and interband pairing and can be enhanced or completely suppressed by cubic anisotropy. Further increasing the spin-orbit coupling recovers the second-order phase transition and finally a time-reversal symmetry-breaking pairing state is stabilised at moderate values of spin-orbit coupling. At low temperatures, the time-reversal symmetry-breaking state displays reentrant behaviour as well as a first-order transition into the time-reversal-symmetric state.

The time-reversal symmetry-breaking state displays Bogoliubov Fermi surfaces and will therefore give rise to a residual density of states around the Fermi energy which can be as large as 20 % of the normal state. The non-unitary part of the gap product can be identified as a subdominant magnetic order parameter, whose expectation value attains a non-zero value with the onset of the time-reversal symmetry-breaking superconducting state. The resulting magnetisation is small even if the Bogoliubov Fermi surfaces are sizeable and the residual density of states is large.

In conclusion, we have found that Bogoliubov Fermi surfaces can be thermodynamically stable even if the residual density of states is large. This result is encouraging for experimental searches for Bogoliubov Fermi surfaces. Since the size of the Bogoliubov Fermi surfaces depends on the ratio of the interband pairing potential to the band splitting, materials where this ratio is as large as possible are the best candidates. Heavy-fermion superconductors are therefore a promising platform and it is intriguing that a large residual density of states has been observed in URu_2Si_2 [141].

Chapter 5

Even-parity chiral superconductivity in Strontium Ruthenate

The material presented in this chapter has been published previously in

[234]   H. G. Suh, H. Menke, P. M. R. Brydon, C. Timm, A. Ramires, and D. F. Agterberg, "Stabilizing even-parity chiral superconductivity in Sr_2RuO_4", Phys. Rev. Research **2**, 032023 (2020).

Since the discovery of high-temperature superconductivity in the cuprates [21], a lot of effort has been made to understand the mechanism behind the unusually high critical temperature of these compounds. It has been conjectured that a key ingredient is the quasi-two-dimensional structure of the intercalated copper oxide planes in these layered perovskites [151]. To further corroborate this hypothesis it was natural to survey other transition metal oxides that crystallize in a perovskite structure and study their superconductivity.

This search was largely unsuccessful but finally Maeno *et al.* [82] discovered superconductivity in strontium ruthenate (Sr_2RuO_4) whose crystal structure is reminiscent of the one in $La_{2-x}Ba_xCuO_4$ as shown in Fig. 5.1. However, the critical temperature of $T_c \approx 1.5\,K$ was much lower than anticipated from the cuprates. It is believed that this is due to the fact that the ruthenium with a $4d^4$ configuration has an even number of electrons, whereas copper in the $3d^9$ configuration has an odd number of electrons which allows for stronger spin fluctuations which have been theorized to be important for a high T_c [152]. Another important difference is that in stoichiometric Sr_2RuO_4 the superconductivity emerges from a metallic state, whereas the stoichiometric cuprates are usually in a Mott insulating state and have to be hole-doped to attain a Fermi surface and exhibit superconductivity [153, 154]. In addition it has been shown that the cuprates violate the Wiedemann-Franz law in the normal state which indicates a breakdown of Fermi liquid theory [155, 156].

The normal state of Sr_2RuO_4 is a strongly two-dimensional Fermi liquid, in contrast to the cuprates where superconductivity arises from a Mott insulating state. The two-dimensionality of the electronic structure of Sr_2RuO_4 is manifest in an anisotropy between in-plane and out-of-plane resistivity. The out-of-plane component is three orders of magnitude larger than in-plane [157]. De Haas-van Alphen measurements [158] and later angle-resolved photo emission experiments [159–161] show the Fermi surface consists of three weakly corrugated cylindrical sheets.

5.1   Basic properties of the superconducting state

The superconducting state shows the same strongly two-dimensional behaviour as the normal state. This can be seen from the anisotropy in the upper critical field H_{c2} which is maximal for the field aligned parallel to the RuO plane and decreases rapidly as the axis of the field deviates from the plane [162].
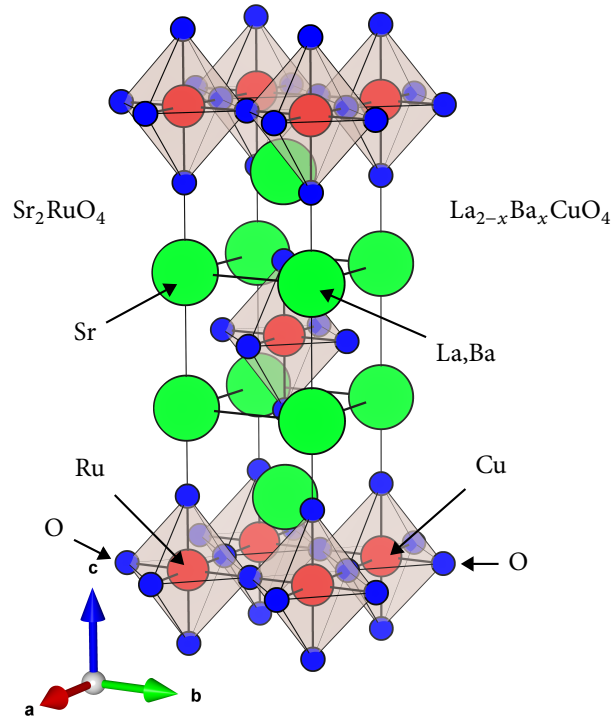
Figure 5.1. Crystal structure of Sr_2RuO_4 in comparison with $La_{2-x}Ba_xCuO_4$. The coordinate system in the lower left corner indicates the directions of the principal crystal axes. *Figure by Aleksandra Krajewska.*

Various experimental techniques provide substantial evidence for a nodal gap [163, 164], however, the direction of these line nodes is disputed. Thermal conductivity measurements have reported vertical line nodes [165], whereas field-angle-dependent specific heat capacity measurements indicate that the nodes are horizontal [166, 167]. Controversial quasiparticle interference imaging measurements have suggested vertical line nodes along the Γ-M line [168].

As per Anderson's theorem, *s*-wave superconductors are robust to scattering from non-magnetic impurities [169]. This implies that any deviation from this behaviour indicates an unconventional pairing state and it has been found that the superconductivity in Sr_2RuO_4 is sensitive to both disorder and doping [170, 171].

Another probe for unconventional superconductivity are tunneling experiments. In point contact spectroscopy the change in current as a function of bias voltage is measured which corresponds to the density of states. A zero-bias anomaly for tunneling into Sr_2RuO_4 indicates an unconventional superconducting state [172].

5.1.1 Time-reversal symmetry-breaking

There is evidence of time-reversal symmetry-breaking in the superconducting phase from both muon-spin relaxation [51] and the Polar Kerr effect [52]. The onset of time-reversal symmetry-breaking coincides with the superconducting transition and is observed in ultra-clean samples. It is therefore believed that time-reversal symmetry-breaking is intrinsic to the superconductivity rather than intrinsic to the material or accidental through the inclusion of magnetic impurities.

Superconductors with broken time-reversal symmetry should generate a spontaneous supercurrent on

the surface or at embedded domain walls. However, scanning Hall bar and superconducting interference device (SQUID) measurements have not been able to detect evidence for these spontaneous edge currents [173]. On the other hand, it has been pointed out that such spontaneous magnetic flux patterns are not a universal feature [174]. This also falls in line with the a recent report of the absence of edge currents in URu_2Si_2 which is widely believed to be a time-reversal symmetry-breaking chiral d-wave superconductor [175].

5.1.2 Two-component order parameter

The order parameter of the superconductivity has two components, i.e. is described by a two-fold degenerate representation of the point group. The presence of a multicomponent order parameter is further supported by tunneling experiments. For instance the behaviour of the temperature dependence of the critical current through $Pb/Ru/Sr_2RuO_4$ junctions shows a topological phase frustration leading to an anomalous suppression of the critical current [176–178]. A similar experiment using $Nb/Ru/Sr_2RuO_4$ junctions showed that below T_c the current-voltage curves becomes noisy and asymmetric due to the motion of chiral domain walls in Sr_2RuO_4 [179–181]. These signatures can only exist if the order parameter has multiple components.

However, none of the above experiments are truly symmetry-sensitive, i.e. they cannot distinguish the pairing state between the different irreducible representations of the point group. This restriction can be alleviated by probing thermodynamic quantities which are manifestly ground-state properties and are therefore guaranteed to represent the true symmetry of the order parameter. One such example of a symmetry-sensitive thermodynamic quantity is the strain tensor. It can be accesses directly by applying strain to the sample [182–185] or indirectly by deducing the elastic moduli from ultrasound attenuation [186–188].

Following [42], the coupling of the order parameter to the strain tensor to first order in strain and second order in the order parameter can be written as

$$F_{\Gamma,\text{strain}}(\eta, \epsilon) = -\sum_{\gamma, m} C(\gamma)\mathcal{V}(\gamma, m; \eta)\epsilon(\gamma, m), \tag{5.1}$$
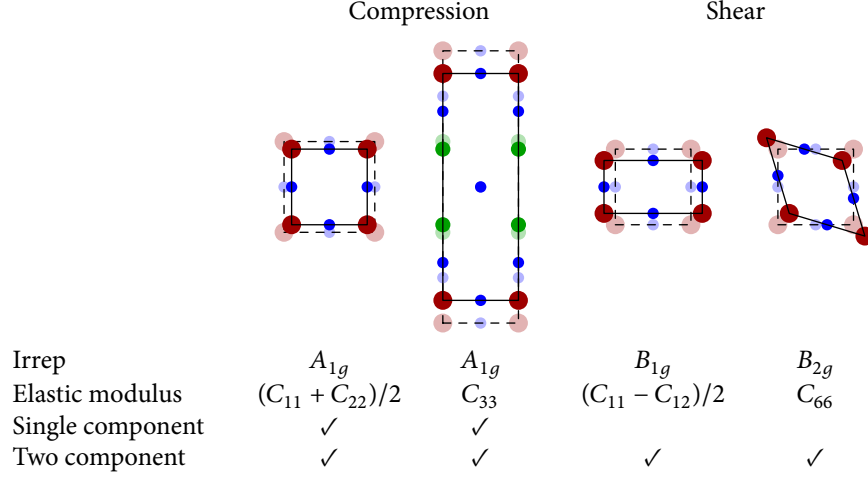
where we have stuck to the notation of [42] where γ runs over all irreducible representations and m enumerates the basis functions, η is the order parameter, $\mathcal{V}(\gamma, m; \eta)$ is a bilinear of η with the symmetry of the basis function (γ, m), and $\epsilon(\gamma, m)$ is a combination of elements of the strain tensor with symmetry (γ, m). The coupling constants $C(\gamma)$ are material-dependent real coefficients which are related to the elastic tensor. Further following [42] we can expand this for a two-component order parameter $\eta = (\eta_1, \eta_2)$ in the D_{4h} point group, which corresponds to the $E_{g/u}$ representation

$$F_{\text{strain}} = \big(C(A_{1g}, 1)\epsilon(A_{1g}, 1) + C(A_{1g}, 2)\epsilon(A_{1g}, 2)\big)\big(|\eta_1|^2 + |\eta_2|^2\big)$$
$$+ C(B_{1g})\epsilon(B_{1g})\big(|\eta_1|^2 - |\eta_2|^2\big) + C(B_{2g})\epsilon(B_{2g})\big(\eta_1^*\eta_2 + \eta_1\eta_2^*\big). \tag{5.2}$$

The A_{1g} representations of strain correspond to a uniform change in the crystal volume and a deformation in z-direction, respectively, whereas the B_{1g} and B_{2g} representations correspond to an anisotropic deformation, cf. Fig. 5.2 for illustrations. Moreover, it shows that an anisotropic deformation couples to a two-component order parameter which is key to identifying the gap symmetry in Sr_2RuO_4.

Stress and strain are related to one another by the elastic tensor of the material. By construction both stress and strain only have six independent components each and therefore the elastic tensor C is a 6×6 matrix. The elastic energy can then be determined by Hooke's law

$$F_{\text{elastic}} = \frac{1}{2}\epsilon^T : C : \epsilon. \tag{5.3}$$

	Compression		Shear	
Irrep	A_{1g}	A_{1g}	B_{1g}	B_{2g}
Elastic modulus	$(C_{11} + C_{22})/2$	C_{33}	$(C_{11} - C_{12})/2$	C_{66}
Single component	✓	✓		
Two component	✓	✓	✓	✓

◼ *Figure 5.2.* Deformations of the tetragonal unit cell of the Sr_2RuO_4 crystal in terms of irreducible representations. Solid lines and dots show the change in crystal structure upon deformation by applied strain. The original crystal structure is shown using dashed lines and faded dots for reference. Red dots denote Ru, blue dots O, and green dots Sr atoms. The second deformation in the second A_{1g} channel is shown as a side-view, the other channels are shown from a top view. There are two more moduli allowed by symmetry, namely C_{13} which couples the two A_{1g} strains and C_{44} which couples to the E_g strains. However, these do not couple to the superconducting order parameter in linear order and are thus omitted from this table.

Not all components of the elastic tensor C are non-zero. Assuming Hookean linear isotropic elasticity all components relating to axial or shear strains immediately have to vanish. Because in the tetragonal system the x and y directions are equivalent the elastic response in these directions has to be the same. This leaves only six elements

$$F_{\text{elastic}} = \frac{1}{2}\Big(C(A_{1g}, 1)\epsilon(A_{1g}, 1)^2 + C(A_{1g}, 2)\epsilon(A_{1g}, 2)^2 + 2C(A_{1g}, 3)\epsilon(A_{1g}, 1)\epsilon(A_{1g}, 2)$$
$$+ C(B_{1g})\epsilon(B_{1g})^2 + C(E_g)(\epsilon(E_g, 1)^2 + \epsilon(E_g, 2)^2) + C(B_{2g})\epsilon(B_{2g})^2 \Big), \quad (5.4)$$

where we identified in terms of irreducible representations $\epsilon(A_{1g}, 1) = \epsilon_{xx} + \epsilon_{yy}$, $\epsilon(A_{1g}, 2) = \epsilon_{zz}$, $\epsilon(B_{1g}) = \epsilon_{xx} - \epsilon_{yy}$, $\epsilon(B_{2g}) = 2\epsilon_{xy}$, and $\epsilon(E_g) = \{2\epsilon_{yz}, 2\epsilon_{xz}\}$ and with coefficients $C(A_{1g}, 1) = (C_{11} + C_{12})/2$, $C(A_{1g}, 2) = C_{33}$, $C(A_{1g}, 3) = C_{13}$, $C(B_{1g}) = (C_{11} - C_{12})/2$, $C(E_g) = 4C_{44}$, and $C(B_{2g}) = 4C_{66}$.

Due to the coupling of the strain to the superconducting order parameter (5.2), the second derivative of the strain free energy will show a jump at T_c. The shear moduli related to a two component order parameter are the ones that couple to $\epsilon(B_{1g})$ and $\epsilon(B_{2g})$. Hence a jump in the shear moduli $(C_{11} - C_{12})/2$ or C_{66} at T_c is a clear indication of a two-component order parameter. This whole discussion is again summarized in Fig. 5.2. A discontinuity in the shear elastic modulus C_{66} at the critical temperature was recently detected using resonant ultrasound spectroscopy [188], which implies that the superconducting order parameter of Sr_2RuO_4 has two components.

Another effect of the shear strains is that they break the tetragonal symmetry of the crystal. If the two-component order parameter is formed from components belonging to the same irrep, then it is expected that the superconducting phase transition is split, because the degeneracy of the components that is protected by crystal symmetry may now be lifted. For a two-component order parameter in a single irrep one would anticipated from (5.2) that the superconducting transition splits in a linear cusp as a function of strain. Instead a quadratic profile as a function of strain with no obvious splitting of the transition was observed [183, 184]. The absence

of a splitting of the transition suggests the components of the order parameter come from different irreps. However, this is also problematic because such a degeneracy of states would require fine-tuning to produce a single superconducting phase transition in the unstrained system, whereas a two-dimensional irrep naturally has this property.

A splitting under strain also implies that if the order parameter of the ground state breaks time-reversal symmetry, the time-reversal symmetry-breaking phase transition will not appear together with superconductivity at the critical temperature but below. This effect was observed in a recent muon-spin relaxation experiment [185].

5.1.3 An electronic analogue of ^{3}He-B?

The evidence for a two-component order parameter that breaks time-reversal symmetry in combination with evidence for strong correlations and the strongly two-dimensional electronic structure [51, 52, 82, 185] made it plausible to assume odd-parity spin-triplet pairing. In Section 2.2.2 we have discussed the possible pairing states for a single-band superconductor on the square lattice. The same classification was applied to Sr_2RuO_4 by assuming that there is only a single dominant band for superconductivity. One of the possible odd-parity pairing states is the chiral p-wave state

$$\boldsymbol{d_k} = (k_x \pm ik_y)\hat{\boldsymbol{z}}. \tag{5.5}$$

This is the same pairing state as it is realized in the B phase of superfluid ^{3}He. The analogy is plausible because the electronic structure exhibits a lot of similarities. The normal state of both Sr_2RuO_4 and ^{3}He are Fermi liquids with similar enhancement factors of the specific heat and the spin susceptibility. Furthermore the ratio of the critical temperature to the Fermi temperature T_c/T_F is of the same order of magnitude [83].

Odd-parity superconductors are very rare in nature, so it was exciting to see a proposal of odd-parity superconductivity in a very accessible solid state platform. High-quality single crystals of Sr_2RuO_4 are relatively easy to make and while experiments still require a dilution fridge, the critical temperature of 1.5 K is still several orders of magnitudes higher than for ^{3}He which has its critical temperature between 1 mK to 3 mK depending on pressure [148, 152].

Only a few materials have been identified as possible spin-triplet superconductors. Many of them are of the class of the Uranium-based heavy-fermion superconductors, such as UBe_{13} [19], UPt_3 [20, 189, 190], UGe_2 [191], or very recently UTe_2 [192–194]. In all of these materials superconductivity arises close to or within a ferromagnetic phase and therefore strong magnetic fluctuations are thought to be key to the pairing mechanism. However, the radioactivity of Uranium makes these materials hard to deal with. Another candidate for spin-triplet superconductivity is Copper-intercalated Bismuth Selenide ($Cu_xBi_2Se_3$) [38, 195], which has a very peculiar structure in that it is globally centrosymmetric but locally non-centrosymmetric. However, the superconductivity in $Cu_xBi_2Se_3$ might not be chiral but nematic, i.e. it breaks the three-fold rotational symmetry of the crystal but time-reversal symmetry is intact [63].

Another important aspect of the chiral p-wave state is its non-trivial topology. This topic is much more recent and was therefore not considered in the original proposal by Rice and Sigrist [83], but has certainly added to the interest in the material. It was shown that that Majorana bound states are pinned in the vortices of a chiral p-wave superconductor. These vortices can carry magnetic flux and are not necessarily pinned in location [196]. This is particularly exciting for type II superconductors like Sr_2RuO_4, which enters the Abrikosov vortex lattice phase in the presence of a magnetic field. In theory, by moving these Majorana vortex cores and interchanging them to exploit their non-Abelian braiding statistics could be used to implement a topological quantum computer [197, 198].

5.1.4 Parity of the order parameter

The result by Yosida [199] describes the response of a spin-singlet superconductor to an applied magnetic field and is discussed in detail in Appendix E. In this case the spin susceptibility and therefore the Knight shift of the nuclear magnetic resonance (NMR) decreases exponentially below T_c. This result is modified if pairing of opposite spins is allowed, i.e. spin-triplet pairing. Triplet pairs are characterized by their $\boldsymbol{d}$ vector and its orientation is key to identifying the NMR response. It was shown by Rice and Sigrist [83] that for a $p_x + ip_y$ pairing state with the $\boldsymbol{d}$ vector along the z-direction, the spin susceptibility does not decay if the field is applied in the plane

$$\frac{\chi_S(T)}{\chi_0} = Y\left(\frac{\Delta_0}{k_B T}\right) \quad \boldsymbol{H} \parallel \boldsymbol{z}, \tag{5.6}$$

$$\frac{\chi_S(T)}{\chi_0} = 1 \qquad \boldsymbol{H} \perp \boldsymbol{z}. \tag{5.7}$$

The projection of this state with $\boldsymbol{d} \parallel \hat{\boldsymbol{z}}$ on the quantization axis is zero, i.e. the spin of the Cooper pair lies in the plane perpendicular to the $\boldsymbol{d}$-vector [148]. If the applied magnetic field is perpendicular to the $\boldsymbol{d}$-vector, the Cooper pairs can orient their spin along the field direction and hence the susceptibility does not change below T_c. If on the other hand the field is applied perpendicular to the plane, i.e. parallel to the $\boldsymbol{d}$-vector, the Cooper pairs cannot reorient, resulting in a reduction of the spin susceptibility.

Hence the chiral p-wave pairing is unaffected by the Fermi surface polarisation due to an external field in the ab-plane and therefore a temperature-independent spin susceptibility throughout the whole superconducting regime is only consistent with spin triplet pairing [152].

In an experiment the magnetic response of a superconductor is usually completely shadowed by the Meissner effect, because an applied field is expelled from the bulk. Trying to work around this using small grain sized powder bears different problems related to surface effects. However, Sr_2RuO_4 is a type-II superconductor, which allows magnetic flux to penetrate for fields above the lower critical field. In the Abrikosov vortex lattice phase, the Knight shift can exceed the Meissner shift and it is feasible to work with single crystal samples [152].

This experiment was performed for high-quality crystals of Sr_2RuO_4 by Ishida *et al.* [200] for the field in the ab-plane. The experiment observed no suppression of the Knight shift below T_c and has been taken as a strong evidence for the realisation of spin triplet pairing in Sr_2RuO_4. A similar experiment was performed a little later by Duffy *et al.* [201] who used polarised neutron scattering to probe the susceptibility with the same result.

This argument was never fully bullet-proof, because it would be expected that the Knight shift is suppressed if the field is aligned along the c-axis, but instead no suppression was found for this configuration either [202]. To remedy this inconsistency it was proposed that the weak testing field might induce a phase transition into a state with $\boldsymbol{d} \parallel \hat{\boldsymbol{x}}$. This is unlikely, however, because such a state would have nodes where the chiral p-wave state does not and the energy barrier to introduce these nodes is larger than the field energy. Additionally, a state with $\boldsymbol{d} \parallel \hat{\boldsymbol{x}}$ is not allowed by tetragonal symmetry and would therefore require a second superconducting transition below T_c which has never been observed [203]. In principle this disqualifies these Knight shift measurements as an argument for the pairing symmetry determination. Nevertheless, it seems that this has been largely ignored by the community.

This paradigm of chiral p-wave pairing in Sr_2RuO_4 as a solid-state analogue to ^{3}He has been recently challenged when the NMR experiments were revisited in a new context. It was observed that organic super-conductors with small gap sizes are very sensitive to heating effects due to NMR pulses. It so happens that the

NMR pulse introduces sufficient energy into the sample to raise the bulk temperature above T_c such that for the time of precession of the nuclear magnetic moments the sample is in a normal state instead of a superconducting state. Therefore the NMR signal will show a normal-state response and not decrease below T_c. This insight led Pustogow *et al.* [84] to revisit the NMR experiment on Sr_2RuO_4 which also has a rather low critical temperature of only $T_c = 1.5\,K$. It was observed that for the field in the *ab*-plane the Knight shift depends on the pulse energy and for lower energies a suppression of the Knight shift is detected. This new result has been confirmed by others [85] and had a huge impact on the community. It is now clear that the pairing in Sr_2RuO_4 is not compatible with chiral *p*-wave pairing.

In the light of these novel results the theoretical situation is again open and unclear. The conventional theoretical methods, like pairing from spin fluctuations in the random phase approximation (RPA), tend to predict triplet pairing which is not consistent with the new experiments [204–208]. The observed drop in the Knight shift has led the community to seriously consider even-parity parity pairing states, after they had been consistently dismissed for a long time [209–211].

This indicates the theoretical literature which has found *p*-wave pairing is obviously missing an important ingredient. In the following we propose that purely local interactions can give rise to a pairing instability in the E_g channel, but only once we consider a full three-dimensional model for the normal state. The resulting pairing state is an *s*-wave orbital-antisymmetric spin-triplet pairing state, which appears as a pseudospin-singlet chiral *d*-wave state at the Fermi surface. This state can be stabilised over other irreps by the inclusion of small symmetry-allowed momentum-dependent spin-orbit couplings which correspond to spin-dependent hopping between layers. The smallness of these hopping integrals leaves the two-dimensional appearance of the Fermi surface intact. The state that we propose is consistent with the evidence of a two-component order parameter [186, 188] and time-reversal symmetry breaking [51, 52, 185]. As already pointed out, the stability of our proposed state depends sensitively on the details of the normal-state band structure, which we now consider in detail.

5.2   Band structure

The Fermi surface of Sr_2RuO_4 consists of three bands which are derived from the T_{2g} manifold of the 4*d* orbitals of Ru. Taking *z* along the *c*-axis, the relevant orbitals are the xy, xz, and yz orbitals. The "two-dimensional" majority xy-band disperses strongly in the *ab* plane, whereas the "one-dimensional" xz- and yz-bands only disperse weakly along k_x and k_y, respectively. Hybridization and spin-orbit coupling leads to the formation of three non-intersecting cylindrical Fermi surface sheets, one hole-like and two electron-like [83, 160].

Spin-orbit coupling does not only lift the band-crossing degeneracies but also leads to a mixing of the orbital character of the xy band with the $\{xz, yz\}$ bands [212]. The expectation value $\langle \boldsymbol{l} \cdot \boldsymbol{s} \rangle$ with $\boldsymbol{l}$ and $\boldsymbol{s}$ being the orbital and spin angular momentum operators, is non-zero over large regions of the three sheets of the Fermi surface, indicating strong momentum-dependent spin-orbital entanglement. This means that the eigenstates cannot be factorized into independent spin and orbital parts and a classification of the Cooper pairs in terms of pure spin singlets and triplets breaks down [160]. Therefore it can be assumed that the superconductivity is not limited to a single band and interband effects must be taken into account as well.

5.2.1   Three orbital system in D_{4h}

Sr_2RuO_4 crystallizes in the tetragonal I4/mmm space group and therefore the crystal point group around the Ru atoms is D_{4h}. This is reminiscent of the configuration of the Cu atoms in the cuprates materials class which
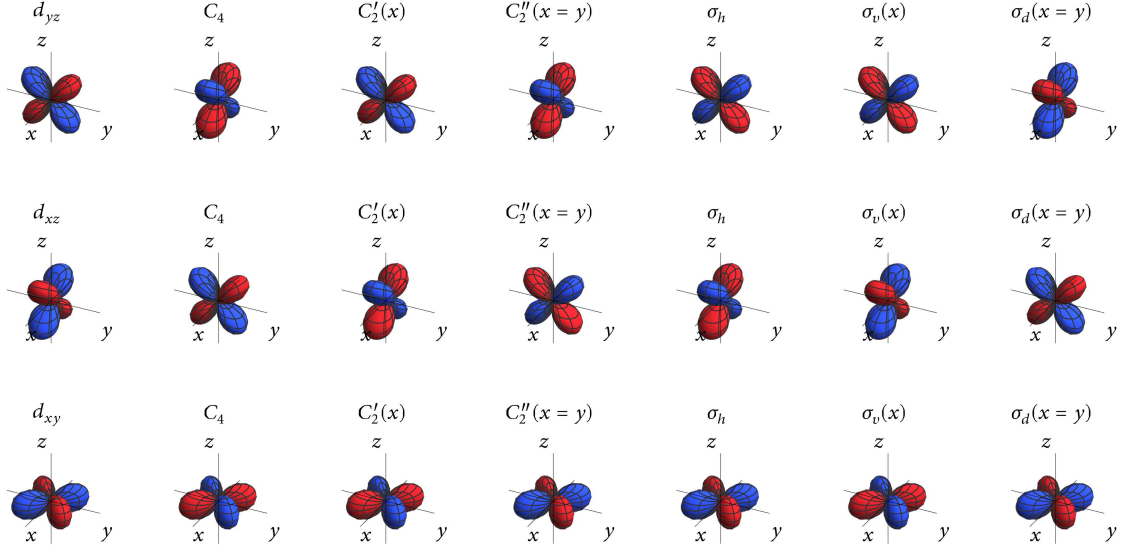
■ *Figure 5.3.* The T_{2g} manifold of the d orbitals. The first column shows the orbitals in their unmodified form, the other columns after application of the transformation as annotated.

are know to be high-temperature superconductors. As can be seen from the sketch of the crystal structure of Sr_2RuO_4 in Fig. 5.1, the crystal structure is almost identical to the one of the cuprates.

As mentioned before the bands are derived from the T_{2g} manifold of the $4d$ electrons of Ru. Therefore the basis set is given by three orbitals d_{yz}, d_{xz}, and d_{xy} (we will assume this order throughout). The effect of the point group symmetry operations on the orbitals can be derived by considering the transformation properties of the angular momentum, which is shown in Appendix B.1. Here we summarize the matrix form of these operations

$$C_4 : \begin{pmatrix} d_{yz} \to -d_{xz} \\ d_{xz} \to d_{yz} \\ d_{xy} \to -d_{xy} \end{pmatrix} \equiv \begin{pmatrix} 0 & 1 & 0 \\ -1 & 0 & 0 \\ 0 & 0 & -1 \end{pmatrix}, \qquad \sigma_h : \begin{pmatrix} d_{yz} \to -d_{yz} \\ d_{xz} \to -d_{xz} \\ d_{xy} \to d_{xy} \end{pmatrix} \equiv \begin{pmatrix} -1 & 0 & 0 \\ 0 & -1 & 0 \\ 0 & 0 & 1 \end{pmatrix},$$

$$C_2'(x) : \begin{pmatrix} d_{yz} \to d_{yz} \\ d_{xz} \to -d_{xz} \\ d_{xy} \to -d_{xy} \end{pmatrix} \equiv \begin{pmatrix} 1 & 0 & 0 \\ 0 & -1 & 0 \\ 0 & 0 & -1 \end{pmatrix}, \qquad \sigma_v(x) : \begin{pmatrix} d_{yz} \to -d_{yz} \\ d_{xz} \to d_{xz} \\ d_{xy} \to -d_{xy} \end{pmatrix} \equiv \begin{pmatrix} -1 & 0 & 0 \\ 0 & 1 & 0 \\ 0 & 0 & -1 \end{pmatrix},$$

$$C_2''(x = y) : \begin{pmatrix} d_{yz} \to -d_{xz} \\ d_{xz} \to -d_{yz} \\ d_{xy} \to d_{xy} \end{pmatrix} \equiv \begin{pmatrix} 0 & -1 & 0 \\ -1 & 0 & 0 \\ 0 & 0 & 1 \end{pmatrix}, \quad \sigma_d(x = y) : \begin{pmatrix} d_{yz} \to d_{xz} \\ d_{xz} \to d_{yz} \\ d_{xy} \to d_{xy} \end{pmatrix} \equiv \begin{pmatrix} 0 & 1 & 0 \\ 1 & 0 & 0 \\ 0 & 0 & 1 \end{pmatrix},$$

$$I : \text{trivial} \equiv \begin{pmatrix} 1 & 0 & 0 \\ 0 & 1 & 0 \\ 0 & 0 & 1 \end{pmatrix}.$$

An illustration of these operations is shown in Fig. 5.3. The transformation properties of the spin have already been listed Section 2.2.1.

The orbital degree of freedom will be encoded in 3×3 matrices. The Gell-Mann matrices form a basis of SU(3) and are therefore a basis for all 3×3 matrices. Using the forms of the symmetry operations above, we can determine the transformation properties of the Gell-Mann matrices. The numbering of the Gell-Mann matrices is not unique and differs throughout the literature. Here we choose the following order

$$\lambda_1 = \begin{pmatrix} 0 & 1 & 0 \\ 1 & 0 & 0 \\ 0 & 0 & 0 \end{pmatrix}, \quad \lambda_2 = \begin{pmatrix} 0 & 0 & 1 \\ 0 & 0 & 0 \\ 1 & 0 & 0 \end{pmatrix}, \quad \lambda_3 = \begin{pmatrix} 0 & 0 & 0 \\ 0 & 0 & 1 \\ 0 & 1 & 0 \end{pmatrix}, \quad \lambda_4 = \begin{pmatrix} 0 & -i & 0 \\ i & 0 & 0 \\ 0 & 0 & 0 \end{pmatrix},$$

$$\lambda_5 = \begin{pmatrix} 0 & 0 & -i \\ 0 & 0 & 0 \\ i & 0 & 0 \end{pmatrix}, \quad \lambda_6 = \begin{pmatrix} 0 & 0 & 0 \\ 0 & 0 & -i \\ 0 & i & 0 \end{pmatrix}, \quad \lambda_7 = \begin{pmatrix} 1 & 0 & 0 \\ 0 & -1 & 0 \\ 0 & 0 & 0 \end{pmatrix}, \quad \lambda_8 = \frac{1}{\sqrt{3}} \begin{pmatrix} 1 & 0 & 0 \\ 0 & 1 & 0 \\ 0 & 0 & -2 \end{pmatrix}. \tag{5.8}$$

These matrices are Hermitian and trace-orthonormal, i.e.

$$\mathrm{Tr}[\lambda_i \lambda_j] = 2\delta_{ij}. \tag{5.9}$$

Additionally we define λ_0 to be proportional to the unit matrix but with the correct normalisation

$$\lambda_0 = \sqrt{\frac{2}{3}} \begin{pmatrix} 1 & 0 & 0 \\ 0 & 1 & 0 \\ 0 & 0 & 1 \end{pmatrix}. \tag{5.10}$$

We proceed to examine the transformation properties of the Gell-Mann matrices under the operations of the point group that we have derived before. We list the character of the matrices under these transformations in the following table

	C_4	C_2'	C_2''	σ_h	σ_v	σ_d
λ_0	+1	+1	+1	+1	+1	+1
λ_1	−1	−1	+1	+1	−1	+1
λ_2	0	0	0	−1	0	0
λ_3	0	0	0	−1	0	0
λ_4	+1	−1	−1	+1	−1	−1
λ_5	0	0	0	−1	0	0
λ_6	0	0	0	−1	0	0
λ_7	−1	+1	−1	+1	+1	−1
λ_8	+1	+1	+1	+1	+1	+1

$$(5.11)$$

Comparing this to the character table of the D_{4h} in Tab. A.1 yields the following classification

$$\lambda_0, \lambda_8 \in A_{1g}, \quad \lambda_1 \in B_{2g}, \quad \lambda_2, \lambda_3 \in E_g, \quad \lambda_4 \in A_{2g}, \quad \lambda_5, \lambda_6 \in E_g, \quad \lambda_7 \in B_{1g}. \tag{5.12}$$

For the Pauli matrices of the spin part the classification is already listed in (2.31).

The normal-state of Sr_2RuO_4 shows no signs of time-reversal symmetry breaking and the crystal is centrosymmetric. Therefore the Hamiltonian may only contain matrices that are even under time-reversal and inversion. The time-reversal operator is defined as $T = i\sigma_2 \mathcal{K}$ where $\mathcal{K}$ is the antiunitary complex conjugation operator and $U_T = i\sigma_2$ is the unitary part. The following table lists the Kronecker products of Gell-Mann and

Pauli matrices that are even under time-reversal. The allowed terms are enclosed in brackets

$$U_T^\dagger (\lambda_\nu \sigma_\mu)^* U_T = \pm \lambda_\nu \sigma_\mu \tag{5.13}$$

	σ_0	σ_1	σ_2	σ_3
λ_0	+1	−1	−1	−1
λ_1	+1	−1	−1	−1
λ_2	+1	−1	−1	−1
λ_3	+1	−1	−1	−1
λ_4	−1	+1	+1	+1
λ_5	−1	+1	+1	+1
λ_6	−1	+1	+1	+1
λ_7	+1	−1	−1	−1
λ_8	+1	−1	−1	−1

$$\tag{5.14}$$

Now we can go ahead and classify the operators according to their point group symmetry using the product table for D_{4h} in Tab. A.3. Again, terms allowed by time-reversal symmetry are enclosed in brackets

	σ_0	σ_1	σ_2	σ_3
λ_0	A_{1g}	E_g	E_g	A_{2g}
λ_1	B_{2g}	E_g	E_g	B_{1g}
λ_2	E_g	$A_{1g} \oplus [A_{2g}] \oplus B_{1g} \oplus B_{2g}$	$A_{1g} \oplus [A_{2g}] \oplus B_{1g} \oplus B_{2g}$	E_g
λ_3	E_g	$A_{1g} \oplus [A_{2g}] \oplus B_{1g} \oplus B_{2g}$	$A_{1g} \oplus [A_{2g}] \oplus B_{1g} \oplus B_{2g}$	E_g
λ_4	A_{2g}	E_g	E_g	A_{1g}
λ_5	E_g	$A_{1g} \oplus [A_{2g}] \oplus B_{1g} \oplus B_{2g}$	$A_{1g} \oplus [A_{2g}] \oplus B_{1g} \oplus B_{2g}$	E_g
λ_6	E_g	$A_{1g} \oplus [A_{2g}] \oplus B_{1g} \oplus B_{2g}$	$A_{1g} \oplus [A_{2g}] \oplus B_{1g} \oplus B_{2g}$	E_g
λ_7	B_{1g}	E_g	E_g	B_{2g}
λ_8	A_{1g}	E_g	E_g	A_{2g}

$$\tag{5.15}$$

There are four operators which have the label $A_{1g} \oplus [A_{2g}] \oplus B_{1g} \oplus B_{2g}$, i.e. the direct product will be a direct sum involving terms in each of these irreducible representations. That means we have to combine the individual products such that each of these representations is exhausted. We find

$$\lambda_5 \sigma_1 - \lambda_6 \sigma_2 \in B_{2g}, \tag{5.16}$$

$$\lambda_5 \sigma_1 + \lambda_6 \sigma_2 \in A_{2g}, \tag{5.17}$$

$$\lambda_5 \sigma_2 - \lambda_6 \sigma_1 \in A_{1g}, \tag{5.18}$$

$$\lambda_5 \sigma_2 + \lambda_6 \sigma_1 \in B_{1g}. \tag{5.19}$$

We can now summarize the results of this classification in the following table which lists all the allowed terms together with their character under the point group transformations, their irreducible representation and what

polynomial they transform like

(a,b)	C_4	$C_2(x)$	$C_2(x=y)$	σ_h	$\sigma_v(x)$	$\sigma_d(x=y)$	irrep	transforms
$(0,0)$	$+1$	$+1$	$+1$	$+1$	$+1$	$+1$	A_{1g}	1
$(4,3)$	$+1$	$+1$	$+1$	$+1$	$+1$	$+1$	A_{1g}	1
$(8,0)$	$+1$	$+1$	$+1$	$+1$	$+1$	$+1$	A_{1g}	1
$(5,2)-(6,1)$	$+1$	$+1$	$+1$	$+1$	$+1$	$+1$	A_{1g}	1
$(5,1)+(6,2)$	$+1$	-1	-1	$+1$	-1	-1	A_{2g}	$xy(x^2-y^2)$
$(7,0)$	-1	$+1$	-1	$+1$	$+1$	-1	B_{1g}	x^2-y^2
$(5,2)+(6,1)$	-1	$+1$	-1	$+1$	$+1$	-1	B_{1g}	x^2-y^2
$(1,0)$	-1	-1	$+1$	$+1$	-1	$+1$	B_{2g}	xy
$(5,1)-(6,2)$	-1	-1	$+1$	$+1$	-1	$+1$	B_{2g}	xy
$(2,0)$	$+(3,0)$	-1	$-(3,0)$	-1	$+1$	$+(3,0)$	E_g	xz
$(3,0)$	$-(2,0)$	$+1$	$-(2,0)$	-1	-1	$+(2,0)$	E_g	yz
$(4,1)$	$+(4,2)$	-1	$-(4,2)$	-1	$+1$	$+(4,2)$	E_g	xz
$(4,2)$	$-(4,1)$	$+1$	$-(4,1)$	-1	-1	$+(4,1)$	E_g	yz
$(5,3)$	$+(6,3)$	$+1$	$+(6,3)$	-1	-1	$-(6,3)$	E_g	yz
$(6,3)$	$-(5,3)$	-1	$+(5,3)$	-1	$+1$	$-(5,3)$	E_g	$-xz$

$$(5.20)$$

This is in agreement with [213].

5.2.2 Microscopic model for the normal-state Hamiltonian

To construct the most general three-dimensional tight-binding Hamiltonian we include the T_{2g} manifold of the Ru d_{yz}, d_{xz}, and d_{xy} orbitals (we will assume this order throughout). Writing the Hamiltonian in terms of Nambu spinors $\Psi_k = (c_{k,2,\uparrow}, c_{k,2,\uparrow}, c_{k,1,\uparrow}, c_{k,1,\downarrow}, c_{k,3,\uparrow}, c_{k,3,\downarrow})$ where we enumerate the orbitals with $1 = d_{xz}$, $2 = d_{yz}$, and $3 = d_{xy}$

$$H_0 = \sum_k \Phi_k^\dagger H_0(k)\Phi_k \tag{5.21}$$

with the BdG-Hamiltonian $H_0(k)$. The BdG-Hamiltonian can be decomposed in terms of Gell-Mann and Pauli matrices as

$$H_0(k) = \sum_{a,b} h_{ab}(k)\lambda_a \otimes \sigma_b. \tag{5.22}$$

Previously we have worked out which terms are allowed for a and b to satisfy time-reversal and inversion symmetry. The allowed combinations are listed in (5.20). The corresponding functional forms of the coefficients h_{ab} are listed in Tab. 5.1. The on-site spin-orbit coupling in the A_{1g} representation is an atomic effect, whereas the momentum-dependent spin-orbit coupling is an effect of the crystal system.

The parameter for the on-site atomic spin-orbit coupling may have different values for the spin in the plane ($\eta_\perp$) and the spin out of plane (η_z). The intra-orbital hoppings $\xi_{11,22,33}(k)$ have been truncated after next-next-nearest neighbours in plane and next-nearest neighbours out of plane. The inter-orbtial hopping between d_{yz} and d_{xz} is parameterised by $\lambda(k)$ and is kept up to next-nearest neighbours in plane and nearest neighbour

(a, b)	Irrep	Type	Explicit form of $h_{ab}(\boldsymbol{k})$
$(0, 0)$	A_{1g}	intra-orb. hopping	$\frac{1}{\sqrt{6}}\left[\xi_{11}(\boldsymbol{k}) + \xi_{22}(\boldsymbol{k}) + \xi_{33}(\boldsymbol{k})\right]$
$(8, 0)$	A_{1g}	intra-orb. hopping	$\frac{1}{2\sqrt{3}}\left[\xi_{11}(\boldsymbol{k}) + \xi_{22}(\boldsymbol{k}) - 2\xi_{33}(\boldsymbol{k})\right]$
$(4, 3)$	A_{1g}	atomic SOC	$-\eta_z$
$(5, 2) - (6, 1)$	A_{1g}	atomic-SOC	$\eta_\perp$
$(5, 1) + (6, 2)$	A_{2g}	$\boldsymbol{k}$-SOC	neglected
$(7, 0)$	B_{1g}	intra-orb. hopping	$\frac{1}{2}\left[\xi_{22}(\boldsymbol{k}) - \xi_{11}(\boldsymbol{k})\right]$
$(5, 2) + (6, 1)$	B_{1g}	$\boldsymbol{k}$-SOC	$2t_{5261}^{\mathrm{SOC}}(\cos k_x a - \cos k_y a)$
$(1, 0)$	B_{2g}	inter-orb. hopping	$\lambda(\boldsymbol{k})$
$(5, 1) - (6, 2)$	B_{2g}	$\boldsymbol{k}$-SOC	$4t_{5162}^{\mathrm{SOC}} \sin k_x a \sin k_y a$
$\{(3, 0), (2, 0)\}$	E_g	inter-orb. hopping	$8t_z^{13} \sin(k_z c/2)\{\cos(k_x a/2)\sin(k_y a/2), \sin(k_x a/2)\cos(k_y a/2)\}$
$\{(4, 2), (4, 1)\}$	E_g	$\boldsymbol{k}$-SOC	$8t_{12z}^{\mathrm{SOC}} \sin(k_z c/2)\{\cos(k_x a/2)\sin(k_y a/2), \sin(k_x a/2)\cos(k_y a/2)\}$
$\{(5, 3), (6, 3)\}$	E_g	$\boldsymbol{k}$-SOC	$8t_{56z}^{\mathrm{SOC}} \sin(k_z c/2)\{\cos(k_x a/2)\sin(k_y a/2), -\sin(k_x a/2)\cos(k_y a/2)\}$

■ *Table 5.1.* List of all symmetry-allowed coefficients $h_{ab}(\boldsymbol{k})$ in the normal-state Hamiltonian $H_0(\boldsymbol{k})$ in (5.22) according to (5.20). For every matrix, denoted by the indices (a, b) the corresponding basis function $h_{ab}(\boldsymbol{k})$ must belong the the same irrep of D_{4h}. The table also lists the physical process associated with each term. For the two-dimensional irreps, the first term always transforms as yz, the second one as xz. In our calculations $a = c = 1$.

out of plane. The inter-orbital hopping between d_{yz}/d_{xz} and d_{xy} emerges from the two-dimensional E_g irrep. Truncating this at a reasonable distance only leaves us with an out-of-plane nearest neighbour hopping. This truncation is also the reason why the term with A_{2g} is neglected, since it only appears at next-next-next-nearest neighbour hopping.

In the table Tab. 5.1, we have omitted the functional form of $\xi_{11,22,33}(\boldsymbol{k})$ and $\lambda(\boldsymbol{k})$, because they are too long. These spin-independent components are consistent with models for the iron pnictides which also realize the D_{4h} point group [108]. The omitted terms are given by

$$
\begin{aligned}
\xi_{11,22}(\boldsymbol{k}) = {} & 2t_{x,y}^{11} \cos k_x a + 2t_{y,x}^{11} \cos k_y a \\
& + 8t_z^{11} \cos(k_x a/2)\cos(k_y a/2)\cos(k_z c/2) \\
& + 4t_{xy}^{11} \cos k_x a \cos k_y a + 2t_{xx,yy}^{11} \cos 2k_x a + 2t_{yy,xx}^{11} \cos 2k_y a \\
& + 4t_{xxy,xyy}^{11} \cos 2k_x a \cos k_y a + 4t_{xyy,xxy}^{11} \cos 2k_y a \cos k_x a \\
& + 2t_{zz}^{11}(\cos k_z c - 1) - \mu,
\end{aligned}
\tag{5.23}
$$

$$
\begin{aligned}
\xi_{33}(\boldsymbol{k}) = {} & 2t_x^{33}(\cos k_x a + \cos k_y a) \\
& + 8t_z^{33} \cos(k_x a/2)\cos(k_y a/2)\cos(k_z c/2) \\
& + 4t_{xy}^{33} \cos k_x a \cos k_y a + 2t_{xx}^{33}(\cos 2k_x a + \cos 2k_y a) \\
& + 4t_{xxy}^{33}(\cos 2k_x a \cos k_y a + \cos 2k_y a \cos k_x a) \\
& + 2t_{zz}^{33}(\cos k_z c - 1) - \mu_1,
\end{aligned}
\tag{5.24}
$$

$$
\begin{aligned}
\lambda(\boldsymbol{k}) = {} & 4t_z^{12} \sin(k_x a/2)\sin(k_y a/2)\cos(k_z c/2) \\
& - 4t_{xy}^{12} \sin k_x a \sin k_y a \\
& - 4t_{xxy}^{12}(\sin 2k_x a \sin k_y a + \sin 2k_y a \sin k_x a).
\end{aligned}
\tag{5.25}
$$

At this point it is worth noting that Tab. 5.1 contains terms which are in accordance with existing literature [214–

216], but others that have so far not been considered. These additional terms are all associated with some kind of momentum-dependent spin-orbit coupling. We included them at the lowest order at which they appear with the exception of the A_{2g} term, which we neglect because the lowest order at which it appears is g-wave, which corresponds to a next-next-next-nearest neighbour hopping, which is assumed to be vanishingly small. This concludes the construction of the normal-state Hamiltonian and we now have a model with 26 free tight-binding parameters.

5.2.3 Determining the tight-binding parameters

Now it is time to give meaningful values to the 26 parameters. To make our model reproduce a faithful description of the Fermi surface of Sr_2RuO_4, we turn to a previous density functional theory (DFT) study by Veenstra *et al.* [160]. In this work the band structure of Sr_2RuO_4 was obtained using *ab initio* DFT calculations. Then, the DFT band structure was fitted with a d-p model including all five d orbitals of the Ru atom, and the three p orbitals of the four inequivalent O atoms, giving 17 orbitals in total. Even though, in principle we already have a tight-binding description using this model, it is not efficient to describe superconductivity due to the large number of bands, most of which are far away from the Fermi surface. It is also not possible to extract just the bands at the Fermi surface by projection because in this model the hopping between Ru atoms is via the O atoms. Therefore we choose a different approach, where we take the tight-binding model derived from DFT by Veenstra *et al.* [160] (which we henceforth refer to as the "DFT model") and fit our microscopic three-orbital model that we derived in the previous section to it using the 26 free parameters.

We are going to focus on the electronic states near the Fermi surface, because there will be deviations away from the Fermi surface due to strong admixture with the oxygen orbitals, especially along the Γ-Z line. This is not an issue because for superconductivity these areas of the band structure do not play a role since they are far away from the Fermi surface. The first and foremost priority of the fit is therefore to faithfully reproduce the Fermi surface. In the DFT model that Fermi surface has some admixture of the oxygen p orbital, but for simplicity we assume that the Fermi surface is dominated entirely by the T_{2g} manifold of the Ru d orbitals.

To this end we extract the Fermi momenta $\tilde{k}_F$ of the DFT model as reference points. Then we evaluate our Hamiltonian (which we henceforth refer to as the "fit") at these momenta and extract several quantities that we want to have reproduced, which are the d_{xy} orbital content, the spin-orbital entanglement, and the in-plane Fermi velocity. These are easily accessible from both the DFT model and our fit. The free parameters are then varied according to a least-squares-like algorithm BOBYQA [217] to optimize the deviation of all of these quantities simultaneously between the fit and the DFT model to a minimum. For this process we define the following measure, where we denote quantities of the DFT model with tilde and quantities of the fit without

$$S = \sum_{n=\alpha,\beta,\gamma,\,\tilde{k}_F} \left[(\epsilon^n(\tilde{k}_F))^2 + (\tilde{d}_{xy}^n(\tilde{k}_F) - d_{xy}^n(\tilde{k}_F))^2 + (\tilde{p}_{SOC}^n(\tilde{k}_F) - p_{SOC}^n(\tilde{k}_F))^2 + (\tilde{v}_{\parallel}^n(\tilde{k}_F) - v_{\parallel}^n(\tilde{k}_F))^2 \right], \quad (5.26)$$

where the sum runs over the Fermi momenta $\tilde{k}_F$ of the DFT model on the three sheets of the Fermi surface which are enumerated by $n = \alpha, \beta, \gamma$. Here we have denoted the energy eigenvalues by $\epsilon^n(k)$, the d_{xy} orbital content by $d_{xy}^n(k)$, the spin-orbital entanglement by $p_{SOC}^n(k)$, and the in-plane Fermi velocity by $\tilde{v}_{\parallel}^n(k)$. The d_{xy}-orbital content is determined by the corresponding components of the eigenvectors of the tight-binding Hamiltonian (5.22) which we denote by V

$$d_{xy}^n(k) = \frac{1}{2} \left(|V_{d_{xy},\uparrow}^{n,\uparrow}(k)|^2 + |V_{d_{xy},\downarrow}^{n,\uparrow}(k)|^2 + |V_{d_{xy},\uparrow}^{n,\downarrow}(k)|^2 + |V_{d_{xy},\downarrow}^{n,\downarrow}(k)|^2 \right). \quad (5.27)$$
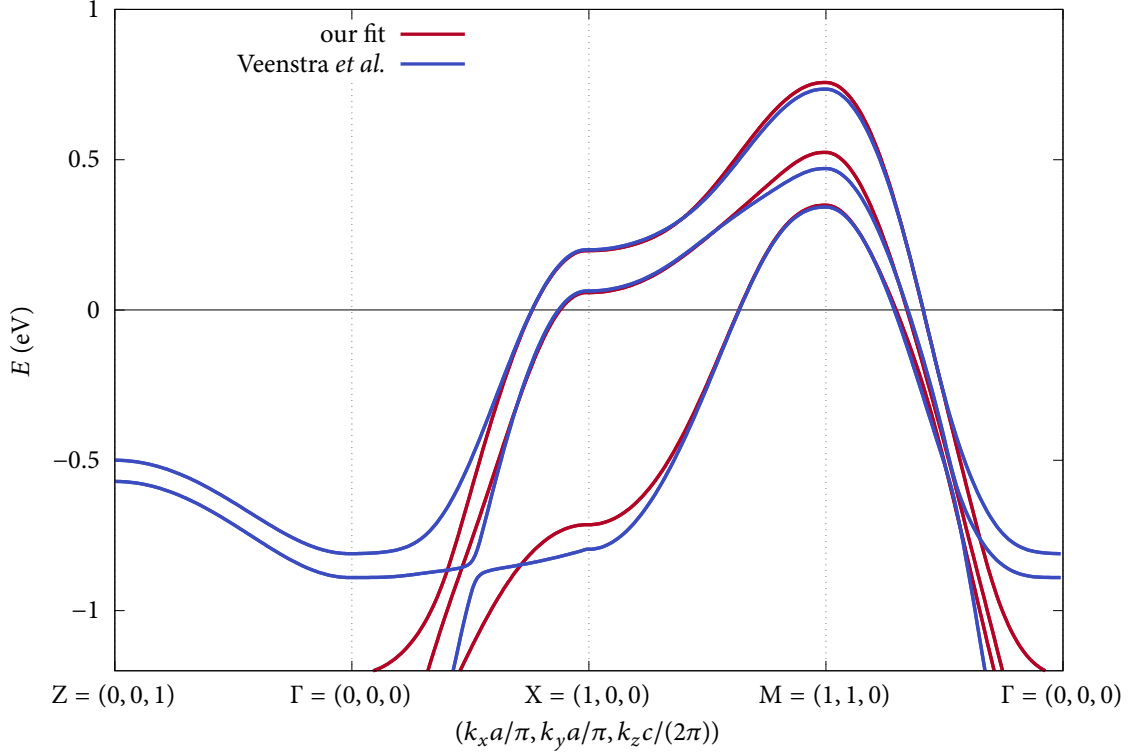
■ *Figure 5.4.* The blue lines are the bands crossing the Fermi surface, extracted the *ab-initio* DFT calculations in [160]. The red lines correspond to the model fitted to the DFT bandstructure. Note the the very nice agreement between our fit and the LDA band structure at low energies, in particular the in-plane velocity.

The spin-orbital entanglement is determined from the expectation value of the atomic spin-orbit coupling Hamiltonian $H_{\text{SOC}} = \lambda_5 \sigma_2 - \lambda_6 \sigma_1 - \lambda_4 \sigma_3$ and represents the expectation value $\langle \boldsymbol{l} \cdot \boldsymbol{s} \rangle$. A non-zero value indicates that the wavefunction cannot be factorized into independent spin and orbital angular momentum parts [160]. We compute this by

$$p_{\text{SOC}}^n(\boldsymbol{k}) = 1 + \left[\frac{1}{2} \operatorname{Re}\left(V^{n,\uparrow T}(\boldsymbol{k}) H_{\text{SOC}} V^{n,\uparrow}(\boldsymbol{k}) + V^{n,\downarrow T}(\boldsymbol{k}) H_{\text{SOC}} V^{n,\downarrow}(\boldsymbol{k}) \right) \right]^{1/3}. \tag{5.28}$$

For the in-plane Fermi velocity we use a simple two-point central finite differences stencil where $\varepsilon_{x,y}$ are small

$$v_{\parallel}^n(\boldsymbol{k}) = \sqrt{ \left| \frac{\epsilon^n(\boldsymbol{k} - \varepsilon_x) - \epsilon^n(\boldsymbol{k} + \varepsilon_x)}{2\varepsilon_x} \right|^2 + \left| \frac{\epsilon^n(\boldsymbol{k} - \varepsilon_y) - \epsilon^n(\boldsymbol{k} + \varepsilon_y)}{2\varepsilon_y} \right|^2 }. \tag{5.29}$$

In Fig. 5.4 we show the band structure of the DFT model and our fit along a high-symmetry line in the $k_z = 0$ plane. In Fig. 5.5 we show the Fermi surface in the *ab* plane at $k_z = 0$ and the value of the observables as a function of the polar angle for both the DFT model and our fit. The agreement of the position, orbital content, and spin polarisation is excellent and more or less indistinguishable from the DFT model. There is a slight deviation in the in-plane Fermi velocity which is likely due to discretisation errors from the simple two-point central finite differences stencil.

However, the good agreement in plane is not sufficient for a faithful reproduction of the Fermi surface. It has been established by various experiments that the Fermi surface of Sr_2RuO_4 is cylindrical with only very
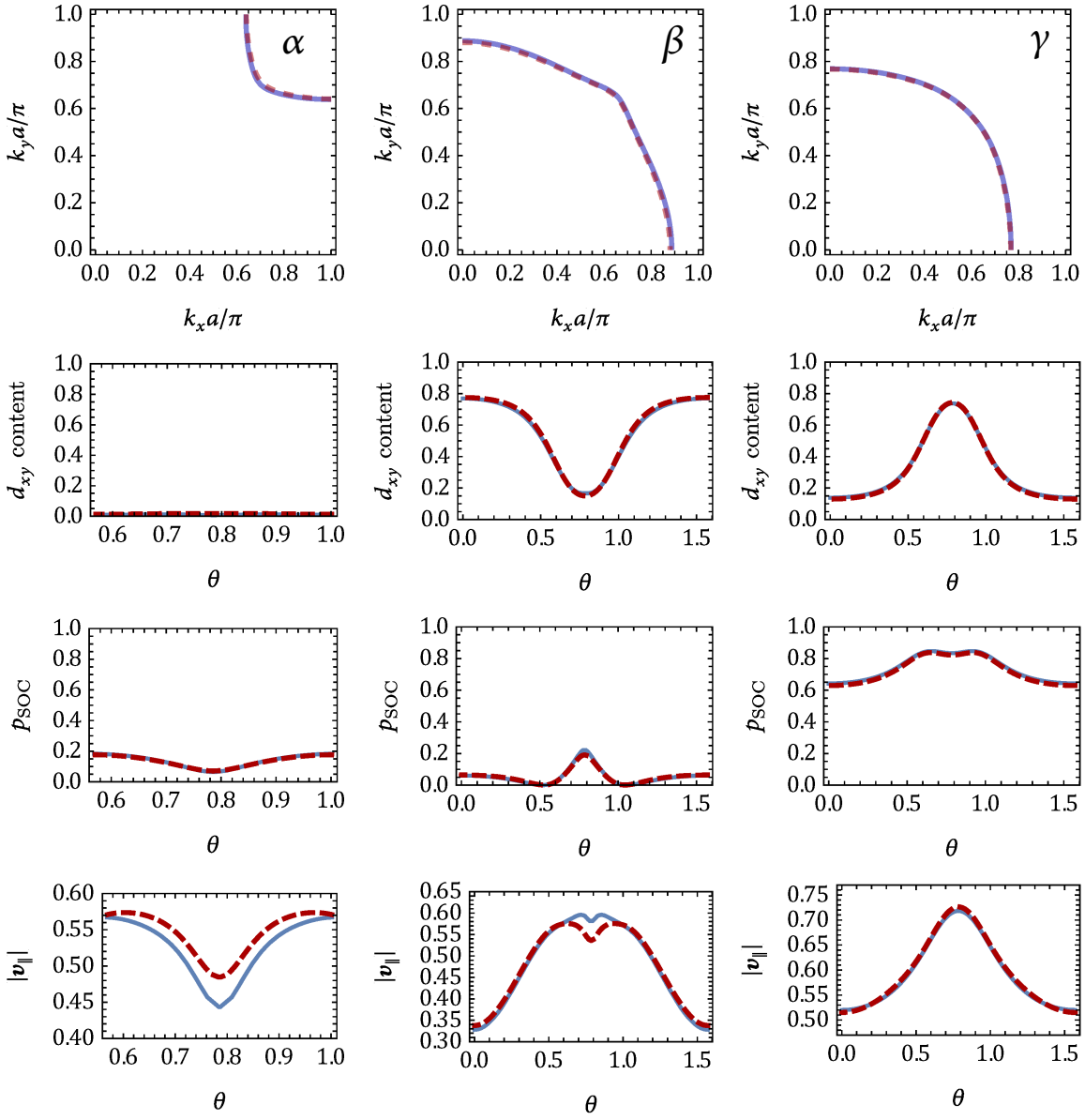
Figure 5.5. Performance of the fit in the $k_z = 0$ plane. The reference data from [160] is plotted with red dashed lines, out fit is shown with solid blue lines. The columns correspond to the α, γ, and β sheets of the Fermi surface, respectively. The first row shows the Fermi surface in the $k_z = 0$ plane. The second row shows the d_{xy} orbital content as a function of the angle around that cut of the Fermi surface. The third row shows the spin polarisation around the cut. The last row shows the Fermi velocity around the cut.
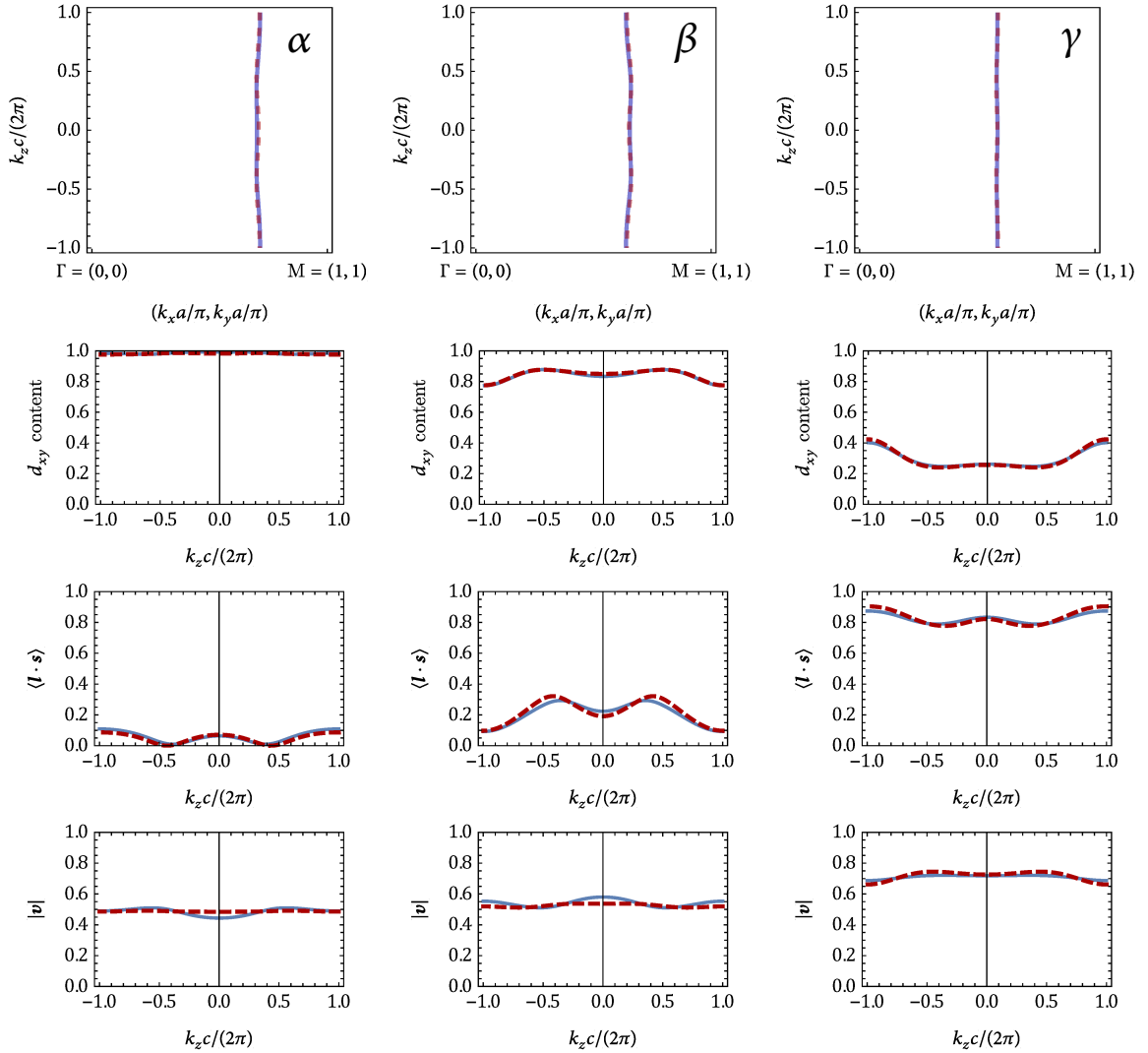
Figure 5.6. Performance of the fit in the k_z direction along the Γ-M line. The reference data from [160] is plotted with red dashed lines, out fit is shown with solid blue lines. Panel (a) shows results for the band structure from Veenstra *et al.* [160], panel (b) for our fit. The columns correspond to the α, γ, and β sheets of the Fermi surface, respectively. The first row shows the Fermi surface along k_z in the Γ-M plane. The second row shows the d_{xy} orbital content in k_z direction along the Fermi surface. The last row shows the spin polarisation along the cut.

(a)

(b)
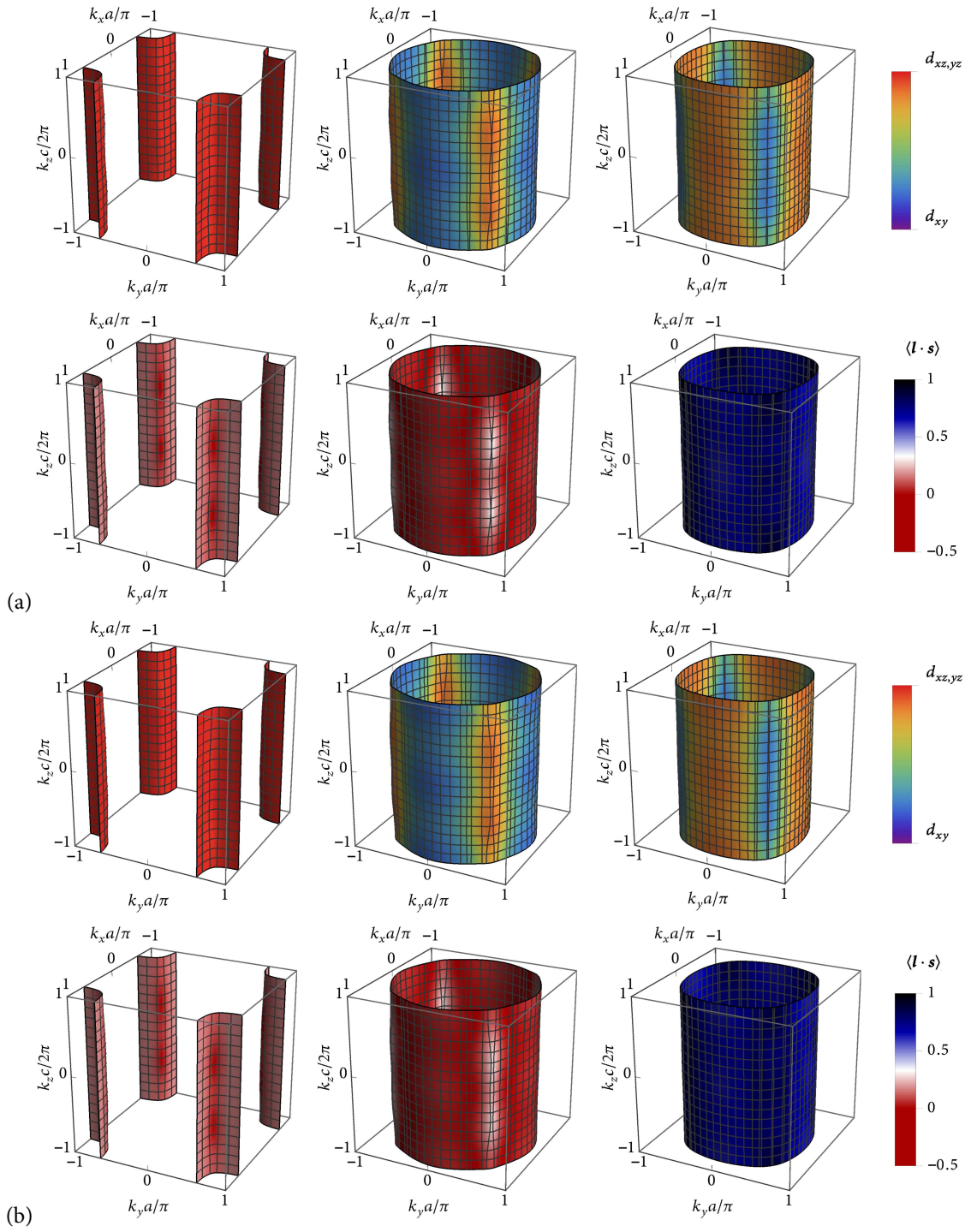
■ *Figure 5.7.* Panel (a) shows results for the band structure from Veenstra *et al.* [160], panel (b) for our fit. This just repeats the results from Fig. 5.5 and Fig. 5.6, but plotted over the 3D Fermi surface.

$t_x^{11} = -362.4$	$t_y^{11} = -134$	$t_x^{33} = -262.4$	$t_{xy}^{11} = -44.01$
$t_{xx}^{11} = -1.021$	$t_{yy}^{11} = -5.727$	$t_{xy}^{33} = -43.73$	$t_{xx}^{33} = 34.23$
$t_{xy}^{12} = 16.25$	$t_{xxy}^{11} = -13.93$	$t_{xyy}^{11} = -7.52$	$t_{xxy}^{33} = 8.069$
$t_{xxy}^{12} = 3.94$	$\eta = 57.39$	$\mu = 438.5$	$\mu_1 = 218.6$
$t_z^{11} = -0.0228$	$t_z^{33} = 1.811$	$t_z^{12} = 19.95$	$t_z^{14} = 8.304$
$t_{zz}^{11} = 2.522$	$t_{zz}^{33} = -3.159$	$t_{56z}^{\mathrm{SOC}} = -1.247$	$t_{12z}^{\mathrm{SOC}} = -3.576$
$t_{5162}^{\mathrm{SOC}} = -1.008$	$t_{5261}^{\mathrm{SOC}} = 0.3779$		

■ *Table 5.2.* Values of the fit parameters of the Hamiltonian (5.22) for a "best" fit where all contributions to the measure were taken into account with equal weight. All values are in meV.

slight corrugation along the k_z [158, 159, 161]. This is correctly captured by the DFT model and our fit also nicely agrees with this result. Note that although there is only a slight corrugation in the Fermi surface, there is a much stronger corrugation in the orbital/spin-orbit content. We again show the Fermi surface and the observables in Fig. 5.6, however this time all quantities are plotted as a function k_z and the Fermi surface is show along the Γ-M line.

Finally we summarize the results in Fig. 5.7 where we plot the full 3D Fermi surface, color coded with the orbital content and the spin polarisation. Visually there is very little difference between the DFT bandstructure and our fit. The fit parameters that were determined by BOBYQA are summarised in Tab. 5.2.

5.3 Atomic interactions

The pairing mechanism in unconventional superconductors is always a matter of dispute. Instead of trying to treat the pairing interaction from first principles or a perturbative approach, we here choose a phenomenological theory with a clear scope. Assume that the electron-electron interaction is described by a function $V(\boldsymbol{x} - \boldsymbol{x}')$ and the electron wavefunctions are described by localized Wannier functions $w_{\gamma,\sigma}(\boldsymbol{x})$ for an electron in orbital γ with spin σ as position $\boldsymbol{x}$. The Coulomb self-energy of the atomic orbitals is given by the overlap integral

$$U = \int w_{\gamma,\sigma}^*(\boldsymbol{x}) w_{\gamma,\sigma'}^*(\boldsymbol{x}) V(\boldsymbol{x} - \boldsymbol{x}') w_{\gamma,\sigma}(\boldsymbol{x}') w_{\gamma,\sigma'}(\boldsymbol{x}') \, d^3 x \, d^3 x'. \tag{5.30}$$

This is the dominant energy scale in any electronic system, because the overlap of electrons in the same orbital is always the largest and therefore other effects are usually neglected. However, it has been realised by Kanamori [218] that in d electron systems, orbital mixing plays a major role for the description of magnetism. This is because due to the orbital mixing, electron wavefunctions are generally a linear combination of Bloch wavefunctions. It is therefore impossible to assign a unique orbital the electronic wavefunction. The corresponding inter-orbital interaction can be divided into three distinct processes. In the case that the electrons remain in their respective orbital after scattering we identify the interaction with an inter-orbital Coulomb repulsion

$$U' = \int w_{\gamma,\sigma}^*(\boldsymbol{x}) w_{\gamma',\sigma'}^*(\boldsymbol{x}) V(\boldsymbol{x} - \boldsymbol{x}') w_{\gamma,\sigma}(\boldsymbol{x}') w_{\gamma',\sigma'}(\boldsymbol{x}') \, d^3 x \, d^3 x'. \tag{5.31}$$

The process of exchanging the electrons between orbitals is referred to as Hund's exchange interaction

$$J = \int w_{\gamma,\sigma}^*(\boldsymbol{x}) w_{\gamma',\sigma'}^*(\boldsymbol{x}) V(\boldsymbol{x} - \boldsymbol{x}') w_{\gamma',\sigma}(\boldsymbol{x}') w_{\gamma,\sigma'}(\boldsymbol{x}') \, d^3 x \, d^3 x'. \tag{5.32}$$

Finally, when electrons are exchanged between orbitals in pairs, we identify the Hund's pair hopping term

$$J' = \int w^*_{\gamma,\sigma}(\boldsymbol{x}) w^*_{\gamma,\sigma'}(\boldsymbol{x}) V(\boldsymbol{x}-\boldsymbol{x}') w_{\gamma',\sigma}(\boldsymbol{x}') w_{\gamma',\sigma'}(\boldsymbol{x}') \, d^3 x \, d^3 x'. \tag{5.33}$$

Since we restricted the set of d orbitals to the T_{2g} manifold, the orbitals can be transformed into each other by properly chosen canonical transformations, assuming the absence of crystal field splitting, which implies that $J = J'$.

Assuming that the interactions are strictly local $V(\boldsymbol{x}-\boldsymbol{x}') = V\delta(\boldsymbol{x}-\boldsymbol{x}')$ we write the interaction Hamiltonian in second quantization. The resulting form is often referred to as the Hubbard-Kanamori Hamiltonian [219, 220]

$$H_{\text{int}} = \frac{U}{2} \sum_{i,\gamma,\sigma\neq\sigma'} n_{i\gamma\sigma} n_{i\gamma\sigma'} + \frac{U'}{2} \sum_{\substack{i,\sigma,\sigma',\\ \gamma\neq\gamma'}} n_{i\gamma\sigma} n_{i\gamma'\sigma'} + \frac{J}{2} \sum_{\substack{i,\sigma,\sigma',\\ \gamma\neq\gamma'}} c^\dagger_{i\gamma\sigma} c^\dagger_{i\gamma'\sigma'} c_{i\gamma\sigma'} c_{i\gamma'\sigma} + \frac{J'}{2} \sum_{\substack{i,\sigma\neq\sigma',\\ \gamma\neq\gamma'}} c^\dagger_{i\gamma\sigma} c^\dagger_{i\gamma\sigma'} c_{i\gamma'\sigma'} c_{i\gamma'\sigma}. \tag{5.34}$$

The interaction Hamiltonian attains spherical symmetry if the interaction constants obey $U' = U - 2J$ [220]. Treating these interactions in full is beyond the scope of this work. Many theoretical treatments of Sr_2RuO_4 or the iron pnictides start from (5.34) and examine how they renormalize the spin- and charge-fluctuations, which are then used to construct an effective pairing interaction. We will treat them on the mean-field level instead. Therefore we will decouple the interaction in the Cooper channel. To this end the intra- and interorbital Columb interactions can be rearranged in terms of Cooper operators

$$\frac{U}{2} \sum_{i,\gamma,\sigma\neq\sigma'} n_{i\gamma\sigma} n_{i\gamma\sigma'} = \frac{U}{2} \sum_{i,\gamma,\sigma\neq\sigma'} c^\dagger_{i\gamma\sigma} c^\dagger_{i\gamma\sigma'} c_{i\gamma\sigma'} c_{i\gamma\sigma}, \tag{5.35}$$

$$\frac{U'}{2} \sum_{\substack{i,\sigma,\sigma',\\ \gamma\neq\gamma'}} n_{i\gamma\sigma} n_{i\gamma'\sigma'} = \frac{U'}{2} \sum_{\substack{i,\sigma,\sigma',\\ \gamma\neq\gamma'}} c^\dagger_{i\gamma\sigma} c^\dagger_{i\gamma'\sigma'} c_{i\gamma'\sigma'} c_{i\gamma\sigma}. \tag{5.36}$$

With that the interaction can be decomposed in terms of the Gell-Mann and Pauli matrices

$$
\begin{aligned}
H_{\text{int}} = &\frac{U}{2} \sum_i \sum_{1234} \left[\left(\frac{1}{2}\lambda_0\lambda_0 + \frac{1}{2}\lambda_7\lambda_7 + \frac{1}{2}\lambda_8\lambda_8 \right) \frac{1}{2}(\bar{\sigma}_0\bar{\sigma}^\dagger_0 + \bar{\sigma}_3\bar{\sigma}^\dagger_3) \right] c^\dagger_{i,1} c^\dagger_{i,2} c_{i,3} c_{i,4} \\
&+ \frac{U'}{2} \sum_i \sum_{1234} \left[\frac{1}{2}\left(\lambda_1\lambda_1 + \lambda_2\lambda_2 + \lambda_3\lambda_3 + \lambda_4\lambda_4 + \lambda_5\lambda_5 + \lambda_6\lambda_6 \right) \frac{1}{2}(\bar{\sigma}_0\bar{\sigma}^\dagger_0 + \bar{\sigma}_1\bar{\sigma}^\dagger_1 + \bar{\sigma}_2\bar{\sigma}^\dagger_2 + \bar{\sigma}_3\bar{\sigma}^\dagger_3) \right] c^\dagger_{i,1} c^\dagger_{i,2} c_{i,3} c_{i,4} \\
&+ \frac{J}{2} \sum_i \sum_{1234} \left[\frac{1}{2}\left(\lambda_1\lambda_1 + \lambda_2\lambda_2 + \lambda_3\lambda_3 - \lambda_4\lambda_4 - \lambda_5\lambda_5 - \lambda_6\lambda_6 \right) \frac{1}{2}(\bar{\sigma}_0\bar{\sigma}^\dagger_0 + \bar{\sigma}_1\bar{\sigma}^\dagger_1 + \bar{\sigma}_2\bar{\sigma}^\dagger_2 + \bar{\sigma}_3\bar{\sigma}^\dagger_3) \right] c^\dagger_{i,1} c^\dagger_{i,2} c_{i,3} c_{i,4} \\
&+ \frac{J'}{2} \sum_i \sum_{1234} \left[\left(\lambda_0\lambda_0 - \frac{1}{2}\lambda_7\lambda_7 - \frac{1}{2}\lambda_8\lambda_8 \right) \frac{1}{2}(\bar{\sigma}_0\bar{\sigma}^\dagger_0 + \bar{\sigma}_3\bar{\sigma}^\dagger_3) \right] c^\dagger_{i,1} c^\dagger_{i,2} c_{i,3} c_{i,4}.
\end{aligned}
\tag{5.37}
$$

where we use the abbreviation $\lambda_\nu\lambda_\nu\bar{\sigma}_\mu\bar{\sigma}^\dagger_\mu = \lambda_{\nu,12}\lambda_{\nu,34}\bar{\sigma}_{\mu,12}\bar{\sigma}^\dagger_{\mu,34}$ with $\bar{\sigma}_\mu = \sigma_\mu U_T = \sigma_\mu i\sigma_2$. The numbers are variables which enumerate the orbital and spin indices, similar to the notation found in [81].

Before can determine the energies of the Cooper we have to determine which ones are allowed by fermionic antisymmetry. We have established in (2.61) that if the unitary part of the time-reversal operator is antisymmetric, then time-reversal symmetry is equivalent to fermionic antisymmetry. This is also the case here, therefore the

allowed Cooper pairs are

$$\lambda_\nu \bar\sigma_\mu = -(\lambda_\nu \bar\sigma_\mu)^T \tag{5.38}$$

	σ_0	σ_1	σ_2	σ_3
λ_0	✓	×	×	×
λ_1	✓	×	×	×
λ_2	✓	×	×	×
λ_3	✓	×	×	×
λ_4	×	✓	✓	✓
λ_5	×	✓	✓	✓
λ_6	×	✓	✓	✓
λ_7	✓	×	×	×
λ_8	✓	×	×	×

$$\tag{5.39}$$

The symmetry of these terms has already been tabulated for the normal state in (5.20). From this we can directly read off the energies of the Cooper pairs

irrep	spin structure	energy	gap structure
A_{1g}	Singlet	$U + 2J'$	$\lambda_0 \bar\sigma_0$
		$U - J'$	$\lambda_8 \bar\sigma_0$
	Triplet	$U' - J$	$\lambda_4 \bar\sigma_3$
			$\lambda_5 \bar\sigma_2 - \lambda_6 \bar\sigma_1$
A_{2g}	Triplet	$U' - J$	$\lambda_5 \bar\sigma_1 + \lambda_6 \bar\sigma_2$
B_{1g}	Singlet	$U - J'$	$\lambda_7 \bar\sigma_0$
	Triplet	$U' - J$	$\lambda_5 \bar\sigma_2 + \lambda_6 \bar\sigma_1$
B_{2g}	Singlet	$U' + J$	$\lambda_1 \bar\sigma_0$
	Triplet	$U' - J$	$\lambda_5 \bar\sigma_1 - \lambda_6 \bar\sigma_2$
E_g	Singlet	$U' + J$	$\lambda_2 \bar\sigma_0$
			$\lambda_3 \bar\sigma_0$
	Triplet	$U' - J$	$\lambda_5 \bar\sigma_3$
			$\lambda_6 \bar\sigma_3$
	Triplet	$U' - J$	$\lambda_4 \bar\sigma_1$
			$\lambda_4 \bar\sigma_2$

$$\tag{5.40}$$

We started from an overall repulsive electronic interaction, but we find channels where the interaction can in principle become negative. These are the channels with interaction $U - J'$ and $U' - J$. The first case is extremely unlikely because the intra-orbital Coulomb interaction is the dominant energy scale in any electronic problem and will always outweigh the Hund's rule interaction, even if the interaction constants are renormalized.

In contrast, the second case is much more likely and therefore we argue that the system will develop a superconducting instability in the orbitally anisotropic pairing channels as soon as the renormalized Hund's rule interaction J exceed the inter-orbital Coulomb repulsion U' [118, 221–225]. Vafek and Chubukov [118]

pointed out that this results in an effective dimensionless coupling constant for pairing in the *s*-wave channel of $N_0(J - U')(\lambda/\mu)^2$, where N_0 is the density of states at the Fermi level, μ is the chemical potential, and λ is the magnitude of the atomic spin-orbit coupling. Such a renormalisation of J has been discussed in the literature in the context of the "Hund's metal" [220, 226–228]. Generally, in the limit of bare local interactions $U' > J$, but the ratio of J/U' depends on the overall energy scale and we assume that $J/U' > 1$ at low energies to facilitate pairing [118, 220–224, 226, 227, 229].

Together with the requirement of spherical symmetry we find the condition

$$U' - J < 0 \quad \text{and} \quad U' = U - 2J \implies \frac{J}{U} > \frac{1}{3}. \tag{5.41}$$

This scenario has been studied previously by Vafek and Chubukov [118] in a two-orbital system in D_{4h}. In this case the A_{1g} representation only contains two local Cooper pairs, one intra-orbital spin-singlet with interaction $U + J$ and another inter-orbital spin-triplet with interaction $U' - J$. In the presence of spin-orbit coupling a finite attractive interaction can gives rise to pairing in this channel. We refer to this state as the "Vafek-Chubukov state". A similar pairing scenario has been proposed for strontium titanate (SrTiO$_3$)/lanthanum aluminate (LaAlO$_3$) interfaces, where the low-energy states are described by the T_{2g} manifold [230].

In the present case of three orbitals, the Vafek-Chubukov state would correspond to the two A_{1g} orbital-antisymmetric spin-triplets with energy $U' - J$. However, the Vafek-Chubukov channel is allowed to mix with every other channel sharing the A_{1g} symmetry. The second singlet A_{1g} channel with energy $U - J$ might or might not become attractive in the presence of renormalized interactions, but the tendency goes more towards repulsive since U is by far the most dominant energy scale. The first singlet A_{1g} channel with energy $U + 2J$ on the other hand will always remain repulsive. Pairing due to local atomic interactions has been discussed before by Puetter and Kee [221] in a purely two-dimensional model of Sr$_2$RuO$_4$ where they find an A_{1g} state to be stable.

The situation is similar for the B_{1g}, B_{2g}, and E_g irreps, where a possibly attractive channel is allowed to mix with a possibly repulsive channel. The only irrep for which this is not the case is A_{2g}, however, as discussed earlier the normal-state Hamiltonian does not contain any term with A_{2g} symmetry, because the lowest order polynomial in this irrep is g-wave.

We propose that these local interactions give rise to a weak-coupling instability in the E_g channel. We are motivated by the fact that this pairing instability has been observed in dynamical mean-field theory studies, which predict that it appears in the strong-coupling limit which corresponds to instabilities at unreasonably high temperatures, i.e. in the case where the interactions are *not* renormalized [231], and also in the presence of strong charge fluctuations [232].

5.4 Projected gap

Before turning to the relative stability of the individual gap functions in the presence of a phenomenological attractive interaction, we can gain some intuition of which irreps might give rise to a stable gap by looking at their projection onto the Fermi surface. This will give us an indication of how large the gap is at the Fermi surface and since we are operating in the weak-coupling limit, a larger gap at the Fermi surface means that the corresponding gap function is more favourable for superconductivity.

To this end we project the pairing into the band basis at every point in momentum space. Let $V_{\mathbf{k}}$ denote the unitary matrix that diagonalises the normal-state Hamiltonian, i.e. the matrix whose columns are the

eigenvectors. The projected Hamiltonian then reads

$$\tilde{H}_{\boldsymbol{k}} \equiv \begin{pmatrix} \tilde{H}_{0,\boldsymbol{k}} & \tilde{\Delta} \\ \tilde{\Delta}^\dagger & -\tilde{H}_{0,-\boldsymbol{k}}^T \end{pmatrix} = \begin{pmatrix} V_{\boldsymbol{k}}^\dagger H_{0,\boldsymbol{k}} V_{\boldsymbol{k}} & V_{\boldsymbol{k}}^\dagger \Delta V_{\boldsymbol{k}}^* \\ V_{\boldsymbol{k}}^T \Delta^\dagger V_{\boldsymbol{k}} & -V_{\boldsymbol{k}}^T H_{0,-\boldsymbol{k}}^T V_{\boldsymbol{k}}^* \end{pmatrix}, \tag{5.42}$$

where we are interested in the upper right hand block

$$\tilde{\Delta} = V_{\boldsymbol{k}}^\dagger \Delta V_{\boldsymbol{k}}^* = \begin{pmatrix} \psi_{\boldsymbol{k},\alpha} i\sigma_2 & (\psi_{\boldsymbol{k},\alpha\beta} - i\boldsymbol{d}_{\boldsymbol{k},\alpha\beta} \cdot \boldsymbol{\sigma}) i\sigma_2 & (\psi_{\boldsymbol{k},\alpha\gamma} - i\boldsymbol{d}_{\boldsymbol{k},\alpha\gamma} \cdot \boldsymbol{\sigma}) i\sigma_2 \\ (\psi_{\boldsymbol{k},\alpha\beta} + i\boldsymbol{d}_{\boldsymbol{k},\alpha\beta} \cdot \boldsymbol{\sigma}) i\sigma_2 & \psi_{\boldsymbol{k},\beta} i\sigma_2 & (\psi_{\boldsymbol{k},\beta\gamma} - i\boldsymbol{d}_{\boldsymbol{k},\beta\gamma} \cdot \boldsymbol{\sigma}) i\sigma_2 \\ (\psi_{\boldsymbol{k},\alpha\gamma} + i\boldsymbol{d}_{\boldsymbol{k},\alpha\beta} \cdot \boldsymbol{\sigma}) i\sigma_2 & (\psi_{\boldsymbol{k},\beta\gamma} + i\boldsymbol{d}_{\boldsymbol{k},\alpha\gamma} \cdot \boldsymbol{\sigma}) i\sigma_2 & \psi_{\boldsymbol{k},\gamma} i\sigma_2 \end{pmatrix}, \tag{5.43}$$

with intraband pairing amplitudes $\psi_{\boldsymbol{k},a}$ in band a, as well as interband pairing amplitudes $\psi_{\boldsymbol{k},ab}$ and interband triplet pairing vectors $\boldsymbol{d}_{\boldsymbol{k},ab}$ between between bands a and b. Note, however that for this form we have assumed that the eigenstates that make up $V_{\boldsymbol{k}}$ transform like a pseudospin which is in general not the case when performing a numerical diagonalisation. Here we are only interested in the intraband pairing amplitudes at the Fermi surface. Despite the fact that the eigenstates in $V_{\boldsymbol{k}}$ might not be a pseudospin, it is still possible to extract the pairing amplitude by taking the Frobenius norm of the corresponding block of the matrix, e.g.

$$|\psi_{\boldsymbol{k},a}| = \|\psi_{\boldsymbol{k},a} i\sigma_2\|_F = \sqrt{\text{Tr}[(\psi_{\boldsymbol{k},a} i\sigma_2)^\dagger (\psi_{\boldsymbol{k},a} i\sigma_2)]}. \tag{5.44}$$

We show the gap magnitude at the Fermi surface for the A_{1g} irrep in Fig. 5.8, for A_{2g} in Fig. 5.9, for B_{1g} in Fig. 5.10, for B_{2g} in Fig. 5.11, and for E_g in Figs. 5.12, 5.13, and 5.14. The color scale is the same for all these figures and has been chosen to be normalized to the maximum gap of all projected gaps. Note that the gap in the A_{2g} irrep does not open a gap at the Fermi surface. The gap functions that will give rise to a chiral d-wave state are those in the E_g irrep, however, their projection is very small. We will have to tune the band parameters to increase the projection of the attractive E_g channels, such that the leading weak-coupling instability is in this irrep.
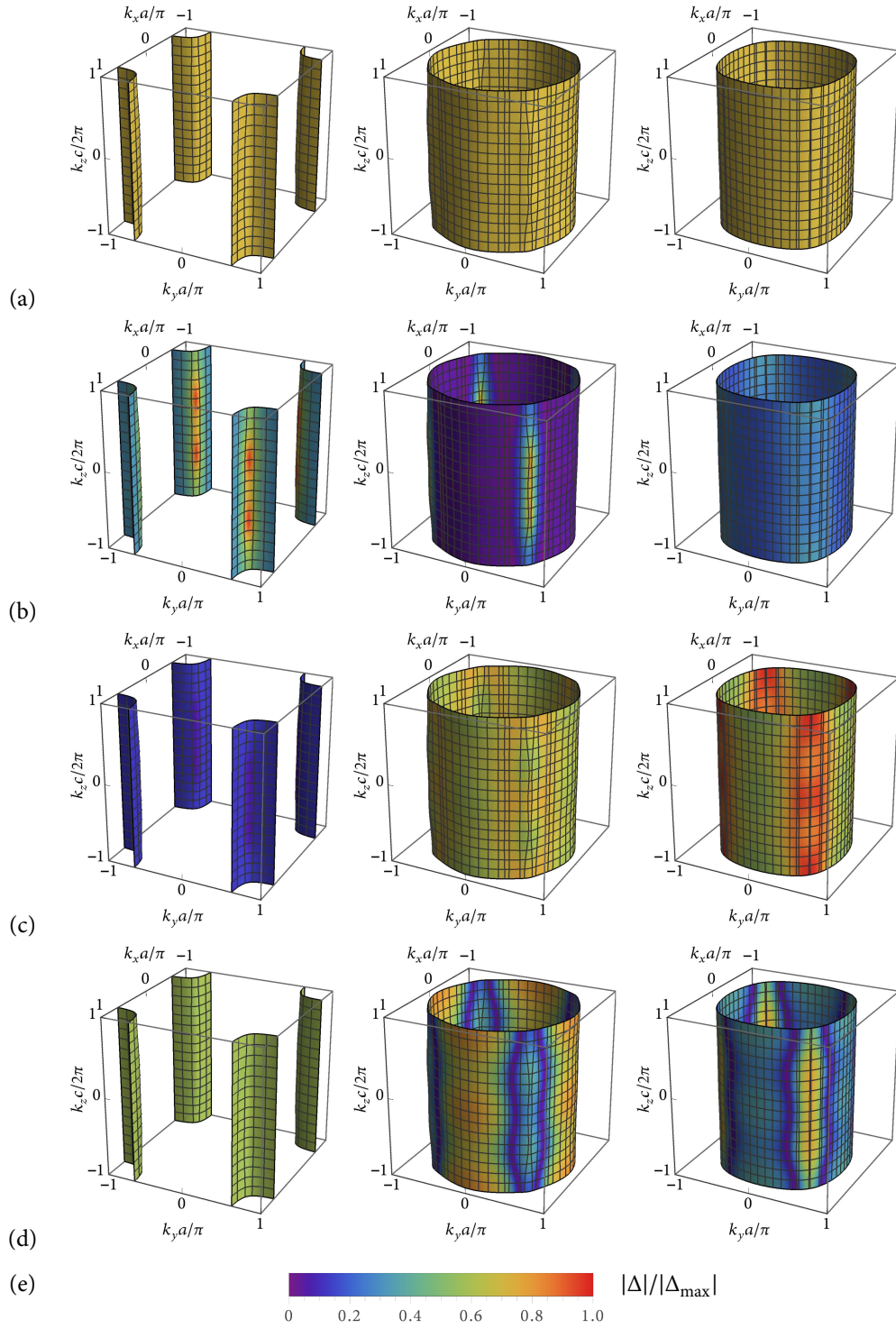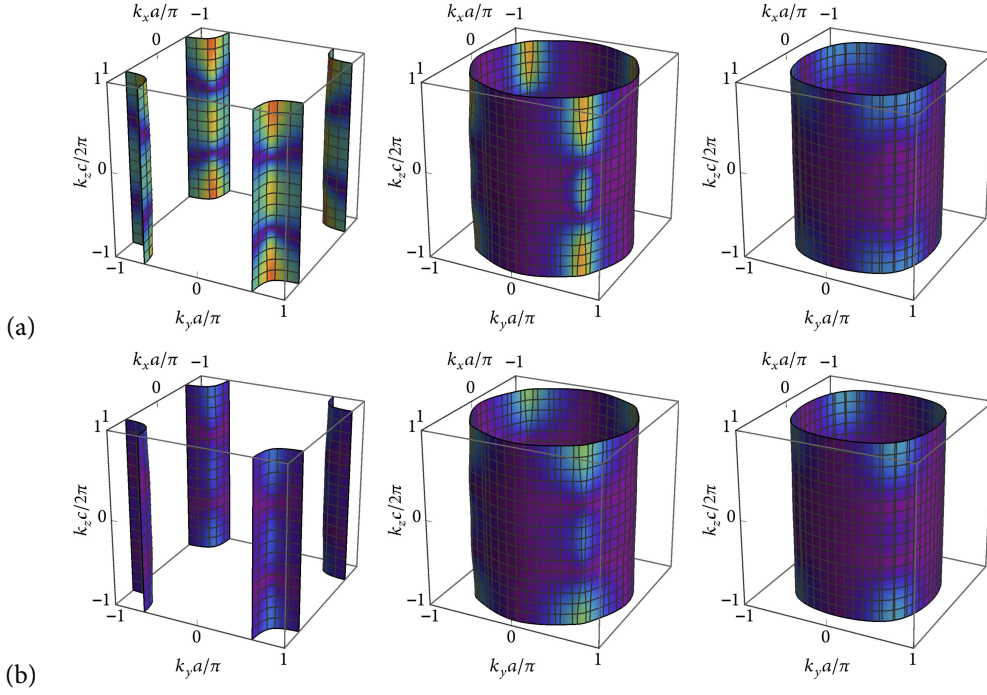
Figure 5.8. Projection of the gaps in the A_{1g} irrep onto the Fermi surface. (a) $\Delta = \lambda_0\sigma_0 i\sigma_2$ (b) $\Delta = \lambda_4\sigma_3 i\sigma_2$ (c) $\Delta = \frac{1}{\sqrt{2}}(\lambda_5\sigma_2 - \lambda_6\sigma_1)i\sigma_2$ (d) $\Delta = \lambda_8\sigma_0 i\sigma_2$. Panel (e) shows the color scale that is used in Figs. 5.8–5.14. Both attractive channels $\lambda_4\sigma_3$ and $\lambda_5\sigma_2 - \lambda_6\sigma_1$ have a very small gap on one of the sheets.
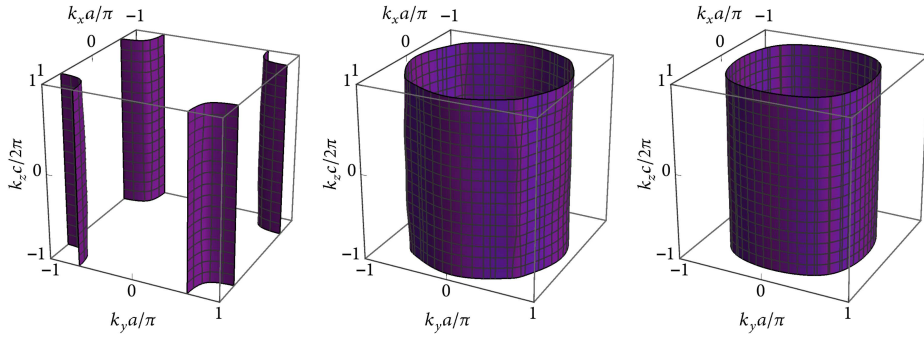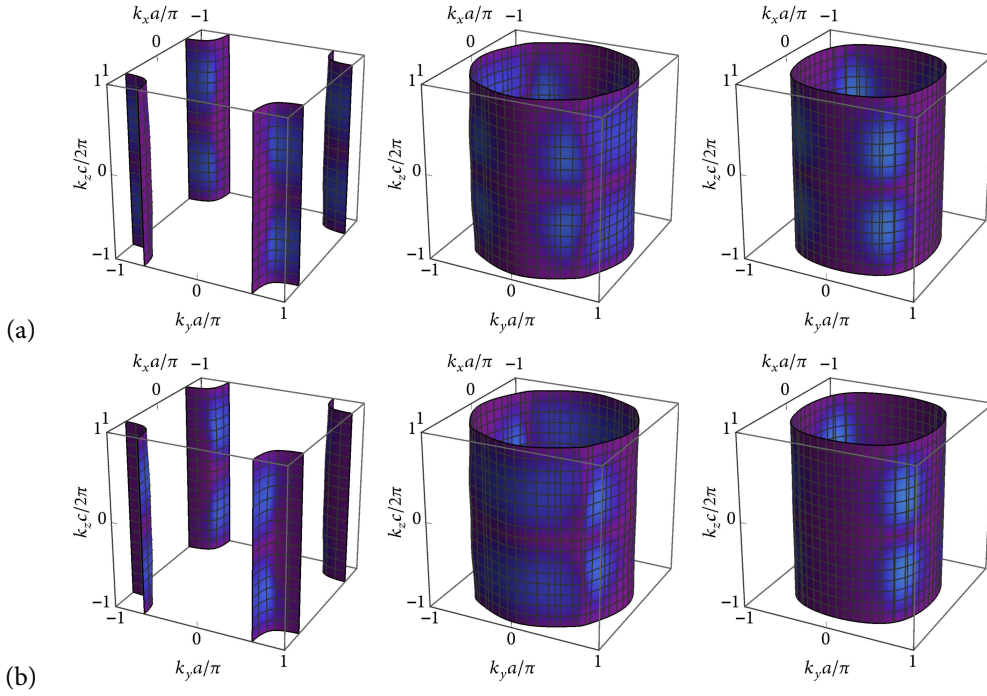
■ *Figure 5.9.* Projection of the gap in the A_{2g} irrep onto the Fermi surface. The only pairing state in this irrep is $\Delta = \frac{1}{\sqrt{2}}(\lambda_5\sigma_1 + \lambda_6\sigma_2)i\sigma_2$. As mentioned earlier, because there is no term with A_{2g} symmetry in the normal-state Hamiltonian, the projection of this irrep onto the Fermi surface is vanishing. The color scale is shown in Fig. 5.8(e).
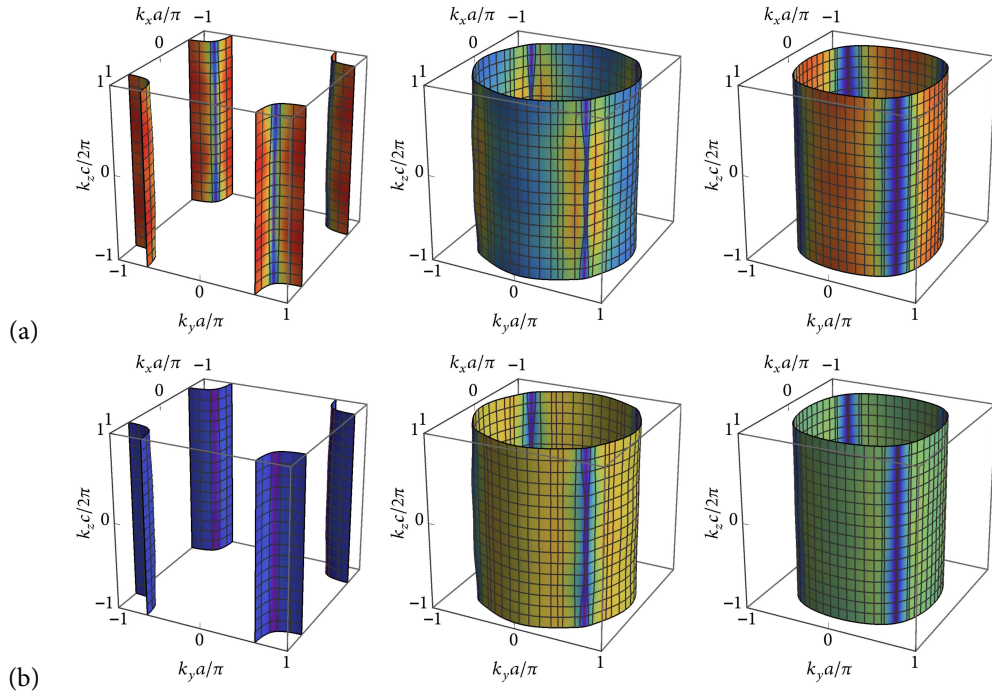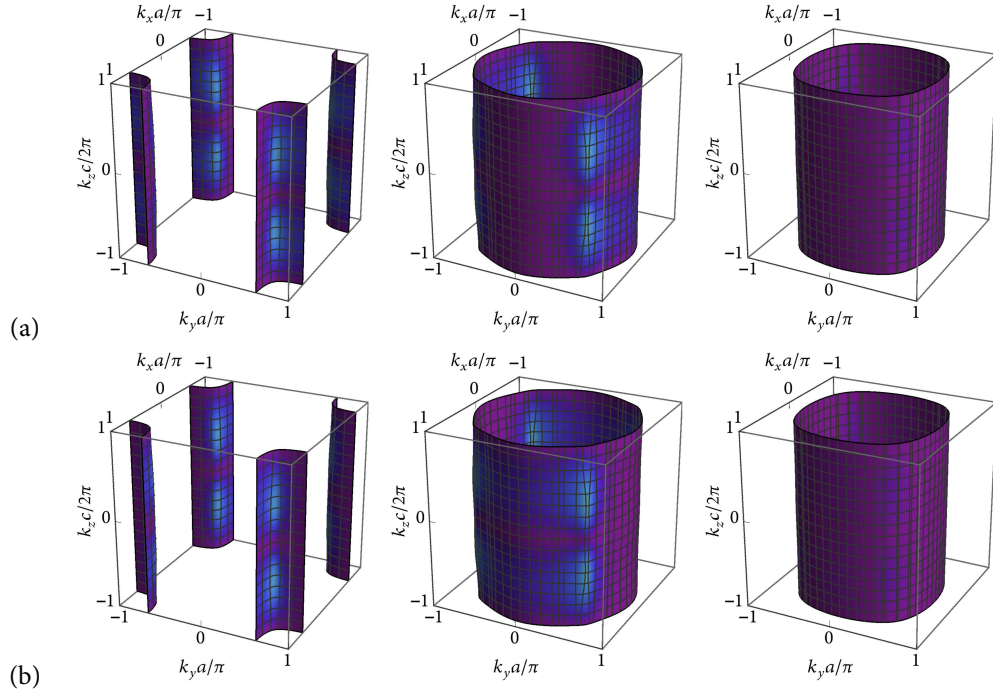

■ *Figure 5.10.* Projection of the gaps in the B_{1g} irrep onto the Fermi surface. (a) $\Delta = \lambda_7\sigma_0 i\sigma_2$ (b) $\Delta = \frac{1}{\sqrt{2}}(\lambda_5\sigma_2 + \lambda_6\sigma_1)i\sigma_2$. Note the vertical line nodes along $k_x^2 - k_y^2 = 0$. The attractive channel $\lambda_5\sigma_2 + \lambda_6\sigma_1$ has a very small gap on one of the sheets. The color scale is shown in Fig. 5.8(e).
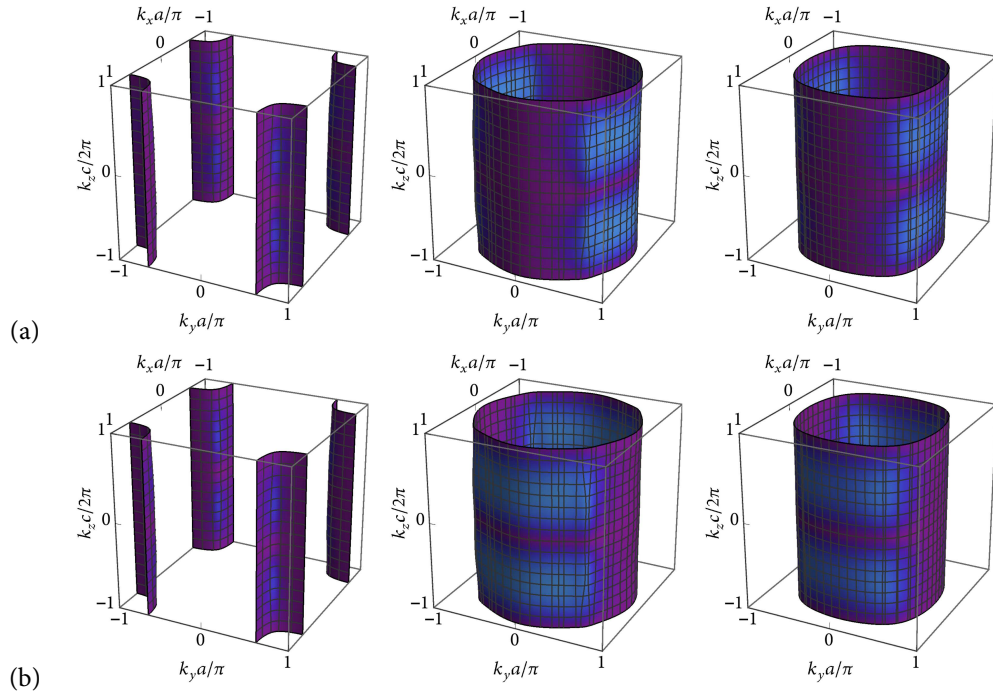
Figure 5.11. Projection of the gaps in the B_{2g} irrep onto the Fermi surface. (a) $\Delta = \lambda_1 \sigma_0 i \sigma_2$ (b) $\Delta = \frac{1}{\sqrt{2}}(\lambda_5 \sigma_1 - \lambda_6 \sigma_2) i \sigma_2$. Note the vertical line node along $k_x k_y = 0$. The horizontal line nodes at around $k_z c = \pi$ are accidental. The color scale is shown in Fig. 5.8(e).

Figure 5.12. Projection of the repulsive gaps in the E_g irrep onto the Fermi surface. (a) $\Delta = \lambda_3 \sigma_0 i \sigma_2$ (b) $\Delta = \lambda_2 \sigma_0 i \sigma_2$. The gap in the upper row transforms like yz, the gap in the lower row like xz. Note the horizontal line nodes at $k_z c / 2\pi = -1, 0, 1$. The color scale is shown in Fig. 5.8(e).

(a)

(b)

■ *Figure 5.13*. Projection of the first set of attractive gaps in the E_g irrep onto the Fermi surface. (a) $\Delta = \lambda_4\sigma_2 i\sigma_2$ (b) $\Delta = \lambda_4\sigma_1 i\sigma_2$. The gap in the upper row transforms like yz, the gap in the lower row like xz. Note the horizontal line nodes at $k_z c/2\pi = -1, 0, 1$. The color scale is shown in Fig. 5.8(e).

(a)

(b)

■ *Figure 5.14*. Projection of the second set of attractive gaps in the E_g irrep onto the Fermi surface. (a) $\Delta = \lambda_5\sigma_3 i\sigma_2$ (b) $\Delta = \lambda_6\sigma_3 i\sigma_2$. The gap in the upper row transforms like yz, the gap in the lower row like xz. Note the horizontal line nodes at $k_z c/2\pi = -1, 0, 1$. The color scale is shown in Fig. 5.8(e).

5.5   Linearized gap equation

Superconductivity forms as a weak-coupling instability in the presence of an infinitesimal attractive interaction. The low critical temperature of only $T_c = 1.5$ K indicates that Sr_2RuO_4 is a weak-coupling superconductor. In the present situation attractive and repulsive channels are allowed to mix. An order parameter develops in each channel at T_c, including the repulsive channels which will cost free energy and will suppress the critical temperature. To examine the relative stability of the irreducible representations we solve the linearized gap equation, which can be derived from the second term of Ginzburg-Landau theory

$$F_2 = \sum_{\boldsymbol{k},\boldsymbol{k}'} \text{Tr}[\Delta_{\boldsymbol{k}} V_{\boldsymbol{k},\boldsymbol{k}'}^{-1} \Delta_{\boldsymbol{k}'}] + k_B T_c \sum_{\boldsymbol{k},i\omega_n} \text{Tr}[G(\boldsymbol{k}, i\omega_n)\Delta_{\boldsymbol{k}} \tilde{G}(\boldsymbol{k}, i\omega_n)\Delta_{\boldsymbol{k}}^{\dagger}]. \tag{5.45}$$

All the irreducible representations in our classification have more than one element. Therefore we write the matrix pairing potential as a linear combination of these. Since we only assume local pairings, the pairing interaction $V_{\boldsymbol{k},\boldsymbol{k}'}$ and therefore the pairing potentials are momentum independent. The pairing potential are given by

$$\Delta = \hat{\Delta} U_T = \sum_i \hat{\Delta}_i U_T = \sum_i \Delta_{0,i} \Gamma_i U_T, \tag{5.46}$$

where i enumerates all elements of a single irreducible representation, $\Delta_{0,i}$ is the amplitude, Γ_i denotes the appropriate matrices, and U_T is the unitary part of the time-reversal operator. For example in the A_{1g} and E_g irreps this would read

$$\hat{\Delta}_{A_{1g}} = \Delta_{0,(0,0)}\Gamma_{(0,0)} + \Delta_{0,(4,3)}\Gamma_{(4,3)} + \Delta_{0,(8,0)}\Gamma_{(8,0)} + \Delta_{0,(5,2)-(6,1)}\Gamma_{(5,2)-(6,1)} \tag{5.47}$$

$$= \Delta_{0,(0,0)}\lambda_0\sigma_0 + \Delta_{0,(4,3)}\lambda_4\sigma_3 + \Delta_{0,(8,0)}\lambda_8\sigma_0 + \Delta_{0,(5,2)+(6,1)}\frac{1}{\sqrt{2}}(\lambda_5\sigma_2 + \lambda_6\sigma_1), \tag{5.48}$$

$$\hat{\Delta}_{E_g} = \Delta_{0,(2,0),(3,0)}(\Gamma_{(2,0)} + \Gamma_{(3,0)}) + \Delta_{0,(4,1),(4,2)}(\Gamma_{(4,1)} + \Gamma_{(4,2)}) + \Delta_{0,(5,3),(6,3)}(\Gamma_{(5,3)} - \Gamma_{(6,3)}) \tag{5.49}$$

$$= \Delta_{0,(2,0),(3,0)}\frac{1}{\sqrt{2}}(\lambda_2\sigma_0 + \lambda_3\sigma_0) + \Delta_{0,(4,1),(4,2)}\frac{1}{\sqrt{2}}(\lambda_4\sigma_1 + \lambda_4\sigma_2) + \Delta_{0,(5,3),(6,3)}\frac{1}{\sqrt{2}}(\lambda_5\sigma_3 - \lambda_6\sigma_3). \tag{5.50}$$

The normalisation factor of $1/\sqrt{2}$ ensures that the matrix parts preserve the trace orthonormality

$$\text{Tr}[\Gamma_i\Gamma_j] = 4\delta_{ij}, \tag{5.51}$$

which is important to assess the relative stability of the irreps. We can simplify the gap equation by using the fact that the hole-like and particle-like Green's function are related to one another by $\tilde{G}(\boldsymbol{k}, i\omega_n) = -G^T(-\boldsymbol{k}, -i\omega_n)$. Using the trace orthonormality we have

$$F_2 = \sum_i \frac{\text{Tr}[\Delta_i\Delta_i^{\dagger}]}{g_i} + k_B T_c \sum_{ij} \sum_{\boldsymbol{k},i\omega_n} \text{Tr}[G(\boldsymbol{k}, i\omega_n)\hat{\Delta}_i U_T(-G^T(-\boldsymbol{k}, -i\omega_n))U_T^{\dagger}\hat{\Delta}_j^{\dagger}]. \tag{5.52}$$

Using time-reversal symmetry we find that $U_T(-G^T(-\boldsymbol{k}, -i\omega_n))U_T^{\dagger} = G(\boldsymbol{k}, -i\omega_n)$ and therefore

$$F_2 = \sum_i \frac{\text{Tr}[\Delta_i\Delta_i^{\dagger}]}{g_i} + k_B T_c \sum_{ij} \sum_{\boldsymbol{k},i\omega_n} \text{Tr}[G(\boldsymbol{k}, i\omega_n)\hat{\Delta}_i G(\boldsymbol{k}, -i\omega_n)\hat{\Delta}_j^{\dagger}]. \tag{5.53}$$

Now we evaluate the trace in the band basis with eigenstates $|\boldsymbol{k}, \alpha\rangle$ such that the Green's functions are diagonal and the frequency summation over this product of Green's functions can be evaluated easily. Decomposing $\hat{\Delta}_i$

into amplitude $\Delta_{0,i}$ and matrix part Γ_i and using the fact that the matrices Γ_i are Hermitian and introducing a Kronecker delta in the first term, we can write the result as

$$F_2 = \sum_{i,j} \left[\delta_{i,j} \frac{\text{Tr}[\Gamma_i \Gamma_i^\dagger]}{g_i} + \sum_{\boldsymbol{k},a,b} \langle \boldsymbol{k},a|\hat{\Gamma}_i|\boldsymbol{k},b\rangle \langle \boldsymbol{k},a|\hat{\Gamma}_j^*|\boldsymbol{k},b\rangle \frac{\tanh\left(\frac{\epsilon_{\boldsymbol{k},a}}{2k_B T_c}\right) + \tanh\left(\frac{\epsilon_{\boldsymbol{k},b}}{2k_B T_c}\right)}{2(\epsilon_{\boldsymbol{k},a} + \epsilon_{\boldsymbol{k},b})} \right] \Delta_{0,i}\Delta_{0,j}^*. \tag{5.54}$$

We can write the term in brackets as a matrix and as for any linear system, non-trivial solutions are possible if the determinant of that matrix vanishes. Therefore the solution of the linearized gap equation can also be written as

$$\det\left(\delta_{i,j} \frac{\text{Tr}[\Gamma_i \Gamma_i^\dagger]}{g_i} + \sum_{\boldsymbol{k},a,b} \langle \boldsymbol{k},a|\hat{\Gamma}_i|\boldsymbol{k},b\rangle \langle \boldsymbol{k},a|\hat{\Gamma}_j^*|\boldsymbol{k},b\rangle \frac{\tanh\left(\frac{\epsilon_{\boldsymbol{k},a}}{2k_B T_c}\right) + \tanh\left(\frac{\epsilon_{\boldsymbol{k},b}}{2k_B T_c}\right)}{2(\epsilon_{\boldsymbol{k},a} + \epsilon_{\boldsymbol{k},b})} \right) = 0, \tag{5.55}$$

In the first term of the determinant in (5.55) the trace $\text{Tr}[\Gamma_i \Gamma_i^\dagger]$ always evaluates to 4 because we have chosen these matrices to be trace orthonormal. In the second term of (5.55) there is a sum over band indices a and b. This can be split into intraband contributions where $a = b$ and interband contributions where $a \neq b$. So it is possible to discard interband effects entirely, in particular because these don't contribute to the extreme weak-coupling limit where $T_c \to 0$.

From the previous discussion about the Hubbard-Kanamori interactions we know that by symmetry we have the restrictions

$$U' = U - 2J \quad \text{and} \quad \frac{J}{U} > \frac{1}{3}. \tag{5.56}$$

By that we fix the ratios U'/U, and J/U and can then use U to determine the overall energy scale. We choose

$$J = \frac{2}{5}U. \tag{5.57}$$

As mentioned earlier the statement that certain superconducting channels with interaction $U' - J$ will become attractive was based on the assumption that the interaction constants are strongly renormalized. Therefore it is probably the case that J is not much larger than U' and the ratio J/U is very close to 1/3. However, moving this ratio very close to 1/3 leads to vert small attractive interactions, which causes numerical instabilities in solving the linearized gap equation. The choice of $J/U = 2/5$ is a good trade-off between the assumed physical reality and numerical stability.

In Fig. 5.15 we show the critical temperature as determined by (5.55). It is clear that for weak coupling, the A_{1g} irrep will always have a higher critical temperature than the B_{1g} irrep. This does not change in the presence of interband pairing effects, although interband pairing *enhances* the critical temperature over all. This is seemingly in contrast to the principle of superconducting fitness [113, 114], which states that interband pairing is expected to suppress the critical temperature. However, this is not a contradiction because in the superconducting fitness the comparison was drawn between a pairing state that has no interband contribution at all to one that has. For a state with interband pairing, the interband pairing still makes a positive contribution to T_c, although by itself it is insufficient to drive a weak-coupling instability. So the theorem of superconducting fitness is not violated. Further we find that at weak coupling $\log \beta_c$ scales linearly and the interband contributions only introduces a constant offset. Additionally, if $J/U' > 1/3$ only close to the Fermi energy, we may ignore the interband contributions on the ground that away from the Fermi energy there will be no attractive pairing potential in these channels. Therefore it is safe to neglect the interband contributions for our further investigations.

Pairing due to on-site Hund's rule interactions in the presence of spin-orbit coupling in a model Hamiltonian for the T_{2g} d-orbitals in a single-layer perovskite very similar to Sr_2RuO_4 has previously been considered in
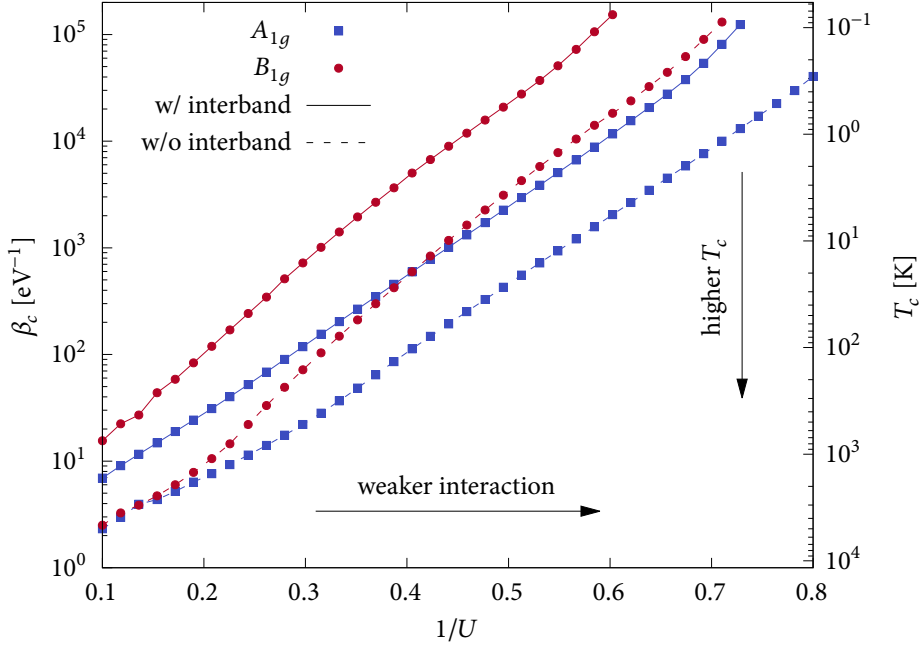
■ *Figure 5.15.* Inverse critical temperature β_c and critical temperature T_c as a function of the energy scaling parameter *s*. The dots are connected by lines as a guide to the eye. Solid lines indicate that interband terms have been taken into account, dashed lines indicate that interband contributions have been neglected.

[221]. An A_{1g} pairing state was found to be most stable which is in accordance with Fig. 5.15. However, in [221] only momentum-independent on-site spin-orbit coupling was considered.

Angle-resolved photo emission (ARPES) experiments have shown that there is a considerable deviation between the DFT results and the experimental data concerning the strength of the spin-orbit coupling [160, 161, 233]. Therefore we survey a wide range of values for the spin-orbit coupling parameters to learn how they affect the selection of a stable pairing state. Care must be taken to not jeopardize qualitative agreement the experimentally established two-dimensionality of the Fermi surface, which puts additional constraints on the parameters that can be varied.

In our exploration we focus on the effects of three of the spin-orbit coupling terms in the normal-state Hamiltonian. These are the atomic on-site spin-orbit coupling which is split into an in-plane component $h_{52} - h_{61} = \eta_{\perp}$ and an out-of-plane component $h_{43} = \eta_z$ and one of the momentum-dependent spin-orbit couplings of the E_g type $\{h_{53}, h_{63}\}$ which is parameterised by t_{56z}^{SOC} and describes an inter-layer hopping between the d_{xy} and the d_{xz} and d_{yz} orbitals. It is conceivable to vary other spin-orbit coupling parameters as well, however, their effect on the selection of the leading instability is negligible within a reasonable range where the Fermi surface qualitatively reproduces the DFT predictions [234]. We also ignore the anisotropy of the atomic on-site spin-orbit coupling and set $\eta_z = \eta_{\perp} = \eta$.

In panel (a) of Fig. 5.16 we show a phase diagram of the leading instabilities as a function of atomic on-site spin-orbit coupling η and momentum-dependent spin-orbit coupling t_{56z}^{SOC}. The most stable pairing states are either in the A_{1g} or the E_g irrep. The A_{2g} and B_{2g} irreps are never competitive, whereas the B_{1g} irrep is a subleading instability in small regions of the phase diagram. The vertical dashed lines indicate the minimal distance between the different sheets of the Fermi surface in fractions of $2\pi/a$. In the limit of very small atomic
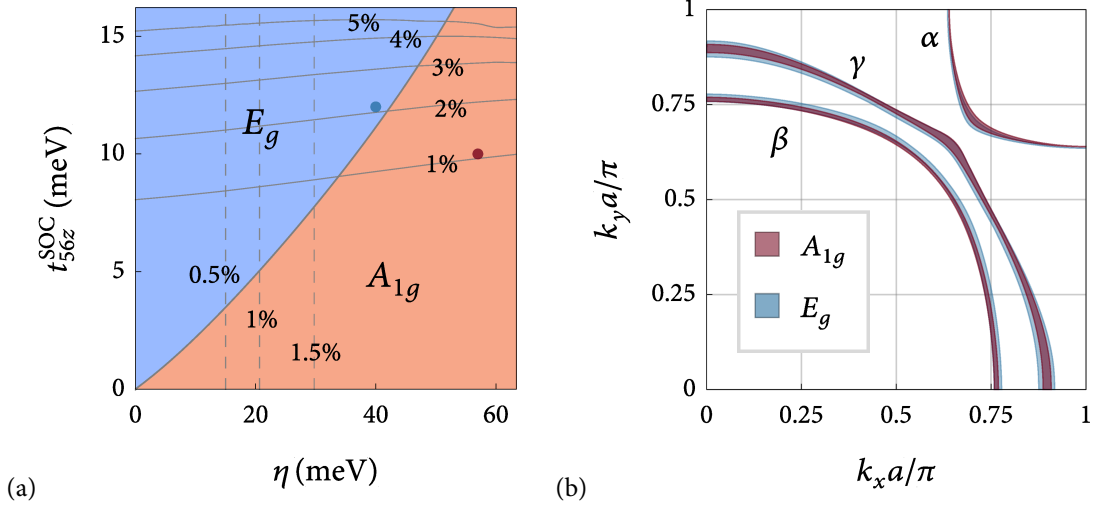
■ *Figure 5.16.* (a) Phase diagram of the leading instabilities as a function of the spin-orbit coupling parameters η and t_{56z}^{SOC}. The vertical dashes lines indicate the minimum distance between the sheets of the Fermi surface in the plane as a percentage of $2\pi/a$. The thin solid lines indicate the variation of the Fermi surface along k_z and are therefore a measure of the two-dimensionality. (b) Envelope of the Fermi surface along the k_z direction for the A_{1g} state and the E_g state marked by the red and blue dot in panel (a), respectively. *Figure provided by Han-Gyeol Suh.*

spin-orbit coupling η the sheets of the Fermi surface would touch which is neither predicted from first principles calculations [160, 212] nor is it consistent with ARPES data [159, 161]. The solid horizontal lines denote the maximal corrugation of the Fermi surface in the k_z direction. If the out-of-plane momentum-dependent spin-orbit coupling is too large, the bands will become too dispersive along k_z, which is again in contradiction to previous observations.

In panel (b) of Fig. 5.16 we show the envelope of the Fermi surface when viewed from the top, i.e. the shape of the Fermi surface projected onto the k_x-k_y-plane, for two sets of band parameters where either the A_{1g} or the E_g pairing state is stabilised. For both sets of parameters the Fermi surface looks very similar. The band parameters for the case of A_{1g} (E_g) pairing correspond to the location of the red (blue) dot in panel (a). That is, for A_1g we have $\eta = 57\,\mathrm{meV}$ and $t_{\mathrm{SOC}}^{56z} = 10\,\mathrm{meV}$, and for E_g we have $\eta = 40\,\mathrm{meV}$ and $t_{\mathrm{SOC}}^{56z} = 12\,\mathrm{meV}$.

The dominant contribution to the E_g pairing state comes from the $\{(6, 3), (5, 3)\}$ channel which is of the same symmetry as the momentum-dependent spin-orbit coupling associated with t_{56z}^{SOC}. The out-of-plane component of the momentum-dependent spin-orbit coupling implies that a large value of t_{56z}^{SOC} will result in a more pronounced corrugation along the k_z direction. Nevertheless, within this reasonable parameter range, it is possible to stabilize an E_g pairing state at a value as small as $t_{56z}^{\mathrm{SOC}} = 5\,\mathrm{meV}$. It is remarkable that such a small variation of the normal-state parameters can have drastic effects on the selection of the pairing state with very different structure.

In Fig. 5.17 we show the projected gap at the Fermi surface for representative parameters sets where the A_{1g} and E_g states are stable, respectively. For both of them, the gap magnitude on the α sheet is much smaller than on the other sheets which have comparable gap magnitude. Therefore it is not possible to isolate a single band for superconductivity which is also in contrast to the original proposal which assumed that only the γ band is dominant [83, 215, 235]. Neither is it possible to choose the pair of almost one-dimensional α and β bands, as proposed in [206]. Also note the deep gap minima in the E_g state on the γ band along the diagonal. It is conceivable that these exhibit characteristics that are similar to vertical line nodes.
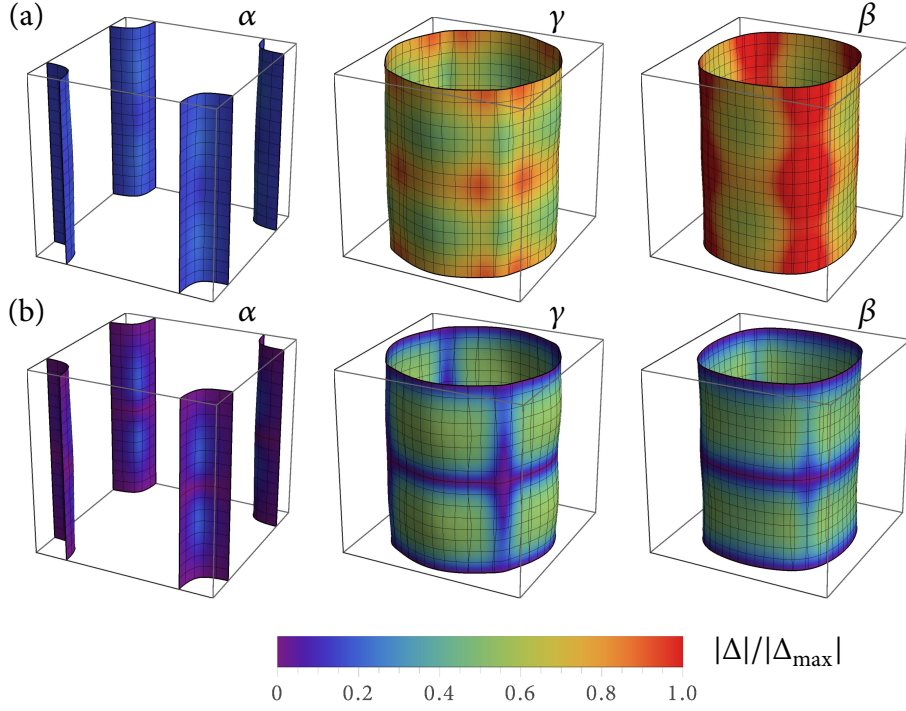
Figure 5.17. Projected gaps on the normal-state Fermi surface in the first Brillouin zone for representative parameter sets where the (a) A_{1g} and (b) E_g states are stable, respectively. The parameters are the same as in Fig. 5.16 at the red (A_{1g}) and blue (E_g) dot. The color scale is the same for both panels and has been normalized to the maximum of the A_{1g} gap.

5.6 Pairing state below the critical temperature

To obtain the superconducting gap as a function of temperature it is not sufficient to solve the linearized gap equation which only yields information about the pairing state just below the critical temperature and the critical temperature itself. Instead it is necessary to solve the full gap equation self-consistently. This in turn poses a problem because a direct minimisation of the free energy (C.46) to obtain the self-consistent gap is not possible due to the presence of repulsive pairing channels. In this case the minima will no longer be located at stationary points. Instead consider the stationary point of the free energy given by the system of equations

$$0 = \frac{\partial F_{\mathrm{MF}}}{\partial \Delta_i^*} = \frac{\mathrm{Tr}[\Gamma_i \Gamma_i^\dagger]}{g_i} \Delta_i - \frac{1}{2} \sum_{\boldsymbol{k},n} \tanh\left(\frac{\beta E_{\boldsymbol{k},n}}{2}\right) \frac{\partial E_{\boldsymbol{k},n}}{\partial \Delta_i^*} \tag{5.58}$$

for each component i of the gap. The derivative of the energy eigenvalue is calculated using the Hellmann-Feynman theorem [236–238] to yield the gap equation

$$\Delta_i = \frac{g_i}{2 \, \mathrm{Tr}[\Gamma_i \Gamma_i^\dagger]} \sum_{\boldsymbol{k},n} \tanh\left(\frac{\beta E_{\boldsymbol{k},n}}{2}\right) \left\langle \boldsymbol{k}, n \left| \frac{\partial H_{\mathrm{BdG}}(\boldsymbol{k})}{\partial \Delta_i^*} \right| \boldsymbol{k}, n \right\rangle, \tag{5.59}$$

where in our case of a momentum independent gap the derivative of the mean-field Hamiltonian takes the simple form

$$\frac{\partial H_{\mathrm{BdG}}(\boldsymbol{k})}{\partial \Delta_i^*} = \begin{pmatrix} 0 & \Gamma_i U_T \\ 0 & 0 \end{pmatrix}. \tag{5.60}$$
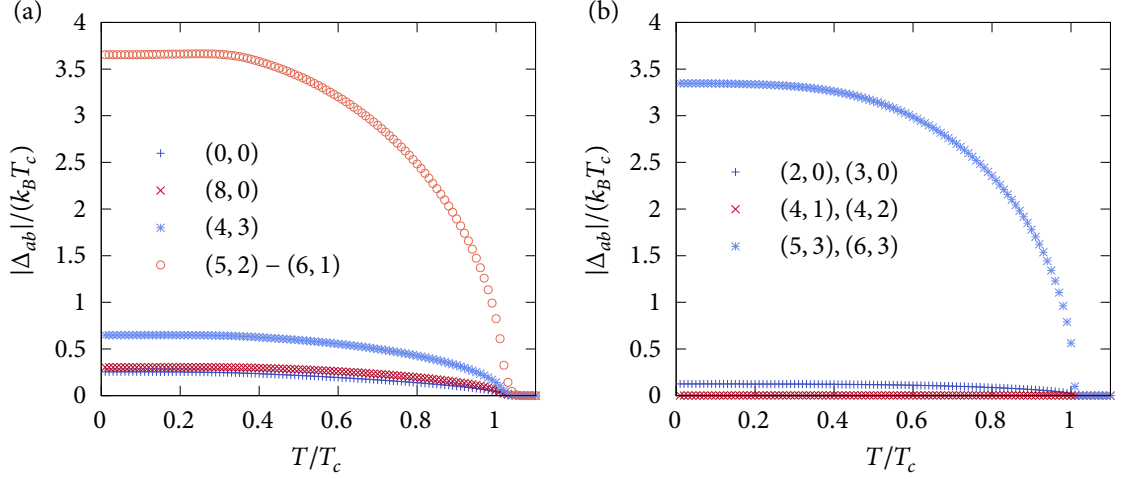
Figure 5.18. Self consistent solution of the gap equation for $T_c = 1.5\,\text{K}$ for (a) the A_{1g} irrep and (b) the E_g irrep. The labels are given in the (a, b) notation of (5.20).

To solve (5.59) self-consistently we have to iterate the equation until all Δ_i converge. This process is numerically not very stable and a few tricks are necessary to not avoid runaway situations. Firstly, it is much easier to start from zero temperature and go to higher temperatures because at lower temperatures the gap is much larger and therefore the numerical convergence is not so susceptible to rounding errors. The next obvious trick is to choose a good starting value. Here we initialize all with $\Delta_i = 1.76\,k_B T_c$ which is the value of the gap at zero temperature for a BCS superconductor. Going to higher temperature we always use the solution of the previous temperature step as a starting point for the next. The last trick is to weight the solutions of the last two steps for next, i.e. the starting value of the $(j + 1)$-th iteration is $\Delta^{(j+1)} = w\Delta^{(j)} + (1 - w)\Delta^{(j-1)}$ where $w \in [0, 1]$. This last trick is crucial to ensure to avoid runaway situations, but it slows down the convergence tremendously. Therefore it is advantageous to implement a step-width control by which the weighting factor w is replaced by a weighting function, e.g. a logistic function $\lambda(w) = 1/(1 + e^{-w})$. The argument of the weighting function can be increased or decreased depending on the size of the previous step $|\Delta^{(j)} - \Delta^{(j-1)}|$. This provides a good trade-off between convergence speed and accuracy.

In Fig. 5.18 we show self-consistent solutions of the gap equation for the both A_{1g} irrep and the E_g irrep. The ratio between the pairing states that is determined from the eigenvector of the linearized gap equation is realised at all temperatures. The chief contribution to both pairing states comes from the orbitally-antisymmetric channels. The pairing potential is much larger than anticipated from BCS theory. This apparent enhancement over the BCS limit stems from the fact that the projection of the orbitally anisotropic states onto the Fermi surface is rather small, so to achieve on average a gap of $1.76\,k_B T_c$ at the Fermi surface, the pairing potential has to be much larger.

5.6.1 Bogoliubov Fermi Surfaces

To connect with the previous chapter, the chiral d-wave state that we propose to be realised in Sr_2RuO_4 ticks all the boxes to be a candidate for Bogoliubov Fermi surfaces:

1. Even parity
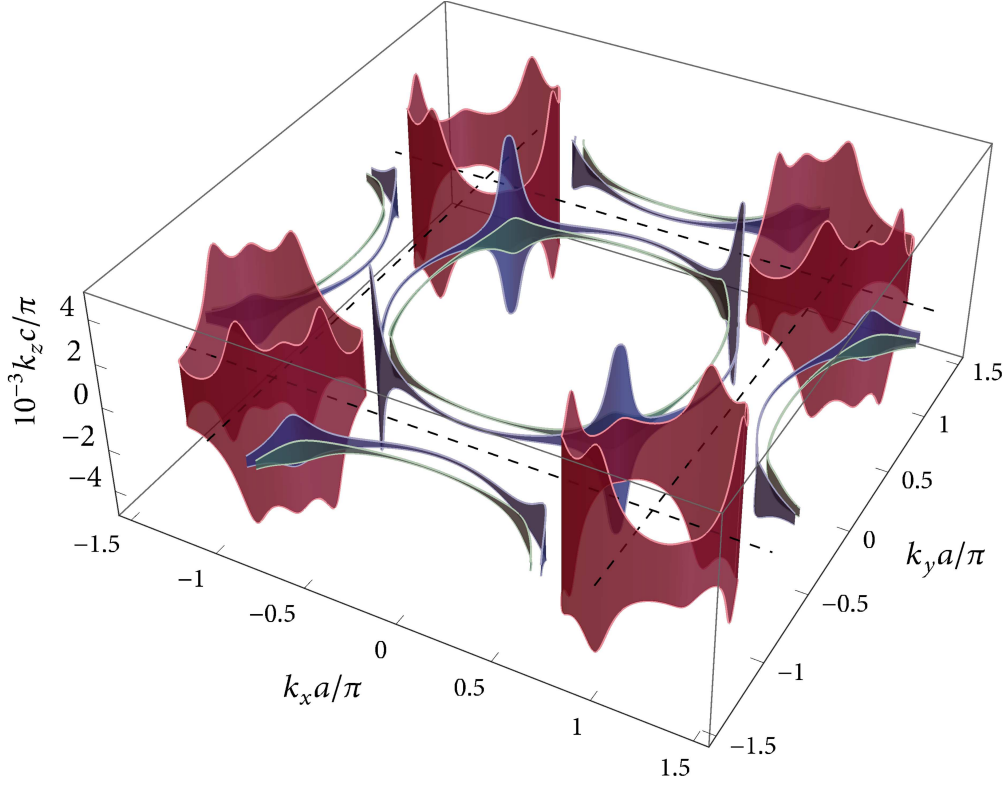
■ *Figure 5.19*. Bogoliubov Fermi surface for the chiral d-wave state. The horizontal line nodes in the $k_z = 0$ plane are inflated into surfaces with a finite extent in k_z. The color code red, green, blue corresponds to the nodal surface on the α, β, γ sheet of the Fermi surface. Dashed lines mark the boundary of the first Brillouin zone in the plane. *Figure prepared with help of Han-Gyeol Suh.*

2. Inter-band pairing

3. Multi-component order parameter

4. Possibility for time-reversal symmetry breaking combination

We therefore search for Bogoliubov Fermi surfaces in the E_g pairing state parameterised by

$$\hat{\Delta}_{E_g} = \Delta_{0,(2,0),(3,0)} \frac{1}{\sqrt{2}} (\lambda_2 \sigma_0 + \lambda_3 \sigma_0) + \Delta_{0,(4,1),(4,2)} \frac{1}{\sqrt{2}} (\lambda_4 \sigma_1 + \lambda_4 \sigma_2) + \Delta_{0,(5,3),(6,3)} \frac{1}{\sqrt{2}} (\lambda_5 \sigma_3 - \lambda_6 \sigma_3), \quad (5.61)$$

with the gap amplitudes determined by the self-consistent solution in Fig. 5.18(b). In Fig. 5.19 we show the Bogoliubov Fermi surfaces that results from a gap magnitude of $\Delta_0 = 0.42$ meV. The very large Bogoliubov Fermi surfaces on the α band and the "peaks" on the γ band reflect the deep gap minima on these sheets also observed in Fig. 5.17. The inflated nodes are very thin in the direction perpendicular to the normal-state Fermi surface, which makes them appear as flat. Their size in the k_z direction is about 0.4 % of the whole k_z axis of the Brillouin zone, so it is unlikely that the corresponding pseudomagnetic field will have a substantial magnitude and therefore the residual density of states will be too small to be unambiguously observed in an experiment.

5.6.2   Spin susceptibility and Knight shift

In light of the recent Knight-shift experiments, it is important to establish the response of the E_g state that we proposed here [84, 85]. This is important in particular because the spin structure of this E_g state is a spin-triplet with in-plane spin polarisation of the Cooper pair which might at first seem contradictory as the new experiments rule out a triplet pairing state. Therefore it seems natural to expect a temperature-independent spin susceptibility for in-plane fields. However, this is not the case because the overall parity of the E_g state is even which implies that the intraband pairing potential is a pseudospin singlet.

In the following we will derive the spin susceptibility in the superconducting state and numerically evaluate the Knight shift as a function of temperature for both the A_{1g} and the E_g state. To determine the Knight shift we start from the dynamic susceptibility (E.5) in the superconducting state

$$\chi^{st}(\boldsymbol{q}, i\omega) = \int_0^\beta d\tau\, e^{i\omega\tau} \langle T_\tau S_s^a(\boldsymbol{q}, \tau) S_t^b(-\boldsymbol{q}, 0) \rangle, \tag{5.62}$$

but this time the magnetic moment has an additional orbital degree of freedom

$$S_s^a = \frac{1}{2N} \sum_{\boldsymbol{k},\alpha\beta} d_{s\alpha}^\dagger(\boldsymbol{k}+\boldsymbol{q}, \tau) \sigma_{\alpha\beta}^a d_{s\beta}(\boldsymbol{k}, \tau). \tag{5.63}$$

We plug in the magnetic moments and rearrange

$$\chi_{st}^{\text{SC}}(\boldsymbol{q}, i\omega) = -\frac{1}{4N^2} \int_0^\beta d\tau\, e^{i\omega\tau} \sum_{\alpha\beta\gamma\delta} \sigma_{\alpha\beta}^a \sigma_{\gamma\delta}^b \sum_{\boldsymbol{k},\boldsymbol{k}'} \langle T_\tau d_{s\beta}(\boldsymbol{k}, \tau) d_{t\gamma}^\dagger(\boldsymbol{k}'-\boldsymbol{q}, 0) d_{t\delta}(\boldsymbol{k}', 0) d_{s\alpha}^\dagger(\boldsymbol{k}+\boldsymbol{q}, \tau) \rangle. \tag{5.64}$$

Equivalent to the single band case discussed in Appendix E we apply Wick's theorem to decompose the expectation value. We proceed to identify the definitions of the Green's function $G_{ab}(\boldsymbol{k}, \tau) = -\langle T_\tau d_a(\boldsymbol{k}, \tau) d_b^\dagger(\boldsymbol{k}, 0) \rangle$ and the anomalous Green's function $F_{ab}(\boldsymbol{k}, \tau) = -\langle T_\tau d_a(\boldsymbol{k}, \tau) d_b(-\boldsymbol{k}, 0) \rangle$ but with additional orbital indices. After Fourier transformation into Matsubara frequency space we have

$$\chi_{st}^{\text{SC}}(\boldsymbol{q}, i\omega) = -\frac{1}{4N\beta} \sum_{\alpha\beta\gamma\delta} \sigma_{\alpha\beta}^a \sigma_{\gamma\delta}^b \sum_{\boldsymbol{k}, i\omega_n} \left(G_{s\beta;t\gamma}(\boldsymbol{k}, i\omega_n) G_{t\delta;s\alpha}(\boldsymbol{k}+\boldsymbol{q}, i\omega_n - i\omega) - F_{s\beta;t\delta}(\boldsymbol{k}, i\omega_n) F_{t\gamma;s\alpha}^\dagger(\boldsymbol{k}+\boldsymbol{q}, i\omega_n - i\omega) \right). \tag{5.65}$$

In contrast to the single band case in Appendix E it is not possible to determine the Green's functions analytically. However, they can be calculated from the spectral form of the Green's functions of the full BdG-Hamiltonian
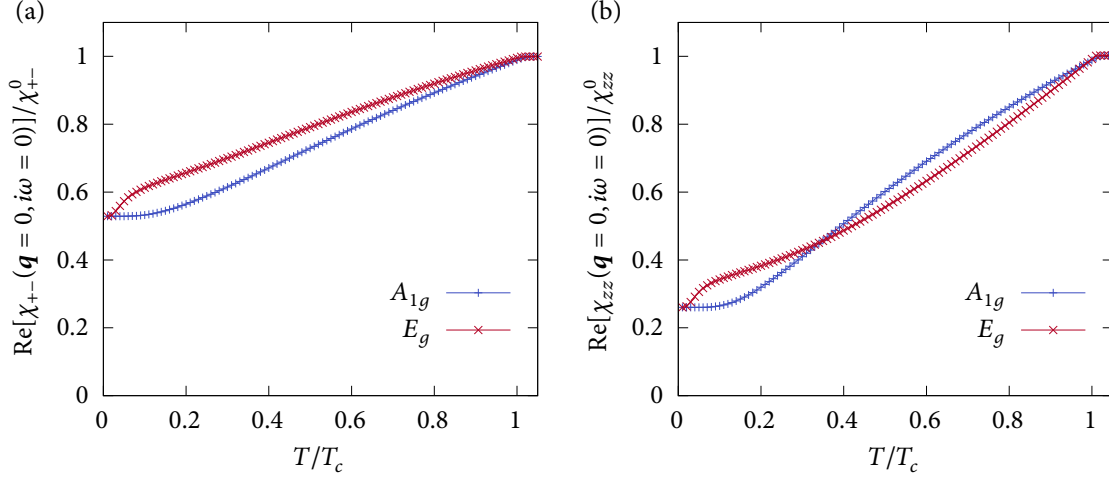
$$\mathcal{G}_{ab}(\boldsymbol{k}, i\omega_n) = \begin{pmatrix} G(\boldsymbol{k}, i\omega_n) & F(\boldsymbol{k}, i\omega_n) \\ F^\dagger(\boldsymbol{k}, i\omega_n) & \tilde{G}(\boldsymbol{k}, i\omega_n) \end{pmatrix}_{ab} \tag{5.66}$$

$$= \sum_\mu \frac{a_\mu^a(\boldsymbol{k}) a_\mu^{b*}(\boldsymbol{k})}{i\omega_n - E_\mu(\boldsymbol{k})} \text{ with } a_\mu^\nu(\boldsymbol{k}) = \begin{pmatrix} \alpha_\mu^\nu(\boldsymbol{k}) \\ \bar{\alpha}_\mu^\nu(\boldsymbol{k}) \end{pmatrix} \tag{5.67}$$

$$= \sum_\mu \frac{1}{i\omega_n - E_\mu(\boldsymbol{k})} \begin{pmatrix} \alpha_\mu^a(\boldsymbol{k}) \alpha_\mu^{b*}(\boldsymbol{k}) & \alpha_\mu^a(\boldsymbol{k}) \bar{\alpha}_\mu^{b*}(\boldsymbol{k}) \\ \bar{\alpha}_\mu^a(\boldsymbol{k}) \alpha_\mu^{b*}(\boldsymbol{k}) & \bar{\alpha}_\mu^a(\boldsymbol{k}) \bar{\alpha}_\mu^{b*}(\boldsymbol{k}) \end{pmatrix} \tag{5.68}$$

where the E_μ are the eigenvalues and a_μ^ν is the ν-th component of the eigenvector corresponding to the μ-th eigenvalue of the BdG Hamiltonian. Selecting the appropriate blocks the susceptibility reads

$$\chi_{st}^{\text{SC}}(\boldsymbol{q}, i\omega) = -\frac{1}{4N\beta} \sum_{\alpha\beta\gamma\delta} \sigma_{\alpha\beta}^a \sigma_{\gamma\delta}^b \sum_{\boldsymbol{k}, i\omega_n} \left(\frac{\alpha_\mu^{s\beta}(\boldsymbol{k}) \alpha_\mu^{t\gamma*}(\boldsymbol{k})}{i\omega_n - E_\mu(\boldsymbol{k})} \frac{\alpha_\nu^{t\delta}(\boldsymbol{k}+\boldsymbol{q}) \alpha_\nu^{s\alpha*}(\boldsymbol{k}+\boldsymbol{q})}{i\omega_n - i\omega - E_\nu(\boldsymbol{k}+\boldsymbol{q})} \right.$$
$$\left. - \frac{\alpha_\mu^{s\beta}(\boldsymbol{k}) \bar{\alpha}_\mu^{t\delta*}(\boldsymbol{k})}{i\omega_n - E_\mu(\boldsymbol{k})} \frac{\bar{\alpha}_\nu^{t\gamma}(\boldsymbol{k}+\boldsymbol{q}) \alpha_\nu^{s\alpha*}(\boldsymbol{k}+\boldsymbol{q})}{i\omega_n - i\omega - E_\nu(\boldsymbol{k}+\boldsymbol{q})} \right). \tag{5.69}$$

■ *Figure 5.20.* Knight shift given by the static magnetic susceptibility in the superconducting state for the field (a) in plane and (b) out of plane. At high temperatures both the A_{1g} and the E_g state exhibit a linear dependence on temperature. The E_g state shows a clear suppression of the Knight shift which qualitatively resembles a singlet response. The Yosida function $Y(T)$ is shown in dashed lines for comparison.

This can be written more compactly using

$$\chi_{st}^{SC}(\boldsymbol{q}, i\omega) = \frac{1}{4} \sum_{\alpha\beta\gamma\delta} \sigma_{\alpha\beta}^a \sigma_{\gamma\delta}^b [\chi_{SC}(\boldsymbol{q}, i\omega)]_{t\delta,s\alpha}^{s\beta,t\gamma}, \tag{5.70}$$

with the generalized susceptibility

$$[\chi_{SC}(\boldsymbol{q}, i\omega)]_{s,t}^{p,q} = -\frac{1}{N} \sum_{\boldsymbol{k}} \big(\alpha_\mu^q(\boldsymbol{k})\alpha_\mu^{s*}(\boldsymbol{k})\alpha_\nu^t(\boldsymbol{k}+\boldsymbol{q})\alpha_\nu^{p*}(\boldsymbol{k}+\boldsymbol{q})$$

$$- \alpha_\mu^q(\boldsymbol{k})\bar{\alpha}_\mu^{t*}(\boldsymbol{k})\bar{\alpha}_\nu^s(\boldsymbol{k}+\boldsymbol{q})\alpha_\nu^{p*}(\boldsymbol{k}+\boldsymbol{q}) \frac{f(E_\mu(\boldsymbol{k})) - f(E_\nu(\boldsymbol{k}+\boldsymbol{q}))}{i\omega + E_\mu(\boldsymbol{k}) - E_\nu(\boldsymbol{k}+\boldsymbol{q})}. \tag{5.71}$$

The physical susceptibility is then derived from the generalized susceptibility as

$$\chi_{ab}^{SC,phys}(\boldsymbol{q}, i\omega) = \frac{1}{4} \sum_{s,t} \sum_{\alpha\beta\gamma\delta} \sigma_{\alpha\beta}^a \sigma_{\gamma\delta}^b [\chi_{SC}(\boldsymbol{q}, i\omega)]_{t\delta,s\alpha}^{s\beta,t\gamma}. \tag{5.72}$$

In the linear response regime, the Knight shift for the field along the α axis is defined by the real part of the magnetic susceptibility at $\boldsymbol{q} = 0$ and in the static limit $i\omega = 0$ [209]

$$K^\alpha = \text{Re}[\chi_{\alpha\alpha}^{SC,phys}(\boldsymbol{q} = 0, i\omega = 0)]. \tag{5.73}$$

In Fig. 5.20 we show the Knight shift for the external field in and out of the plane for the A_{1g} and E_g irreps. The onset of both the Knight shift below T_c is linear in T for both states and a suppression of the Knight shift for the E_g state below T_c is clearly present. This confirms that despite the microscopic spin-triplet structure of the matrix pairing potential, both the A_{1g} and the E_g states manifest themselves as a pseudospin singlet with the magnetic response of a true singlet. In particular the suppression for the in-plane fields is qualitatively in accordance with [84, 85]. The anisotropy between in-plane and out-of-plane fields is likely due to the inclusion of the momentum-dependent spin-orbit coupling terms in the normal-state Hamiltonian.

At low temperature the response of the A_{1g} and the E_g states differ qualitatively. While the response of the A_{1g} state is reminiscent of the Yosida function with an additional offset at zero temperature, the response of the E_g state has an additional feature at very low temperatures. A possible explanation for this anomaly is that the gap on the α band in the E_g state is much smaller than on the other bands. It was pointed out by Agterberg *et al.* [235] that if the bands are weakly coupled, the very small gap on one band gives rise to essentially gapless excitations for temperatures that are larger than this small gap. These excitations will appear as low temperature anomalies in various thermodynamic and transport properties. For the E_g state this effect might be very pronounced in the present case, because the gap on the α sheet of the Fermi surface is mostly vanishing, cf. Fig. 5.17. One might argue that the situation is similar for the A_{1g} where the gap is also much smaller on the α sheet, however, the gap remains finite over the whole sheet which could explain why the effect is suppressed for the A_{1g} state.

5.7 Discussion

The pairing state that we have proposed is an orbital-antisymmetric spin-triplet state that results in a Knight shift below T_c, breaks time-reversal symmetry, and produces a jump in the shear modulus C_{66} at T_c which is in qualitative agreement with the experiments [51, 52, 84, 85, 186–188]. However, it predicts a linear cusp for the splitting of the phase transition under uniaxial strain which has not been observed [183, 184]. It also has a horizontal line node at $k_z = 0, \pm 2\pi/c$ and thermal conductivity [165], ultrasound attenuation [187], field-angle-dependent heat capacity [239], and quasiparticle interference [168] seem to suggest vertical line nodes along the Γ-M direction, but the situation is disputed and some experiments suggest horizontal line nodes instead [166, 167]. The other problem is that the gap node at $k_z = 0$ seems to imply that the pairing strength approaches zero in the limit of very small interlayer coupling. We have worked around this by suggesting that weak momentum-dependent spin-orbit couplings in the out-of-plane direction stabilize a purely local pairing state with the same symmetry. The existence of these terms is hypothetical at this point and has not been widely examined. Additionally the horizontal line nodes are inflated into Bogoliubov Fermi surfaces and may mimic diagonal vertical line nodes.

The pairing state that we have proposed is a natural choice, because of the two-component nature of the E_g irrep. Another possibility that has been recently proposed and has gained some attention is a state with $d_{x^2-y^2} \pm ig_{xy(x^2-y^2)}$ symmetry, because it is consistent with both broken time-reversal symmetry and the jump in the c_{66} shear modulus and it might explain the absence of a linear cusp under uniaxial strain [188, 211, 240]. This pairing state would only have vertical line nodes and even though the location and direction of the line nodes is disputed, the idea of vertical line nodes is generally more popular than horizontal line nodes [165, 168, 187, 239]. On the other hand, this state is a less natural choice because it mixes the B_{1g} and the A_{2g} irreducible representations. Pairing states belonging to different irreps do not necessarily have the same critical temperature so this state requires fine-tuning to explain why superconductivity and time-reversal symmetry breaking set in at the same temperature [42]. Finally the *g*-wave form factor might seem improbable because of the very long-range pairing that it implies, but it has been pointed out that nearest-neighbor Coulomb repulsion leads to a competitive instability in this channel at weak-coupling [241].

5.8 Summary

In this chapter we have discussed the possibility of even-parity chiral superconductivity in Sr_2RuO_4 [234]. This material has long been the best candidate for odd-parity spin-triplet chiral p-wave superconductivity [82, 83]. This proposal became a well-established fact, but the recent revisiting of old Knight shift measurements is inconsistent with this scenario [84, 85]. The spin-singlet response detected in the new measurements cannot be unified with a chiral p-wave state and the community is now more amenable to considering an even-parity pairing state. There is substantial evidence for a two-component order parameter from the onset of time-reversal symmetry breaking [51, 52, 185] and a jump in the shear modulus c_{66} [186–188] at the critical temperature. A chiral d-wave state with E_g symmetry is naturally consistent with these observations, but has been dismissed previously because of the quasi-two-dimensional electronic structure [157–161].

We fit DFT results from [160] to the most general tight-binding Hamiltonian for a three-orbital system in the D_{4h} point group. Models of this type have been considered in the literature before [214–216], however, symmetry-allowed momentum-dependent spin-orbit coupling terms have not been included so far. To stay faithful to the shape of the Fermi surface, we parameterize our tight-binding model by fitting it to the DFT band structure given in [160]. We assume on-site interactions of the Hubbard-Kanamori type [218, 219] for a purely local pairing interaction. Following the established literature we assume that the interaction constants are sufficiently renormalized such that Hund's coupling can stabilize superconductivity [118, 224]. The chiral d-wave nature of the order parameter with E_g symmetry is encoded in the orbital degree, where it is expressed as an s-wave orbitally-antisymmetric spin-triplet state. We find that the orbitally non-trivial E_g state becomes energetically favorable once we take into account the symmetry-allowed momentum-dependent spin-orbit coupling terms. These terms tune the ground state between order parameters of different symmetry already for surprisingly small values. This is important because their smallness implies that the experimentally established two-dimensionality of the Fermi surface remains intact.

Below the critical temperature we solve the gap equation by iteration to obtain the self-consistent gap magnitude in the A_{1g} and the E_g state. An interesting fact about the E_g state that we have proposed is that because it combines even parity, time-reversal symmetry breaking, and interband pairing it naturally gives rise to Bogoliubov Fermi surfaces [133, 140, 234]. Although they are expected to be small, these might have profound implications on the low-energy structure of the quasiparticles and for thermodynamic observables [93, 140]. To be consistent with the experimental observations the superconducting state has to result in a suppression of the Knight shift below the critical temperature which we verify for both the A_{1g} and the E_g state.

Chapter 6

Conclusion

In this thesis we explore novel phenomena in multiband superconductors. The common theme of all chapters is that orbitally non-trivial pairing can give rise to anomalous pairing states which have interesting properties.

In Chapter 3 we have presented the concept of Bogoliubov Fermi surfaces [133]. They generically appear in centrosymmetric even-parity superconductors with multiple bands that break time-reversal symmetry. The presence of orbitally non-trivial pairing channels implies that the gap product is non-unitary. A non-zero time-reversal odd part of the non-unitary gap product is directly responsible for the appearance of Bogoliubov Fermi surfaces, as can be understood within a low-energy effective theory. There the time-reversal odd part gives rise to a pseudomagnetic field which lifts the pseudospin degeneracy and inflates point and line nodes into extended Bogoliubov Fermi surfaces. The Bogoliubov Fermi surfaces are protected by a $\mathbb{Z}_2$ topological invariant. We have demonstrated the properties of the Bogoliubov Fermi surfaces on the example of the Luttinger-Kohn Hamiltonian of $j = 3/2$ fermions in the cubic crystal system. This model has served as a paradigmatic model in the literature [66, 76, 77, 133, 135, 136].

The topological protection of the Bogoliubov Fermi surfaces alone does not guarantee their existence. The inflation of the nodes increases the nodal area in momentum space and thus costs condensation energy, which is expected to be detrimental for superconductivity [90]. Therefore, in Chapter 4 we investigate the thermodynamic stability of a time-reversal symmetry-breaking pairing state with Bogoliubov Fermi surfaces in contrast to one that preserves time-reversal symmetry [140]. Using BCS mean-field theory we compute the phase diagram as a function of spin-orbit coupling and temperature. We find a rich phase diagram which supports stable Bogoliubov Fermi surfaces. In the limit of vanishing spin-orbit coupling we confirm the prediction by Ho and Yip [137] that a time-reversal symmetric pairing state is stable. For increasing spin-orbit coupling, the multiband nature of the model gives rise to a first-order phase transition from the normal into the superconducting state. This can be understood by the competition between intra- and interband pairing which is controlled by cubic anisotropy. For moderate values of the spin-orbit coupling we find a time-reversal symmetry-breaking state with Bogoliubov Fermi surfaces, which confirms the prediction from [66]. Close to the time-reversal symmetric phase and at low temperatures this state is reentrant and shows a first-order transition into the time-reversal symmetric state. Due to the lifting of the pseudospin degeneracy, the time-reversal symmetry-breaking state exhibits a residual density of states around the Fermi energy as large as 20 % of the normal state. Furthermore, the superconductivity gives rise to a subdominant magnetic order parameter which, however, is small even for large values of the residual density of states, which confirms the hypothesis that time-reversal symmetry-breaking superconductors only have a weak intrinsic magnetisation [148]. These result are encouraging for experimental searches of Bogoliubov Fermi surfaces. Heavy-fermion superconductors are a promising platform and it is intriguing that a large residual density of states has been observed in URu_2Si_2 [141].

In Chapter 5 we turned our attention the unconventional superconductor Sr_2RuO_4 [82] which has recently attracted a lot of attention. For several decades it was believed that this was a textbook example of an odd-parity

chiral p-wave superconductor [83]. A recent repetition of early Knight shift experiments has cast serious doubt on this paradigm and strongly suggests a spin-singlet pairing state [84, 85]. We propose an alternative pairing state that is consistent with the updated experimental situation. We employ existing DFT results [160] and fit the most general normal-state Hamiltonian for the tetragonal point group to obtain a quantitatively faithful model of the Fermi surface. In contrast to existing work [214–216], we also include symmetry-allowed momentum-dependent spin-orbit coupling terms. Starting from on-site interactions of the Hubbard-Kanamori type [219, 220] we derived all the possible even-parity Cooper pairs. By a similar reasoning as in [118] we argue that these interactions can give rise to a weak-coupling instability. Solving the linearized gap equation, we are able to show it is possible to tune the leading instability into an even-parity state with E_g symmetry by varying spin-orbit coupling parameters with a small range. This does not affect the experimentally observed two-dimensionality of the Fermi surface. Because this pairing state has even-parity it acts as a pseudospin-singlet and gives rise to a singlet response in the spin susceptibility. This purely local E_g pairing state is orbitally non-trivial and because it breaks time-reversal symmetry it is expected to host Bogoliubov Fermi surfaces.

Outlook

There are some obvious extensions to the work presented in this thesis. In Chapter 3 we have presented the basic theory of Bogoliubov Fermi surfaces, which are surfaces of ungapped quasiparticles in momentum space. One interesting question is to what extent these Bogoliubov Fermi surfaces behave like regular Fermi surfaces. The main reason for this question is that the quasiparticles that make up the Bogoliubov Fermi surfaces have no definite charge because they are superpositions of particle- and hole-like excitations, whereas the Fermi surface of a regular metal always consists of regular charged particles. Hence it is interesting to investigate whether Bogoliubov Fermi surfaces are able to exhibit quantum oscillations, which would also be a possible step towards their observation. In previous work, strain has been used to simulate quantum oscillations in nodal superconductors [242–244].

The work in Chapter 4 shows that Bogoliubov Fermi surfaces are stable in large parts of the parameter space. Due to the lifting of the pseudospin degeneracy, they lead to a residual density of states at zero energy and therefore also to a residual value at zero temperature in several thermodynamic observables. Since the size of the Bogoliubov Fermi surfaces and therefore the magnitude of the residual values depends on the ratio of the interband pairing potential to the band splitting, materials where this ratio is as large as possible are the best candidates. Heavy-fermion superconductors satisfy these criteria and are therefore a promising platform. A residual thermal conductivity at zero field and at low temperatures has been observed in the heavy-fermion compound URu_2Si_2 [141]. Identifying a particular experimental platform for the Bogoliubov Fermi surfaces is an important step and material-specific *ab initio* studies are necessary to make quantitative predictions.

Only very briefly we have touched upon the topic of "superconducting fitness" [113, 114]. The superconducting fitness is a concept similar to Anderson's theorem to make statements concerning the stability of different superconducting states. It introduces measures to identify terms in the normal-state Hamiltonian that are beneficial or detrimental to a weak-coupling instability. Currently this concept is limited to determining the critical temperature of the superconductor. In Chapter 4 and in Appendix D we have studied the time-reversal symmetry-breaking phase transition in detail. A possible extension of superconducting fitness is to identify terms in the normal-state Hamiltonian that are beneficial or detrimental to a time-reversal symmetry broken state.

In Chapter 5 we have studied superconductivity a realistic three-dimensional model of the layered perovskite

superconductor Sr_2RuO_4. As a simple model for the pairing mechanism we assumed purely local interaction of the Hubbard-Kanamori type. This will inadvertently only give rise to local Cooper pairs and even-parity pairing. Within this framework we have found that an orbitally-antisymmetric spin-triplet state in the E_g irrep can be stabilised. Spin fluctuations have usually been thought important for the pairing mechanism in Sr_2RuO_4 so it is interesting to study how our prediction holds up in this scenario [205, 208, 245–248]. Studying pairing from spin fluctuations within the random-phase approximation [209] is a good first step and can be complemented and extended by other methodologies, such as the fluctuation-exchange approximation [249] or the weak-coupling renormalization group [250, 251]. However, in contrast to previous work our full three-dimensional model of the normal-state band structure has to be considered. In addition, our newly proposed pairing state calls for the reevaluation of the theoretical predictions for the various experimental probes that are available.

Appendix A

Character tables

In mathematics a group is the combination of a set G with an operation $\cdot$, usually denoted by $(G, \cdot)$. The operation between acts between any two elements of the set such that the result is also an element of that set, i.e. the group is closed under the operation. Any group must satisfy the four group axioms:

Closure For all $a, b \in G$ the result of $a \cdot b \in G$.

Associativity For all $a, b, c \in G$ it holds that $a \cdot (b \cdot c) = (a \cdot b) \cdot c$.

Identity There is one element $e \in G$ such that $e \cdot g = g$ and $g \cdot e = g$ for any $g \in G$.

Inverse For each element $g \in G$ there is an element $g^{-1} \in G$ such that $g^{-1} \cdot g = g \cdot g^{-1} = e$.

These group axioms are very abstract and apply independent of the representation of the group. The linear representation D of a group is G on a vector space V is a group homomorphism

$$D : G \to \mathrm{GL}(V), \tag{A.1}$$
$$g \mapsto D(g), \tag{A.2}$$

where $\mathrm{GL}(V)$ is the general linear group over V which is usually expressed as a set of invertible matrices.

A representation D of the group G is said to be reducible if there is an invariant subspace $W \subset V$ such that $D(g)w \in W$ for all $w \in W$ and all $g \in G$. The representation is called reducible if a non-trivial invariant subspace exists, otherwise it is called irreducible.

Two elements $a, b \in G$ are said to be conjugate if there exists an element $g \in G$ such that $b = g^{-1}ag$. Conjugacy is an equivalence relation and therefore partition G into equivalence classes called conjugacy classes.

In crystallography the point group is a group of symmetry operations which leave at least one point fixed. Because the point groups have to leave the lattice invariant, we can restrict ourselves to finite point groups. One such finite point group is the D_{4h} tetragonal point group. The group contains the following symmetry operations

$$D_{4h} = \{E, 2C_4, C_2, 2C_2', 2C_2'', I, 2S_4, \sigma_h, 2\sigma_v, 2\sigma_d\}, \tag{A.3}$$

where E is the identity, $2C_4$ are clockwise and counterclockwise four-fold rotations around the z axis (principal axis), C_2 is a two-fold rotations around are the z axis, $2C_2'$ are two-fold rotations around the x and y axis, $2C_2''$ are two-fold rotations around the axes $x = y$ and $x = -y$, I is inversion, $2S_4$ are rotoinversions which are combinations of $2C_4$ and I, σ_h is reflection at the $z = 0$ plane, $2\sigma_v$ are reflections at the $x = 0$ and $y = 0$ planes, and $2\sigma_d$ are reflections at the $(x - y) = 0$ and $(x + y) = 0$ planes.

We can express each symmetry operation as a matrix which represents how vectors or functions that were chosen as a basis set transform under the action of the symmetry operations. The form of these matrices depends on the choice of the basis, however, the trace of the matrix is independent of the basis and is referred

irrep	e	I	C_4	C_2	C_2'	C_2''	S_4	σ_h	σ_v	σ_d
A_{1g}	1	1	1	1	1	1	1	1	1	1
A_{2g}	1	1	1	1	−1	−1	1	1	−1	−1
B_{1g}	1	1	−1	1	1	−1	−1	1	1	−1
B_{2g}	1	1	−1	1	−1	1	−1	1	−1	1
E_g	2	2	0	−2	0	0	0	−2	0	0
A_{1u}	1	−1	1	1	1	1	−1	−1	−1	−1
A_{2u}	1	−1	1	1	−1	−1	−1	−1	1	1
B_{1u}	1	−1	−1	1	1	−1	1	−1	−1	1
B_{2u}	1	−1	−1	1	−1	1	1	−1	1	−1
E_u	2	−2	0	−2	0	0	0	2	0	0

■ *Table A.1.* Character table for D_{4h}.

irrep	Rot	d	g
A_{1g}		z^2	$(x^2 - y^2)^2 - 4x^2y^2, z^4$
A_{2g}	R_z		$xy(x^2 - y^2)$
B_{1g}		$x^2 - y^2$	$z^2(x^2 - y^2)$
B_{2g}		xy	xyz^2
E_g	$\{R_x, R_y\}$	$\{xz, yz\}$	$\{xz(x^2 - 3y^2), yz(3x^2 - y^2)\}, \{xz^3, yz^3\}$
		p	f
A_{1u}			
A_{2u}		z	z^3
B_{1u}			xyz
B_{2u}			$z(x^2 - y^2)$
E_u		$\{x, y\}$	$\{x(x^2 - 3y^2), y(3x^2 - y^2)\}, \{xz^2, yz^2\}$

■ *Table A.2.* Symmetry of rotations and Cartesian products for the point group D_{4h}.

to as the character of the symmetry operation. An interesting property is that all elements of a conjugacy class have the same character. This allows to write these characters as a table where the rows are irreducible representations and the columns are the characters of the conjugacy classes of the group elements. For the point group D_{4h} we give this so called character table in Tab. A.1.

The normal-state Hamiltonian of the electrons in a crystal is invariant under the operations of the point group. Therefore it is possible to write it as a linear combination of basis states which belong to different irreducible representations. These basis states are usually either rotations or spherical harmonics. Their character under the symmetry operations classifies them according to the irreducible representations. The symmetries of rotations and real spherical harmonics (also called Cartesian products) for the D_{4h} point group are listed in Tab. A.2.

In practice, for the one-dimensional irreducible representations the character indicates a sign change under the corresponding symmetry operation. For example chose the lowest-order polynomial of the B_{1g} representation from Tab. A.2 and apply the C_4 operation. The effect of C_4 it to let $x \to y$ and $y \to -x$, which

	A_{1g}	A_{2g}	B_{1g}	B_{2g}	E_g	A_{1u}	A_{2u}	B_{1u}	B_{2u}	E_u
A_{1g}	A_{1g}	A_{2g}	B_{1g}	B_{2g}	E_g	A_{1u}	A_{2u}	B_{1u}	B_{2u}	E_u
A_{2g}	A_{2g}	A_{1g}	B_{2g}	B_{1g}	E_g	A_{2u}	A_{1u}	B_{2u}	B_{1u}	E_u
B_{1g}	B_{1g}	B_{2g}	A_{1g}	A_{2g}	E_g	B_{1u}	B_{2u}	A_{1u}	A_{2u}	E_u
B_{2g}	B_{2g}	B_{1g}	A_{2g}	A_{1g}	E_g	B_{2u}	B_{1u}	A_{2u}	A_{1u}	E_u
E_g	E_g	E_g	E_g	E_g	$A_{1g} \oplus [A_{2g}] \oplus B_{1g} \oplus B_{2g}$	E_u	E_u	E_u	E_u	$A_{1u} \oplus A_{2u} \oplus B_{1u} \oplus B_{2u}$
A_{1u}	A_{1u}	A_{2u}	B_{1u}	B_{2u}	E_u	A_{1g}	A_{2g}	B_{1g}	B_{2g}	E_g
A_{2u}	A_{2u}	A_{1u}	B_{2u}	B_{1u}	E_u	A_{2g}	A_{1g}	B_{2g}	B_{1g}	E_g
B_{1u}	B_{1u}	B_{2u}	A_{1u}	A_{2u}	E_u	B_{1g}	B_{2g}	A_{1g}	A_{2g}	E_g
B_{2u}	B_{2u}	B_{1u}	A_{2u}	A_{1u}	E_u	B_{2g}	B_{1g}	A_{2g}	A_{1g}	E_g
E_u	E_u	E_u	E_u	E_u	$A_{1u} \oplus A_{2u} \oplus B_{1u} \oplus B_{2u}$	E_g	E_g	E_g	E_g	$A_{1g} \oplus [A_{2g}] \oplus B_{1g} \oplus B_{2g}$

■ *Table A.3.* Product table for the D_{4h} point group between the irreps of odd and even parity. In the products of two identical degenerate representations, those terms antisymmetric with respect to particle permutation are indicated by square brackets.

implies

$$C_4(x^2 - y^2) = (y)^2 - (-x)^2 = -(x^2 - y^2), \tag{A.4}$$

which is consistent with the character -1 in Tab. A.1.

For the two-dimensional irreducible representations the character indicates the trace of the matrix the corresponds to the symmetry operations. For example chose the lowest-order polynomials of the E_u representation from Tab. A.2 and again apply the C_4 operation

$$C_4 \begin{pmatrix} x \\ y \end{pmatrix} = \begin{pmatrix} y \\ -x \end{pmatrix} = \begin{pmatrix} 0 & 1 \\ -1 & 0 \end{pmatrix} \begin{pmatrix} x \\ y \end{pmatrix}. \tag{A.5}$$

The trace of this matrix is zero which is consistent with the character in Tab. A.1.

In multi-orbital systems it happens that we have to form the direct product of the orbital and spin Hilbert spaces. The orbital and spin degrees of freedom may transform differently under the symmetry operations of the point group. To find the irreducible representation of the resulting direct product we have to form the group product. The products are tabulated in product table as for the D_{4h} point group in Tab. A.3.

Appendix B

Angular momentum

A good understanding of the quantum mechanical angular momentum is very important in solid state physics. In a solid, the electrons are tightly bound to the atomic cores in their respective atomic orbitals. The atomic orbitals are described by the principal quantum number n, the orbital angular momentum quantum number l, and the magnetic quantum number m. Generally, we are only interested in the effects of itinerant electrons in the solid, so only the valence shell electrons of the atoms really count. These all have the same quantum numbers n and l. In this appendix we will briefly review how the point group operations act on the orbital angular momentum and how orbital and spin angular momentum interact.

B.1 Point group operations for angular momentum

Defining the quantization axis along the z direction, the z component of the angular momentum operator is defined as

$$L_z|l,m\rangle = \hbar m|l,m\rangle, \tag{B.1}$$

with angular momentum eigenstates $|l,m\rangle$ with orbital angular momentum quantum number l and magnetic quantum number m. By a simple counting argument, the ladder operators for the angular momentum states can be derived as

$$L_\pm|l,m\rangle = \hbar\sqrt{l(l+1) - m(m\pm 1)}|l,m\pm 1\rangle. \tag{B.2}$$

The commutation relations imply for the remaining components that

$$L_x = \frac{1}{2}(L_+ + L_-), \tag{B.3}$$

$$L_y = \frac{1}{2i}(L_+ - L_-). \tag{B.4}$$

Equipped with these definitions we can easily derive the functional form of the angular momentum operator for $l = 2$. This corresponds to the d orbitals which we use often throughout this thesis. In the basis $(|2,2\rangle, |2,1\rangle, |2,0\rangle, |2,-1\rangle, |2,-2\rangle)^T$ the matrix form of these operators is

$$L_x = \hbar \begin{pmatrix} 0 & 1 & 0 & 0 & 0 \\ 1 & 0 & \sqrt{\frac{3}{2}} & 0 & 0 \\ 0 & \sqrt{\frac{3}{2}} & 0 & \sqrt{\frac{3}{2}} & 0 \\ 0 & 0 & \sqrt{\frac{3}{2}} & 0 & 1 \\ 0 & 0 & 0 & 1 & 0 \end{pmatrix}, \tag{B.5}$$

$$L_y = \hbar \begin{pmatrix} 0 & -i & 0 & 0 & 0 \\ i & 0 & -i\sqrt{\frac{3}{2}} & 0 & 0 \\ 0 & i\sqrt{\frac{3}{2}} & 0 & -i\sqrt{\frac{3}{2}} & 0 \\ 0 & 0 & i\sqrt{\frac{3}{2}} & 0 & -i \\ 0 & 0 & 0 & i & 0 \end{pmatrix}, \tag{B.6}$$

$$L_z = \hbar \begin{pmatrix} 2 & 0 & 0 & 0 & 0 \\ 0 & 1 & 0 & 0 & 0 \\ 0 & 0 & 0 & 0 & 0 \\ 0 & 0 & 0 & -1 & 0 \\ 0 & 0 & 0 & 0 & -2 \end{pmatrix}. \tag{B.7}$$

Now we are interested in deriving the form of the point group operations for the $l = 2$ orbitals. We choose the D_{4h} tetragonal point group, again because we use it often throughout this thesis. The group contains the following symmetry operations

$$D_{4h} = \{E, 2C_4, C_2, 2C_2', 2C_2'', I, 2S_4, \sigma_h, 2\sigma_v, 2\sigma_d\}, \tag{B.8}$$

where E is the identity, $2C_4$ are clockwise and counterclockwise four-fold rotations around the z axis (principal axis), C_2 is a two-fold rotations around are the z axis, $2C_2'$ are two-fold rotations around the x and y axis, $2C_2''$ are two-fold rotations around the axes $x = y$ and $x = -y$, I is inversion, $2S_4$ are rotoinversions which are combinations of $2C_4$ and I, σ_h is reflection at the $z = 0$ plane, $2\sigma_v$ are reflections at the $x = 0$ and $y = 0$ planes, and $2\sigma_d$ are reflections at the $(x - y) = 0$ and $(x + y) = 0$ planes.

The identity E and inversion I are trivial and we neglect the rotoinversion S_4 for brevity. As a reminder, the rotation operator of an angular momentum $\boldsymbol{L}$ around an axis parallel to $\boldsymbol{n}$ by an angle ϕ is given by

$$D_{\boldsymbol{n}}(\phi) = \exp\left(-i\frac{\phi}{\hbar}\boldsymbol{n} \cdot \boldsymbol{L}\right). \tag{B.9}$$

This implies for the rotations

$$C_4 = \exp\left(-i\frac{\pi}{2}L_z\right), \tag{B.10}$$

$$C_2'(x) = \exp(-i\pi L_x), \tag{B.11}$$

$$C_2''(x = y) = \exp\left(-i\frac{\pi}{\sqrt{2}}(L_x + L_y)\right). \tag{B.12}$$

The reflection operation can also be cast into the form of a rotation. In fact, reflection at a plane with normal vector $\boldsymbol{n}$ is equivalent to rotation by π around the axis parallel to $\boldsymbol{n}$. Hence, we find for the reflection operators

$$\sigma_h = \exp(-i\pi L_z), \tag{B.13}$$

$$\sigma_v(x) = \exp(-i\pi L_y), \tag{B.14}$$

$$\sigma_d(x = y) = \exp\left(-i\frac{\pi}{\sqrt{2}}(L_x - L_y)\right). \tag{B.15}$$

The position space representation of the $l = 2$ spherical harmonics is complex, but the probability density of atomic orbitals shall be real. Therefore, to find the correspondence of the $l = 2$ spherical harmonics with the

d orbitals, we recombine them into the *real spherical harmonics*

$$|d_{3z^2-r^2}\rangle = |2,0\rangle, \tag{B.16}$$

$$|d_{x^2-y^2}\rangle = \frac{1}{\sqrt{2}}(|2,-2\rangle + |2,2\rangle), \tag{B.17}$$

$$|d_{yz}\rangle = \frac{i}{\sqrt{2}}(|2,-1\rangle + |2,1\rangle), \tag{B.18}$$

$$|d_{xz}\rangle = \frac{1}{\sqrt{2}}(|2,-1\rangle - |2,1\rangle), \tag{B.19}$$

$$|d_{xy}\rangle = \frac{i}{\sqrt{2}}(|2,-2\rangle - |2,2\rangle). \tag{B.20}$$

In this thesis we are only interested in a submanifold of these real spherical harmonics, which is why we project the symmetry operations derived above into the subspace spanned by d_{yz}, d_{xz}, and d_{xy}. The matrix elements of the symmetry operation O are then given by $O_{ab} = \langle d_a | O | d_b \rangle$ with $a, b \in \{yz, xz, xy\}$. In the basis $(|d_{yz}\rangle, |d_{xz}\rangle, |d_{xy}\rangle)^T$ the matrix form of the symmetry operations is

$$C_4 = \begin{pmatrix} 0 & 1 & 0 \\ -1 & 0 & 0 \\ 0 & 0 & -1 \end{pmatrix}, \qquad C_2'(x) = \begin{pmatrix} 1 & 0 & 0 \\ 0 & -1 & 0 \\ 0 & 0 & -1 \end{pmatrix}, \qquad C_2''(x=y) = \begin{pmatrix} 0 & -1 & 0 \\ -1 & 0 & 0 \\ 0 & 0 & 1 \end{pmatrix}, \tag{B.21}$$

$$\sigma_h = \begin{pmatrix} -1 & 0 & 0 \\ 0 & -1 & 0 \\ 0 & 0 & 1 \end{pmatrix}, \qquad \sigma_v(x) = \begin{pmatrix} -1 & 0 & 0 \\ 0 & 1 & 0 \\ 0 & 0 & -1 \end{pmatrix}, \qquad \sigma_d(x=y) = \begin{pmatrix} 0 & 1 & 0 \\ 1 & 0 & 0 \\ 0 & 0 & 1 \end{pmatrix}, \tag{B.22}$$

and for reference, in the even more restricted basis of $(|d_{yz}\rangle, |d_{xz}\rangle)^T$ we have

$$C_4 = \begin{pmatrix} 0 & 1 \\ -1 & 0 \end{pmatrix}, \qquad C_2'(x) = \begin{pmatrix} 1 & 0 \\ 0 & -1 \end{pmatrix}, \qquad C_2''(x=y) = \begin{pmatrix} 0 & -1 \\ -1 & 0 \end{pmatrix}, \tag{B.23}$$

$$\sigma_h = \begin{pmatrix} -1 & 0 \\ 0 & -1 \end{pmatrix}, \qquad \sigma_v(x) = \begin{pmatrix} -1 & 0 \\ 0 & 1 \end{pmatrix}, \qquad \sigma_d(x=y) = \begin{pmatrix} 0 & 1 \\ 1 & 0 \end{pmatrix}. \tag{B.24}$$

B.2 Angular momentum coupling

We want to briefly investigate how the coupling between $l = 1$ orbital angular momentum and $s = 1/2$ spin angular momentum gives rise to $j = 3/2$ states. For the angular momenta $l = 1$ and $s = 1/2$ we have the following states

$$|l, m_l\rangle = \begin{cases} |1,1\rangle, \\ |1,0\rangle, \\ |1,-1\rangle, \end{cases} \qquad |s, m_s\rangle = \begin{cases} \left|\frac{1}{2}, \frac{1}{2}\right\rangle, \\ \left|\frac{1}{2}, -\frac{1}{2}\right\rangle. \end{cases} \tag{B.25}$$

The total angular momentum j takes on the values $j = l + s, \dots, |l - s|$, i.e. $j = 3/2, 1/2$. This implies the following six states in the new basis of the total angular momentum

$$|j, m_j\rangle = \left\{ \left|\frac{3}{2}, \frac{3}{2}\right\rangle, \left|\frac{3}{2}, \frac{1}{2}\right\rangle, \left|\frac{3}{2}, -\frac{1}{2}\right\rangle, \left|\frac{3}{2}, -\frac{3}{2}\right\rangle, \left|\frac{1}{2}, \frac{1}{2}\right\rangle, \left|\frac{1}{2}, -\frac{1}{2}\right\rangle \right\}. \tag{B.26}$$

Because it holds that $m_j = m_s + m_l$, we can immediately relate the state $|3/2, 3/2\rangle$ to the one in the basis of l and s

$$\left|\frac{3}{2}, \frac{3}{2}\right\rangle = \left|1, \frac{1}{2}\right\rangle \tag{B.27}$$

Then we apply $J_- = L_- + S_-$ on this state to find the remaining ones with $j = 3/2$. In the following we write the states in the form $|j, m_j\rangle$ on the left-hand side and in the form $|m_l, m_s\rangle$ on the right-hand side. As an example, to find $|3/2, 1/2\rangle$ we apply J_- to $|3/2, 3/2\rangle$

$$J_- \left|\frac{3}{2}, \frac{3}{2}\right\rangle = (L_- + S_-) \left|1, \frac{1}{2}\right\rangle$$
$$\hbar\sqrt{3} \left|\frac{3}{2}, \frac{1}{2}\right\rangle = \hbar\sqrt{2} \left|0, \frac{1}{2}\right\rangle + \hbar \left|1, -\frac{1}{2}\right\rangle$$
$$\left|\frac{3}{2}, \frac{1}{2}\right\rangle = \sqrt{\frac{2}{3}} \left|0, \frac{1}{2}\right\rangle + \sqrt{\frac{1}{3}} \left|1, -\frac{1}{2}\right\rangle. \tag{B.28}$$

$$\tag{B.29}$$

Similarly, we proceed down the chain to find the two other states

$$\left|\frac{3}{2}, \frac{1}{2}\right\rangle = \sqrt{\frac{2}{3}} \left|0, -\frac{1}{2}\right\rangle + \sqrt{\frac{1}{3}} \left|-1, \frac{1}{2}\right\rangle. \tag{B.30}$$

$$\left|\frac{3}{2}, -\frac{3}{2}\right\rangle = \left|-1, -\frac{1}{2}\right\rangle \tag{B.31}$$

For the states with quantum number $j = 1/2$ we use the fact that states have to orthonormal in quantum mechanics. To obtain the quantum number $m_j = 1/2$ we have to combine either $l = 0, s = 1/2$ or $l = 1, s = -1/2$, so we choose the ansatz

$$\left|\frac{1}{2}, \frac{1}{2}\right\rangle = c_1 \left|1, -\frac{1}{2}\right\rangle + c_2 \left|0, \frac{1}{2}\right\rangle. \tag{B.32}$$

From the normalization condition we obtain

$$\left\langle\frac{1}{2}, \frac{1}{2} \middle| \frac{1}{2}, \frac{1}{2}\right\rangle = 1 = |c_1|^2 + |c_2|^2$$
$$\implies |c_1|^2 = 1 - |c_2|^2, \tag{B.33}$$

and from the orthogonality requirement we obtain a second condition for the coefficients

$$\left\langle\frac{3}{2}, \frac{1}{2} \middle| \frac{1}{2}, \frac{1}{2}\right\rangle = 0 = c_1 \sqrt{\frac{1}{3}} + c_2 \sqrt{\frac{2}{3}}. \tag{B.34}$$

Solving this system of equations is easy and under consideration of the established phase conventions [252] we find

$$\left|\frac{1}{2}, \frac{1}{2}\right\rangle = \sqrt{\frac{2}{3}} \left|1, -\frac{1}{2}\right\rangle - \sqrt{\frac{1}{3}} \left|0, \frac{1}{2}\right\rangle |0, 1/2\rangle. \tag{B.35}$$

Then again, applying the J_- operator to find the $|1/2, -1/2\rangle$ state as

$$\left|\frac{1}{2}, -\frac{1}{2}\right\rangle = \sqrt{\frac{1}{3}} \left|0, -\frac{1}{2}\right\rangle - \sqrt{\frac{2}{3}} \left|-1, \frac{1}{2}\right\rangle. \tag{B.36}$$

In summary we have

$$\left| \frac{3}{2}, \frac{3}{2} \right\rangle = \left| 1, \frac{1}{2} \right\rangle, \tag{B.37}$$

$$\left| \frac{3}{2}, \frac{1}{2} \right\rangle = \sqrt{\frac{2}{3}} \left| 0, \frac{1}{2} \right\rangle + \sqrt{\frac{1}{3}} \left| 1, -\frac{1}{2} \right\rangle, \tag{B.38}$$

$$\left| \frac{3}{2}, \frac{1}{2} \right\rangle = \sqrt{\frac{2}{3}} \left| 0, -\frac{1}{2} \right\rangle + \sqrt{\frac{1}{3}} \left| -1, \frac{1}{2} \right\rangle, \tag{B.39}$$

$$\left| \frac{3}{2}, -\frac{3}{2} \right\rangle = \left| -1, -\frac{1}{2} \right\rangle, \tag{B.40}$$

$$\left| \frac{1}{2}, \frac{1}{2} \right\rangle = \sqrt{\frac{2}{3}} \left| 1, -\frac{1}{2} \right\rangle - \sqrt{\frac{1}{3}} \left| 0, \frac{1}{2} \right\rangle, \tag{B.41}$$

$$\left| \frac{1}{2}, -\frac{1}{2} \right\rangle = \sqrt{\frac{1}{3}} \left| 0, -\frac{1}{2} \right\rangle - \sqrt{\frac{2}{3}} \left| -1, \frac{1}{2} \right\rangle. \tag{B.42}$$

Appendix C

Path integrals

A central quantity in the description of superconductors is the free energy. From this all the thermodynamic properties can be derived. Moreover, in the weak-coupling theory the pairing state that is most stable is the one that minimizes the free energy. Therefore, it plays a major role in the selection of the pairing symmetry. The free energy is derived from the partition function of a quantum system which can conveniently be described as a path integral [253].

C.1   Path integral for free fermions

The propagator of the Schrödinger equation between a initial state $|i\rangle$ and a final state $|f\rangle$ is described by an integral over all paths connecting $\boldsymbol{r}_i$ at time t_i to $\boldsymbol{r}_f$ at time t_f, which is given as the path integral

$$\langle f|e^{-iHt/\hbar}|i\rangle = K(\boldsymbol{r}_f, t; \boldsymbol{r}_i, 0) = \int \mathcal{D}[\boldsymbol{r}]\, e^{iS[\boldsymbol{r}]/\hbar} \tag{C.1}$$

where we introduce the action

$$S[\boldsymbol{r}] = \int_0^t dt'\, \mathcal{L}(\boldsymbol{r}, \dot{\boldsymbol{r}}, t') = \int_0^t dt'\, [\boldsymbol{p}\dot{\boldsymbol{r}} - H(\boldsymbol{r}, \boldsymbol{p}, t')] \tag{C.2}$$

with conjugate variables $\boldsymbol{p}$ and $\boldsymbol{q}$ and the Lagrangian $\mathcal{L}(\boldsymbol{r}, \dot{\boldsymbol{r}}, t)$ which is related to the Hamiltonian by Legendre transformation. The canonical partition function is defined as the sum of the Boltzmann factors of all microstates λ which is usually written as a trace and can be related to the propagator with an imaginary time

$$Z = \mathrm{Tr}[e^{-\beta H}] = \sum_\lambda \langle \lambda|e^{-\beta H}|\lambda\rangle = K(t_f = -i\beta\hbar; t_i = 0). \tag{C.3}$$

This transformation of the statistical average into a path integral over periodic paths in imaginary time is also known as a *Wick rotation*. Hence we can write the partition function as a path integral in terms of conjugate variables with imaginary time $\tau = it/\hbar$

$$Z = \oint \mathcal{D}[\boldsymbol{r}] \exp(-S_E) = \oint \mathcal{D}[\boldsymbol{r}] \exp\left[-\int_0^\beta d\tau \left(-\frac{i}{\hbar}\boldsymbol{p}\partial_\tau \boldsymbol{r} + H(\boldsymbol{r}, \boldsymbol{p}, t')\right)\right]. \tag{C.4}$$

In canonical quantization we replace the conjugate variables by conjugate quantum fields $\boldsymbol{r} \to \phi$ and $\boldsymbol{p} \to i\hbar\bar{\phi}$ where ϕ is the complex conjugate of $\bar{\phi}$. The partition function and the action then take the form

$$Z = \int \mathcal{D}[\bar{\phi}, \phi] \exp[-S_E]$$
$$S_E = \int_0^\beta d\tau\, (\bar{\phi}\partial_\tau \phi + H[\bar{\phi}, \phi]) \tag{C.5}$$

with the measure

$$\mathcal{D}[\bar{\phi}, \phi] \equiv \prod_\tau d\bar{\phi}(\tau)\, d\phi(\tau). \tag{C.6}$$

The free energy can be derived from the partition function by taking the logarithm

$$F = -\frac{1}{\beta} \ln Z. \tag{C.7}$$

The path integral and therefore the partition function and all derived quantities can not only be evaluated for single-particle problems but also in many-body systems. Here we will evaluate it for free fermions to show the generic mechanics of this approach and also because we will use this result later in the context of symmetry-broken phases. The Hamiltonian for free fermions is given in momentum space as

$$H = \sum_{\boldsymbol{k}} \epsilon_{\boldsymbol{k}} c_{\boldsymbol{k}}^\dagger c_{\boldsymbol{k}}. \tag{C.8}$$

Before attempting the more complicated approach of path integrals we briefly recapitulate what result for the partition function the free energy we expect. The partition function can be determined by summing the Boltzmann factors of all microstates which can be expressed as a trace

$$Z = \mathrm{Tr}[e^{-\beta H}] = \mathrm{Tr}\left[\exp\left(-\beta \sum_{\boldsymbol{k}} \epsilon_{\boldsymbol{k}} c_{\boldsymbol{k}}^\dagger c_{\boldsymbol{k}}\right)\right]. \tag{C.9}$$

We carry out the trace in the eigenbasis of the Hamiltonian, where the eigenvalues of the number operator $c_{\boldsymbol{k}}^\dagger c_{\boldsymbol{k}}$ are simply the occupation numbers $n_{\boldsymbol{k}}$.

$$Z = \mathrm{Tr}\left[\prod_{\boldsymbol{k}} \exp(-\beta \epsilon_{\boldsymbol{k}} n_{\boldsymbol{k}})\right]. \tag{C.10}$$

Since we are dealing with fermions, there are only two possible occupations, $n_{\boldsymbol{k}} = 0$ and $n_{\boldsymbol{k}} = 1$, so the trace evaluates to

$$Z = \prod_{\boldsymbol{k}} [1 + \exp(-\beta \epsilon_{\boldsymbol{k}})], \tag{C.11}$$

and we get the free energy by taking the logarithm

$$F = -\frac{1}{\beta} \sum_{\boldsymbol{k}} \ln[1 + \exp(-\beta \epsilon_{\boldsymbol{k}})]. \tag{C.12}$$

For the path integral formulation we first construct the action by inserting the Lagrangian that we derive straight-forwardly from the Hamiltonian. The resulting action in imaginary time takes the simple form

$$S_E = \int_0^\beta d\tau \left[\sum_{\boldsymbol{k}} \bar{c}_{\boldsymbol{k}} \partial_\tau c_{\boldsymbol{k}} + H[\bar{c}, c]\right] = \int_0^\beta d\tau \left[\sum_{\boldsymbol{k}} \bar{c}_{\boldsymbol{k}} (\partial_\tau + \epsilon_{\boldsymbol{k}}) c_{\boldsymbol{k}}\right]. \tag{C.13}$$

Because the propagator is periodic in imaginary time it makes sense to transform the integral over imaginary time to frequency space. The transformation is conventionally chosen as

$$c = \frac{1}{\sqrt{\beta}} \sum_{i\omega_n} c_n e^{-i\omega_n \tau}, \tag{C.14}$$

with the fermionic Matsubara frequencies $\omega_n = (2n+1)\pi/\beta$. Expressed in terms of a sum over frequencies, the action reads

$$S_E = \sum_{\boldsymbol{k}, i\omega_n} \bar{c}_{\boldsymbol{k}n} (-i\omega_n + \epsilon_{\boldsymbol{k}}) c_{\boldsymbol{k}n}. \tag{C.15}$$

To formulate the partition function we plug in the action and the measure

$$Z = \int \prod_{\boldsymbol{k},i\omega_n} d\bar{c}_{\boldsymbol{k}n}\, dc_{\boldsymbol{k}n}\, \exp\left[-\sum_{\boldsymbol{k},i\omega_n} \bar{c}_{\boldsymbol{k}n}(-i\omega_n + \epsilon_{\boldsymbol{k}})c_{\boldsymbol{k}n}\right]. \tag{C.16}$$

Because the action is quadratic in fields, this integral resembles a Gaussian integral in higher dimensions. In fact, the following holds

$$\int d\bar{\phi}\, d\phi\, e^{-a\bar{\phi}\phi} = a \quad\overset{\text{multiple variables}}{\Longrightarrow}\quad \int \prod_j d\bar{\phi}_j\, d\phi_j\, e^{-\sum_j a_j \bar{\phi}_j \phi_j} = \prod_j a_j. \tag{C.17}$$

Hence the path integral can be evaluated directly and we find for the partition function in frequency space

$$Z = \prod_{\boldsymbol{k},i\omega_n}(-i\omega_n + \epsilon_{\boldsymbol{k}}). \tag{C.18}$$

Again the free energy is derived from the partition function by taking the logarithm. The logarithm of a product can be written as a sum of logarithms and we have

$$F = -\frac{1}{\beta}\sum_{\boldsymbol{k},i\omega_n} \ln(-i\omega_n + \epsilon_{\boldsymbol{k}}). \tag{C.19}$$

The trick to evaluate the sum over Matsubara frequencies is to rewrite it as a contour integral with the Fermi-Dirac distribution function $f(z) = (1 + e^{-\beta z})^{-1}$ which has simple poles at the Matsubara frequencies $z = i\omega_n$

$$\frac{1}{\beta}\sum_{i\omega_n} g(i\omega_n) = \frac{1}{2\pi i}\oint_\Gamma f(z)g(z)\,dz. \tag{C.20}$$

The contour integral will pick up these residues which is equivalent to a summation per the residue theorem. Because in our case $g(z)$ has a branch cut along the real axis we have to decompose the integral, as illustrated in Fig. C.1

$$\oint_\Gamma f(z)\ln(\epsilon_{\boldsymbol{k}} - z)\,dz = \oint_\gamma f(z)\ln(\epsilon_{\boldsymbol{k}} - z)\,dz$$
$$+ \lim_{\delta \to 0}\left(\int_{\epsilon_{\boldsymbol{k}}}^{\infty} f(z)\ln(\epsilon_{\boldsymbol{k}} - (z + i\delta))\,dz + \int_{\infty}^{\epsilon_{\boldsymbol{k}}} f(z)\ln(\epsilon_{\boldsymbol{k}} - (z - i\delta))\,dz\right). \tag{C.21}$$

By Cauchy's theorem the integral over γ vanishes. Swapping the limits in the second integral, it is possible to combine the remaining terms

$$\oint_\Gamma f(z)\ln(\epsilon_{\boldsymbol{k}} - z)\,dz = \lim_{\delta \to 0}\int_{\epsilon_{\boldsymbol{k}}}^{\infty}\left[f(z)\ln(\epsilon_{\boldsymbol{k}} - (z + i\delta)) - f(z)\ln(\epsilon_{\boldsymbol{k}} - (z - i\delta))\right]dz. \tag{C.22}$$

As we let $\delta \to 0$, the logarithm picks up a phase difference of 2π across the branch cut

$$\oint_\Gamma f(z)\ln(\epsilon_{\boldsymbol{k}} - z)\,dz = \int_{\epsilon_{\boldsymbol{k}}}^{\infty}\left\{f(z)[\ln(\epsilon_{\boldsymbol{k}} - z) + 2\pi i] - f(z)\ln(\epsilon_{\boldsymbol{k}} - z)\right\}dz \quad = 2\pi i\int_{\epsilon_{\boldsymbol{k}}}^{\infty} f(z)\,dz. \tag{C.23}$$
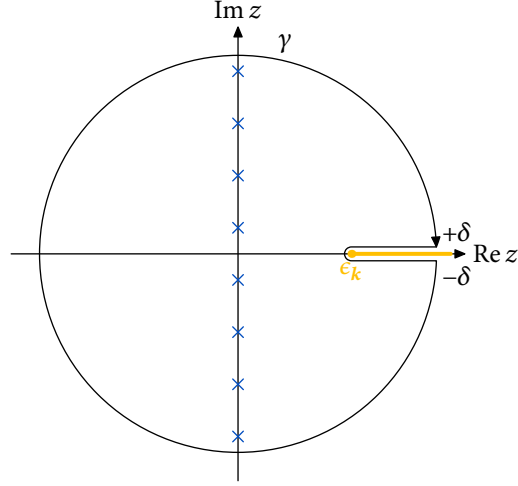
Thus the Matsubara sum has been transformed into to a simple one-dimensional integral and the free energy becomes

$$F = -\sum_{\boldsymbol{k}}\int_{\epsilon_{\boldsymbol{k}}}^{\infty} f(z)\,dz = -\sum_{\boldsymbol{k}}\int_{\epsilon_{\boldsymbol{k}}}^{\infty} \frac{1}{1 + e^{\beta z}}\,dz. \tag{C.24}$$

After straightforward substitution ($u = 1 + e^{\beta z}$) we find

$$F = -\sum_{\boldsymbol{k}}\left[-\frac{1}{\beta}\ln(1 + e^{-\beta z})\right]_{\epsilon_{\boldsymbol{k}}}^{\infty} = -\frac{1}{\beta}\sum_{\boldsymbol{k}}\ln(1 + e^{-\beta \epsilon_{\boldsymbol{k}}}). \tag{C.25}$$

This is the same as (C.12).

■ *Figure C.1.* Transformation of a Matsubara frequency sum into a contour integral. The blue crosses along the imaginary axis are the simple poles of the Fermi-Dirac distribution function which correspond to the fermionic Matsubara frequencies. In the case of free fermions, there is a branch cut along the positive real axis emanating from $\epsilon_{\boldsymbol{k}}$. The contour γ thus has to be deformed to exclude this branch cut as illustrated.

C.2 Path integral formulation of the free energy

As mentioned earlier, at weak coupling that superconducting state that is selected below the critical temperature T_c is the one that minimizes the mean-field free energy. In the following we will derive expressions for the mean-field free energy using the path integral formalism. The derivation closely follows and extends [253].

We start from a general interaction

$$H_{\text{int}} = -\sum_{\boldsymbol{k},\boldsymbol{k}',a} A^{\dagger}_{\boldsymbol{k},a} V_{\boldsymbol{k},\boldsymbol{k}';a} A_{\boldsymbol{k}',a}, \tag{C.26}$$

with the Grassmann variables for the fermion bilinears $A_{\boldsymbol{k},a} = c_{-\boldsymbol{k}}\gamma_a c_{\boldsymbol{k}}$ and basis matrices γ_a which encode the electronic degrees of freedom such as spin and orbital. The partition function is defined as the path integral

$$Z = \int \mathcal{D}[c^{\dagger},c]\exp\left[-\int_0^{\beta} d\tau(c^{\dagger}\partial_{\tau}c + H[c^{\dagger},c])\right] = \int \mathcal{D}[c^{\dagger},c]\exp(-S[c^{\dagger},c]), \tag{C.27}$$

with the action

$$S = \int_0^{\beta} d\tau\left[\sum_{\boldsymbol{k}} c^{\dagger}_{\boldsymbol{k}}(\partial_{\tau} + \vec{\epsilon}_{\boldsymbol{k}} \cdot \vec{\gamma})c_{\boldsymbol{k}} - \sum_{\boldsymbol{k},\boldsymbol{k}',a} A^{\dagger}_{\boldsymbol{k},a} V_{\boldsymbol{k},\boldsymbol{k}';a} A_{\boldsymbol{k}',a}\right]. \tag{C.28}$$

where $\vec{\epsilon}_{\boldsymbol{k}} \cdot \gamma$ denotes the free electron Hamiltonian expanded in terms of the basis matrices γ_a. We will now perform the Hubbard-Stratonovich decomposition of the interaction term. Therefore we introduce a fluctuating field α.

$$Z_{\alpha} = \int \mathcal{D}[\alpha^{\dagger},\alpha]\exp\left[-\int_0^{\beta} d\tau \sum_{\boldsymbol{k},\boldsymbol{k}',a} \alpha^{\dagger}_{\boldsymbol{k},a} V^{-1}_{\boldsymbol{k},\boldsymbol{k}';a}\alpha_{\boldsymbol{k}',a}\right]. \tag{C.29}$$

Adding this to the original partition function we obtain

$$Z = \int \mathcal{D}[c^{\dagger},c]\mathcal{D}[\alpha^{\dagger},\alpha]\,e^{-S},$$

$$S = \int_0^{\beta} d\tau\left[\sum_{\boldsymbol{k}} c^{\dagger}_{\boldsymbol{k}}(\partial_{\tau} + \vec{\epsilon}_{\boldsymbol{k}} \cdot \vec{\gamma})c_{\boldsymbol{k}} + \sum_{\boldsymbol{k},\boldsymbol{k}',a} \underbrace{(-A^{\dagger}_{\boldsymbol{k},a} V_{\boldsymbol{k},\boldsymbol{k}';a} A_{\boldsymbol{k}',a} + \alpha^{\dagger}_{\boldsymbol{k},a} V^{-1}_{\boldsymbol{k},\boldsymbol{k}';a}\alpha_{\boldsymbol{k}',a})}_{H_I}\right]. \tag{C.30}$$

We now introduce paring fields in terms of the fluctuating field $\Delta_{k,a} = \alpha_{k,a} - \sum_{k'} V_{k,k';a} A_{k',a}$ such that

$$
\begin{aligned}
H_I &= \sum_{k,k',a} \left(-A_{k,a}^\dagger V_{k,k';a} A_{k',a} + \alpha_{k,a}^\dagger V_{k,k';a}^{-1} \alpha_{k',a} \right) \\
&= \sum_{k,k',a} \left[-A_{k,a}^\dagger V_{k,k';a} A_{k',a} + \left(\Delta_{k,a}^\dagger + \sum_{k'',a} A_{k'',a}^\dagger V_{k'',k;a} \right) V_{k,k';a}^{-1} \left(\Delta_{k',a} + \sum_{k''',a} V_{k',k''';a} A_{k''',a} \right) \right] \\
&= \sum_{k,a} \left(A_{k,a}^\dagger \Delta_{k,a} + \Delta_{k,a}^\dagger A_{k,a} + \Delta_{k,a}^\dagger V_{k,k';a}^{-1} \Delta_{k',a} \right).
\end{aligned}
\tag{C.31}
$$

After this transformation we can write the partition function and the action in terms of the pairing field with the BdG-Hamiltonian $h_k[\Delta^\dagger, \Delta]$

$$
\begin{aligned}
Z &= \int \mathcal{D}[c^\dagger, c] \mathcal{D}[\Delta^\dagger, \Delta] \, e^{-S}, \\
S &= \int_0^\beta d\tau \left[\sum_k c_k^\dagger (\partial_\tau + h_k[\Delta^\dagger, \Delta]) c_k + \sum_{k,k',a} \Delta_{k,a}^\dagger V_{k,k';a}^{-1} \Delta_{k',a} \right].
\end{aligned}
\tag{C.32}
$$

In the following we will denote the sum over the basis matrices by a trace

$$
\sum_{k,k',a} \Delta_{k,a}^\dagger V_{k,k';a}^{-1} \Delta_{k',a} = \sum_{k,k'} \mathrm{Tr}[\Delta_k^\dagger V_{k,k'}^{-1} \Delta_{k'}]
\tag{C.33}
$$

The first term in the action is explicitly quadratic and therefore represents a Gaussian integral which can be integrated trivially by the rules of path integrals, which are outlined in detail in [253]

$$
Z = \int \mathcal{D}[\Delta^\dagger, \Delta] \int_0^\beta d\tau \prod_k \det(\partial_\tau + h_k[\Delta^\dagger, \Delta]) \exp\left[-\int_0^\beta d\tau \sum_{k,k'} \mathrm{Tr}[\Delta_k^\dagger V_{k,k'}^{-1} \Delta_{k'}] \right].
\tag{C.34}
$$

Writing the determinant back into the exponent we obtain the partition function with the effective action S_{eff} of the field Δ

$$
Z = \int \mathcal{D}[\Delta^\dagger, \Delta] e^{-S_{\mathrm{eff}}} = \int \mathcal{D}[\Delta^\dagger, \Delta] \exp\left\{ \int_0^\beta d\tau \left[\sum_k \mathrm{Tr} \ln(\partial_\tau + h_k[\Delta^\dagger, \Delta]) - \sum_{k,k'} \mathrm{Tr}[\Delta_k^\dagger V_{k,k'}^{-1} \Delta_{k'}] \right] \right\}.
\tag{C.35}
$$

The next step is to perform the mean-field approximation. We assume that the chief contribution to the path integral originates from the configuration $\Delta_k^{(0)}$ which is static in τ and minimizes the free energy. That is to say, that the value of the integral is simply the integrand evaluated at this configuration. For brevity we immediately drop the index (0). In mean-field approximation the partition function is given by

$$
Z_{\mathrm{MF}} = \exp\left\{ \int_0^\beta d\tau \left[\sum_k \mathrm{Tr} \ln(\partial_\tau + h_k[\Delta^\dagger, \Delta]) - \sum_{k,k'} \mathrm{Tr}[\Delta_k^\dagger V_{k,k'}^{-1} \Delta_{k'}] \right] \right\}.
\tag{C.36}
$$

Next we transform the integral from the imaginary time domain to the Matsubara frequency domain. The Matsubara frequencies are discrete, hence the integral transforms into a sum. Remember that we have assumed the Δ is independent of τ. We get

$$
Z_{\mathrm{MF}} = \exp\left[\sum_{k,i\omega_n} \mathrm{Tr} \ln(h_k[\Delta^\dagger, \Delta] - i\omega_n) - \beta \sum_{k,k'} \mathrm{Tr}[\Delta_k^\dagger V_{k,k'}^{-1} \Delta_{k'}] \right].
\tag{C.37}
$$

Then using identity $\mathrm{Tr} \ln = \ln \det$ we can unravel part of the exponential function

$$
Z_{\mathrm{MF}} = \prod_{k,i\omega_n} \det(h_k[\Delta^\dagger, \Delta] - i\omega_n) \exp\left[-\beta \sum_{k,k'} \mathrm{Tr}[\Delta_k^\dagger V_{k,k'}^{-1} \Delta_{k'}] \right].
\tag{C.38}
$$

At this point we can use the partition function to compute the free energy using its definition

$$F_{\mathrm{MF}} = -\frac{1}{\beta} \ln Z_{\mathrm{MF}} = -\frac{1}{\beta} \ln\left\{ \prod_{k,i\omega_n} \det(h_k[\Delta^\dagger, \Delta] - i\omega_n) \exp\left[-\beta \sum_{k,k'} \mathrm{Tr}[\Delta_k^\dagger V_{k,k'}^{-1} \Delta_{k'}]\right] \right\}$$
$$= -\frac{1}{\beta} \sum_{k,i\omega_n} \ln(\det(h_k[\Delta^\dagger, \Delta] - i\omega_n)) + \sum_{k,k'} \mathrm{Tr}[\Delta_k^\dagger V_{k,k'}^{-1} \Delta_{k'}]. \tag{C.39}$$

Taking the determinant of the BdG-Hamiltonian is equivalent to forming the product of all eigenvalues, so the determinant evaluates to

$$\det(h_k[\Delta^\dagger, \Delta] - i\omega_n) = \prod_\nu (E_{k,\nu} - i\omega_n) \tag{C.40}$$

with the eigenvalues $E_{k,\nu}$ of the BdG-Hamiltonian $h_k[\Delta^\dagger, \Delta]$. Plugging this back into the free energy and rearranging

$$F_{\mathrm{MF}} = -\frac{1}{\beta} \sum_{k,i\omega_n} \ln\left[\prod_\nu (E_{k,\nu} - i\omega_n) \right] + \sum_{k,k'} \mathrm{Tr}[\Delta_k^\dagger V_{k,k'}^{-1} \Delta_{k'}] \tag{C.41}$$

$$= -\frac{1}{\beta} \sum_{k,i\omega_n,\nu} \ln[(E_{k,\nu} - i\omega_n)] + \sum_{k,k'} \mathrm{Tr}[\Delta_k^\dagger V_{k,k'}^{-1} \Delta_{k'}] \tag{C.42}$$

$$= -\frac{1}{\beta} \sum_{k,i\omega_n,\nu} \ln(E_{k,\nu} - i\omega_n) + \sum_{k,k'} \mathrm{Tr}[\Delta_k^\dagger V_{k,k'}^{-1} \Delta_{k'}]. \tag{C.43}$$

In fact, we can evaluate the Matsubara sum, because the first term simply represents the free energy of free fermions, for which the contour integral can be evaluated easily, see Appendix C. As a reminder:

$$\frac{1}{\beta} \sum_{i\omega_n} \ln(E_k - i\omega_n) = \frac{1}{\beta} \ln(1 + e^{-\beta E_k}). \tag{C.44}$$

With that result the mean-field free energy takes on a compact form

$$F_{\mathrm{MF}} = -\frac{1}{\beta} \sum_{k,\nu} \ln(1 + e^{-\beta E_{k,\nu}}) + \sum_{k,k'} \mathrm{Tr}[\Delta_k^\dagger V_{k,k'}^{-1} \Delta_{k'}]. \tag{C.45}$$

However, we can simplify this result further, because of particle-hole symmetry which guarantees that there are always two eigenvalues with opposite sign. This property is also called Nambu doubling. We can hence split up the sum over ν into a single sum over n which only runs over the positive part of the spectrum. Applying some simplifications we then have the mean-field free energy

$$F_{\mathrm{MF}} = -\sum_{k,n} \left[E_{k,n} + \frac{2}{\beta} \ln(1 + e^{-\beta E_{k,n}}) \right] + \sum_{k,k'} \mathrm{Tr}[\Delta_k^\dagger V_{k,k'}^{-1} \Delta_{k'}]. \tag{C.46}$$

This is sometimes also written as

$$F_{\mathrm{MF}} = -\frac{1}{\beta} \sum_{k,n} \ln\left[2 \cosh\left(\frac{\beta E_{k,n}}{2} \right) \right] + \sum_{k,k'} \mathrm{Tr}[\Delta_k^\dagger V_{k,k'}^{-1} \Delta_{k'}]. \tag{C.47}$$

This free energy has to be evaluated numerically in general because the functional form of $E_{k,n}$ might not be known and the sum is not computable.

Appendix D

Ginzburg-Landau free energy

An alternative approach to analyze the free energy just below the critical temperature is to expand it in powers of the pairing potential to obtain the Ginzburg-Landau form. Let's go back to the effective action (C.35)

$$Z = \int \mathcal{D}[\Delta^\dagger, \Delta] \exp\left\{\int_0^\beta d\tau\left[\sum_{\boldsymbol{k}} \mathrm{Tr}\ln(\partial_\tau + h_{\boldsymbol{k}}[\Delta^\dagger, \Delta]) - \sum_{\boldsymbol{k},\boldsymbol{k}'} \mathrm{Tr}[\Delta_{\boldsymbol{k}}^\dagger V_{\boldsymbol{k},\boldsymbol{k}'}^{-1}\Delta_{\boldsymbol{k}'}]\right]\right\}. \tag{D.1}$$

This time we will not evaluate the first term directly but rather identify the full propagator of the system as $\mathcal{G}^{-1} = (\partial_\tau + h_{\boldsymbol{k}}[\Delta^\dagger, \Delta])$.

$$Z = \int \mathcal{D}[\Delta^\dagger, \Delta] \exp\left\{\int_0^\beta d\tau\left[\mathrm{Tr}\ln\mathcal{G}^{-1}(\tau) - \sum_{\boldsymbol{k},\boldsymbol{k}'} \mathrm{Tr}[\Delta_{\boldsymbol{k}}^\dagger V_{\boldsymbol{k},\boldsymbol{k}'}^{-1}\Delta_{\boldsymbol{k}'}]\right]\right\}. \tag{D.2}$$

Again we determine the free energy from the partition function, analogous to the previous calculation. This time the free energy in mean-field approximation reads

$$F_{\mathrm{MF}} = -\frac{1}{\beta}\int_0^\beta d\tau\left[\mathrm{Tr}\ln\mathcal{G}^{-1}(\tau) + \sum_{\boldsymbol{k},\boldsymbol{k}'} \mathrm{Tr}[\Delta_{\boldsymbol{k}}^\dagger V_{\boldsymbol{k},\boldsymbol{k}'}^{-1}\Delta_{\boldsymbol{k}'}]\right]. \tag{D.3}$$

Now we assume the pairing to be a perturbation to the normal state, so that $h_{\boldsymbol{k}}[\Delta^\dagger, \Delta]) = H_0 + \Sigma$, where Σ is the pairing. The Green's function of the normal state is $G_0^{-1} = (\partial_\tau - H_0)$ and therefore $\mathcal{G}^{-1} = G_0^{-1} - \Sigma$. Then we can apply some logarithm identities

$$\ln\mathcal{G}^{-1} = \ln(G_0^{-1} - \Sigma) = \ln[G_0^{-1}(1 - G_0\Sigma)] = \ln G_0^{-1} + \ln(1 - G_0\Sigma) \tag{D.4}$$

and expand the matrix logarithm analogous to the scalar logarithm

$$\ln(1 + x) = \sum_{n=1}^\infty (-1)^{n+1}\frac{x^n}{n} \approx x - \frac{x^2}{2} + \frac{x^3}{3} - \frac{x^4}{4} + \cdots. \tag{D.5}$$

Therefore we find

$$\ln(1 - G_0\Sigma) \approx -G_0\Sigma - \frac{1}{2}G_0\Sigma G_0\Sigma - \frac{1}{3}G_0\Sigma G_0\Sigma G_0\Sigma - \frac{1}{4}G_0\Sigma G_0\Sigma G_0\Sigma G_0\Sigma. \tag{D.6}$$

Remember that G_0 was block diagonal and Σ was block off-diagonal, i.e.

$$G_0 = \begin{pmatrix} G(\boldsymbol{k}, i\omega_n) & 0 \\ 0 & \tilde{G}(\boldsymbol{k}, i\omega_n) \end{pmatrix} \quad \text{and} \quad \Sigma = \begin{pmatrix} 0 & \Delta_{\boldsymbol{k}} \\ \Delta_{\boldsymbol{k}}^\dagger & 0 \end{pmatrix}. \tag{D.7}$$

Some simple matrix algebra confirms that all the odd orders in the free energy will vanish. With this at hand we can write the free energy as

$$F_{\mathrm{GL}} \equiv F_{\mathrm{MF}} - F_0 = \frac{1}{\beta}\int_0^\beta d\tau\left\{\sum_{\boldsymbol{k},\boldsymbol{k}'} \mathrm{Tr}[\Delta_{\boldsymbol{k}}^\dagger V_{\boldsymbol{k},\boldsymbol{k}'}^{-1}\Delta_{\boldsymbol{k}'}] + \sum_{\boldsymbol{k}}\sum_{n=1}^\infty \frac{1}{n}\mathrm{Tr}[(\Delta_{\boldsymbol{k}}\tilde{G}(\boldsymbol{k}, \tau)\Delta_{\boldsymbol{k}}^\dagger G(\boldsymbol{k}, \tau))^n]\right\}, \tag{D.8}$$

or after Matsubara transformation

$$F_{\mathrm{GL}} = \sum_{k,k'} \mathrm{Tr}[\Delta_k^\dagger V_{k,k'}^{-1} \Delta_{k'}] + \frac{1}{\beta} \sum_k \sum_{n=1}^{\infty} \frac{1}{n} \mathrm{Tr}[(\Delta_k \tilde{G}(k, i\omega_n)\Delta_k^\dagger G(k, i\omega_n))^n]. \tag{D.9}$$

In the previous Appendix we have derived the form of the Ginzburg-Landau free energy in (D.9). The second-order term which is quadratic in Δ_k ($n = 1$) and the fourth-order term which is quartic in Δ_k are important for the description of phase transitions. The second-order determines the leading instability, whereas the fourth-order term selects the ground state from the leading manifold.

For the even-parity two-band superconductor in Chapter 3 we can compute the traces in the second term for $n = 1$ and $n = 2$ using the notation of the pairing potential in the pseudospin basis. The traces have a simple form

$$\mathrm{Tr}[\Delta_k \tilde{G}(k, \omega)\Delta_k^\dagger G(k, \omega)] = 2(|\psi_{k,I}|^2 + |d_k|^2)(\tilde{G}_+ G_- + \tilde{G}_- G_+) + 2|\psi_{k,+}|^2\tilde{G}_+ G_+ + 2|\psi_{k,-}|^2\tilde{G}_- G_-, \tag{D.10}$$

$$\frac{1}{2}\mathrm{Tr}[(\Delta_k\tilde{G}(k,\omega)\Delta_k^\dagger G(k,\omega))^2]$$
$$= \big(2(|\psi_{k,I}|^2 + |d_k|^2)^2 - |\psi_{k,I}^2 + d_k \cdot d_k|^2\big)(\tilde{G}_-^2 G_+^2 + \tilde{G}_+^2 G_-^2)$$
$$+ (|\psi_{k,I}|^2 + |d_k|^2)(2|\psi_{k,+}|^2\tilde{G}_+ G_+ + 2|\psi_{k,-}|^2\tilde{G}_- G_-)(\tilde{G}_+ G_- + \tilde{G}_- G_+)$$
$$+ 4\,\mathrm{Re}[\psi_{k,+}^*\psi_{k,-}^*(\psi_{k,I}^2 + d_k \cdot d_k)]\tilde{G}_+\tilde{G}_- G_+ G_- + |\psi_{k,+}|^4\tilde{G}_+^2 G_+^2 + |\psi_{k,-}|^4\tilde{G}_-^2 G_-^2$$
$$= \frac{1}{4}\Big(\mathrm{Tr}[\Delta_k\tilde{G}(k,\omega)\Delta_k^\dagger G(k,\omega)]\Big)^2 + \big((|\psi_{k,I}|^2 + |d_k|^2)^2 - |\psi_{k,I}^2 + d_k \cdot d_k|^2\big)(\tilde{G}_-^2 G_+^2 + \tilde{G}_+^2 G_-^2)$$
$$+ \big(4\,\mathrm{Re}[\psi_{k,+}^*\psi_{k,-}^*(\psi_{k,I}^2 + d_k \cdot d_k)] - 2(|\psi_{k,I}|^2 + |d_k|^2)^2 - 2|\psi_{k,+}\psi_{k,-}|^2\big)\tilde{G}_+\tilde{G}_- G_+ G_-, \tag{D.11}$$

with the particle-like and hole-like single-band Green's functions $G_\pm = (i\omega - \epsilon_\pm)^{-1}$ and $\tilde{G}_\pm = (i\omega + \epsilon_\pm)^{-1}$, respectively. The real part is an abbreviation for

$$2\,\mathrm{Re}[\psi_{k,+}^*\psi_{k,-}^*(\psi_{k,I}^2 + d_k \cdot d_k)] = |\psi_{k,+}\psi_{k,-} + \psi_{k,I}^2 + d_k \cdot d_k|^2 - |\psi_{k,+}\psi_{k,-}|^2 - |\psi_{k,I}^2 + d_k \cdot d_k|^2. \tag{D.12}$$

As we have seen previously, the expressions for the intraband paring potential $\psi_{k,\pm}$, and the interband pairing potentials $\psi_{k,I}$ and d_k depend on the choice of the pseudospin basis and turn out to be rather unwieldy. Luckily certain combinations have a form that does not depend on this choice which allows us to relate the pairing potentials in the pseudospin basis to their counterparts in the orbital basis. We have taken care to express the second- and fourth-order term above only using these "basis-agnostic" quantities, which are for completeness

$$\psi_{k,\pm} = \eta_{k,0} \pm \frac{\vec{\epsilon}_k \cdot \vec{\eta}_k}{|\vec{\epsilon}_k|}, \tag{D.13}$$

$$|\psi_{k,I}|^2 + |d_k|^2 = |\vec{\eta}_k|^2 - \frac{|\vec{\epsilon}_k \cdot \vec{\eta}_k|^2}{|\vec{\epsilon}_k|^2}, \tag{D.14}$$

$$\psi_{k,I}^2 + d_k \cdot d_k = \vec{\eta}_k \cdot \vec{\eta}_k - \frac{(\vec{\epsilon}_k \cdot \vec{\eta}_k)^2}{|\vec{\epsilon}_k|^2}. \tag{D.15}$$

Evaluation of the Ginzburg-Landau free energy

For the investigation of the time-reversal symmetry-breaking phase transition we will evaluate the fourth-order coefficient of the Ginzburg-Landau free energy, i.e. the momentum and frequency summations over (D.11).

First we perform a change of variables from momentum to energy for which it is convenient to write the two normal-state energy eigenvalues as

$$\epsilon_{\pm} = \left(1 \pm \frac{f(\theta,\phi)}{\alpha + 5\beta/4}\right)\epsilon_0 \pm \frac{f(\theta,\phi)}{\alpha + 5\beta/4}\mu \tag{D.16}$$

where $\epsilon_0 = (\alpha + 5\beta/4)k^2$ and $f(\theta,\phi) = [\sum_i(\beta^2\hat{k}_i^4 + (3\gamma^2 - \beta^2)\hat{k}_i^2\hat{k}_{i+1}^2)]^{1/2}$. In the spherical limit $\beta = \gamma$ there is no cubic anisotropy and the term reduces to $f(\theta,\phi) = \beta$ which is angle independent. In this case we can introduce a renormalized spin-orbit coupling $\tilde{\beta} = \beta/(\alpha + 5\beta/4)$

$$\epsilon_{\pm} = \left(1 \pm \frac{\beta}{\alpha + 5\beta/4}\right)\epsilon_0 \pm \frac{\beta}{\alpha + 5\beta/4}\mu \equiv (1 \pm \tilde{\beta})\epsilon_0 \pm \tilde{\beta}\mu. \tag{D.17}$$

Because the pairing is momentum-independent, the coefficients of the Green's functions in (D.11) will only depend on the angular part of the momentum, whereas the Green's functions will only depend on the magnitude of the momentum. With the above parameterization we can then rewrite the sum over k as an integral over ϵ_0

$$\sum_{k,\omega} \rightarrow \int_{\mathbb{S}_2} d\Omega \sum_{\omega} \int_{-\infty}^{\infty} d\epsilon_0 D(\epsilon_0), \tag{D.18}$$

with the density of states

$$D(\epsilon_0) = \frac{\sqrt{\epsilon_0 + \mu}}{2(\alpha + 5\beta/4)^{3/2}}. \tag{D.19}$$

Generally the assumption of constant density of states at the Fermi surface is taken, i.e. $D(\epsilon_0) \approx D(0)$. That completely neglects any particle-hole asymmetry of the normal state. The density of states cannot be treated in full, but it can be expanded. In the results shown in Figs. 4.2 and 4.3, we expanded the density of states up to first order

$$D(\epsilon_0) \approx \frac{\sqrt{\mu}}{2(\alpha + 5\beta/4)^{3/2}}\left(1 + \frac{\epsilon_0}{2\mu}\right). \tag{D.20}$$

Without the first-order correction to the density of states, the integrals evaluate to

$$k_B T \sum_{i\omega_n} \int_{-\infty}^{\infty} d\epsilon_0 (\tilde{G}_-^2 G_+^2 + \tilde{G}_+^2 G_-^2) = \frac{2}{16\pi^2(k_B T)^2}\left(\tilde{\beta}^2 - 1\right)\text{Re}\left[\psi^{(2)}\left(\frac{1}{2} - \frac{i\mu\tilde{\beta}}{2k_B T\pi}\right)\right], \tag{D.21}$$

$$k_B T \sum_{i\omega_n} \int_{-\infty}^{\infty} d\epsilon_0 (\tilde{G}_+ \tilde{G}_- G_+ G_-) = \frac{1}{4\mu^2\tilde{\beta}^2}\left(2\,\text{Re}\left[H_{-\frac{1}{2} - \frac{i\mu\tilde{\beta}}{2k_B T\pi}}\right] + \log(16)\right), \tag{D.22}$$

$$k_B T \sum_{i\omega_n} \int_{-\infty}^{\infty} d\epsilon_0 (\tilde{G}_- \tilde{G}_- G_- G_+ + \tilde{G}_- \tilde{G}_+ G_- G_-) = -\frac{1}{8\pi k_B T\mu^2\tilde{\beta}}\left(4\pi k_B T\,\text{Re}\left[\psi^{(0)}\left(\frac{1}{2} - \frac{i\mu\tilde{\beta}}{2k_B T\pi}\right)\right]\right.$$
$$\left. - 2\mu\left(\tilde{\beta} + 1\right)\text{Im}\left[\psi^{(1)}\left(\frac{1}{2} - \frac{i\mu\tilde{\beta}}{2k_B T\pi}\right)\right] + 4\pi k_B T(\gamma + \log(4))\right), \tag{D.23}$$

$$k_B T \sum_{i\omega_n} \int_{-\infty}^{\infty} d\epsilon_0 (\tilde{G}_+ \tilde{G}_+ G_- G_+ + \tilde{G}_+ \tilde{G}_- G_+ G_+) = \frac{1}{8\pi k_B T\mu^2\tilde{\beta}}\left(4\pi k_B T\,\text{Re}\left[\psi^{(0)}\left(\frac{1}{2} - \frac{i\mu\tilde{\beta}}{2k_B T\pi}\right)\right]\right.$$
$$\left. - 2\mu\left(\tilde{\beta} - 1\right)\text{Im}\left[\psi^{(1)}\left(\frac{1}{2} - \frac{i\mu\tilde{\beta}}{2k_B T\pi}\right)\right] + 4\pi k_B T(\gamma + \log(4))\right), \tag{D.24}$$

$$k_B T \sum_{i\omega_n} \int_{-\infty}^{\infty} d\epsilon_0 (\tilde{G}_+^2 G_+^2 + \tilde{G}_-^2 G_-^2) = -\frac{7\zeta(3)}{4\pi^2(k_B T)^2\left(\tilde{\beta}^2 - 1\right)}. \tag{D.25}$$

Taking into account the correction term, the integrals evaluate to

$$k_B T \sum_{i\omega_n} \int_{-\infty}^{\infty} d\epsilon_0 \left(1 + \frac{\epsilon_0}{2\mu}\right) (\tilde{G}_-^2 G_+^2 + \tilde{G}_+^2 G_-^2) = \frac{1}{16\pi^2 (k_B T)^2 \mu} \left(-4\pi k_B T \tilde{\beta} \, \text{Im} \left[\psi^{(1)} \left(\frac{1}{2} - \frac{i\mu\tilde{\beta}}{2k_B T\pi}\right)\right]\right.$$

$$\left. + 2\mu \left(\tilde{\beta}^2 - 1\right) \text{Re} \left[\psi^{(2)} \left(\frac{1}{2} - \frac{i\mu\tilde{\beta}}{2k_B T\pi}\right)\right]\right), \quad \text{(D.26)}$$

$$k_B T \sum_{i\omega_n} \int_{-\infty}^{\infty} d\epsilon_0 \left(1 + \frac{\epsilon_0}{2\mu}\right) (\tilde{G}_+ \tilde{G}_- G_+ G_-) = \frac{1}{4\mu^2 \tilde{\beta}^2} \left(2 \, \text{Re} \left[H_{-\frac{1}{2} - \frac{i\mu\tilde{\beta}}{2k_B T\pi}}\right] + \log(16)\right), \quad \text{(D.27)}$$

$$k_B T \sum_{i\omega_n} \int_{-\infty}^{\infty} d\epsilon_0 \left(1 + \frac{\epsilon_0}{2\mu}\right) (\tilde{G}_- \tilde{G}_- G_- G_+ + \tilde{G}_- \tilde{G}_+ G_- G_-) = -\frac{1}{8\pi k_B T\mu^2 \tilde{\beta}} \left(2\pi k_B T \, \text{Re} \left[\psi^{(0)} \left(\frac{1}{2} - \frac{i\mu\tilde{\beta}}{2k_B T\pi}\right)\right]\right.$$

$$\left. - 2\mu \left(\tilde{\beta} + 1\right) \text{Im} \left[\psi^{(1)} \left(\frac{1}{2} - \frac{i\mu\tilde{\beta}}{2k_B T\pi}\right)\right] + 2\pi k_B T(\gamma + \log(4))\right), \quad \text{(D.28)}$$

$$k_B T \sum_{i\omega_n} \int_{-\infty}^{\infty} d\epsilon_0 \left(1 + \frac{\epsilon_0}{2\mu}\right) (\tilde{G}_+ \tilde{G}_+ G_- G_+ + \tilde{G}_+ \tilde{G}_- G_+ G_+) = -\frac{1}{8\pi k_B T\mu^2 \tilde{\beta}} \left(-2\pi k_B T \, \text{Re} \left[\psi^{(0)} \left(\frac{1}{2} - \frac{i\mu\tilde{\beta}}{2k_B T\pi}\right)\right]\right.$$

$$\left. + 2\mu \left(\tilde{\beta} - 1\right) \text{Im} \left[\psi^{(1)} \left(\frac{1}{2} - \frac{i\mu\tilde{\beta}}{2k_B T\pi}\right)\right] - 2\pi k_B T(\gamma + \log(4))\right), \quad \text{(D.29)}$$

$$k_B T \sum_{i\omega_n} \int_{-\infty}^{\infty} d\epsilon_0 \left(1 + \frac{\epsilon_0}{2\mu}\right) (\tilde{G}_+^2 G_+^2 + \tilde{G}_-^2 G_-^2) = \frac{7\zeta(3)}{4\pi^2 (k_B T)^2 \left(\tilde{\beta}^2 - 1\right)^2}. \quad \text{(D.30)}$$

The form of the prefactors of these terms depends on the pairing state. A generic form of these coefficients is already given in (D.11). In the spherical limit all the time-reversal symmetric states are degenerate. The same holds for the time-reversal symmetry-breaking states.

Appendix E

Spin susceptibility and Knight shift

In metals, the Knight shift is proportional to the paramagnetic susceptibility of the material. In superconductors, the Knight shift is in fact the only reliable probe of the bulk susceptibility because diamagnetic shielding by supercurrent will shadow all other contributions [254].

The conduction electrons of a metal are susceptible to external magnetic fields. At the same time, their coupling to the nuclear spins of the atoms is very weak. This can be exploited to probe the magnetic response of a material with good sensitivity using nuclear magnetic resonance (NMR) techniques. The induced field will oppose the applied field as per Lenz's law which will shift the magnetic resonance away from the Larmor frequency. This is known as the Knight shift.

To calculate the spin susceptibility we start from the interaction of the electron magnetic moment with an applied ac magnetic field as such

$$V(t) = -\boldsymbol{m} \cdot \boldsymbol{H} e^{-i\omega t}, \tag{E.1}$$

$$\boldsymbol{m} = g\mu_0 \sum_i \boldsymbol{S}_i, \tag{E.2}$$

where $V(t)$ denotes the time-dependent interaction and $\boldsymbol{m}$ is the magnetic moment associated with the electron spin $\boldsymbol{S}$.

We may now calculate the physical magnetization in linear response by computing the expectation value of the electron magnetic moment in the interaction picture by expanding the S matrix to first-order of perturbation theory. This yields

$$M_\alpha(t) = \langle m_\alpha(t) \rangle_t \approx -i \int_{-\infty}^t \langle [m_\alpha(t), V(t')] \rangle \, dt'. \tag{E.3}$$

It is convenient to switch to imaginary time, such that we can evaluate the expectation value in Matsubara space

$$M_\alpha(i\omega) = \int_0^\tau e^{i\omega\tau} \langle T_\tau m_\alpha(\tau) m_\beta(0) \rangle H_\beta \, d\tau. \tag{E.4}$$

At this point we identify the *dynamical susceptibility* which is usually written momentum-resolved

$$\chi_{\alpha\beta}(\boldsymbol{q}, i\omega) \equiv \int_0^\tau e^{i\omega\tau} \langle T_\tau m_\alpha(\boldsymbol{q}, \tau) m_\beta(-\boldsymbol{q}, 0) \rangle \, d\tau \tag{E.5}$$

where

$$m_\alpha(\boldsymbol{q}, \tau) \propto \sum_i S_i(\tau) = \frac{1}{N} \sum_{\boldsymbol{k},\boldsymbol{q},a,b} d_a^\dagger(\boldsymbol{k}+\boldsymbol{q}, \tau) \sigma_{ab}^\alpha d_b(\boldsymbol{k}, \tau). \tag{E.6}$$

Plugging in the magnetic moment as defined above we find an expression for the spin-, momentum-, and frequency-resolved magnetic susceptibility

$$\chi_{\alpha\beta}(\boldsymbol{q}, i\omega) = \frac{1}{N^2} \sum_{\boldsymbol{k},\boldsymbol{k}',a,b} \int_0^\tau e^{i\omega\tau} \sigma_{ab}^\alpha \sigma_{cd}^\beta \langle T_\tau d_a^\dagger(\boldsymbol{k}+\boldsymbol{q}, \tau) d_b(\boldsymbol{k}, \tau) d_c^\dagger(\boldsymbol{k}'-\boldsymbol{q}, 0) d_d(\boldsymbol{k}', 0) \rangle \, d\tau. \tag{E.7}$$

This expression is completely general and agnostic to the microscopic details of the model, which enter in the evaluation of the expectation value. To evaluate this expectation value we apply Wick's theorem, but since we are dealing with a superconductor we have to be wary of anomalous averages which usually vanish in the metallic case. In the case of a single-band singlet superconductor without spin-orbit coupling, the spin directions are all equivalent and we can therefore drop the spin indices

$$\chi(\boldsymbol{q}, i\omega) = \frac{1}{N^2} \sum_{\boldsymbol{k},\boldsymbol{k}'} \int_0^\tau e^{i\omega\tau} \langle T_\tau d^\dagger(\boldsymbol{k}+\boldsymbol{q},\tau) d(\boldsymbol{k},\tau) d^\dagger(\boldsymbol{k}'-\boldsymbol{q},0) d(\boldsymbol{k}',0) \rangle \, d\tau. \tag{E.8}$$

We rearrange the terms and apply Wick's theorem to decompose the expectation value and identify the definition of the Green's functions $G(\boldsymbol{k},\tau) = \langle T_\tau d(\boldsymbol{k},\tau) d^\dagger(\boldsymbol{k},0) \rangle$ and the anomalous Green's functions $F(\boldsymbol{k},\tau) = \langle T_\tau d(\boldsymbol{k},\tau) d(-\boldsymbol{k},0) \rangle$. Fourier transforming the result into Matsubara space we find

$$\chi = -\frac{1}{N\beta} \sum_{\boldsymbol{k}, i\omega_n} \left(G(\boldsymbol{k}, i\omega_n) G(\boldsymbol{k}+\boldsymbol{q}, i\omega_n - i\omega) - F(\boldsymbol{k}, i\omega_n) F^*(\boldsymbol{k}+\boldsymbol{q}, i\omega_n - i\omega) \right). \tag{E.9}$$

Further we can determine the normal and anomalous Green's functions by solving the Gor'kov equations, assuming that $\epsilon_{\boldsymbol{k}} = \epsilon_{-\boldsymbol{k}}$ and abbreviating $i\omega_n = i\omega$. Because everything is scalar, solving these equations is straightforward and we find the following textbook solution [253]

$$G(\boldsymbol{k}, i\omega) = \frac{\frac{1}{2}\left(1 + \frac{\epsilon_{\boldsymbol{k}}}{E_{\boldsymbol{k}}}\right)}{i\omega - E_{\boldsymbol{k}}} + \frac{\frac{1}{2}\left(1 - \frac{\epsilon_{\boldsymbol{k}}}{E_{\boldsymbol{k}}}\right)}{i\omega + E_{\boldsymbol{k}}}, \tag{E.10}$$

$$F(\boldsymbol{k}, i\omega) = -\frac{\frac{\Delta}{2E_{\boldsymbol{k}}}}{i\omega - E_{\boldsymbol{k}}} + \frac{\frac{\Delta}{2E_{\boldsymbol{k}}}}{i\omega + E_{\boldsymbol{k}}}. \tag{E.11}$$

It is now possible to evaluate the Matsubara frequency summation. The summations in the present case are well-known and usually tabulated.

To relate the susceptibility to the Knight shift, we assume an external magnetic field and therefore the momentum transfer is $\boldsymbol{q} = 0$. We also neglect the frequency dependence, i.e. we assume the static limit $\omega \to 0$. With this we have the spin susceptibility in the static limit which corresponds to the Knight shift due to an external magnetic field. We can perform a final transformation from the momentum space summation to integration over energies where $D_0(E)$ denotes the density of states in the normal-state

$$\chi(\boldsymbol{q}=0, i\omega=0) = \frac{1}{4N} \sum_{\boldsymbol{k}} \operatorname{sech}^2\left(\frac{E_{\boldsymbol{k}}}{2kT}\right) \tag{E.12}$$

$$= \frac{1}{4} \frac{1}{(2\pi)^3} \int_{\mathbb{R}^3} d^3k \, \operatorname{sech}^2\left(\frac{E_{\boldsymbol{k}}}{2kT}\right) \tag{E.13}$$

$$= \frac{1}{4} \int_{-\infty}^{\infty} d\epsilon_{\boldsymbol{k}} \, D_0(\epsilon_{\boldsymbol{k}}) \operatorname{sech}^2\left(\frac{E_{\boldsymbol{k}}}{2kT}\right) \tag{E.14}$$

$$\approx \frac{D_0(0)}{4} \int_{-\infty}^{\infty} d\epsilon_{\boldsymbol{k}} \, \operatorname{sech}^2\left(\frac{E_{\boldsymbol{k}}}{2kT}\right). \tag{E.15}$$

This result is familiar from Yosida [199]. The Yosida function $Y(T)$ is usually defined as

$$Y(T) = \frac{1}{4} \int_{-\infty}^{\infty} d\epsilon_{\boldsymbol{k}} \, \operatorname{sech}^2\left(\frac{E_{\boldsymbol{k}}}{2kT}\right). \tag{E.16}$$

Bibliography

[1] H. Kamerlingh Onnes, "Further experiments with liquid helium", in Koninklijke Nederlandsche Akademie van Wetenschappen, Vol. 13 (1911), pages 1274–1276 (cited on page 7).

[2] W. Meissner and R. Ochsenfeld, "Ein neuer Effekt bei Eintritt der Supraleitfähigkeit", Die Naturwissenschaften **21**, 787 (1933) (cited on page 7).

[3] J. Schmalian, "Failed theories of superconductivity", Modern Physics Letters B **24**, 2679 (2010) (cited on page 7).

[4] A. B. Pippard, "Trapped flux in superconductors", Philosophical Transactions of the Royal Society of London. Series A, Mathematical and Physical Sciences **248**, 97 (1955) (cited on page 7).

[5] F. London and H. London, "The electromagnetic equations of the supraconductor", Proceedings of the Royal Society of London. Series A - Mathematical and Physical Sciences **149**, 71 (1935) (cited on page 7).

[6] V. L. Ginzburg and L. D. Landau, "On the theory of superconductivity", Zh. Eksp. Teor. Fiz., English version published in [7], 1064 (1950) (cited on page 7).

[7] V. L. Ginzburg and L. D. Landau, "On the Theory of Superconductivity", in *On Superconductivity and Superfluidity* (Springer Berlin Heidelberg, 2009), pages 113–137 (cited on pages 7, 133).

[8] L. N. Cooper, "Bound Electron Pairs in a Degenerate Fermi Gas", Phys. Rev. **104**, 1189 (1956) (cited on page 7).

[9] J. Bardeen, L. N. Cooper, and J. R. Schrieffer, "Microscopic Theory of Superconductivity", Phys. Rev. **106**, 162 (1957) (cited on pages 7, 13).

[10] J. Bardeen, L. N. Cooper, and J. R. Schrieffer, "Theory of Superconductivity", Phys. Rev. **108**, 1175 (1957) (cited on pages 7, 13).

[11] B. T. Matthias, T. H. Geballe, and V. B. Compton, "Superconductivity", Rev. Mod. Phys. **35**, 1 (1963) (cited on page 7).

[12] J. Eisenstein, "Superconducting Elements", Rev. Mod. Phys. **26**, 277 (1954) (cited on page 7).

[13] E. Maxwell, "Isotope Effect in the Superconductivity of Mercury", Phys. Rev. **78**, 477 (1950) (cited on page 7).

[14] C. A. Reynolds, B. Serin, W. H. Wright, and L. B. Nesbitt, "Superconductivity of Isotopes of Mercury", Phys. Rev. **78**, 487 (1950) (cited on page 7).

[15] J. R. Schrieffer, *Theory of superconductivity* (Advanced Book Program, Perseus Books, Reading, Mass, 1999) (cited on pages 7, 13).

[16] F. Steglich, C. Bredl, W. Lieke, U. Rauchschwalbe, and G. Sparn, "Heavy fermion superconductivity", Physica B+C **126**, 82 (1984) (cited on page 7).

[17]   G. R. Stewart, "Heavy-fermion systems", Rev. Mod. Phys. **56**, 755 (1984) (cited on page 7).

[18]   F. Steglich, J. Aarts, C. D. Bredl, W. Lieke, D. Meschede, W. Franz, and H. Schäfer, "Superconductivity in the Presence of Strong Pauli Paramagnetism: $CeCu_2Si_2$", Phys. Rev. Lett. **43**, 1892 (1979) (cited on page 7).

[19]   H. R. Ott, H. Rudigier, Z. Fisk, and J. L. Smith, "UBe_{13}: An Unconventional Actinide Superconductor", Phys. Rev. Lett. **50**, 1595 (1983) (cited on pages 7, 73).

[20]   G. R. Stewart, Z. Fisk, J. O. Willis, and J. L. Smith, "Possibility of Coexistence of Bulk Superconductivity and Spin Fluctuations in UPt_3", Phys. Rev. Lett. **52**, 679 (1984) (cited on pages 7, 73).

[21]   J. G. Bednorz and K. A. Müller, "Possible high T_c superconductivity in the Ba-La-Cu-O system", Zeitschrift für Physik B Condensed Matter **64**, 189 (1986) (cited on pages 8, 69).

[22]   M. K. Wu, J. R. Ashburn, C. J. Torng, P. H. Hor, R. L. Meng, L. Gao, Z. J. Huang, Y. Q. Wang, and C. W. Chu, "Superconductivity at 93 K in a new mixed-phase Y-Ba-Cu-O compound system at ambient pressure", Phys. Rev. Lett. **58**, 908 (1987) (cited on page 8).

[23]   H. Maeda, Y. Tanaka, M. Fukutomi, and T. Asano, "A New High-T_c Oxide Superconductor without a Rare Earth Element", Japanese Journal of Applied Physics **27**, 209 (1988) (cited on page 8).

[24]   L. Lawrence Jr, C. Cox, and D. Broman, *High temperature superconductivity: The products and their benefits*, technical report ORNL/Sub-97-SX339V/2 (Oak Ridge National Lab., TN (United States), 1998) (cited on page 8).

[25]   G. R. Stewart, "Superconductivity in iron compounds", Rev. Mod. Phys. **83**, 1589 (2011) (cited on pages 8, 24, 25).

[26]   P. Dai, "Antiferromagnetic order and spin dynamics in iron-based superconductors", Rev. Mod. Phys. **87**, 855 (2015) (cited on page 8).

[27]   W. L. Yang, A. P. Sorini, C.-C. Chen, B. Moritz, W.-S. Lee, F. Vernay, P. Olalde-Velasco, J. D. Denlinger, B. Delley, J.-H. Chu, J. G. Analytis, I. R. Fisher, Z. A. Ren, J. Yang, W. Lu, Z. X. Zhao, J. van den Brink, Z. Hussain, Z.-X. Shen, and T. P. Devereaux, "Evidence for weak electronic correlations in iron pnictides", Phys. Rev. B **80**, 014508 (2009) (cited on pages 9, 25).

[28]   A. A. Kordyuk, "Iron-based superconductors: Magnetism, superconductivity, and electronic structure (Review Article)", Low Temperature Physics **38**, 888 (2012) (cited on page 9).

[29]   Y. Kamihara, H. Hiramatsu, M. Hirano, R. Kawamura, H. Yanagi, T. Kamiya, and H. Hosono, "Iron-Based Layered Superconductor: LaOFeP", Journal of the American Chemical Society **128**, 10012 (2006) (cited on page 9).

[30]   Y. Kamihara, T. Watanabe, M. Hirano, and H. Hosono, "Iron-Based Layered Superconductor $La[O_{1-x}F_x]FeAs$ ($x = 0.05 - 0.12$) with $T_c = 26$ K", Journal of the American Chemical Society **130**, 3296 (2008) (cited on pages 9, 25).

[31]   X. H. Chen, T. Wu, G. Wu, R. H. Liu, H. Chen, and D. F. Fang, "Superconductivity at 43 K in $SmFeAsO_{1-x}F_x$", Nature **453**, 761 (2008) (cited on pages 9, 25).

[32]   G. F. Chen, Z. Li, D. Wu, G. Li, W. Z. Hu, J. Dong, P. Zheng, J. L. Luo, and N. L. Wang, "Superconductivity at 41 K and Its Competition with Spin-Density-Wave Instability in Layered CeO$_{1-x}$F$_x$FeAs", Phys. Rev. Lett. **100**, 247002 (2008) (cited on pages 9, 25).

[33]   G. Wu, Y. L. Xie, H. Chen, M. Zhong, R. H. Liu, B. C. Shi, Q. J. Li, X. F. Wang, T. Wu, Y. J. Yan, J. J. Ying, and X. H. Chen, "Superconductivity at 56 K in samarium-doped SrFeAsF", Journal of Physics: Condensed Matter **21**, 142203 (2009) (cited on page 9).

[34]   J.-F. Ge, Z.-L. Liu, C. Liu, C.-L. Gao, D. Qian, Q.-K. Xue, Y. Liu, and J.-F. Jia, "Superconductivity above 100 K in single-layer FeSe films on doped SrTiO3", Nature Materials **14**, 285 (2014) (cited on page 9).

[35]   P. A. Frigeri, D. F. Agterberg, A. Koga, and M. Sigrist, "Superconductivity without Inversion Symmetry: MnSi versus CePt$_3$Si", Phys. Rev. Lett. **92**, 097001 (2004) (cited on pages 9, 16).

[36]   E. Bauer, G. Hilscher, H. Michor, C. Paul, E. W. Scheidt, A. Gribanov, Y. Seropegin, H. Noël, M. Sigrist, and P. Rogl, "Heavy Fermion Superconductivity and Magnetic Order in Noncentrosymmetric CePt$_3$Si", Phys. Rev. Lett. **92**, 027003 (2004) (cited on page 9).

[37]   A. P. Schnyder and S. Ryu, "Topological phases and surface flat bands in superconductors without inversion symmetry", Phys. Rev. B **84**, 060504 (2011) (cited on page 9).

[38]   L. Fu and E. Berg, "Odd-Parity Topological Superconductors: Theory and Application to Cu$_x$Bi$_2$Se$_3$", Phys. Rev. Lett. **105**, 097001 (2010) (cited on pages 9, 10, 24, 73).

[39]   S. Sasaki, M. Kriener, K. Segawa, K. Yada, Y. Tanaka, M. Sato, and Y. Ando, "Topological Superconductivity in Cu$_x$Bi$_2$Se$_3$", Phys. Rev. Lett. **107**, 217001 (2011) (cited on page 9).

[40]   N. P. Butch, P. Syers, K. Kirshenbaum, A. P. Hope, and J. Paglione, "Superconductivity in the topological semimetal YPtBi", Phys. Rev. B **84**, 220504 (2011) (cited on page 9).

[41]   U. Rössler, *Solid State Theory* (Springer Berlin Heidelberg, 2004) (cited on page 9).

[42]   M. Sigrist and K. Ueda, "Phenomenological theory of unconventional superconductivity", Rev. Mod. Phys. **63**, 239 (1991) (cited on pages 9, 10, 21, 23, 24, 40, 41, 50, 51, 67, 71, 104).

[43]   M. Sigrist, R. Joynt, and T. M. Rice, "Behavior of anisotropic superconductors under uniaxial stress", Phys. Rev. B **36**, 5186 (1987) (cited on page 10).

[44]   G. Volovik, *Exotic Properties of Superfluid ^{3}He*, Series in Modern Condensed Matter Physics (World Scientific, 1992) (cited on page 10).

[45]   E. R. Schemm, W. J. Gannon, C. M. Wishne, W. P. Halperin, and A. Kapitulnik, "Observation of broken time-reversal symmetry in the heavy-fermion superconductor UPt3", Science **345**, 190 (2014) (cited on page 10).

[46]   G. M. Luke, A. Keren, L. P. Le, W. D. Wu, Y. J. Uemura, D. A. Bonn, L. Taillefer, and J. D. Garrett, "Muon spin relaxation in UPt$_3$", Phys. Rev. Lett. **71**, 1466 (1993) (cited on page 10).

[47]   R. H. Heffner, J. L. Smith, J. O. Willis, P. Birrer, C. Baines, F. N. Gygax, B. Hitti, E. Lippelt, H. R. Ott, A. Schenck, E. A. Knetsch, J. A. Mydosh, and D. E. MacLaughlin, "New phase diagram for (U,Th)Be$_{13}$: A muon-spin-resonance and H_{c1} study", Phys. Rev. Lett. **65**, 2816 (1990) (cited on page 10).

[48]   E. R. Schemm, R. E. Baumbach, P. H. Tobash, F. Ronning, E. D. Bauer, and A. Kapitulnik, "Evidence for broken time-reversal symmetry in the superconducting phase of URu_2Si_2", Phys. Rev. B **91**, 140506 (2015) (cited on page 10).

[49]   Y. Aoki, A. Tsuchiya, T. Kanayama, S. R. Saha, H. Sugawara, H. Sato, W. Higemoto, A. Koda, K. Ohishi, K. Nishiyama, and R. Kadono, "Time-Reversal Symmetry-Breaking Superconductivity in Heavy-Fermion $PrOs_4Sb_{12}$ Detected by Muon-Spin Relaxation", Phys. Rev. Lett. **91**, 067003 (2003) (cited on page 10).

[50]   E. M. Levenson-Falk, E. R. Schemm, Y. Aoki, M. B. Maple, and A. Kapitulnik, "Polar Kerr Effect from Time-Reversal Symmetry Breaking in the Heavy-Fermion Superconductor $PrOs_4Sb_{12}$", Phys. Rev. Lett. **120**, 187004 (2018) (cited on page 10).

[51]   G. M. Luke, Y. Fudamoto, K. M. Kojima, M. I. Larkin, J. Merrin, B. Nachumi, Y. J. Uemura, Y. Maeno, Z. Q. Mao, Y. Mori, H. Nakamura, and M. Sigrist, "Time-reversal symmetry-breaking superconductivity in Sr_2RuO_4", Nature **394**, 558 (1998) (cited on pages 10, 70, 73, 75, 104, 105).

[52]   J. Xia, Y. Maeno, P. T. Beyersdorf, M. M. Fejer, and A. Kapitulnik, "High Resolution Polar Kerr Effect Measurements of Sr_2RuO_4: Evidence for Broken Time-Reversal Symmetry in the Superconducting State", Phys. Rev. Lett. **97**, 167002 (2006) (cited on pages 10, 70, 73, 75, 104, 105).

[53]   P. K. Biswas, H. Luetkens, T. Neupert, T. Stürzer, C. Baines, G. Pascua, A. P. Schnyder, M. H. Fischer, J. Goryo, M. R. Lees, H. Maeter, F. Brückner, H.-H. Klauss, M. Nicklas, P. J. Baker, A. D. Hillier, M. Sigrist, A. Amato, and D. Johrendt, "Evidence for superconductivity with broken time-reversal symmetry in locally noncentrosymmetric SrPtAs", Phys. Rev. B **87**, 180503 (2013) (cited on page 10).

[54]   X. Gong, M. Kargarian, A. Stern, D. Yue, H. Zhou, X. Jin, V. M. Galitski, V. M. Yakovenko, and J. Xia, "Time-reversal symmetry-breaking superconductivity in epitaxial bismuth/nickel bilayers", Science Advances **3**, e1602579 (2017) (cited on page 10).

[55]   Y. Gao, W.-P. Su, and J.-X. Zhu, "Interorbital pairing and its physical consequences for iron pnictide superconductors", Phys. Rev. B **81**, 104504 (2010) (cited on page 10).

[56]   A. Nicholson, W. Ge, J. Riera, M. Daghofer, A. Moreo, and E. Dagotto, "Pairing symmetries of a hole-doped extended two-orbital model for the pnictides", Phys. Rev. B **85**, 024532 (2012) (cited on page 10).

[57]   R. Nourafkan, G. Kotliar, and A.-M. S. Tremblay, "Correlation-Enhanced Odd-Parity Interorbital Singlet Pairing in the Iron-Pnictide Superconductor LiFeAs", Phys. Rev. Lett. **117**, 137001 (2016) (cited on page 10).

[58]   T. Ong, P. Coleman, and J. Schmalian, "Concealed d-wave pairs in the $s_{\pm}$ condensate of iron-based superconductors", Proceedings of the National Academy of Sciences **113**, 5486 (2016) (cited on pages 10, 32).

[59]   E. M. Nica, R. Yu, and Q. Si, "Orbital-selective pairing and superconductivity in iron selenides", npj Quantum Materials **2**, 10.1038/s41535-017-0027-6 (2017) (cited on pages 10, 38).

[60]   A. V. Chubukov, O. Vafek, and R. M. Fernandes, "Displacement and annihilation of Dirac gap nodes in d-wave iron-based superconductors", Phys. Rev. B **94**, 174518 (2016) (cited on pages 10, 38).

[61]   D. F. Agterberg, T. Shishidou, J. O'Halloran, P. M. R. Brydon, and M. Weinert, "Resilient Nodeless d-Wave Superconductivity in Monolayer FeSe", Phys. Rev. Lett. **119**, 267001 (2017) (cited on page 10).

[62] L. Fu, "Odd-parity topological superconductor with nematic order: Application to $Cu_xBi_2Se_3$", Phys. Rev. B **90**, 100509 (2014) (cited on page 10).

[63] S. Yonezawa, K. Tajiri, S. Nakata, Y. Nagai, Z. Wang, K. Segawa, Y. Ando, and Y. Maeno, "Thermodynamic evidence for nematic superconductivity in $Cu_xBi_2Se_3$", Nature Physics **13**, 123 (2016) (cited on pages 10, 73).

[64] P. M. R. Brydon, L. Wang, M. Weinert, and D. F. Agterberg, "Pairing of $j = 3/2$ Fermions in Half-Heusler Superconductors", Phys. Rev. Lett. **116**, 177001 (2016) (cited on pages 10, 38, 40, 49, 52).

[65] C. Timm, A. P. Schnyder, D. F. Agterberg, and P. M. R. Brydon, "Inflated nodes and surface states in superconducting half-Heusler compounds", Phys. Rev. B **96**, 094526 (2017) (cited on pages 10, 40).

[66] D. F. Agterberg, P. M. R. Brydon, and C. Timm, "Bogoliubov Fermi Surfaces in Superconductors with Broken Time-Reversal Symmetry", Phys. Rev. Lett. **118**, 127001 (2017) (cited on pages 10, 33, 35, 36, 38, 40, 48, 49, 51, 57, 107).

[67] W. Yang, T. Xiang, and C. Wu, "Majorana surface modes of nodal topological pairings in spin-$\frac{3}{2}$ semimetals", Phys. Rev. B **96**, 144514 (2017) (cited on pages 10, 40).

[68] Y. Yanase, "Nonsymmorphic Weyl superconductivity in UPt_3 based on E_{2u} representation", Phys. Rev. B **94**, 174502 (2016) (cited on page 10).

[69] A. M. Black-Schaffer and A. V. Balatsky, "Odd-frequency superconducting pairing in multiband superconductors", Phys. Rev. B **88**, 104514 (2013) (cited on page 10).

[70] J. W. F. Venderbos, L. Savary, J. Ruhman, P. A. Lee, and L. Fu, "Pairing States of Spin-$\frac{3}{2}$ Fermions: Symmetry-Enforced Topological Gap Functions", Phys. Rev. X **8**, 011029 (2018) (cited on pages 10, 37, 49).

[71] L. Savary, J. Ruhman, J. W. F. Venderbos, L. Fu, and P. A. Lee, "Superconductivity in three-dimensional spin-orbit coupled semimetals", Phys. Rev. B **96**, 214514 (2017) (cited on pages 10, 40).

[72] B. Roy, S. A. A. Ghorashi, M. S. Foster, and A. H. Nevidomskyy, "Topological superconductivity of spin-3/2 carriers in a three-dimensional doped Luttinger semimetal", Phys. Rev. B **99**, 054505 (2019) (cited on pages 10, 40).

[73] I. Boettcher and I. F. Herbut, "Critical phenomena at the complex tensor ordering phase transition", Phys. Rev. B **97**, 064504 (2018) (cited on pages 10, 51).

[74] I. Boettcher and I. F. Herbut, "Superconducting quantum criticality in three-dimensional Luttinger semimetals", Phys. Rev. B **93**, 205138 (2016) (cited on pages 10, 54).

[75] J. Yu and C.-X. Liu, "Singlet-quintet mixing in spin-orbit coupled superconductors with $j = \frac{3}{2}$ fermions", Phys. Rev. B **98**, 104514 (2018) (cited on pages 10, 40).

[76] G. Sim, A. Mishra, M. J. Park, Y. B. Kim, G. Y. Cho, and S. Lee, "Topological $d + s$ wave superconductors in a multiorbital quadratic band touching system", Phys. Rev. B **100**, 064509 (2019) (cited on pages 10, 40, 48, 107).

[77] G. Sim, A. Mishra, M. Jip Park, Y. B. Kim, G. Y. Cho, and S. Lee, "Multipolar superconductivity in Luttinger semimetals", Nov. 2019, arXiv:1911.13224 [cond-mat.str-el] (cited on pages 10, 40, 48, 107).

[78] H. Kim, K. Wang, Y. Nakajima, R. Hu, S. Ziemak, P. Syers, L. Wang, H. Hodovanets, J. D. Denlinger, P. M. R. Brydon, D. F. Agterberg, M. A. Tanatar, R. Prozorov, and J. Paglione, "Beyond Triplet: Unconventional Superconductivity in a Spin-3/2 Topological Semimetal", Sci. Adv. **4**, eaao4513 (2018) (cited on page 10).

[79] Q.-Z. Wang, J. Yu, and C.-X. Liu, "Unconventional superconductivity and surface pairing symmetry in half-Heusler compounds", Phys. Rev. B **97**, 224507 (2018) (cited on pages 10, 40).

[80] T. Nomoto and H. Ikeda, "Exotic Multigap Structure in UPt$_3$ Unveiled by a First-Principles Analysis", Phys. Rev. Lett. **117**, 217002 (2016) (cited on page 10).

[81] T. Nomoto, K. Hattori, and H. Ikeda, "Classification of "multipole" superconductivity in multiorbital systems and its implications", Phys. Rev. B **94**, 174513 (2016) (cited on pages 10, 87).

[82] Y. Maeno, H. Hashimoto, K. Yoshida, S. Nishizaki, T. Fujita, J. G. Bednorz, and F. Lichtenberg, "Superconductivity in a layered perovskite without copper", Nature **372**, 532 (1994) (cited on pages 11, 69, 73, 105, 107).

[83] T. M. Rice and M. Sigrist, "Sr$_2$RuO$_4$: an electronic analogue of ^{3}He?", Journal of Physics: Condensed Matter **7**, L643 (1995) (cited on pages 11, 73–75, 98, 105, 108).

[84] A. Pustogow, Y. Luo, A. Chronister, Y.-S. Su, D. A. Sokolov, F. Jerzembeck, A. P. Mackenzie, C. W. Hicks, N. Kikugawa, S. Raghu, E. D. Bauer, and S. E. Brown, "Constraints on the superconducting order parameter in Sr$_2$RuO$_4$ from oxygen-17 nuclear magnetic resonance", Nature **574**, 72 (2019) (cited on pages 11, 75, 102–105, 108).

[85] K. Ishida, M. Manago, K. Kinjo, and Y. Maeno, "Reduction of the ^{17}O Knight Shift in the Superconducting State and the Heat-up Effect by NMR Pulses on Sr$_2$RuO$_4$", Journal of the Physical Society of Japan **89**, 034712 (2020) (cited on pages 11, 75, 102–105, 108).

[86] M. Tinkham, *Introduction to Superconductivity*, 2nd edition, Vol. 1 (Dover Publications, June 2004) (cited on page 14).

[87] D. N. Basov and A. V. Chubukov, "Manifesto for a higher T_c", Nature Physics **7**, 272 (2011) (cited on page 15).

[88] M. Smidman, M. B. Salamon, H. Q. Yuan, and D. F. Agterberg, "Superconductivity and spin-orbit coupling in non-centrosymmetric materials: a review", Reports on Progress in Physics **80**, 036501 (2017) (cited on page 16).

[89] S. Yip, "Noncentrosymmetric Superconductors", Annual Review of Condensed Matter Physics **5**, 15 (2014) (cited on page 16).

[90] C. Kallin and J. Berlinsky, "Chiral superconductors", Reports on Progress in Physics **79**, 054502 (2016) (cited on pages 21, 50, 107).

[91] P. W. Anderson and P. Morel, "Generalized Bardeen-Cooper-Schrieffer States and the Proposed Low-Temperature Phase of Liquid He^3", Phys. Rev. **123**, 1911 (1961) (cited on page 23).

[92] B. Mazidian, J. Quintanilla, A. D. Hillier, and J. F. Annett, "Anomalous thermodynamic power laws near topological transitions in nodal superconductors", Phys. Rev. B **88**, 224504 (2013) (cited on page 24).

[93] C. J. Lapp, G. Börner, and C. Timm, "Experimental consequences of Bogoliubov Fermi surfaces", Phys. Rev. B **101**, 024505 (2020) (cited on pages 24, 63, 105).

[94] Y. Saito, Y. Nakamura, M. S. Bahramy, Y. Kohama, J. Ye, Y. Kasahara, Y. Nakagawa, M. Onga, M. Tokunaga, T. Nojima, Y. Yanase, and Y. Iwasa, "Superconductivity protected by spin–valley locking in ion-gated MoS2", Nature Physics **12**, 144 (2015) (cited on page 24).

[95] C. B. Bishop, G. Liu, E. Dagotto, and A. Moreo, "On-site attractive multiorbital Hamiltonian for d-wave superconductors", Phys. Rev. B **93**, 224519 (2016) (cited on page 24).

[96] Z. A. Ren, J. Yang, W. Lu, W. Yi, G. C. Che, X. L. Dong, L. L. Sun, and Z. X. Zhao, "Superconductivity at 52 K in iron based F doped layered quaternary compound $Pr[O_{1-x}F_x]FeAs$", Materials Research Innovations **12**, 105 (2008) (cited on page 25).

[97] H.-H. Wen, G. Mu, L. Fang, H. Yang, and X. Zhu, "Superconductivity at 25 K in hole-doped $(La_{1-x}Sr_x)OFeAs$", EPL (Europhysics Letters) **82**, 17009 (2008) (cited on page 25).

[98] S. Onari, H. Kontani, and M. Sato, "Structure of neutron-scattering peaks in both s_{++}-wave and $s_\pm$-wave states of an iron pnictide superconductor", Phys. Rev. B **81**, 060504 (2010) (cited on page 25).

[99] R. J. McQueeney, S. O. Diallo, V. P. Antropov, G. D. Samolyuk, C. Broholm, N. Ni, S. Nandi, M. Yethiraj, J. L. Zarestky, J. J. Pulikkotil, A. Kreyssig, M. D. Lumsden, B. N. Harmon, P. C. Canfield, and A. I. Goldman, "Anisotropic Three-Dimensional Magnetism in $CaFe_2As_2$", Phys. Rev. Lett. **101**, 227205 (2008) (cited on page 25).

[100] J. Zhao, D. T. Adroja, D.-X. Yao, R. Bewley, S. Li, X. F. Wang, G. Wu, X. H. Chen, J. Hu, and P. Dai, "Spin waves and magnetic exchange interactions in $CaFe_2As_2$", Nature Physics **5**, 555 (2009) (cited on page 25).

[101] M. Gang, Z. Xi-Yu, F. Lei, S. Lei, R. Cong, and W. Hai-Hu, "Nodal Gap in Fe-Based Layered Superconductor $LaO_{0.9}F_{0.1-\delta}FeAs$ Probed by Specific Heat Measurements", Chinese Physics Letters **25**, 2221 (2008) (cited on page 25).

[102] G. Mu, H. Luo, Z. Wang, L. Shan, C. Ren, and H.-H. Wen, "Low temperature specific heat of the hole-doped $Ba_{0.6}K_{0.4}Fe_2As_2$ single crystals", Phys. Rev. B **79**, 174501 (2009) (cited on page 25).

[103] S. L. Bud'ko, N. Ni, and P. C. Canfield, "Jump in specific heat at the superconducting transition temperature in $Ba(Fe_{1-x}Co_x)_2As_2$ and $Ba(Fe_{1-x}Ni_x)_2As_2$ single crystals", Phys. Rev. B **79**, 220516 (2009) (cited on page 25).

[104] K. Gofryk, A. S. Sefat, M. A. McGuire, B. C. Sales, D. Mandrus, J. D. Thompson, E. D. Bauer, and F. Ronning, "Doping-dependent specific heat study of the superconducting gap in $Ba(Fe_{1-x}Co_x)_2As_2$", Phys. Rev. B **81**, 184518 (2010) (cited on page 25).

[105] V. Cvetkovic and Z. Tesanovic, "Multiband magnetism and superconductivity in Fe-based compounds", EPL (Europhysics Letters) **85**, 37002 (2009) (cited on page 25).

[106] K. Wang, H. Lei, and C. Petrovic, "Thermoelectric studies of $K_xFe_{2-y}Se_2$ indicating a weakly correlated superconductor", Phys. Rev. B **83**, 174503 (2011) (cited on page 25).

[107]   K. Kuroki, S. Onari, R. Arita, H. Usui, Y. Tanaka, H. Kontani, and H. Aoki, "Unconventional Pairing Originating from the Disconnected Fermi Surfaces of Superconducting LaFeAsO$_{1-x}$F$_x$", Phys. Rev. Lett. **101**, 087004 (2008) (cited on page 25).

[108]   S. Graser, T. A. Maier, P. J. Hirschfeld, and D. J. Scalapino, "Near-degeneracy of several pairing channels in multiorbital models for the Fe pnictides", New Journal of Physics **11**, 025016 (2009) (cited on pages 25, 80).

[109]   M. Daghofer, A. Nicholson, A. Moreo, and E. Dagotto, "Three orbital model for the iron-based super-conductors", Phys. Rev. B **81**, 014511 (2010) (cited on page 25).

[110]   Y.-Y. Tai, J.-X. Zhu, M. J. Graf, and C. S. Ting, "Calculated phase diagram of doped BaFe$_2$As$_2$ super-conductor in a C_4-symmetry breaking model", EPL (Europhysics Letters) **103**, 67001 (2013) (cited on page 25).

[111]   S. Raghu, X.-L. Qi, C.-X. Liu, D. J. Scalapino, and S.-C. Zhang, "Minimal two-band model of the superconducting iron oxypnictides", Phys. Rev. B **77**, 220503 (2008) (cited on pages 25, 28).

[112]   I. I. Mazin, D. J. Singh, M. D. Johannes, and M. H. Du, "Unconventional Superconductivity with a Sign Reversal in the Order Parameter of LaFeAsO$_{1-x}$F$_x$", Phys. Rev. Lett. **101**, 057003 (2008) (cited on page 25).

[113]   A. Ramires and M. Sigrist, "Identifying detrimental effects for multiorbital superconductivity: Application to Sr$_2$RuO$_4$", Phys. Rev. B **94**, 104501 (2016) (cited on pages 31, 96, 108).

[114]   A. Ramires, D. F. Agterberg, and M. Sigrist, "Tailoring T_c by symmetry principles: The concept of superconducting fitness", Phys. Rev. B **98**, 024501 (2018) (cited on pages 31, 96, 108).

[115]   Y. Zhang, L. X. Yang, M. Xu, Z. R. Ye, F. Chen, C. He, H. C. Xu, J. Jiang, B. P. Xie, J. J. Ying, X. F. Wang, X. H. Chen, J. P. Hu, M. Matsunami, S. Kimura, and D. L. Feng, "Nodeless superconducting gap in A$_x$Fe$_2$Se$_2$ (A=K,Cs) revealed by angle-resolved photoemission spectroscopy", Nature Materials **10**, 273 (2011) (cited on page 31).

[116]   D. Liu, W. Zhang, D. Mou, J. He, Y.-B. Ou, Q.-Y. Wang, Z. Li, L. Wang, L. Zhao, S. He, Y. Peng, X. Liu, C. Chen, L. Yu, G. Liu, X. Dong, J. Zhang, C. Chen, Z. Xu, J. Hu, X. Chen, X. Ma, Q. Xue, and X. Zhou, "Electronic origin of high-temperature superconductivity in single-layer FeSe superconductor", Nature Communications **3**, 10.1038/ncomms1946 (2012) (cited on page 31).

[117]   K. Okazaki, Y. Ota, Y. Kotani, W. Malaeb, Y. Ishida, T. Shimojima, T. Kiss, S. Watanabe, C. T. Chen, K. Kihou, C. H. Lee, A. Iyo, H. Eisaki, T. Saito, H. Fukazawa, Y. Kohori, K. Hashimoto, T. Shibauchi, Y. Matsuda, H. Ikeda, H. Miyahara, R. Arita, A. Chainani, and S. Shin, "Octet-Line Node Structure of Superconducting Order Parameter in KFe$_2$As$_2$", Science **337**, 1314 (2012) (cited on page 32).

[118]   O. Vafek and A. V. Chubukov, "Hund Interaction, Spin-Orbit Coupling, and the Mechanism of Superconductivity in Strongly Hole-Doped Iron Pnictides", Phys. Rev. Lett. **118**, 087003 (2017) (cited on pages 32, 88, 89, 105, 108).

[119]   P. M. R. Brydon, D. S. L. Abergel, D. F. Agterberg, and V. M. Yakovenko, "Loop Currents and Anomalous Hall Effect from Time-Reversal Symmetry-Breaking Superconductivity on the Honeycomb Lattice", Phys. Rev. X **9**, 031025 (2019) (cited on pages 35, 64).

[120] Y. X. Zhao, A. P. Schnyder, and Z. D. Wang, "Unified Theory of *PT* and *CP* Invariant Topological Metals and Nodal Superconductors", Phys. Rev. Lett. **116**, 156402 (2016) (cited on page 35).

[121] C.-K. Chiu, J. C. Y. Teo, A. P. Schnyder, and S. Ryu, "Classification of topological quantum matter with symmetries", Rev. Mod. Phys. **88**, 035005 (2016) (cited on page 35).

[122] S. Kobayashi, K. Shiozaki, Y. Tanaka, and M. Sato, "Topological Blount's theorem of odd-parity superconductors", Phys. Rev. B **90**, 024516 (2014) (cited on page 35).

[123] J. M. Luttinger and W. Kohn, "Motion of Electrons and Holes in Perturbed Periodic Fields", Phys. Rev. **97**, 869 (1955) (cited on page 38).

[124] J. M. Luttinger, "Quantum Theory of Cyclotron Resonance in Semiconductors: General Theory", Phys. Rev. **102**, 1030 (1956) (cited on page 38).

[125] P. Y. Yu and M. Cardona, *Fundamentals of Semiconductors* (Springer Berlin Heidelberg, 2010) (cited on page 38).

[126] T. Kondo, M. Nakayama, R. Chen, J. J. Ishikawa, E.-G. Moon, T. Yamamoto, Y. Ota, W. Malaeb, H. Kanai, Y. Nakashima, Y. Ishida, R. Yoshida, H. Yamamoto, M. Matsunami, S. Kimura, N. Inami, K. Ono, H. Kumigashira, S. Nakatsuji, L. Balents, and S. Shin, "Quadratic Fermi node in a 3D strongly correlated semimetal", Nature Communications **6**, `10.1038/ncomms10042` (2015) (cited on page 38).

[127] M. Nakayama, T. Kondo, Z. Tian, J. J. Ishikawa, M. Halim, C. Bareille, W. Malaeb, K. Kuroda, T. Tomita, S. Ideta, K. Tanaka, M. Matsunami, S. Kimura, N. Inami, K. Ono, H. Kumigashira, L. Balents, S. Nakatsuji, and S. Shin, "Slater to Mott Crossover in the Metal to Insulator Transition of $Nd_2Ir_2O_7$", Phys. Rev. Lett. **117**, 056403 (2016) (cited on page 38).

[128] B. Cheng, T. Ohtsuki, D. Chaudhuri, S. Nakatsuji, M. Lippmaa, and N. P. Armitage, "Dielectric anomalies and interactions in the three-dimensional quadratic band touching Luttinger semimetal $Pr_2Ir_2O_7$", Nature Communications **8**, `10.1038/s41467-017-02121-y` (2017) (cited on page 38).

[129] A. Szabo, R. Moessner, and B. Roy, "Interacting spin-3/2 fermions in a Luttinger (semi)metal: competing phases and their selection in the global phase diagram", Nov. 2018, arXiv:1811.12415 `[cond-mat.str-el]` (cited on page 38).

[130] H. Lin, L. A. Wray, Y. Xia, S. Xu, S. Jia, R. J. Cava, A. Bansil, and M. Z. Hasan, "Half-Heusler ternary compounds as new multifunctional experimental platforms for topological quantum phenomena", Nature Materials **9**, 546 (2010) (cited on page 38).

[131] Z. K. Liu, L. X. Yang, S.-C. Wu, C. Shekhar, J. Jiang, H. F. Yang, Y. Zhang, S.-K. Mo, Z. Hussain, B. Yan, C. Felser, and Y. L. Chen, "Observation of unusual topological surface states in half-Heusler compounds LnPtBi (Ln=Lu, Y)", Nature Communications **7**, `10.1038/ncomms12924` (2016) (cited on page 38).

[132] J. Yu, B. Yan, and C.-X. Liu, "Model Hamiltonian and time reversal breaking topological phases of antiferromagnetic half-Heusler materials", Phys. Rev. B **95**, 235158 (2017) (cited on page 38).

[133] P. M. R. Brydon, D. F. Agterberg, H. Menke, and C. Timm, "Bogoliubov Fermi surfaces: General theory, magnetic order, and topology", Phys. Rev. B **98**, 224509 (2018) (cited on pages 39, 41, 43, 44, 46, 48, 49, 63, 105, 107).

[134] I. Boettcher and I. F. Herbut, "Unconventional Superconductivity in Luttinger Semimetals: Theory of Complex Tensor Order and the Emergence of the Uniaxial Nematic State", Phys. Rev. Lett. **120**, 057002 (2018) (cited on pages 40, 51, 52, 54).

[135] H. Oh and E.-G. Moon, "Instability of $j = 3/2$ Bogoliubov Fermi-surfaces", Nov. 2019, arXiv:1911. 08487 [cond-mat.str-el] (cited on pages 40, 48, 107).

[136] S.-T. Tamura, S. Iimura, and S. Hoshino, "Electronic multipoles and multiplet pairs induced from Pomeranchuk and Cooper instabilities of Bogoliubov Fermi surfaces", Apr. 2020, arXiv:2004.06925 [cond-mat.supr-con] (cited on pages 40, 48, 107).

[137] T.-L. Ho and S. Yip, "Pairing of Fermions with Arbitrary Spin", Phys. Rev. Lett. **82**, 247 (1999) (cited on pages 49, 50, 52, 54, 67, 107).

[138] T.-L. Ho, "Spinor Bose Condensates in Optical Traps", Phys. Rev. Lett. **81**, 742 (1998) (cited on page 49).

[139] N. D. Mermin, "d-wave pairing near the transition temperature", Phys. Rev. A **9**, 868 (1974) (cited on page 49).

[140] H. Menke, C. Timm, and P. M. R. Brydon, "Bogoliubov Fermi surfaces stabilized by spin-orbit coupling", Phys. Rev. B **100**, 224505 (2019) (cited on pages 53, 55, 56, 59, 60, 62, 64, 105, 107).

[141] Y. Kasahara, T. Iwasawa, H. Shishido, T. Shibauchi, K. Behnia, Y. Haga, T. D. Matsuda, Y. Onuki, M. Sigrist, and Y. Matsuda, "Exotic Superconducting Properties in the Electron-Hole-Compensated Heavy-Fermion "Semimetal" URu_2Si_2", Phys. Rev. Lett. **99**, 116402 (2007) (cited on pages 54, 68, 107, 108).

[142] I. F. Herbut, I. Boettcher, and S. Mandal, "Ground state of the three-dimensional BCS d-wave superconductor", Phys. Rev. B **100**, 104503 (2019) (cited on page 54).

[143] P. Goswami, B. Roy, and S. Das Sarma, "Competing orders and topology in the global phase diagram of pyrochlore iridates", Phys. Rev. B **95**, 085120 (2017) (cited on page 63).

[144] I. Boettcher and I. F. Herbut, "Anisotropy induces non-Fermi-liquid behavior and nematic magnetic order in three-dimensional Luttinger semimetals", Phys. Rev. B **95**, 075149 (2017) (cited on page 63).

[145] E. Fradkin, S. A. Kivelson, and J. M. Tranquada, "Colloquium: Theory of intertwined orders in high temperature superconductors", Rev. Mod. Phys. **87**, 457 (2015) (cited on page 64).

[146] R. M. Fernandes, P. P. Orth, and J. Schmalian, "Intertwined Vestigial Order in Quantum Materials: Nematicity and Beyond", Annual Review of Condensed Matter Physics **10**, 133 (2019) (cited on page 64).

[147] E. K. Dahl and A. Sudbø, "Derivation of the Ginzburg-Landau equations for a ferromagnetic p-wave superconductor", Phys. Rev. B **75**, 144504 (2007) (cited on page 64).

[148] V. P. Mineev and K. V. Samokhin, *Introduction to Unconventional Superconductivity* (Gordon and Breach Science Publishers, New York, 1999) (cited on pages 67, 73, 74, 107).

[149] M. C. Cross, "A Generalized Ginzburg-Landau Approach to the Superfluidity of Helium 3", J. Low Temp. Phys. **21**, 525 (1975) (cited on page 67).

[150] N. D. Mermin and P. Muzikar, "Cooper pairs versus Bose condensed molecules: The ground-state current in superfluid ^3He-A", Phys. Rev. B **21**, 980 (1980) (cited on page 67).

[151] S. Maekawa and M. Sato, *Physics of High-Temperature Superconductors*, Springer Series in Solid-State Sciences (Springer Berlin Heidelberg, 2012) (cited on page 69).

[152] A. P. Mackenzie and Y. Maeno, "The superconductivity of Sr_2RuO_4 and the physics of spin-triplet pairing", Rev. Mod. Phys. **75**, 657 (2003) (cited on pages 69, 73, 74).

[153] J. J. Randall and R. Ward, "The Preparation of Some Ternary Oxides of the Platinum Metals1,2", Journal of the American Chemical Society **81**, 2629 (1959) (cited on page 69).

[154] A. Callaghan, C. W. Moeller, and R. Ward, "Magnetic Interactions in Ternary Ruthenium Oxides", Inorganic Chemistry **5**, 1572 (1966) (cited on page 69).

[155] R. Franz and G. Wiedemann, "Über die Wärme-Leitungsfähigkeit der Metalle", Annalen der Physik und Chemie **165**, 497 (1853) (cited on page 69).

[156] R. W. Hill, C. Proust, L. Taillefer, P. Fournier, and R. L. Greene, "Breakdown of Fermi-liquid theory in a copper-oxide superconductor", Nature **414**, 711 (2001) (cited on page 69).

[157] N. E. Hussey, A. P. Mackenzie, J. R. Cooper, Y. Maeno, S. Nishizaki, and T. Fujita, "Normal-state magnetoresistance of Sr_2RuO_4", Phys. Rev. B **57**, 5505 (1998) (cited on pages 69, 105).

[158] C. Bergemann, A. P. Mackenzie, S. R. Julian, D. Forsythe, and E. Ohmichi, "Quasi-two-dimensional Fermi liquid properties of the unconventional superconductor Sr_2RuO_4", Advances in Physics **52**, 639 (2003) (cited on pages 69, 86, 105).

[159] A. Damascelli, D. H. Lu, K. M. Shen, N. P. Armitage, F. Ronning, D. L. Feng, C. Kim, Z.-X. Shen, T. Kimura, Y. Tokura, Z. Q. Mao, and Y. Maeno, "Fermi Surface, Surface States, and Surface Reconstruction in Sr_2RuO_4", Phys. Rev. Lett. **85**, 5194 (2000) (cited on pages 69, 86, 98, 105).

[160] C. N. Veenstra, Z.-H. Zhu, M. Raichle, B. M. Ludbrook, A. Nicolaou, B. Slomski, G. Landolt, S. Kittaka, Y. Maeno, J. H. Dil, I. S. Elfimov, M. W. Haverkort, and A. Damascelli, "Spin-Orbital Entanglement and the Breakdown of Singlets and Triplets in Sr_2RuO_4 Revealed by Spin- and Angle-Resolved Photoemission Spectroscopy", Phys. Rev. Lett. **112**, 127002 (2014) (cited on pages 69, 75, 81–85, 97, 98, 105, 108).

[161] A. Tamai, M. Zingl, E. Rozbicki, E. Cappelli, S. Riccò, A. de la Torre, S. McKeown Walker, F. Y. Bruno, P. D. C. King, W. Meevasana, M. Shi, M. Radovi ć, N. C. Plumb, A. S. Gibbs, A. P. Mackenzie, C. Berthod, H. U. R. Strand, M. Kim, A. Georges, and F. Baumberger, "High-Resolution Photoemission on Sr_2RuO_4 Reveals Correlation-Enhanced Effective Spin-Orbit Coupling and Dominantly Local Self-Energies", Phys. Rev. X **9**, 021048 (2019) (cited on pages 69, 86, 97, 98, 105).

[162] K. Deguchi, M. A. Tanatar, Z. Mao, T. Ishiguro, and Y. Maeno, "Superconducting Double Transition and the Upper Critical Field Limit of Sr_2RuO_4 in Parallel Magnetic Fields", Journal of the Physical Society of Japan **71**, 2839 (2002) (cited on page 69).

[163] K. Ishida, H. Mukuda, Y. Kitaoka, Z. Q. Mao, Y. Mori, and Y. Maeno, "Anisotropic Superconducting Gap in the Spin-Triplet Superconductor Sr_2RuO_4: Evidence from a Ru-NQR Study", Phys. Rev. Lett. **84**, 5387 (2000) (cited on page 70).

[164] I. Bonalde, B. D. Yanoff, M. B. Salamon, D. J. Van Harlingen, E. M. E. Chia, Z. Q. Mao, and Y. Maeno, "Temperature Dependence of the Penetration Depth in Sr_2RuO_4: Evidence for Nodes in the Gap Function", Phys. Rev. Lett. **85**, 4775 (2000) (cited on page 70).

[165]   E. Hassinger, P. Bourgeois-Hope, H. Taniguchi, S. René de Cotret, G. Grissonnanche, M. S. Anwar, Y. Maeno, N. Doiron-Leyraud, and L. Taillefer, "Vertical Line Nodes in the Superconducting Gap Structure of Sr_2RuO_4", Phys. Rev. X **7**, 011032 (2017) (cited on pages 70, 104).

[166]   S. Kittaka, S. Nakamura, T. Sakakibara, N. Kikugawa, T. Terashima, S. Uji, D. A. Sokolov, A. P. Mackenzie, K. Irie, Y. Tsutsumi, K. Suzuki, and K. Machida, "Searching for Gap Zeros in Sr_2RuO_4 via Field-Angle-Dependent Specific-Heat Measurement", Journal of the Physical Society of Japan **87**, 093703 (2018) (cited on pages 70, 104).

[167]   K. Machida, K. Irie, K. Suzuki, H. Ikeda, and Y. Tsutsumi, "Theoretical studies for identifying horizontal line nodes via angle-resolved density-of-states measurements: Application to Sr_2RuO_4", Phys. Rev. B **99**, 064510 (2019) (cited on pages 70, 104).

[168]   R. Sharma, S. D. Edkins, Z. Wang, A. Kostin, C. Sow, Y. Maeno, A. P. Mackenzie, J. C. S. Davis, and V. Madhavan, "Momentum-resolved superconducting energy gaps of Sr2RuO4 from quasiparticle interference imaging", Proceedings of the National Academy of Sciences **117**, 5222 (2020) (cited on pages 70, 104).

[169]   P. Anderson, "Theory of dirty superconductors", Journal of Physics and Chemistry of Solids **11**, 26 (1959) (cited on page 70).

[170]   A. P. Mackenzie, R. K. W. Haselwimmer, A. W. Tyler, G. G. Lonzarich, Y. Mori, S. Nishizaki, and Y. Maeno, "Extremely Strong Dependence of Superconductivity on Disorder in Sr_2RuO_4", Phys. Rev. Lett. **80**, 161 (1998) (cited on page 70).

[171]   N. Kikugawa, A. Peter Mackenzie, and Y. Maeno, "Effects of In-Plane Impurity Substitution in Sr_2RuO_4", Journal of the Physical Society of Japan **72**, 237 (2003) (cited on page 70).

[172]   F. Laube, G. Goll, H. v. Löhneysen, M. Fogelström, and F. Lichtenberg, "Spin-Triplet Superconductivity in Sr_2RuO_4 Probed by Andreev Reflection", Phys. Rev. Lett. **84**, 1595 (2000) (cited on page 70).

[173]   J. R. Kirtley, C. Kallin, C. W. Hicks, E.-A. Kim, Y. Liu, K. A. Moler, Y. Maeno, and K. D. Nelson, "Upper limit on spontaneous supercurrents in Sr_2RuO_4", Phys. Rev. B **76**, 014526 (2007) (cited on page 71).

[174]   S. B. Etter, A. Bouhon, and M. Sigrist, "Spontaneous surface flux pattern in chiral p-wave superconductors", Phys. Rev. B **97**, 064510 (2018) (cited on page 71).

[175]   Y. Iguchi, I. Zhang, E. Bauer, F. Ronning, and K. A. Moler, "Study of chiral d-wave superconductor candidate URu_2Si_2 by using scanning SQUID microscopy", APS2019, X08.10 (cited on page 71).

[176]   T. Nakamura, T. Sumi, S. Yonezawa, T. Terashima, M. Sigrist, H. Kaneyasu, and Y. Maeno, "Essential Configuration of $Pb/Ru/Sr_2RuO_4$ Junctions Exhibiting Anomalous Superconducting Interference", Journal of the Physical Society of Japan **81**, 064708 (2012) (cited on page 71).

[177]   T. Nakamura, R. Nakagawa, T. Yamagishi, T. Terashima, S. Yonezawa, M. Sigrist, and Y. Maeno, "Topological competition of superconductivity in $Pb/Ru/Sr_2RuO_4$ junctions", Phys. Rev. B **84**, 060512 (2011) (cited on page 71).

[178]   H. Kaneyasu and M. Sigrist, "Nucleation of Vortex State in Ru-Inclusion in Eutectic Ruthenium Oxide Sr_2RuO_4-Ru", Journal of the Physical Society of Japan **79**, 053706 (2010) (cited on page 71).

[179] M. S. Anwar, R. Ishiguro, T. Nakamura, M. Yakabe, S. Yonezawa, H. Takayanagi, and Y. Maeno, "Multicomponent order parameter superconductivity of Sr_2RuO_4 revealed by topological junctions", Phys. Rev. B **95**, 224509 (2017) (cited on page 71).

[180] M. S. Anwar, T. Nakamura, S. Yonezawa, M. Yakabe, R. Ishiguro, H. Takayanagi, and Y. Maeno, "Anomalous switching in Nb/Ru/Sr2RuO4 topological junctions by chiral domain wall motion", Scientific Reports **3**, 2480 (2013) (cited on page 71).

[181] S. B. Etter, H. Kaneyasu, M. Ossadnik, and M. Sigrist, "Limiting mechanism for critical current in topologically frustrated Josephson junctions", Phys. Rev. B **90**, 024515 (2014) (cited on page 71).

[182] C. W. Hicks, J. R. Kirtley, T. M. Lippman, N. C. Koshnick, M. E. Huber, Y. Maeno, W. M. Yuhasz, M. B. Maple, and K. A. Moler, "Limits on superconductivity-related magnetization in Sr_2RuO_4 and $PrOs_4Sb_{12}$ from scanning SQUID microscopy", Phys. Rev. B **81**, 214501 (2010) (cited on page 71).

[183] C. W. Hicks, D. O. Brodsky, E. A. Yelland, A. S. Gibbs, J. A. N. Bruin, M. E. Barber, S. D. Edkins, K. Nishimura, S. Yonezawa, Y. Maeno, and A. P. Mackenzie, "Strong Increase of T_c of Sr_2RuO_4 Under Both Tensile and Compressive Strain", Science **344**, 283 (2014) (cited on pages 71, 72, 104).

[184] A. Steppke, L. Zhao, M. E. Barber, T. Scaffidi, F. Jerzembeck, H. Rosner, A. S. Gibbs, Y. Maeno, S. H. Simon, A. P. Mackenzie, and C. W. Hicks, "Strong peak in T_c of Sr_2RuO_4 under uniaxial pressure", Science **355**, `10.1126/science.aaf9398` (2017) (cited on pages 71, 72, 104).

[185] V. Grinenko, S. Ghosh, R. Sarkar, J.-C. Orain, A. Nikitin, M. Elender, D. Das, Z. Guguchia, F. Brückner, M. E. Barber, J. Park, N. Kikugawa, D. A. Sokolov, J. S. Bobowski, T. Miyoshi, Y. Maeno, A. P. Mackenzie, H. Luetkens, C. W. Hicks, and H.-H. Klauss, "Split superconducting and time-reversal symmetry-breaking transitions, and magnetic order in Sr_2RuO_4 under uniaxial stress", 2020, arXiv:2001.08152 `[cond-mat.supr-con]` (cited on pages 71, 73, 75, 105).

[186] C. Lupien, "Ultrasound Attenuation in the Unconventional Superconductor Sr_2RuO_4", PhD thesis (University of Toronto, 2001) (cited on pages 71, 75, 104, 105).

[187] C. Lupien, W. A. MacFarlane, C. Proust, L. Taillefer, Z. Q. Mao, and Y. Maeno, "Ultrasound Attenuation in Sr_2RuO_4: An Angle-Resolved Study of the Superconducting Gap Function", Phys. Rev. Lett. **86**, 5986 (2001) (cited on pages 71, 104, 105).

[188] S. Ghosh, A. Shekhter, F. Jerzembeck, N. Kikugawa, D. A. Sokolov, A. P. Mackenzie, C. W. Hicks, and B. J. Ramshaw, "Thermodynamic evidence for a two-component superconducting order parameter in Sr_2RuO_4", Feb. 2020, arXiv:2002.06130 `[cond-mat.supr-con]` (cited on pages 71, 72, 75, 104, 105).

[189] H. Tou, Y. Kitaoka, K. Ishida, K. Asayama, N. Kimura, Y. Ōnuki, E. Yamamoto, Y. Haga, and K. Maezawa, "Nonunitary Spin-Triplet Superconductivity in UPt_3: Evidence from ^{195}Pt Knight Shift Study", Phys. Rev. Lett. **80**, 3129 (1998) (cited on page 73).

[190] Y. Tsutsumi, K. Machida, T. Ohmi, and M.-a. Ozaki, "A Spin Triplet Superconductor UPt_3", Journal of the Physical Society of Japan **81**, 074717 (2012) (cited on page 73).

[191] A. Huxley, I. Sheikin, E. Ressouche, N. Kernavanois, D. Braithwaite, R. Calemczuk, and J. Flouquet, "UGe_2: A ferromagnetic spin-triplet superconductor", Phys. Rev. B **63**, 144519 (2001) (cited on page 73).

[192] L. Jiao, S. Howard, S. Ran, Z. Wang, J. O. Rodriguez, M. Sigrist, Z. Wang, N. P. Butch, and V. Madhavan, "Chiral superconductivity in heavy-fermion metal UTe$_2$", Nature **579**, 523 (2020) (cited on page 73).

[193] J. Ishizuka, S. Sumita, A. Daido, and Y. Yanase, "Insulator-Metal Transition and Topological Superconductivity in UTe$_2$ from a First-Principles Calculation", Phys. Rev. Lett. **123**, 217001 (2019) (cited on page 73).

[194] S. Ran, C. Eckberg, Q.-P. Ding, Y. Furukawa, T. Metz, S. R. Saha, I.-L. Liu, M. Zic, H. Kim, J. Paglione, and N. P. Butch, "Nearly ferromagnetic spin-triplet superconductivity", Science **365**, 684 (2019) (cited on page 73).

[195] Y. S. Hor, A. J. Williams, J. G. Checkelsky, P. Roushan, J. Seo, Q. Xu, H. W. Zandbergen, A. Yazdani, N. P. Ong, and R. J. Cava, "Superconductivity in Cu$_x$Bi$_2$Se$_3$ and its Implications for Pairing in the Undoped Topological Insulator", Phys. Rev. Lett. **104**, 057001 (2010) (cited on page 73).

[196] N. Read and D. Green, "Paired states of fermions in two dimensions with breaking of parity and time-reversal symmetries and the fractional quantum Hall effect", Phys. Rev. B **61**, 10267 (2000) (cited on page 73).

[197] A. Y. Kitaev, "Unpaired Majorana fermions in quantum wires", Physics-Uspekhi **44**, 131 (2001) (cited on page 73).

[198] M. Sato and Y. Ando, "Topological superconductors: a review", Reports on Progress in Physics **80**, 076501 (2017) (cited on page 73).

[199] K. Yosida, "Paramagnetic Susceptibility in Superconductors", Phys. Rev. **110**, 769 (1958) (cited on pages 74, 132).

[200] K. Ishida, H. Mukuda, Y. Kitaoka, K. Asayama, Z. Q. Mao, Y. Mori, and Y. Maeno, "Spin-triplet superconductivity in Sr$_2$RuO$_4$ identified by ^{17}O Knight shift", Nature **396**, 658 (1998) (cited on page 74).

[201] J. A. Duffy, S. M. Hayden, Y. Maeno, Z. Mao, J. Kulda, and G. J. McIntyre, "Polarized-Neutron Scattering Study of the Cooper-Pair Moment in Sr$_2$RuO$_4$", Phys. Rev. Lett. **85**, 5412 (2000) (cited on page 74).

[202] H. Murakawa, K. Ishida, K. Kitagawa, Z. Q. Mao, and Y. Maeno, "Measurement of the ^{101}Ru-Knight Shift of Superconducting Sr$_2$RuO$_4$ in a Parallel Magnetic Field", Phys. Rev. Lett. **93**, 167004 (2004) (cited on page 74).

[203] I. Žutić and I. Mazin, "Phase-Sensitive Tests of the Pairing State Symmetry in Sr$_2$RuO$_4$", Phys. Rev. Lett. **95**, 217004 (2005) (cited on page 74).

[204] I. I. Mazin and D. J. Singh, "Competitions in Layered Ruthenates: Ferromagnetism versus Antiferromagnetism and Triplet versus Singlet Pairing", Phys. Rev. Lett. **82**, 4324 (1999) (cited on page 75).

[205] T. Kuwabara and M. Ogata, "Spin-Triplet Superconductivity due to Antiferromagnetic Spin-Fluctuation in Sr$_2$RuO$_4$", Phys. Rev. Lett. **85**, 4586 (2000) (cited on pages 75, 109).

[206] S. Raghu, A. Kapitulnik, and S. A. Kivelson, "Hidden Quasi-One-Dimensional Superconductivity in Sr$_2$RuO$_4$", Phys. Rev. Lett. **105**, 136401 (2010) (cited on pages 75, 98).

[207] Q. H. Wang, C. Platt, Y. Yang, C. Honerkamp, F. C. Zhang, W. Hanke, T. M. Rice, and R. Thomale, "Theory of superconductivity in a three-orbital model of Sr$_2$RuO$_4$", EPL (Europhysics Letters) **104**, 17013 (2013) (cited on page 75).

[208] J.-W. Huo, T. M. Rice, and F.-C. Zhang, "Spin Density Wave Fluctuations and p-Wave Pairing in Sr_2RuO_4", Phys. Rev. Lett. **110**, 167003 (2013) (cited on pages 75, 109).

[209] A. T. Rømer, D. D. Scherer, I. M. Eremin, P. J. Hirschfeld, and B. M. Andersen, "Knight Shift and Leading Superconducting Instability from Spin Fluctuations in Sr_2RuO_4", Phys. Rev. Lett. **123**, 247001 (2019) (cited on pages 75, 103, 109).

[210] H. S. Røising, T. Scaffidi, F. Flicker, G. F. Lange, and S. H. Simon, "Superconducting order of Sr_2RuO_4 from a three-dimensional microscopic model", Phys. Rev. Research **1**, 033108 (2019) (cited on page 75).

[211] S. A. Kivelson, A. C. Yuan, B. J. Ramshaw, and R. Thomale, "A proposal for reconciling diverse experiments on the superconducting state in Sr_2RuO_4", Feb. 2020, arXiv:2002.00016 [cond-mat.supr-con] (cited on pages 75, 104).

[212] M. W. Haverkort, I. S. Elfimov, L. H. Tjeng, G. A. Sawatzky, and A. Damascelli, "Strong Spin-Orbit Coupling Effects on the Fermi Surface of Sr_2RuO_4 and Sr_2RhO_4", Phys. Rev. Lett. **101**, 026406 (2008) (cited on pages 75, 98).

[213] A. Ramires and M. Sigrist, "Superconducting order parameter of Sr_2RuO_4: A microscopic perspective", Phys. Rev. B **100**, 104501 (2019) (cited on page 79).

[214] M. Gradhand, K. I. Wysokinski, J. F. Annett, and B. L. Györffy, "Kerr rotation in the unconventional superconductor Sr_2RuO_4", Phys. Rev. B **88**, 094504 (2013) (cited on pages 80, 105, 108).

[215] T. Scaffidi, J. C. Romers, and S. H. Simon, "Pairing symmetry and dominant band in Sr_2RuO_4", Phys. Rev. B **89**, 220510 (2014) (cited on pages 80, 98, 105, 108).

[216] W. Huang and H. Yao, "Possible Three-Dimensional Nematic Odd-Parity Superconductivity in Sr_2RuO_4", Phys. Rev. Lett. **121**, 157002 (2018) (cited on pages 80, 105, 108).

[217] D. E. King, "Dlib-ml: A Machine Learning Toolkit", Journal of Machine Learning Research **10**, 1755 (2009) (cited on page 81).

[218] J. Kanamori, "Electron Correlation and Ferromagnetism of Transition Metals", Progress of Theoretical Physics **30**, 275 (1963) (cited on pages 86, 105).

[219] A. M. Oleś, "Antiferromagnetism and correlation of electrons in transition metals", Phys. Rev. B **28**, 327 (1983) (cited on pages 87, 105, 108).

[220] A. Georges, L. de'Medici, and J. Mravlje, "Strong Correlations from Hund's Coupling", Annual Review of Condensed Matter Physics **4**, 137 (2013) (cited on pages 87, 89, 108).

[221] C. M. Puetter and H.-Y. Kee, "Identifying spin-triplet pairing in spin-orbit coupled multi-band superconductors", EPL (Europhysics Letters) **98**, 27010 (2012) (cited on pages 88, 89, 97).

[222] J. Spałek, "Spin-triplet superconducting pairing due to local Hund's rule and Dirac exchange", Phys. Rev. B **63**, 104513 (2001) (cited on pages 88, 89).

[223] J. E. Han, "Spin-triplet s-wave local pairing induced by Hund's rule coupling", Phys. Rev. B **70**, 054513 (2004) (cited on pages 88, 89).

[224] A. K. C. Cheung and D. F. Agterberg, "Superconductivity in the presence of spin-orbit interactions stabilized by Hund coupling", Phys. Rev. B **99**, 024516 (2019) (cited on pages 88, 89, 105).

[225] A. W. Lindquist and H.-Y. Kee, "Distinct reduction of Knight shift in superconducting state of Sr_2RuO_4 under uniaxial strain", Dec. 2019, arXiv:1912.02215 [`cond-mat.supr-con`] (cited on page 88).

[226] K. Haule and G. Kotliar, "Coherence–incoherence crossover in the normal state of iron oxypnictides and importance of Hund's rule coupling", New Journal of Physics **11**, 025021 (2009) (cited on page 89).

[227] J. Hu, "Iron-Based Superconductors as Odd-Parity Superconductors", Phys. Rev. X **3**, 031004 (2013) (cited on page 89).

[228] L. Fanfarillo, G. Giovannetti, M. Capone, and E. Bascones, "Nematicity at the Hund's metal crossover in iron superconductors", Phys. Rev. B **95**, 144511 (2017) (cited on page 89).

[229] T. Miyake, K. Nakamura, R. Arita, and M. Imada, "Comparison of Ab initio Low-Energy Models for LaFePO, LaFeAsO, $BaFe_2As_2$, LiFeAs, FeSe, and FeTe: Electron Correlation and Covalency", Journal of the Physical Society of Japan **79**, 044705 (2010) (cited on page 89).

[230] Y. Fukaya, S. Tamura, K. Yada, Y. Tanaka, P. Gentile, and M. Cuoco, "Interorbital topological superconductivity in spin-orbit coupled superconductors with inversion symmetry breaking", Phys. Rev. B **97**, 174522 (2018) (cited on page 89).

[231] S. Hoshino and P. Werner, "Superconductivity from Emerging Magnetic Moments", Phys. Rev. Lett. **115**, 247001 (2015) (cited on page 89).

[232] O. Gingras, R. Nourafkan, A.-M. S. Tremblay, and M. Côté, "Superconducting Symmetries of Sr_2RuO_4 from First-Principles Electronic Structure", Phys. Rev. Lett. **123**, 217005 (2019) (cited on page 89).

[233] G. Zhang, E. Gorelov, E. Sarvestani, and E. Pavarini, "Fermi Surface of Sr_2RuO_4: Spin-Orbit and Anisotropic Coulomb Interaction Effects", Phys. Rev. Lett. **116**, 106402 (2016) (cited on page 97).

[234] H. G. Suh, H. Menke, P. M. R. Brydon, C. Timm, A. Ramires, and D. F. Agterberg, "Stabilizing even-parity chiral superconductivity in Sr_2RuO_4", Phys. Rev. Research **2**, 032023 (2020) (cited on pages 97, 105).

[235] D. F. Agterberg, T. M. Rice, and M. Sigrist, "Orbital Dependent Superconductivity in Sr_2RuO_4", Phys. Rev. Lett. **78**, 3374 (1997) (cited on pages 98, 104).

[236] R. P. Feynman, "Forces in Molecules", Phys. Rev. **56**, 340 (1939) (cited on page 99).

[237] H. Hellmann, *Einführung in die Quantenchemie*, OL 21481721M (J.W. Edwards, Ann Arbor, Mich, 1944) (cited on page 99).

[238] C. Timm, S. Rex, and P. M. R. Brydon, "Surface instability in nodal noncentrosymmetric superconductors", Phys. Rev. B **91**, 180503 (2015) (cited on page 99).

[239] K. Deguchi, Z. Q. Mao, H. Yaguchi, and Y. Maeno, "Gap Structure of the Spin-Triplet Superconductor Sr_2RuO_4 Determined from the Field-Orientation Dependence of the Specific Heat", Phys. Rev. Lett. **92**, 047002 (2004) (cited on page 104).

[240] R. Willa, "Symmetry-mixed bound-state order: extended degeneracy of $(d + ig)$-superconductivity in Sr_2RuO_4", May 2020, arXiv:2005.04124 [`cond-mat.str-el`] (cited on page 104).

[241] S. Raghu, E. Berg, A. V. Chubukov, and S. A. Kivelson, "Effects of longer-range interactions on unconventional superconductivity", Phys. Rev. B **85**, 024516 (2012) (cited on page 104).

[242] G. Massarelli, G. Wachtel, J. Y. T. Wei, and A. Paramekanti, "Pseudo-Landau levels of Bogoliubov quasiparticles in strained nodal superconductors", Phys. Rev. B **96**, 224516 (2017) (cited on page 108).

[243] T. Liu, M. Franz, and S. Fujimoto, "Quantum oscillations and Dirac-Landau levels in Weyl superconductors", Phys. Rev. B **96**, 224518 (2017) (cited on page 108).

[244] T. Kvorning, T. H. Hansson, A. Quelle, and C. M. Smith, "Proposed Spontaneous Generation of Magnetic Fields by Curved Layers of a Chiral Superconductor", Phys. Rev. Lett. **120**, 217002 (2018) (cited on page 108).

[245] M. Tsuchiizu, Y. Yamakawa, S. Onari, Y. Ohno, and H. Kontani, "Spin-triplet superconductivity in Sr_2RuO_4 due to orbital and spin fluctuations: Analyses by two-dimensional renormalization group theory and self-consistent vertex-correction method", Phys. Rev. B **91**, 155103 (2015) (cited on page 109).

[246] T. Takimoto, "Orbital fluctuation-induced triplet superconductivity: Mechanism of superconductivity in Sr_2RuO_4", Phys. Rev. B **62**, R14641 (2000) (cited on page 109).

[247] N. Kikugawa, C. Bergemann, A. P. Mackenzie, and Y. Maeno, "Band-selective modification of the magnetic fluctuations in Sr_2RuO_4: A study of substitution effects", Phys. Rev. B **70**, 134520 (2004) (cited on page 109).

[248] Y. Sidis, M. Braden, P. Bourges, B. Hennion, S. NishiZaki, Y. Maeno, and Y. Mori, "Evidence for Incommensurate Spin Fluctuations in Sr_2RuO_4", Phys. Rev. Lett. **83**, 3320 (1999) (cited on page 109).

[249] Y. Yanase, T. Jujo, T. Nomura, H. Ikeda, T. Hotta, and K. Yamada, "Theory of superconductivity in strongly correlated electron systems", Physics Reports **387**, 1 (2003) (cited on page 109).

[250] S. Raghu, S. A. Kivelson, and D. J. Scalapino, "Superconductivity in the repulsive Hubbard model: An asymptotically exact weak-coupling solution", Phys. Rev. B **81**, 224505 (2010) (cited on page 109).

[251] S. Wolf, T. L. Schmidt, and S. Rachel, "Unconventional superconductivity in the extended Hubbard model: Weak-coupling renormalization group", Phys. Rev. B **98**, 174515 (2018) (cited on page 109).

[252] E. U. Condon and G. Shortley, *The theory of atomic spectra* (Cambridge University Press, Cambridge, 1951) (cited on page 118).

[253] P. Coleman, *Introduction to Many-Body Physics* (Cambridge University Press, Cambridge, U.K., 2015) (cited on pages 121, 124, 125, 132).

[254] D. E. MacLaughlin, "Magnetic Resonance in the Superconducting State", in *Solid State Physics* (Elsevier, 1976), pages 1–69 (cited on page 131).